

This electronic thesis or dissertation has been downloaded from the King's Research Portal at <https://kclpure.kcl.ac.uk/portal/>



Design Strategies for Optical Tactile Sensors in Minimally Invasive Surgery

De Chiara, Federica De Chiara

Awarding institution:
King's College London

The copyright of this thesis rests with the author and no quotation from it or information derived from it may be published without proper acknowledgement.

END USER LICENCE AGREEMENT



Unless another licence is stated on the immediately following page this work is licensed

under a Creative Commons Attribution-NonCommercial-NoDerivatives 4.0 International

licence. <https://creativecommons.org/licenses/by-nc-nd/4.0/>

You are free to copy, distribute and transmit the work

Under the following conditions:

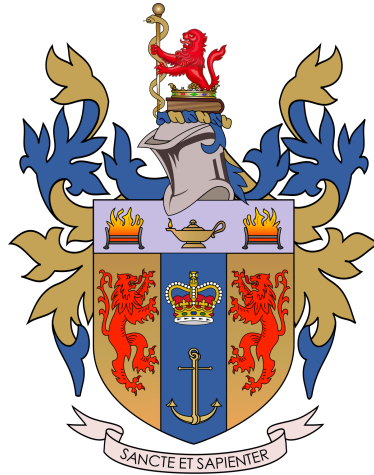
- Attribution: You must attribute the work in the manner specified by the author (but not in any way that suggests that they endorse you or your use of the work).
- Non Commercial: You may not use this work for commercial purposes.
- No Derivative Works - You may not alter, transform, or build upon this work.

Any of these conditions can be waived if you receive permission from the author. Your fair dealings and other rights are in no way affected by the above.

Take down policy

If you believe that this document breaches copyright please contact librarypure@kcl.ac.uk providing details, and we will remove access to the work immediately and investigate your claim.

Design Strategies For Optical Tactile Sensors In Minimally Invasive Surgery



by

Federica De Chiara

Submitted for the degree of

Doctor of Philosophy

SCHOOL OF BIOMEDICAL ENGINEERING AND IMAGING SCIENCES

FACULTY OF LIFE SCIENCES AND MEDICINE

KING'S COLLEGE LONDON

April 2022

The copyright in this thesis is owned by the author. Any quotation from the thesis or use of any of the information contained in it must acknowledge this thesis as the source of the quotation or information.

Abstract

The possibility to provide a sensing feedback during endoscopic interventions can significantly improve the perception of the endoscopist of the pressures applied to the inner tissues of the patient. Current sensing technologies are still too big and often present significant dead zones to be applied to flexible endoscopes. The development of sensing technologies with high spatial resolution aimed to sense normal pressures applied to the non-planar external surface of an endoscope is still an open challenge. Flexibility, sterilization, robustness and magnetic resonance compatibility are also common challenges for electronic sensors. Optical sensors can potentially fulfil these important requirements.

In this thesis three different optical sensing strategies are explored as prove of concept to expand the capabilities of current optical sensor designs. All the three approaches propose alternative methods to (i) reduce the number of optical channels, (ii) detect pressures perpendicular to the endoscope surface, (iii) enhance the spatial resolution, (iv) be fabricated through a simple and scalable manufacturing process. The sensitivity of all the three designs widely stretches over the range of pressures $[0 - 30kPa]$ usually applied during endoscopic interventions. All the three designs lend themselves to biocompatibility, sterilisation and magnetic resonance compatibility. The first design proposes an array sensor based on lab-made soft channels integrated on a rigid substrate. Its drawbacks, such as lack of flexibility and limited sensing area, are addressed by the second design presenting a flexible sensing skin able to detect pressures in any point of its surface. Fluorescence was employed to enhance the signal-to-noise ratio from ~ 22 of the first design to ~ 117 , so reaching an improvement of over 5 times. In the third design, the use of quantum dots was preferred respect to fluorescent dyes, because of their better photostability and photoefficiency. It was proved that the quantum dots based sensor can enhance the signal-to-noise ratio up to ~ 280 , so 2.5 times respect to the sensor based on fluorescent dyes. The third design also offers a sensitivity up to 3 times better respect to the first two designs, with a value of $0.020kPa^{-1}$. The piezoelectric effect of the quantum dots integrated in a polymer waveguide, allowed to simultaneously detect a pressure and provide information regarding its application point along the waveguide. This third design offers promising characteristics for the development of a sensing skin able to measure pressures applied during endoscopic interventions and it is worthy to be further investigated in future studies.

Dedication

This thesis is dedicated to my beloved parents who devoted their lives to ensure that I had all the means to reach my current achievements. I am very grateful for the love and the education they gave to me, which laid the foundations of the woman I am now.

Thank you, mom and dad.

Acknowledgements

I want to thank my mom Giuseppina and my dad Pasquale to which this thesis is dedicated. They propped up my choice to move to England and they continue to support me in all the challenges of my life.

A unique thanks to my dear husband Riccardo, who loves me with gentle care, outstanding devotion and renewed enthusiasm every day.

An exceptional thought to my brother Luca, to whom I wish complete fulfilment and great joy in his special calling.

An affectionate thought to my dearest friends, in particular Chiara and Antonio, Maria Laura, Ivana, Sesa, Eleonora and Francesco, Maria, Anastasia, Lucrezia and Francesco, Ilaria and Niccolò, Martina and Luca. A special mention to my friends in England, for having made this country from the harsh climate much warmer.

I also greet all my relatives, my uncles and cousins, always very affectionate, although the impediments in seeing each other often.

And last but not least, a special thanks to my colleagues at Oxford Lasers, who encouraged me a lot during the last months of my thesis writing and they warmly shared my joy for the successful completion of my PhD. Among the others, a particular mention to Sharron, Mike G., Kas, Lewis, Mike B., Seamus and all the directors.

TABLE OF CONTENTS

1	Introduction	1
1.1	Tactile sensors in Minimally Invasive Surgery	1
1.2	Need of Haptic Feedback in Colonoscopy	2
1.3	Force sensing technologies	5
1.3.1	Piezoresistive sensors	5
1.3.2	Capacitive sensors	8
1.3.3	Piezoelectric sensors	9
1.3.4	Optical sensors	11
1.3.5	Discussion	17
1.4	Haptic feedback technologies	19
1.5	Design specifications	20
1.6	Objective of the work	22
2	Background	25
2.1	Light interaction	25
2.1.1	Total Internal Reflection	25
2.1.2	Light transmission in optical waveguides	26
2.1.3	Role of the cladding	27
2.1.4	Reflectance, absorbance and transmittance	28
2.2	Properties of a laser source	30
2.3	Fluorescence	32
2.4	Nanomaterials	34
2.4.1	Optical properties	36
2.4.2	Core-shell QDs	38
2.4.3	Piezoelectric effect	38
3	Optical waveguide channels for 3D distributed tactile sensing	41
3.1	Sensing principle	43
3.2	Waveguide losses	44
3.3	Manufacturing process of polymer waveguides on a rigid substrate	47
3.3.1	Selection of materials	47
3.3.2	Manufacturing process	51
3.3.3	Absorption of the core material	52
3.3.4	Absorption measurement through a straight waveguide	55
3.3.5	Simulation	58
3.3.6	Bending losses	65
3.4	Single splitter	67
3.4.1	Experimental setup	68
3.4.2	Results	69
3.4.3	Simulation for design optimisation	71
3.5	Optimisation process for a multi-splitter design	73
3.5.1	Curvature optimisation	73
3.6	Multi-splitter design	76
3.6.1	Simulation	77
3.6.2	Evaluation experiments	80

3.7	Conclusion	83
4	Soft tactile skin employing fluorescence based optical sensing	85
4.1	Sensing principle	87
4.2	Manufacturing process	88
4.2.1	Angled tip realisation	88
4.2.2	Sensor fabrication	91
4.3	Imaging system	91
4.4	Results	93
4.4.1	Spectral acquisition	93
4.4.2	Calibration	93
4.4.3	Photobleaching	95
4.5	Extension to a soft tactile array sensor	97
4.5.1	Image processing algorithm	97
4.5.2	Position calculation	99
4.6	Conclusion	100
5	Design of Polymer/QDs Composites for Waveguide Applications	102
5.1	Comparison between fluorophores and QDs	105
5.2	Selection of materials	107
5.3	Manufacturing process	109
5.4	QDs-PMMA composite waveguide photostability	111
5.5	QD luminescence modulation under compression	115
5.6	Ray tracing simulation	117
5.6.1	Experimental setup	120
5.6.2	Experimental results	121
5.7	Spectral characterisation	124
5.8	QDs concentration in a waveguide	128
5.9	Reduction of acquisition time	132
5.10	Conclusion	136
6	Conclusion and future work	139
A	Touch sensing device, electronic device, earphones, and watch	143
A.1	Abstract	143
A.2	Technical field	143
A.3	Background technique	144
A.4	Summary of the invention	144
B	Design of optical waveguide channels for 3D distributed tactile sensing	146
B.1	Abstract	146
B.2	Introduction	146
B.3	Polymer waveguides for sensing	148
B.3.1	Materials and manufacturing process	148
B.3.2	Light losses and sensing principle	149
B.4	Optimisation process for sensor design	150
B.5	Evaluation experiments	151
B.6	Conclusion	153

C	Creating a Soft Tactile Skin employing Fluorescence based Optical Sensing	154
C.1	Abstract	154
C.2	Introduction	154
C.3	Sensing concepts	157
C.3.1	Total Internal Reflection and Prismatic-Tip Optical Fiber	157
C.3.2	Physical Principles of Fluorescence	158
C.3.3	Physical Design of the Sensor and Working Principle	158
C.4	Imaging system	159
C.5	Evaluation experiments	160
C.5.1	Calibration	161
C.5.2	Photobleaching	161
C.6	Extension to a soft tactile array sensor	162
C.7	Conclusion and future work	164
D	Sensing applied pressure by triggering electronic quantum many-body excitations in an optical waveguide	166
D.1	Abstract	166
D.2	Introduction	166
D.3	Results and discussion	167
D.3.1	Model of a single QD emission	167
D.3.2	Ray tracing simulation	170
D.3.3	Experimental results	175
D.4	Methods	178
D.4.1	Light propagation in a waveguide	178
D.4.2	Waveguide fabrication	178
E	Image processing algorithm for ROI identification	180

LIST OF TABLES

1.1	Pressure sensors. Advantages and disadvantages of piezoresistive, capacitive, piezoelectric and optical sensors.	18
3.1	Beam reducer effect. Laser beam parameters and simulated output power with and without using the beam reducer.	61
3.2	Study of divergence modulation. Simulated light loss due to the increase of beam divergence.	63
3.3	Bending losses. Experimental results.	66
3.4	Bending losses. Simulation results.	66
3.5	Curvature losses. P_{out} ratio and absorption coefficient α across the waveguide curvature radius.	67
3.6	Splitter configuration. P_{out} ratio at the output of each one of the two channels varying α	72
3.7	Splitter configuration. P_{out} ratio at the output of each one of the two channels varying the section shape.	72
3.8	Splitter configuration. P_{out} ratio at the output of each one of the two channels varying the section shape.	75
3.9	Simulation parameters. Divergence modulation on a multi-splitter configuration.	79
6.1	Design strategies comparison. Advantages and disadvantages in relation to the requirements for the application to endoscopy.	142

FIGURE TABLE

1.1	Examples of commercially available robotic MIS system. (a) “Da Vinci System” by intuitive surgical [12], (b) “Flex Robotic System” by Medrobotics (readapted from [13]) and (c) “SPORT robotic system” by Titan medical (readapted from [14]).	2
1.2	Colon anatomy. Parts of the colon (readapted from [16]).	3
1.3	Working principle of flexible piezoresistive sensors. The polymer matrix is doped with conductive material and placed between two flexible undoped, nonconductive layers. When subject to an external force the volume of the doped layer decreases as its resistance thanks to the higher density of the dopant particles that get closer. Picture from [43].	7
1.4	Working principle of a capacitive pressure sensor. One the sensor is subject to a compressive external force the distance between the two capacitor plates decreases increasing the overall capacity of the device. Picture from [43].	9
1.5	Working principle of piezoelectric sensors. When subject to a force the material molecules react by dislocating with respect to their unperturbed position and generates an electric field. Picture taken from [43].	10
1.6	Examples of intensity modulation optical force sensors. (a) 1D force sensor. Two fibres, one emitter and one receiver, are aligned in front of reflective surface. When a force is applied the distance between the reflective surface decreases and the signal intensity detected by the receiver increases accordingly [66]. (b) 1D force sensor with reference fibre. The principle is the same as (a) but this time receiver and emitter are the same fibre. The backward and forward signal are split outside the sensing head via an optical beam coupler. A second pair of receiver and emitter is used as a reference signal to compensate any misreading due to the bending of the fibre [69]. (c) 3D force sensor. 8 fibre sensor head: 2 are the receiver and emitter for the reference signal, while the reaming 6 provides, via a 3 points feedback, the position of a reflective surface. The reflector is free to move in XYZ and constitutes the pivot point of a roller [68].	13
1.7	Working principle of an FBG. A narrowband spectral line within a broadband light source will undergo constructive interference in reflection if satisfies the Bragg Law. The central wavelength of the reflected signal depends on the pitch of the grating and the effective index of refraction of the fibre. Picture taken from [70].	14
1.8	Example of 3D FBG sensor from [73]. 3 FBG are placed on 60 degrees configuration on the final section of the tool shaft. By receiving an independent feedback from each FBG the force vector components in XY and Z can be calculated and the full force direction established.	15

1.9	Fabry Perot interferometer. (a) Schematic of a Fabry Perot interferometer and an example of interference pattern generated by the device. The light source is channelled into the cavity composed by M1 and M2 mirrors. M2 is only partially reflective. When the light is recombined after exiting the cavity by a focusing lens an interference pattern is generated. Picture readapted from Wikipedia. (b) a guided fiber based FP resonator. The cavity is formed between two fiber sections. The cleaved faces of the sections are employed as cavity mirrors. When a force is applied the cavity length d is reduced and the interference pattern generated by the signals R1 and R2 changes accordingly. Picture readapted from [76]. (c) An example of unguided FP fiber sensor. In this case M1 and M2 are obtained by thin film deposition directly onto the fiber. When a pressure is applied, the cavity length L changes and so does the relative phase difference between the two backward signals. Pictures taken from [77].	16
1.10	Example of a 3D Fabry Perot Fiber sensor. 3 Fibers are arranged in a triangular pattern to define tip, tilt and Z position of a needle for eye surgery. Picture readapted from [78].	17
2.1	Total internal reflection. (a) Light transmission through an interface between two media (readapted from [98]). (b) When the incidence angle is higher than the critical angle, total internal reflection (TIR) occurs (readapted from [98]).	26
2.2	Refractive-index profile in a waveguide. (a) Basic structure of a refractive-index profile of the optical waveguide. (b) This configuration allows to change the propagation direction of 90° .	27
2.3	Role of the cladding. Comparison between light transmission in a waveguide without cladding (a) and with cladding (b).	28
2.4	Light interaction with a substance. A monochromatic light interacting with a sample is partially reflected, absorbed and transmitted. The emergent light I has lower intensity than the incident light I_0 .	29
2.5	Gaussian source. Gaussian irradiance profile. The emergent light I has lower intensity than the incident light I_0 .	32
2.6	Fluorescence. (a) Excitation light is absorbed causing an electron of a molecule to leave the ground state and reach a higher energy level. Fluorescence occurs when the electron relaxes again to its ground state by releasing energy in the form of visible light (fluorescence). (b) Typical absorption and emission spectra of Rhodamine B (readapted from [103]).	33
2.7	Nanomaterials and their density of electron states. Schematic representation of zero-dimensional (0D), one-dimensional (1D), two-dimensional (2D), and three-dimensional (3D) nanomaterials and density of electron states of a semiconductor by varying dimension, where $g(E)$ is the density of states (fig. from [111]).	35
2.8	Band gap tunability. (a) Valence and conduction bands of bulk materials are continuous, while nano-scale materials present discrete energy levels (fig. readapted from [111]). (b) The band gap increases by decreasing the material size.	36

2.9	Fluorescence modulation across the nanoparticle size. (a) Fluorescence of CdSe-CdS core-shell nanoparticles with a diameter of 1.7nm (blue) up to 6nm (red), giving evidence of the scaling of the semiconductor bandgap with particle size. (b) Schematic representation of the size effect on the gap between the valence band (VB), the conduction band (CB), the absorption (up arrow) and fluorescence (down arrow). Smaller particles have a wider band gap (fig. readapted from [117]).	37
2.10	Bandgap alignment in core/shell QDs. Scheme of the bandgap alignment between the core (black) and the shell (red) material in a core-shell system. From left to right: Type I, Type II (two cases) and Inverse Type I. Fig. readapted from [123].	39
2.11	Wurtzite structure. (a) Wurtzite structure of semiconducting materials such as CdSe. (b) Sublattice of Cd and Se atoms with tetrahedral coordination between each other, in the resting condition. (c) Generation of dipoles and piezo-potential when the sublattice is under compression (fig. readapted from [130]).	40
3.1	Distributed pressure sensing based on optical waveguides. The light travels through the channels of the waveguide structure and it is measured by a camera [143].	43
3.2	Sensing principle of microbending. (a) Optical waveguides use TIR to transmit light through the core. (b) When a force is applied on the waveguide, a deformation of the core may occur and the conditions for TIR may not be satisfied anymore, determining light attenuation detectable at the output of the waveguide.	44
3.3	Light coupling from a collimated laser source to a multi-mode waveguide. Coupling losses are mainly due to a beam displacement with respect to the waveguide optical axis: axial displacement, when the beam propagates parallel to the optical axis but it is not collinear to it (a), angular displacement when the laser doesn't propagate parallel to the optical axis (b) and imperfect finish of the waveguide surfaces resulting in the beam not being perpendicular to the waveguide tip (c).	46
3.4	Polymer waveguide channels on rigid substrate. Multi-splitter configuration of soft core channels (refractive index of ~ 1.5 for commercial plastic optical fiber) integrated on a rigid cladding substrate fulfilling the role of cladding (refractive index of ~ 1.4 for commercial plastic optical fiber).	48
3.5	Optical characterisation of the core material. (a) Transmission rate relative to air considering a 1cm path length. (b) Dispersion diagram measured at 25°C. Plots re-adapted from product data sheet (Nusil, LS1-3252).	50
3.6	Manufacturing process. A CNC machined PTFE part is used as mould, a soft material with refractive index higher than PTFE is injected into the machined channels, a PTFE sheet is used as cover and the mould is left drying.	52
3.7	Fabrication of the core material sample. A CNC machined mould made by two parts which can be unscrewed facilitates the removal of the sample, once cured. The resulting sample seems to have pretty smooth surfaces and good transparency.	53

3.8	Absorption rate of core material. Measured through a sample of $9mm$ thickness over the visible range between $[350 - 550]nm$. The error on each measurement is lower than 1%.	55
3.9	Experimental setup. The laser light is coupled into the waveguide and measured at the output by the detector.	56
3.10	Absorption coefficient. Light propagation through the waveguide across its length.	58
3.11	PTFE optical properties. Transmittance rate (readapted from [151]) and dispersion data (readapted from [152]).	59
3.12	Simulation setup. (a) Straight waveguide with semicircular section with radius of $1.5mm$ and length of $10cm$. (b) Light injected perpendicularly into the input facet. (c) Light collected by a detector (white rectangle) placed right in front of the output facet.	61
3.13	Section of the waveguide core $20\mu m$ after the input surface. The intensity is not uniform but more intense at the centre, because a laser beam is gaussian.	62
3.14	Divergence angle of the light source. Dependence of the power ratio across the divergence angle θ_d	63
3.15	Roughness on a CNC-machined PTFE part. (a) Image re-adapted from [153]. (b) Component parallel to the light propagation direction. (c) Perpendicular component. (d) Output power across the length of a waveguide with perpendicular component of roughness.	64
3.16	Bending losses measurement. Moulded waveguides with different curvature radius. Light is injection onto the input facet and collected from the output facet by a power meter.	65
3.17	Light loss in bent waveguides. Bending losses across the curvature radius of the waveguide were obtained experimentally (yellow trend) and by simulation (blue trend).	67
3.18	Single splitter design. An initial straight channel divergences in two output channels.	68
3.19	Single splitter setup. The force is applied by a metal probe mounted on a translation stage.	69
3.20	Evaluation experiments. (a-b) Calibration results for channel 1 and 2 of the splitter. (c-d) Hysteresis results for channel 1 and 2 of the splitter. . .	70
3.21	Section geometry of the waveguide core. Three section geometry have been considered: U-shape, semicircular and rectangular section.	72
3.22	Curvature study. Optimisation of the curvature of a single branch of a multi-splitter design.	74
3.23	Curvature study. Optimisation of the curvature of a single branch of a multi-splitter design.	75
3.24	Multi-splitter configuration. (a) Enlarged U-shape section. (b) Final design with detail of channels separation.	77
3.25	Simulation results. (a) Sub-splitter configuration simulated individually. (b) Output power ratio for each sub-splitter.	78
3.26	Simulation results. (a) Output ratio modulation for the divergence angle of the beam equal to $\theta_d = 0.04rad$, (b) $0.08rad$, (c) $0.12rad$ and (d) $0.21rad$	79

3.27	Experimental setup. The laser light is coupled into the device and an optical fiber carries the light from the output to the camera for detection. The core is compressed by a metal rod mounted on a calibration force sensor.	81
3.28	Evaluation results. Calibration curve of the force across the intensity measured by the camera.	82
4.1	Tactile skin for medical tools. The design is adaptable to non-planar surfaces such as the outer surface of an endoscope [155].	87
4.2	Tactile skin. (a) Design of the sensor. (b) The same fiber is used as emitter and receiver thanks to the combined effect of fluorescence and the angled tip optica fiber. (c) When a pressure is applied, the deformation causes the enhancement of the fluorescent emission measured. (d) The prototype of tactile skin equipped with four tactile elements has a compact geometry, it is compressible and flexible.	88
4.3	Angled tip fiber fabrication and integration. (a) The fiber is cut with a cleaver equipped with a sharp blade. (b) A polishing disc with the same cut angle of the fiber is used for lapping. (c) Once the fiber has a very clean and smooth surface, it can be placed and fixed into the mould where the soft material of the sensor body will be poured in. This ensures that the fiber is integrated into the sensor body after curing.	89
4.4	Polishing procedure. (a) After the cleaver cut, the fiber presents a broken surface. Fiber surface after being polished using a sheet with granularity of $3\mu m$ (b), $1\mu m$ (c) and $0.3\mu m$ (d). The fiber looks very smooth (e) and the cut at 45° well defined (f).	90
4.5	Fluorescence imaging system. The excitation light (green arrow) is reflected at 90° and reaches the sensor. Then, fluorescence emission is released by the dopped silicone layer and transmitted back to the camera (yellow arrow).	92
4.6	Acquired spectra. (a) Original light source spactrum. (b) Narrowed light source spectrum. (c) Coexistence of excitation light and fluorescence emission. (d) Light source is completely filtered out. Thus, the camera of the imaging system just detects the fluorescence signal.	94
4.7	Experimental evaluation. (a) scheme of the experimental setup employed for pressure measurements (b) Calibration curve: 30 measurements for each point were acquired to carry out the repeatability experiment.	94
4.8	Measure of photobleaching. The slope of the intensity decay over 8 hours was measured three times, giving values within the same order of magnitude.	96
4.9	ROI identification. (a) Starting image. (b) The image is cropped in four sub-images. (c) Selection of the intensity threshold. (d) Presence of multiple selected regions and gaps. (e) Identification of pixels belonging to the fiber output. (f) ROI identification of the four fibers.	98

4.10	Measurement of the application point of the pressure on the sensor. A pressure was applied on five different locations of the flexible array sensor: on the tip of each of the four fibers (grey circles) and at the center of the sensor. The sensor was pressed 10 times for each location, using a probe with a diameter of $3mm$. The blue circles represent the real position of the probe. An algorithm calculates the centre of mass on the basis of the intensity of the four fibers to evaluate the point of the pressure application (red dot). The error is the standard deviation of the repeated measurements and corresponds to the radius of the red circles.	100
5.1	Skin of waveguides dopped with QDs. The application of multiple fluorescent waveguides to the external surface of an endoscope constitutes a sensing skin able to return pressure feedback.	104
5.2	Waveguide manufacturing process. The PMMA powder is diluted, QDs are added and mixed together, the solution is left in a ultrasonic bath for air bubbles removal and then injected into PTFE tubes. The waveguide is left curing at 60°	110
5.3	Waveguide prototype. The plain waveguide (without QDs integration) is (a) transparent and (b) flexible. (c) The light injected at the input is transmitted through the waveguide and (d) reaches the output. (e) Final design of QDs-PMMA composite waveguide. (f) Fluorescence emission of the composite waveguide irradiated with UV light.	111
5.4	Plain VS QDs-PMMA waveguide (WG). Output spetrum of a plain waveguide (without integration of QDs) and a QDs-PMMA composite waveguide. The photoluminescence emission is clearly visible in the latter (yellow peak stretching over the range $[550 - 650]nm$).	112
5.5	Photobleaching of QDs-PMMA composite waveguide. (a) Amplitude and (b) wavelength decrease across the time. (c) Measure of wavelength decrease across the time from literature [209].	114
5.6	Single QD photoemission spectra. Normalised emission spectra of a single QD: the feature blue-shifts and increases in amplitude under compression.	116
5.7	Ray-tracing outcomes. a) Stacked bar chart illustrating the breakdown of ray tracing events. b) Stacked histograms resolved in wavelengths showing the further split of the 'Emission' events in a) with a force of $6\ nN$ applied on the quantum dots of the middle waveguide segment. c) Wireframe structure diagram of a scaled down example of the ray tracing simulation.	118
5.8	Simulated trend of the intensity and wavelength. a) Theoretical amplitude of the photonic distribution measured at the detector as a function of the applied force, where the latter is applied near the detector (source) and labelled in blue (green). The applied forces (F) are normalised by the saturation limit (F_{sat}). b) Wavelength shift of the maxima of the distribution's peak, as a function of waveguide compression.	119
5.9	Schema of the experimental setup. A probe mounted on a calibration force sensor apply a pressure on the waveguide at different distances from its input surface. The modulation of photoluminescence emission is detected by a spectrometer.	120

5.10	Amplitude modulation and wavelength shift calibration. The waveguide was compressed on two different locations: 3 <i>cm</i> and 4 <i>cm</i> from its input surface. For each force value, amplitude modulation a) and wavelength shift b) were measured.	122
5.11	Time-dependent relaxation of the polymer waveguide. a) The amplitude modulation $A(t)$ shows a negative exponential behaviour, typical of stress-relaxation in viscoelastic materials. b) The wavelength shift presents a linear fashion.	123
5.12	Spectral characterisation of CdSe/ZnS QDs diluted in toluene. (a) Experimental setup. (b) Normalised excitation spectra and (c) normalised emission spectra for each wavelength sub-range. (d) Absorbance spectrum of CdSe/ZnS QDs as provided by the supplier.	125
5.13	Excitation light wavelength. (a) Light is injected into the PMMA-QDs composite waveguide by a collimated laser and the spectrum is acquired by a spectrometer. (b) Output spectra obtaining by exciting the waveguide using two laser with different wavelength emission (at 532nm and at 355nm). (c) The photoluminescence peak is slightly higher when the UV light source is used.	127
5.14	Relation between QDs concentration and waveguide diameter. Emission spectrum across different QDs concentrations for a waveguide with diameter of (a) $\sim 1mm$, (b) 2mm and (c) 3mm.	129
5.15	Wavelength shift across the QDs concentration. Photoluminescence red-shift across the concentration increase.	131
5.16	Experimental setup. (a) The laser injects light into the waveguide. The output signal is collected by the spectrometer and recorded by the PC. (b) The waveguide is firmly fixed to the breadboard at its two tips and is pressed by a circular probe with diameter of 8.0mm.	133
5.17	Experimental setup: alignment improvement. Light collected by the spectrometer without use of any lens. The alignment was improved introducing two degree of freedom for the spectrometer to translate in the plane X-Y.	134
5.18	Photoluminescence signal enhancement. (a) Photoluminescence signal obtained using the first presented version of the experimental setup. (b) Photoluminescence signal obtained using experimental setup with improved alignment capability. The integration time is reduced up to a factor of 10.	135
5.19	Photoluminescence signal enhancement. The photoluminescence signal is increased of a factor of ~ 2.25 by doubling the QDs concentration in the waveguide.	136
B.1	Distributed pressure sensing based on optical waveguides. The light travels through the channels of the waveguide structure and it is measured by a camera.	149
B.2	Waveguide channels with multi splitter design. Several splitters have been coupled to create a complex design able to equally split the light at the output of the 8 branches. The power percentage at the output of each branch of the three sub-splitters was obtained through simulation.	151

B.3	Setup and experimental results. (a) The sensor has an 18 mm height, a 48 mm length and a 3.0 mm depth. The output channels are 2 mm distant from each other, providing a good spatial resolution. The eight sensing elements are red circled. (b) Calibration and hysteresis of the eight output channels.	152
C.1	Stretchable tactile array sensor based on fluorescence. (a) Light passing through two transparent media with different refractive indices is totally internal reflected When the incidence angle is higher than the critical angle (readapted from [98]). This is applicable to optical fibers where the tip is cut at an angle higher than the critical angle. (b) Absorption and emission spectra of Rhodamine B are presented (readapted from [103]). (c) The proposed sensor is characterized by a layer structure of soft material. The optical fiber is embedded into the lower transparent layer. Its angled tip implements the TIR principle: the light of the light source (green arrow) reaches the fluorescent layer and the fluorescence emission (yellow arrow) is transmitted by the fiber to the imaging system. When a force is applied to the sensor, the lower surface of the fluorescent layer gets closer to the fiber and a higher light intensity can be detected by the camera. (d) The use of multiple optical fibers can lead to a flexible tactile array sensor. (e) The proposed sensor can be applied to the external surface of medical tool shafts, such as the one of an endoscope.	156
C.2	Experimental setup and acquired spectra. (a) The array sensor is connected to the fluorescence imaging system using a bundle of angled tip optical fibers. The light emitted by the LED reaches the sensor which consequently emits fluorescence light. (b) As a result of the applied filtering system, the spectra of the excitation light source and fluorescence emission cover different wavelength ranges. Thus, the camera of the imaging system is able to detect the fluorescence signal filtering out the light source completely.	160
C.3	Experimental evaluation. (a) Calibration curve: 30 measurements for each point were acquired to carry out the repeatability experiment. (b) Measure of photobleaching: the slope of the intensity decay over 8 hours was measured 3 times, giving values within the same order of magnitude.	162
C.4	Measurement of the application point of the pressure on the sensor. A pressure was applied on five different locations of the flexible array sensor: on the tip of each of the four fibers (grey circles) and at the center of the sensor. The sensor was pressed 10 times for each location, using a probe with a diameter of 3mm. The blue circles represent the real position of the probe. An algorithm calculates the centre of mass on the basis of the intensity of the four fibers to evaluate the point of the pressure application (red dot). The error is the standard deviation of the repeated measurements and corresponds to the radius of the red circles.	164

D.1	Single QD photoemission spectra. a) Normalised emission spectra of a single QD: the feature blue-shifts and increases in amplitude under compression. b) Heat map of the single QD photoemission effect under compression (in vacuum). The lower wavelength band (pointed out by the black arrow) corresponds to the Lorentzian peak, whereas the upper wavelength band (in the dashed box) corresponds to the piezoelectric dipole emission. Dotted-line box indicates the region shown in c). c) Dotted line as a guide to the eye for the blue shift trend of the piezo-electric feature under compression. The colour scheme for b) is logarithmic whereas c) is linear.	169
D.2	Ray-tracing outcomes. a) Stacked bar chart illustrating the breakdown of ray tracing events. b) Stacked histograms resolved in wavelengths showing the further split of the 'Emission' events in a) with a force of 6 nN applied on the quantum dots of the middle waveguide segment. c) Wireframe structure diagram of a scaled down example of the ray tracing simulation.	171
D.3	Statistical analysis of simulated detected photons. a) Spectral analysis of the detected photons after transmission through the waveguide, colour coded into three groups: $\lambda \leq 650 \text{ nm}$, $650 \text{ nm} < \lambda \leq 800 \text{ nm}$ and $800 \text{ nm} < \lambda$. b) Spatially resolved cross-section of the measured photons. c) Angular distributions in terms of normalised momentum vector with respect to the c) perpendicular and d) parallel components.	173
D.4	Simulated trend of the intensity and wavelength. a) Theoretical amplitude of the photonic distribution measured at the detector as a function of the applied force, where the latter is applied near the detector (source) and labelled in blue (green). The applied forces (F) are normalised by the saturation limit (F_{sat}). b) Wavelength shift of the maxima of the distribution's peak, as a function of waveguide compression.	174
D.5	QDs piezoelectric effect in composite polymer waveguides. a) Schema of the experimental setup. b) Output spectrum of a plain polymer waveguide (without QDs) and a QDs-doped waveguide. c) Waveguide prototype: compact, flexible and compressible.	175
D.6	Amplitude modulation and wavelength shift calibration. The waveguide was compressed on two different locations: 3 cm and 4 cm from its input surface. For each force value, amplitude modulation a) and wavelength shift b) were measured.	176
E.1	ROI detection algorithm. Flow chart for the algorithm of identification of the ROI for each fiber contained in the starting image.	185

GLOSSARY

ABS Acrylonitrile Butadiene Styrene.

BL Bending Losses.

BPP Beam Parameter Product.

CB Conduction Band.

CL Coupling Losses.

CNC Computer Numerical Control.

CNT Carbon Nanotube.

DC Direct Current.

DMF Dimethylformamide.

FBG Fiber Bragg Gratings.

FL Fresnel Losses.

fPCBs Flexible Printed Circuit Boards.

FWHM Full Width at Half Maximum.

GOFs Glass Optical Fiber.

IL Insertion Losses.

LDR Light Dependent Resistor.

LED Light Emitting Diode.

MEI Magnetic endoscopic imaging.

MIS Minimal Invasive Surgery.

MRI Magnetic Resonance Imaging.

NA Numerical Aperture.

PC Polycarbonate.

PDMS Polydimethylsiloxane.

PE Polyelectrolytes.

PL Propagation Losses.

PLQY Photoluminescence Quantum Yield.

PMMA Polymethyl Methacrylate.

POFs Plastic Optical Fibers.

PP Polypropylene.

PVA Polyvinyl Alcohol.

PVDF Polyvinylidene Fluoride.

PZT Lead Zirconate-Titanate.

QD Quantum Dot.

QE Quantum Efficiency.

QY Quantum Yield.

ROI Region of Interest.

SQDs Semiconductor Quantum Dot.

TIR Total Internal Reflection.

UV Ultra Violet.

VB Valence Band.

List Of Publications

Patents

- Wang Steven, Liu Hongbin, Hu Jian, De Chiara Federica and Ni Gang. "Touch sensing device, electronic device, earphones, and watch". European patent ltd. Huawei Technologies co. Dec. 23, 2021. URL: <https://patents.google.com/patent/WO2021253420A1/en?q=WO2021253420A1>.

As co-author of this patent, I was a significant contributor to many aspects of the studies. I have verified the functioning of the working principle of this technology through simulations using the professional software Optic Studio by Zemax, and through experimental measurements. I have worked on the improvement and optimisation of the technology design and collaborated with the team on the drafting of the patent. Part of the patent is reported in Appendix [A](#).

Journal Papers

- De Chiara Federica, Wang Shuxin and Liu Hongbin. "Creating a Soft Tactile Skin Employing Fluorescence Based Optical Sensing". In: *IEEE Robotics and Automation Letters*, Vol. PP, 2020. DOI: [10.1109/LRA.2020.2976303](https://doi.org/10.1109/LRA.2020.2976303).

As the first author of this manuscript, I have worked on all aspects of the study as well as the manuscript preparation. Specifically, I have worked on design study of both tactile skin and setup for testing, data collection and analysis, writing of the manuscript. The full paper is reported in Appendix [C](#).

- De Chiara Federica, Hovan Lee, Cedric Weber and Liu Hongbin. "Sensing applied pressure by triggering electronic quantum many body excitations in an optical waveguide". 2022. Pre-print available at: [arXiv:2106.13004](https://arxiv.org/abs/2106.13004).

This manuscript comes from a joint collaboration with the Physics department of King's College London. I was a significant contributor to the study as well as the manuscript preparation. Specifically, I focused on the design of the sensing optical waveguide,

collection of all data, interpretation of the data and analysis. Dr Cedric Weber, Reader at the Physics department, supervised the research, providing guidance and support throughout the entire process. One student of his team, Hovan Lee, worked on the simulation analysis. I worked on the writing of the manuscript with the help of Hovan, who has integrated with the sections regarding the simulation analysis. The full paper is reported in Appendix [D](#).

Conference Papers

- De Chiara Federica, Hu Jian, Wang Stephen, Wang Rong and Liu Hongbin. "Design of optical waveguide channels for 3D distributed tactile sensing". In: *IEEE Sensors, 2021*. DOI: [10.1109/SENSOR47087.2021.9639611](https://doi.org/10.1109/SENSOR47087.2021.9639611).

As the first author of this manuscript, I have worked on all aspects of the study as well as the manuscript preparation. Specifically, I have worked on design study of both optical waveguide channel and setup for testing, data collection and analysis, writing of the manuscript. I have personally presented this work at the IEEE International Conference IEEE Sensors 2021. The full paper is reported in Appendix [B](#).

- De Chiara Federica, Wang Shuxin and Liu Hongbin. "Creating a Soft Tactile Skin Employing Fluorescence Based Optical Sensing". In: *IEEE International Conference on Robotics and Automation (ICRA) 2020*. DOI: [10.1109/LRA.2020.2976303](https://doi.org/10.1109/LRA.2020.2976303).

As the first author of this manuscript, I have worked on all aspects of the study as well as the manuscript preparation. Specifically, I have worked on design study of both tactile skin and setup for testing, data collection and analysis, writing of the manuscript. I have personally presented this work at the IEEE International Conference on Robotics and Automation (ICRA) 2020. The full paper is reported in Appendix [C](#).

Conference Posters

- De Chiara Federica, Frisani Mauro, Greco Michela and Bussa Maria. "Analisi della densitometria del cristallino attraverso il processamento di immagini Scheimpflug". In: *X Italian Optometry society (SOptI) congress, 2014*. DOI: [10.13140/RG.2.2.25911.57763](https://doi.org/10.13140/RG.2.2.25911.57763).

This poster comes from the work carried out during my Master thesis at University of Turin, Italy. As the first author of this poster, I have worked on all aspects of the study,

such as the data collection, interpretation and analysis. This work was presented at the X Italian Optometry society (SOptI) congress 2014.

Chapter 1

Introduction

1.1 Tactile Sensors In Minimally Invasive Surgery

Over the last 50 years Minimal Invasive Surgery (MIS) has progressively replaced traditional surgery, meeting patient demands for smaller incisions which lead to reduced postoperative pain, shorter hospital stay, decreased surgical site infections, and faster recovery time [1, 2]. More recently MIS has benefitted from the broad application of robotic aid unlocking surgical intervention in increasingly more constrained environment with higher precision and miniaturisation (fig. 1.1). This is possible thanks to the robotic system additional degrees of freedom compared to the human wrist and arm, firmness of position at constant speed, and the high resolution of both movements and vision. Despite all these advantages robotic assisted MIS is not necessarily quicker with respect to manual minimal invasive surgery [3]. One of the reasons for this inefficiency is the lack of haptic sensing associated to the lack of a direct contact between the surgeon and the patient body [4]. This can lead first to an extremely steep learning curve, where only experience surgeons can confidently operate a MIS robotic system solely based on visual feedback [4, 5]. Second, the lack of the sense of touch can lead to the application of an inadequate pressure during intervention. Surgeons usually rely on their sense of touch to estimate the correct amount of pressure and evaluate the area of intervention. Providing a real time during robotic assisted MIS, haptic feedback has therefore become a priority in recent years [6]. Combining haptic feedback with high resolution imaging during surgical intervention has proven to not only further enhance the surgeon accuracy but also the intervention speed even under stressing conditions [7, 8]. It would also prevent the application of excessive pressures with consequent damage or perforation of internal tissues [9], allow to apply the pressure only where needed [10], and reduce patient discomfort which is one of the main reason preventing people from attending periodic screening tests [11].



Figure 1.1: **Examples of commercially available robotic MIS system.** (a) “Da Vinci System” by intuitive surgical [12], (b) “Flex Robotic System” by Medrobotics (readapted from [13]) and (c) “SPORT robotic system” by Titan medical (readapted from [14]).

1.2 Need Of Haptic Feedback In Colonoscopy

Colonoscopy is a medical procedure aimed to the examination of the colon for diagnosis and treatment, which requires the insertion of a long flexible tube with a camera and light via the anal canal. The insertion tube of most adult colonoscopes is approximately $1.6m$ long and its external diameter ranges from $12mm$ up to $15mm$. It has a camera with light illumination on the tip, a waterjet lens cleaning, air and water insufflation and one or two channels with the dual capability of biopsy and suction to remove residual stool [15]. The colonoscopy procedure is prone to not only discomfort for the patient, but also potential injury to the colon wall, as the scope is inserted into the rectum and advanced through the colon. The anatomy of the colon presents several flexures, as shown in fig. 1.2:

- The cecum is the first part of the colon in the lower right abdomen. From there, the ascending colon travels up the right side of the abdomen. A first flexure can be identified between the ascending colon and the transverse colon, which runs across

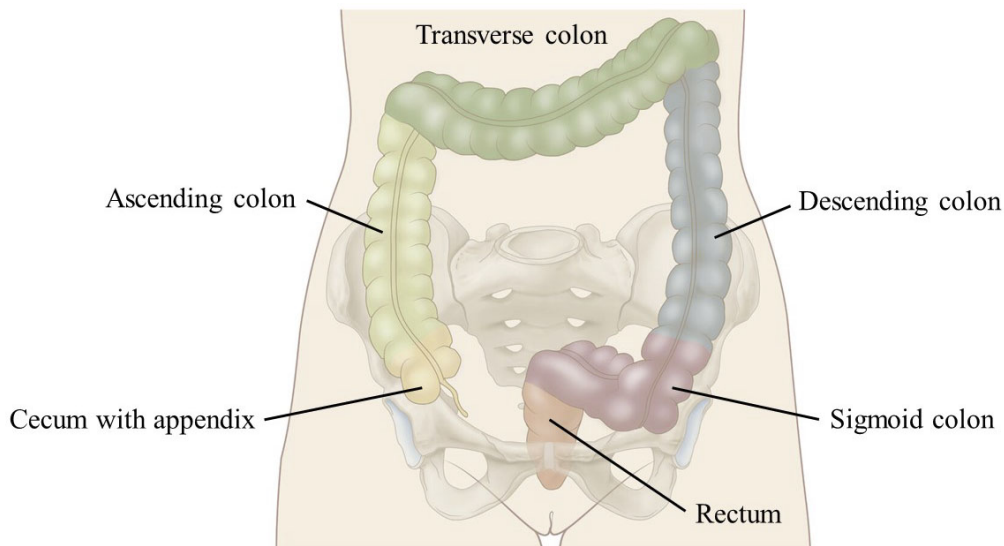


Figure 1.2: **Colon anatomy.** Parts of the colon (readapted from [16]).

the abdomen.

- A second flexure is between the transverse colon and the descending colon, which travels down the left abdomen.
- A third flexure is between the descending colon and the sigmoid colon, which is a short curving section of the colon just before the rectum.
- A fourth flexure is identifiable between the sigmoid colon and rectum.

Frequently, these anatomic flexures result in loops being formed by the flexible scope as it is advanced through the colon. These loops are responsible for the majority of the discomfort during the procedure, and can increase the risk of complications during the intervention such as internal bleeding, splenic injury and colon perforation [17].

Bleeding is a rare complication [18], but is seen more frequently caused by therapeutic maneuvers from the endoscopist to prevent looping or to straighten already formed loops. Splenic injury, generally caused by a direct blow (trauma) to the spleen, is a rare but serious complication from colonoscopy that can result in significant intraperitoneal bleeding and it is usually a result of blunt injury and looping [19]. Colon perforation, although rare with incidence ranging from 0.03% to 0.65% [20, 21], commonly require surgical interventions and can imply mortality risk [22, 23]. However mechanical trauma from loop formation results in the most significant damage to the colon wall [24]. Given the high number of colonoscopy procedures performed, and the severity of the resulting complications, even

rare complications remain a significant concern.

The fear for complications and discomfort makes patients less willing to undergo colonoscopy procedures [25]. In colonoscopic screening regimens, which require regular interval examinations, maximising patient compliance is crucial to the success of the program.

Hence, the introduction of a technology able to prevent or reduce the formation of loops which introduces discomfort and risk of complications represents an important achievement in endoscopy.

Magnetic endoscopic imaging (MEI) provides a realtime three-dimensional visualisation of the colonoscope, which allows the endoscopist to see when loops are being formed and intervene to avoid their formation through different operations, such as repositioning the colonoscope by twisting and retracting the shaft, applying counter-pressure to the patient's lower abdomen or changing the positioning of the patient [26, 27].

Some studies have demonstrated that MEI helps decreasing procedural times and pain for the patient, when compared with standard colonoscopy [28]. However, the capability to intervene when the MEI shows the possible occurrence of a loop formation is strongly dependent on the experience of the endoscopist, since the required techniques demand subtle manipulation of the scope and careful decision-making to promptly choose the appropriate strategy. It was also verified that expert endoscopists are able to advance the scope through the colon with a reduction in colonic displacement, then containing the discomfort for the patient, compared to their novice counterparts [17].

The learning curve for endoscopy, and similarly the decline in complication rates, extends beyond the training period for many endoscopists, and into practice. Hence the need to integrate the visual information provided by the MEI with a quantitative feedback about the amount of pressure being applied. The combination of visual and tactile feedback would be a crucial advancement in colonoscopy and a potential marker of competence that could be incorporated into colonoscopy training programs. Specifically, a technology able to provide measurements of force along the shaft of the colonoscope would provide a valuable and immediate feedback for both trainees and practicing endoscopists. The benefits of haptic feedback typically include increased manipulation accuracy, increased perception accuracy, decreased completion time, and decreased peak and mean force applied to the remote environment [29, 30, 31, 32, 33], with the consequent effect to reduce discomfort for the patient and rate of complications during the procedure.

The main challenge for which the current surgical robots have very limited haptic

feedback is related to the grounded forces outputted by the sensing technology, which can lead to undesired oscillations of the system interfering with the surgery and being dangerous for the patient [34, 35]. To avoid stability issues, many researchers have turned to sensory substitution techniques, wherein force information is presented via an alternative feedback channel, such as vibrotactile [36], auditory [37], or visual cues [38]. However, although sensory substitution techniques make teleoperation systems intrinsically stable, the stimuli provided substantially differ from a force feedback and no haptic forces are displayed to the operating surgeon. For these reasons, sensory substitution often shows performance inferior to that achieved with unaltered force feedback [35, 33].

The development of technologies able to get haptic feedback without compromising the stability of the system is still an open challenge which, if addressed, would determine a crucial advancement in colonoscopy for both training programs and medical procedures for use in patients. For educational use, such a device would supplement current simulators to alert trainees of unsafe force application as they develop their skills handling the instrument. In clinical use, an immediate force feedback would help minimising the discomfort for the patients and, most importantly, maximising safety during the procedure.

1.3 Force Sensing Technologies

Every MIS application will impose on a given sensing technology different requirements in terms of sensitivity, dynamic range and response time. Several methods have been exploited to develop performing tactile sensors. The most diffuse technologies for flexible pressure sensing are piezoresistive, capacitive, piezoelectric and optical sensors [39, 40]. Some of these technologies have been employed to obtain haptic feedback in endoscopic interventions as detailed later, in section 1.4.

1.3.1 Piezoresistive sensors

Piezoresistive sensors are devices that experience a change of resistance when subject to an external force. The resistance R of a material can be defined as

$$R = \rho \frac{L}{S} \quad (1.1)$$

where ρ is the material resistivity, L is the length of the resistor and S is the resistor cross section area. They are some of the most widely used sensor technology for tactile

application [41]. Piezoresistive sensors are referred as active sensors, since they need a constant current flow to read out any resistivity change. The change of resistance can be caused by either a change of the sensor geometry (length and section) or a change of the material resistivity. The sensitivity S of a piezoresistive sensor can be defined as

$$S = \frac{\Delta R}{\Delta P} \quad (1.2)$$

where ΔR is the resistance variation in response to the application of a force and ΔP is the pressure difference. Ideally a good piezoresistive sensor should have very little initial resistance and very large variation when subject to a small pressure. Different materials and design have been employed over time for the development of flexible piezoresistive force sensors. The most established design is probably the thin metallic strain gauge. This type of gauges is made of a few micron thick conductive metal strip over a membrane, typically a polymer carrier [41, 42]. The strip is usually arranged in a long grid pattern. A long thin strip is usually preferred because, due to the large area and the small section, when such a grid is stretched the change in resistance will be more evident with respect to a bulk cable deformation. This sensor design is very cost effective and can be easily mass produced. It is very stable and robust over time with a simple read out circuit, usually a Wheatstone bridge, that allows high accuracy measurement. The output is linear with pressure and the response time is typically in the order of a tens of milliseconds. There are also several drawbacks. This metal foil technology can detect very efficiently longitudinal forces, parallel to the surface of the strip grid, but usually cannot measure with the same efficiency transverse force, perpendicular to the strip surface. This is because a change of the strip length will have a higher impact on the resistance than a change of the strip section, already very small. Also, if a very small force is required to bend the strip, a much higher force would be needed to further compress its section. This makes this type of sensor not very suitable for a flexible distributed sensors capable of measuring both longitudinal and transverse forces within the same dynamic range. Thin strip gauges are usually temperature dependent. The temperature dependence can be minimised by carefully balanced the Wheatstone bridge and taking into account the leads resistance as well. Still, temperature dependence works against the miniaturisation of flexible devices. The thinner is the metal strip the higher will be the resistance. A higher resistance means that temperature will further rise when current is delivered through the sensor by Joule effect. All of the above can drastically reduce the sensor accuracy.

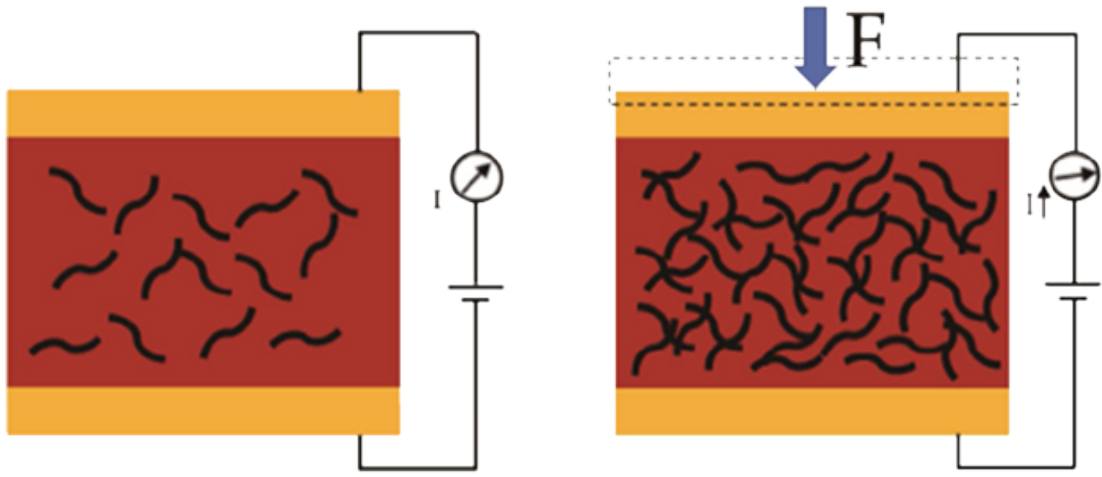


Figure 1.3: **Working principle of flexible piezoresistive sensors.** The polymer matrix is doped with conductive material and placed between two flexible undoped, nonconductive layers. When subject to an external force the volume of the doped layer decreases as its resistance thanks to the higher density of the dopant particles that get closer. Picture from [43].

More recently designs employing soft materials such as polymers, rubbers and resins have been studied. These materials such as polydimethylsiloxane (PDMS), polypropylene (PP), polycarbonate (PC), polymethyl methacrylate (PMMA), polyelectrolytes (PE), flexible epoxy and polyvinyl alcohol (PVA) [41] are nonconductive, sturdy and compliant. When doped with a conductive filler above a certain threshold, they present conductive properties and among different conductive fillers carbon nanomaterials seem to be the most popular [44, 45]. The doped flexible material is usually sandwiched between two flexible substrates. A fixed voltage is applied between the two substrates. When the entire assembly is subject to an external pressure, the stack deforms, and the distance between the fillers particles decreases (fig. 1.3). This reduces the resistance of the doped layer and increases the current flowing between the top and bottom substrates [46]. The change in the contact resistance caused by the variation of the contact area between two components is proportional to the inverse square root of the force [47]. For this reason, this type of sensor has a dynamic range expandable to smaller force values compare to the metallic one, because they can cover more easily larger areas. These sensors are easy to prepare and generally low cost, but they suffer from high non-linearity and a high degree of hysteresis. Also, it is difficult for polymers composites to offer homogeneous properties across large areas [48].

1.3.2 Capacitive sensors

Capacitive tactile sensor works on the principle that an applied force changes the capacity by mechanically change the geometry of a capacitor. For capacitor made up by two plates divided by a dielectric material the capacitance is defined as

$$C = \epsilon \frac{A}{d} \quad (1.3)$$

Where A is the area over which the two plates face each other, d is the distance between the plates and ϵ is the dielectric permittivity of the dielectric between the plates. ϵ is an intrinsic property of the dielectric and therefore does not change when a force is applied on the plates. Therefore, to change the capacitance, the force must act either on the plates area or on their relative distance (fig. 1.4).

These type of sensors are characterised by a good frequency response, high spatial resolution and dynamic range, and high sensitivity [49]. The sensitivity for a capacitive sensor is defined as follows [50]

$$S = \frac{\Delta C}{\Delta P} \quad (1.4)$$

where ΔC is the capacitance variation in response to the application of a force and ΔP is the pressure difference. Therefore, for a given ΔP , the highest sensitivity is reached when ΔC is maximised. One possible route to maximise the variation of capacity is the mesa structuring of the dielectric layer, for example in form rectangular stripes [51], pyramids [52] and cylindrical pillars [53]. A different design approach for a capacitive sensor makes use of the gate capacitance of a field effect transistor. The advantage of this configuration is to make the integration of the device with the read out circuit less complex [50, 54]. Capacitive sensors measure well both static and dynamic forces since capacitance can be easily maintained over time without degrading too much. They possess high dynamic range with a minimum detection limit often close to zero Pascal [40]. Like the piezoresistive technology, this type of sensor is considered active, but the power consumption is generally lower than the piezoresistive sensors, since there is no DC current flowing through the sensor element due to its nature. Capacitive sensors can operate over a wide temperature range and they are very tolerant of short-term overpressure conditions. In comparison to piezoresistive sensors, capacitive pressure sensors may require more complex signal conditioning circuits and calibration algorithms, but they have higher accuracy, frequency response and dynamic range [55]. Thus, very low power sensing systems, can be designed

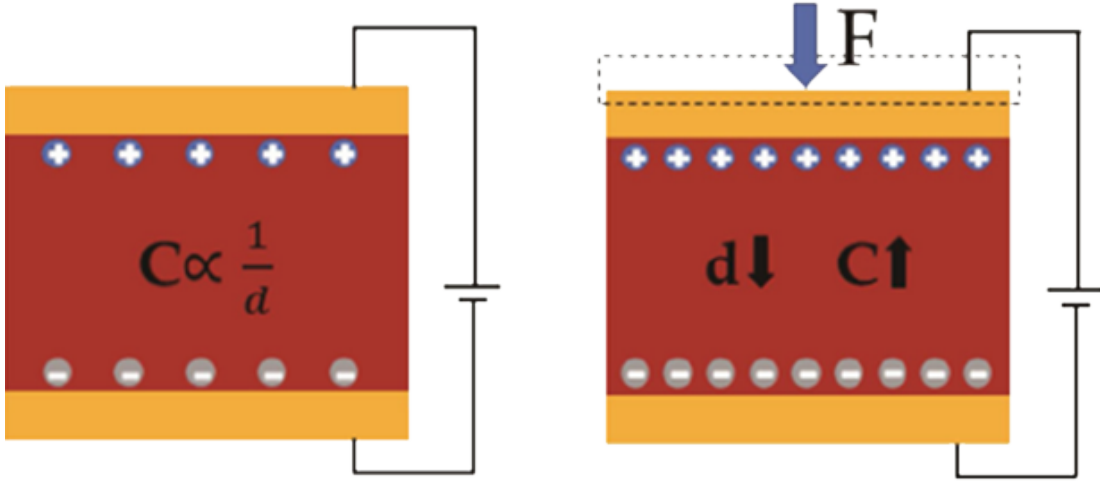


Figure 1.4: **Working principle of a capacitive pressure sensor.** One the sensor is subject to a compressive external force the distance between the two capacitor plates decreases increasing the overall capacity of the device. Picture from [43].

and implemented requiring only a small bias to the circuit by an external reader, making them ideal for remote or implanted medical applications. However, capacitive sensors are affected by noise coming from stray capacitance (i.e. the parasitic capacitance that exist just because two layers of the device are within close proximity) that limits the lower limit of their dynamic range, and crosstalk between the sensor elements [49, 56].

1.3.3 Piezoelectric sensors

If a material undergoing a deformation due to the effect of an external force experience the presence of an electric field between its extremes, the material is said to have piezoelectric properties. The effect is caused by the material molecular dipoles that, under the action of the external force, moves from the original position of electrical neutrality to a new perturbed position where the electric field is formed along the direction of the applied force (fig. 1.5). The readout circuit can either measure directly the voltage or collect the positive and negative charges at the material extremes to establish the magnitude of the applied force. Since the electric field is generated by the material under compression, this type of sensor is considered active in contrast to the capacitive and piezoresistive design.

In recent years different active piezoelectric materials have been employed such as barium titanate BaTiO₃ [57], lead zirconate-titanate PZT [58], zinc oxide ZnO [59] and graphene [60]. These materials are usually rigid ceramic and crystals. To achieve the

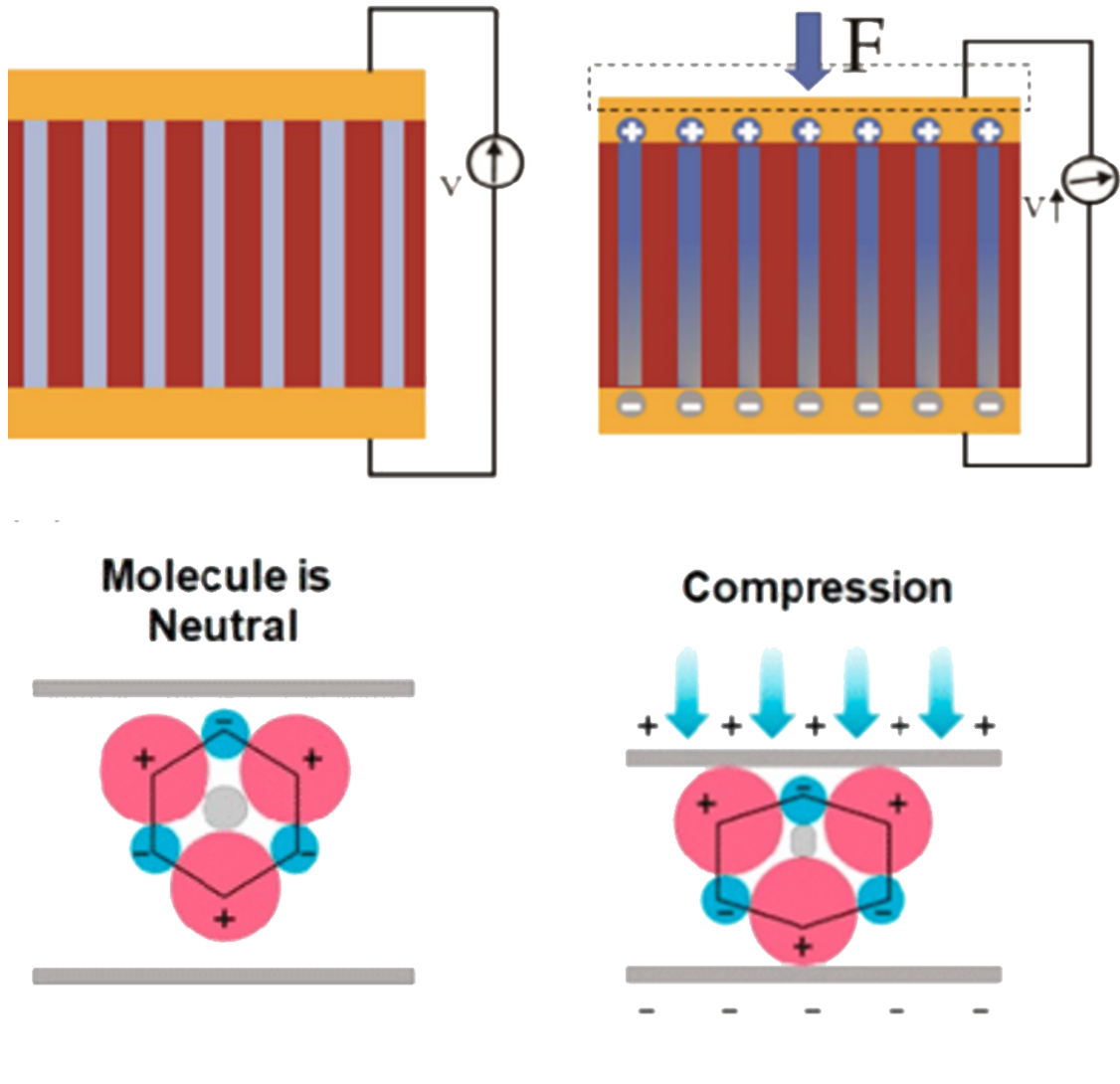


Figure 1.5: **Working principle of piezoelectric sensors.** When subject to a force the material molecules react by dislocating with respect to their unperturbed position and generates an electric field. Picture taken from [43].

desired flexibility they are employed in the form of nanoparticle embedded into flexible polymers [39]. More recently Polyvinylidene fluoride PVDF and its composites has been employed for its lightweight, flexibility, and simplicity of fabrication [40]: when stretched PVDF orients its molecular poles and gains its piezoelectric properties. Piezoelectric sensors present probably the broadest dynamic range among other sensing technologies. The reason is that when no force is applied the electric field is zero. As a result, there is virtually no zero offset value and extremely small pressure variations can be measured. This is an advantage compared to piezoresistive and capacitive sensors where the variation of resistance and capacitance is not absolute but always measured with respect to an initial unperturbed state. Piezoelectric sensors can give nearly real time reading with a response

time of tens of microseconds while piezoresistive and capacitive pressure sensors have a response time in the order of tens or hundreds of milliseconds [40]. The electric field generated under pressure however, decreases exponentially over time [61], making this technology mostly suitable for the measurement of time-varying forces. Some attempts have been done to overcome this limitation measuring other parameters of the piezoelectric active material such as the shift in natural resonant frequency [62]. Because of all the above reasons the readout circuit for a piezoelectric sensors is generally more complex than the one needed for capacitive and piezoresistive sensors since it often requires higher frequency data processing. Another drawback of this type of sensors is their pyroelectric properties that makes them extremely sensitive to temperature variation.

1.3.4 Optical sensors

All the above-mentioned technologies are based on electrical signals. This leads, more or less depending on the sensing principle, to electromagnetic interference and channel cross talk when spatial resolution is increased. Moreover, the above sensor cannot be considered fully magnetic resonance imaging (MRI) compatible. An MRI-compatible device is such when neither it does not disturb the scanner function, nor it creates image artifacts and, at the same time, the scanner does not disturb the device [63]. This is not the case when electrical devices are exposed to a magnetic field of a few tesla, especially if the sensing is needed for “inside bore” or “near to bore” applications where the magnetic field is strongest [64]. Optical tactile sensors can be a good alternative to the above sensing technologies for MIS. This type of sensors detect the magnitude of the applied force by measuring the modulation of the light signal either in intensity, wavelength or phase. Light travels from the source to the point of measure usually via optical fibres or waveguides. These channels, usually made of plastic or glass, are composed by two regions: a central high refractive index core surrounded by a lower refractive index cladding. Light is confined within the core and propagates coaxially with it. These types of sensors are light, compact and easily sterilisable. Sensors based on optical waveguides can be classified in intrinsic sensor, when the sensing region is within the fiber, and extrinsic, when the light must leave the fiber to be modulated before being reinjected into the fiber [64]. Waveguide based optical sensors can be classified depending on the light property modulated by the application of the force, usually intensity, wavelength or phase. Intensity modulation base optical sensors convert a mechanical movement, following the application of a force, into

a light intensity variation (fig. 1.6). A typical design consists in attaching on the tip of an optical fiber a flexure mount holding a micro mirror [65]. The mirror faces the tip of the fiber and its function is to reflect back the light into the system. The light coming from a source is channelled into the optical fiber and emitted towards the mirror. When a force is applied to the flexure the relative position of the mirror with respect to the tip of the optical fiber changes and consequently this changes the amount of light reflected back into the system. The applied force can be established by calibrating the pressure on the sensor against the amount of light received. Depending of the degree of freedom of the flexure the displacement can be measured in one dimension, coaxially with the fiber [66] or on multiple axis [67, 68]. Each degree of freedom to be detected requires an emitter, a light source sending the signal to the tip, typically an LED or a laser, and a receiver, a device that detect the reflected light, typically a camera or a photodiode. Depending on the sensor design the forward and backward light signals can be joined via a splitter and share the same fibre [69].

The main disadvantage of intensity based force sensors is that light signals leave the fiber to get the applied force feedback. This makes the sensor very sensitive to losses and fibers misalignment. Fiber misalignment can be caused by excessive bending and torsion that can dislocate the sensor tip. Consequently, backward signal is coupled properly into the fiber generating a misreading. To compensate for false readings due to bending and torsion effects, a reference fiber can be added, to subtract the signal coming from unwanted mechanical distortions. This allows a more reliable reading at the expenses of one additional channel. Still such effects pose a limitation on the flexibility of this sensor design, at least towards the sensor tip.

Wavelength modulation optical sensors employ Bragg grating written directly into the fiber [71]. Fiber Bragg Gratings (FBG) are obtained by periodically modulating the index of refraction of the core of a single mode optical fibre. When light crosses the area with a periodic pattern, at each index step it will be partially transmitted and reflected. If the distance between two steps of refractive index is equivalent to half the reflected wavelength, all reflections will interfere constructively and move backward as a single homogeneous reflected signal [72]. This is known as the Bragg conditions and the wavelength at which the constructive interference is verified is the Bragg wavelength $\lambda_B = 2n_e\Lambda$ where n_e is the effective index of refraction of the fibre core and Λ is the pitch of the grating (fig. 1.7).

If now the fibre is compressed or stretched due to the application of an external force,

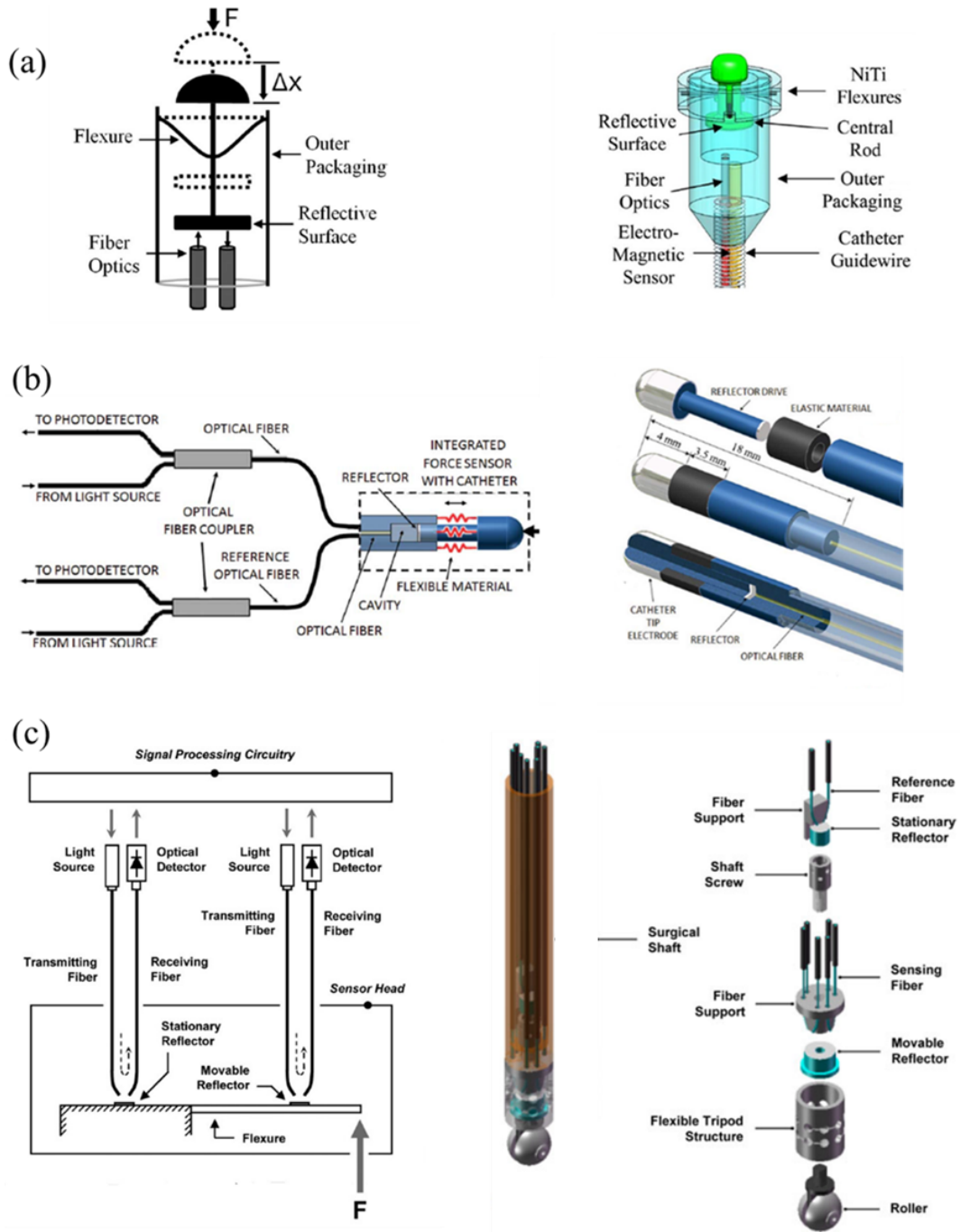


Figure 1.6: **Examples of intensity modulation optical force sensors.** (a) 1D force sensor. Two fibres, one emitter and one receiver, are aligned in front of reflective surface. When a force is applied the distance between the reflective surface decreases and the signal intensity detected by the receiver increases accordingly [66]. (b) 1D force sensor with reference fibre. The principle is the same as (a) but this time receiver and emitter are the same fibre. The backward and forward signal are split outside the sensing head via an optical beam coupler. A second pair of receiver and emitter is used as a reference signal to compensate any misreading due to the bending of the fibre [69]. (c) 3D force sensor. 8 fibre sensor head: 2 are the receiver and emitter for the reference signal, while the remaining 6 provides, via a 3 points feedback, the position of a reflective surface. The reflector is free to move in XYZ and constitutes the pivot point of a roller [68].

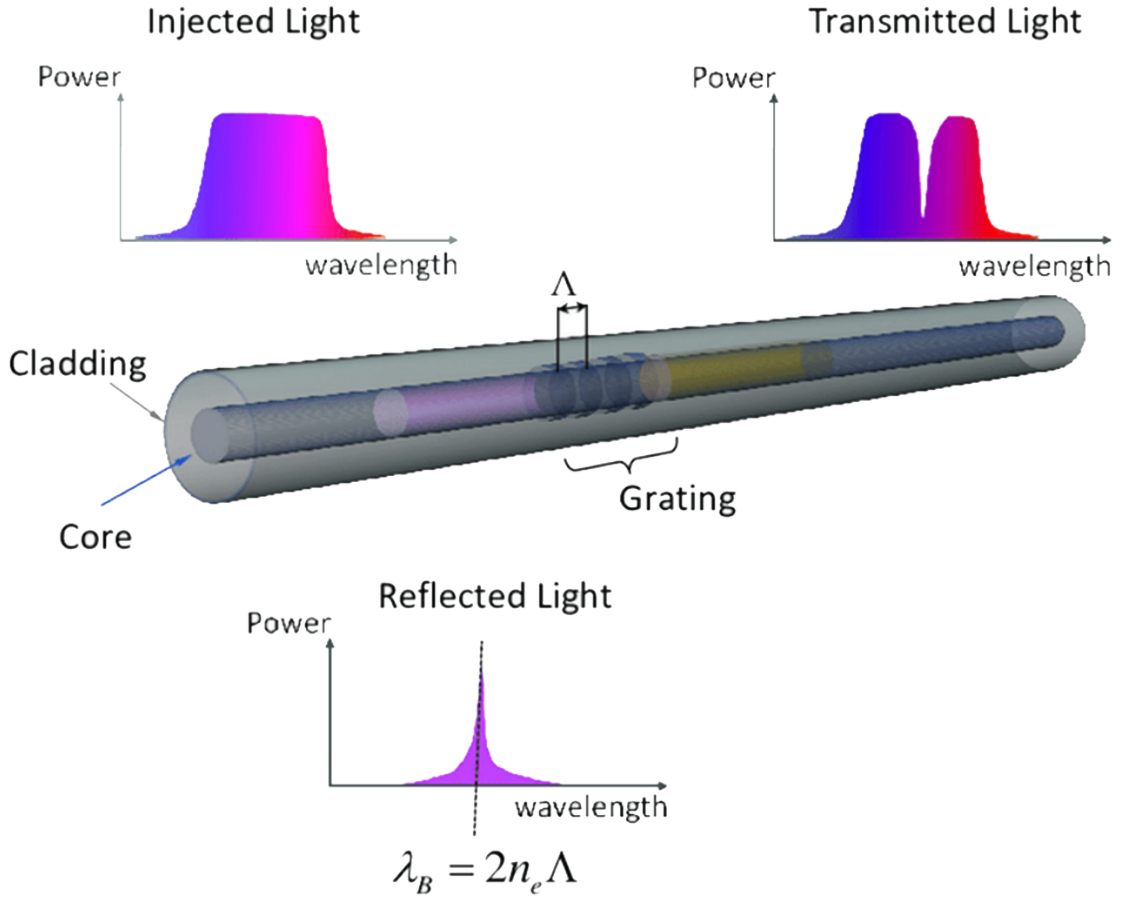


Figure 1.7: **Working principle of an FBG.** A narrowband spectral line within a broadband light source will undergo constructive interference in reflection if satisfies the Bragg Law. The central wavelength of the reflected signal depends on the pitch of the grating and the effective index of refraction of the fibre. Picture taken from [70].

the wavelength under which constructive interference is verified changes, since the period of the refractive index modulation has been modified. Thanks to this effect, by linking the reflected wavelength against the applied force, the fiber sensor is calibrated. By multiplying the number of fibre, or by writing multiple FBG within the same fiber, sensors with multiple degrees of freedom can be made (fig. 1.8) [73, 74]. FBG force sensors are sensitive to temperature due to both the thermal expansion of the fiber and the index of refraction dependency over temperature. A change of temperature can therefore change the pitch of the grating and the transmission properties, hence the wavelength at which the Bragg condition is verified. A wavelength shift can be caused by a combination of strain and temperature variation. These two contributions can be decoupled via calibration. The actual fiber with the modulation of the index of refraction can be mass produced at low cost, but the interrogation unit can be expensive. The read-out circuit of such gratings is

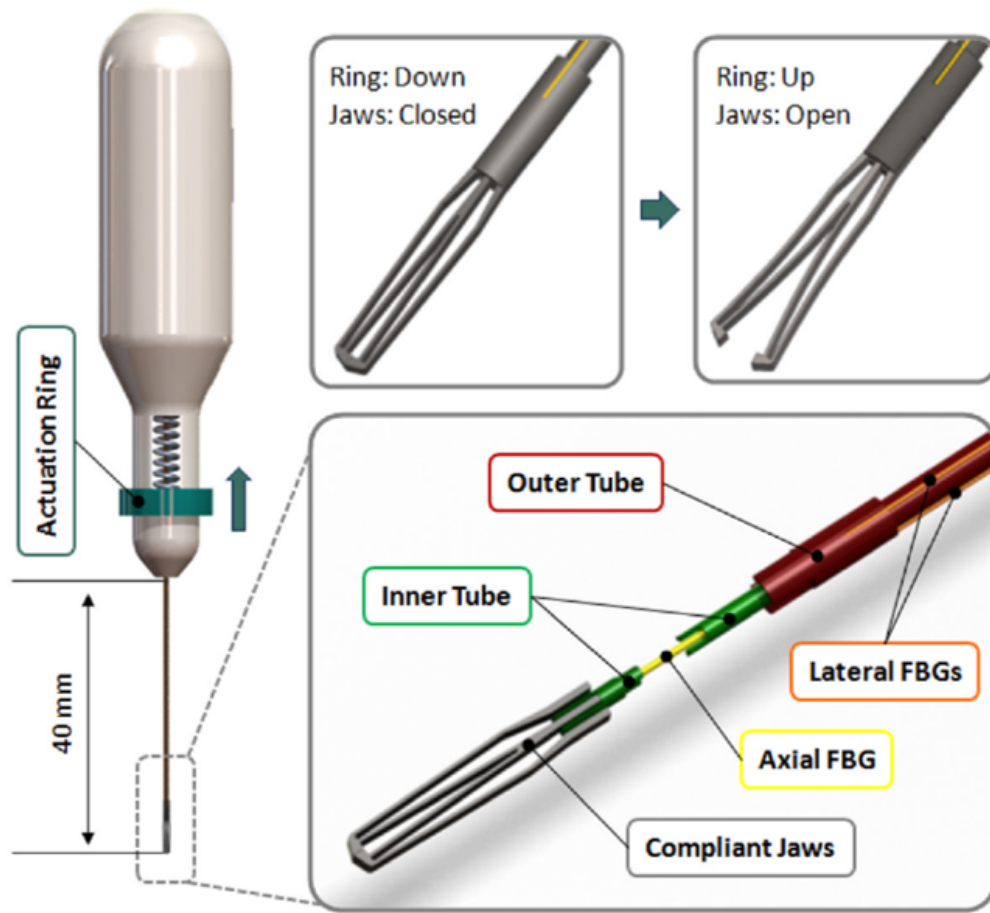


Figure 1.8: **Example of 3D FBG sensor from [73].** 3 FBG are placed on 60 degrees configuration on the final section of the tool shaft. By receiving an independent feedback from each FBG the force vector components in XY and Z can be calculated and the full force direction established.

usually complex since it includes a spectrometer capable of resolving wavelength shift of less than 1nm . Alternatively, a photodiode can be used in case the light source has a narrow tuneable line width instead of being broad band [75].

Phase modulation fiber sensors are based on the interference between two light signals. To undergo an interference phenomenon, two light signals must be coherent, i.e. they must have identical waves with constant phase difference, and they must be monochromatic. Usually, to achieve this condition, a monochromatic and coherent light source, such as a laser, is intensity split in two signals. This signals have identical waves since they come from the same source. After walking a different optical path the two beams are recombined. Because of the different optical path the beamlets will have different phase and, once overlapped, an interference pattern will appear. If the light source is not monochromatic, the interference pattern will be given by the superposition of multiple fringes generated by the different wavelengths in the source spectrum. The splitting and recombination of the

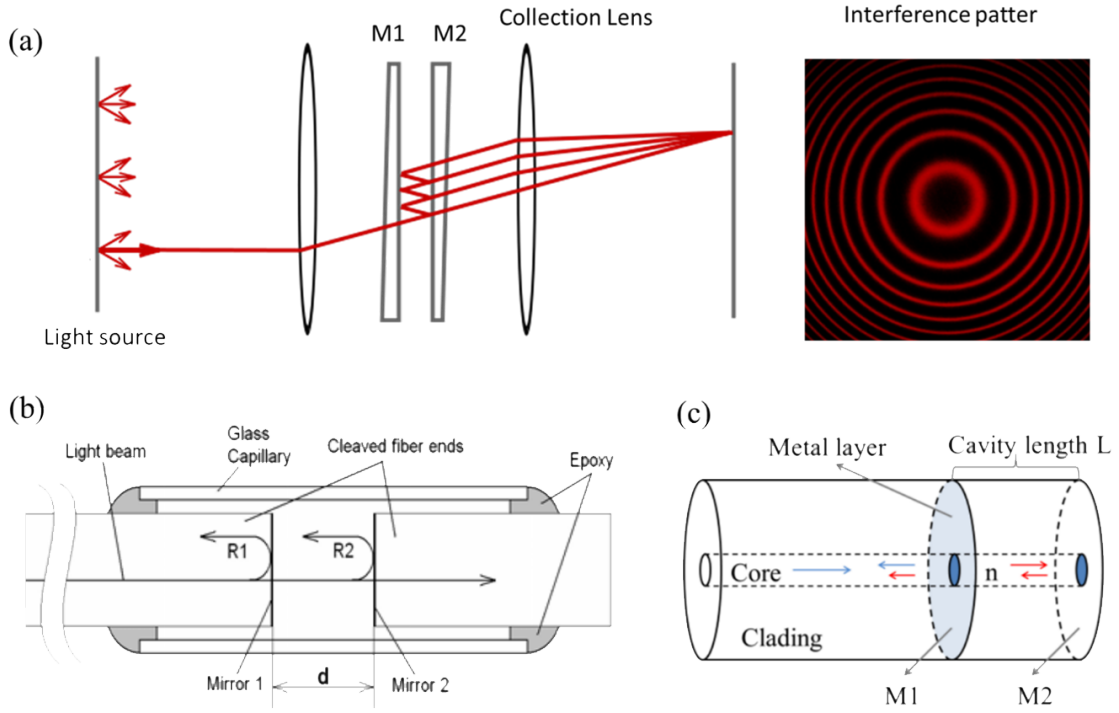


Figure 1.9: **Fabry Perot interferometer.** (a) Schematic of a Fabry Perot interferometer and an example of interference pattern generated by the device. The light source is channelled into the cavity composed by M1 and M2 mirrors. M2 is only partially reflective. When the light is recombined after exiting the cavity by a focusing lens an interference pattern is generated. Picture readapted from Wikipedia. (b) a guided fiber based FP resonator. The cavity is formed between two fiber sections. The cleaved faces of the sections are employed as cavity mirrors. When a force is applied the cavity length d is reduced and the interference pattern generated by the signals R1 and R2 changes accordingly. Picture readapted from [76]. (c) An example of unguided FP fiber sensor. In this case M1 and M2 are obtained by thin film deposition directly onto the fiber. When a pressure is applied, the cavity length L changes and so does the relative phase difference between the two backward signals. Pictures taken from [77].

light source can occur in different configurations. One of the most popular is the Fabry-Perot (FP) interferometer (fig. 1.9). A Fabry-Perot interferometer is a cavity obtained by facing two opposite mirrors. One of the mirrors is partially reflective. As a result the light entering the cavity will experience one or more reflection before being fully transmitted. When the light transmitted is recombined, due to the optical path difference given by the multiple reflections, it will generate an interference pattern. A fibre FP cavity can be guided or unguided. A guided FB cavity is obtained by splitting a fiber inside a capillary and using the end faces of the two section as mirrors [76]. For the unguided configuration the cavity is added directly inside the fiber by changing the index of refraction or by thin film deposition [77].

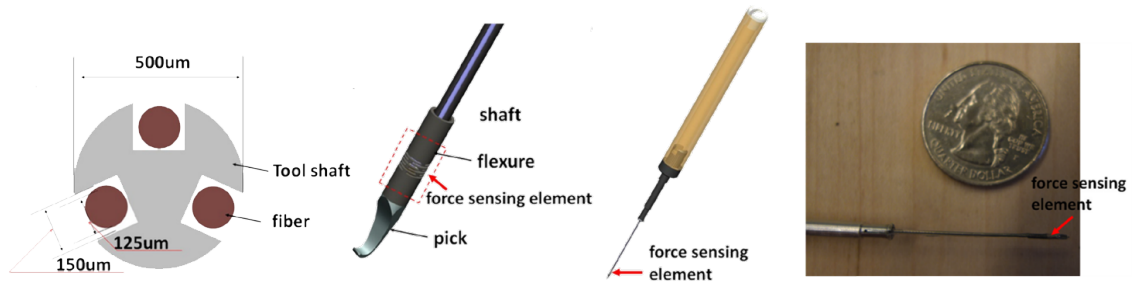


Figure 1.10: **Example of a 3D Fabry Perot Fiber sensor.** 3 Fibers are arranged in a triangular pattern to define tip, tilt and Z position of a needle for eye surgery. Picture readapted from [78].

As for the FBG based sensor this principle have been applied from 1D sensing head for minimal invasive surgery [79, 80] to 3D sensing head by increasing the number of fibres (fig. 1.10) [78]. Since the performance of the sensor are dependent on the length of the cavity which must be controlled to a fraction of micron, this type of device is extremely sensitive to temperature and require accurate calibration to compensate for thermal effects [79]. Also, as for the FBG based sensor the interrogation set up could be quite expensive since the light source require good coherence. White light FB fiber sensors have been developed to reduce costs but, since the interference patten is given by the overlap of multiple wavelengths, this restricts the overall device performance [81].

1.3.5 Discussion

Advantages and disadvantages of piezoresistive, capacitive, piezoelectric and optical pressure sensors are summarised in table 1.1.

Piezoresistive pressure sensors are very cost effective with their easy fabrication methods. They are stable and robust over the time and present simple readout circuits. They employ polymer composite materials to provide flexible pressure sensors, however they are affected by high non-linearity and hysteresis and are not able to provide homogeneous responses over large areas.

Compared to piezoresistive sensors, capacitive sensors present higher accuracy of static and dynamic pressure, better frequency response, more extended dynamic range and lower power consumption. However, they are affected by noise coming from stray capacitance and present complex readout circuits.

Piezoelectric pressure sensors are characterised by very broad dynamic range with no zero

Pressure sensors	Advantages	Disadvantages
Piezoresistive	Very cost effective and easy fabrication, stable and robust over time with simple readout circuit.	High non-linearity and hysteresis, not homogeneous over large areas. Response time of <i>tens/hundreds ms</i> .
Capacitive	Higher accuracy of static and dynamic pressures, frequency response and dynamic range than piezoresistive, as well as lower power consumption.	Affected by noise from stray capacitance. Response time of <i>tens/hundreds ms</i> . Complex readout circuit.
Piezoelectric	Very broad dynamic range (no zero offset value). Response time of <i>tens μs</i> .	The electric field generated under pressure decreases exponentially over time. More complex readout circuit and sensitive to temperature variation.
Optical	Electromagnetically immune, long life, good accuracy, manufacturing simplicity, low cost and high reliability.	Requiring multi-fibers configuration at the expense of miniaturisation and flexibility. May be very sensitive to losses, fibers misalignment and temperature variation. May be expensive and require complex read-out circuit.

Table 1.1: **Pressure sensors.** Advantages and disadvantages of piezoresistive, capacitive, piezoelectric and optical sensors.

offset value. While piezoresistive and capacitive sensors have comparable response time of *tens/hundreds ms*, piezoelectric sensors present a much shorter response time of *tens μ s*. However, the electric field generated under pressure in the piezoelectric sensors is not stable over the time but decreases exponentially. Additionally this type of sensors present complex readout circuits and are sensitive to temperature variation.

Optical pressure sensors present very advantageous characteristics with respect to their electric counterparts, such as electromagnetical immunity, long life, good accuracy, flexibility, manufacturing simplicity and low cost. However, also these technologies have their own disadvantages. Intensity based optical sensors are usually very sensitive to losses and fibers misalignments. Instead, FBG and phase based optical sensors are sensitive

to temperature variation, expensive and require complex readout circuits. Additionally, optical pressure sensors generally require multi-fibers configuration to increase the spatial resolution, at the expense of miniaturisation and flexibility of the final device.

In this work, optical based pressure sensing technologies have been selected as best candidates to address the challenge to provide haptic feedback during endoscopic interventions. The characteristics of this type of sensors, in particular electromagnetic immunity, flexibility, manufacturing simplicity and low cost, are particularly relevant for the specific application to colonoscopy, as detailed later, in sections 1.5 and 1.6. The sensing strategies proposed in this work are intended to overcome some of the limitations of optical based pressure sensors, for example limiting the number of fibers (or waveguides) used to increase the spatial resolution.

1.4 Haptic Feedback Technologies

To obtain haptic feedback, researchers have proposed sensors to be directly mounted on medical probes using various sensing techniques, including sensors of displacement [82], pressure [83], resistance [84], capacitance [85], piezoelectricity [86], vibration [87], and optical properties [88, 89]. However, most of the force sensors are still too big to be applied to flexible endoscopes as they were intended for larger and rigid laparoscopic tools. Sterilization and robustness are also the common challenges for those electronic and structurally complicated sensors [90].

Watanabe et al. [91] realised a force sensing system based on highly elastic fabric to measure forces applied during colonoscopy. This approach imposes the use of a camera located into the endoscope shaft and looking towards the endoscope tip to detect the fabric deformation related to an applied force and it is able to measure forces just at the tip of the endoscope rather than along its external surface.

A design capable of measuring forces along the external surface of the colonoscope proposed by Dogramadzi et al. [92] was based on a set of conductive silicon rubber sleeves alternated by a set of conductive copper tapes. The array of sensors was covering 50cm of the whole colonoscope length and the sensing regions were spaced 6cm apart from each other, leading to significant dead zones. Furthermore, the addition of this sensor sheath to an endoscope increases its diameter by 15–20%.

Lai et al. [90] employed optical based sensors using Fiber Bragg Gratings (FBGs) for the detection of forces applied to the external surface of endoscopes. Each single FBG was

placed on the sheath in the direction parallel to the endoscope axis and it is able to provide the compression force on the endoscope sheath, but no information is given on the force location along the endoscope, in terms of distance from the endoscope tip. Furthermore, a set of FBGs should be applied all around the sheath to minimise the dead zones.

Hawel et al. [17] developed a layered sensing flexible sleeve of $0.7mm$ thickness which can be wrapped around the outside of the endoscope. The sensing sleeve is made by three layers: a the piezoresistive material in the middle, the resistance of which varies with the pressure applied, and two outer layers of flexible printed circuit boards (fPCBs) which carry the electric signal to be converted in pressure. However, due to fabrication limitations which impose restricted dimensions to the fPCBs, a sensing sleeve able to cover the most of the endoscope length is obtained by soldering together several sub-sleeves sections, making the fabrication process more time-consuming and expensive.

McCandless et al. [93] developed a soft robotic sleeve to provide sensor feedback coupled with soft actuators which can be inflated in case of critical contact forces applied by the colonoscope to the colon to guarantee pressure redistribution on a larger contact area. The sensing device is based on three soft optical waveguides placed on the colonoscope sheath in parallel with its axis and separated from each other by 120° . The sensing principle is based on the detection of light losses due to the compression of the core of the waveguides as a result of a force applied by the colonoscope sheath to the colon. However, the thickness of the proposed soft robotic sleeve is $3.5mm$, leading to a critical increase of 23 – 30% of a typical endoscope diameter.

1.5 Design Specifications

During its navigation within the human body, an endoscope applies pressures to blood vessels or internal organs via its tip and the external surface of its main frame. In order to effectively simulate the surgeon skin, a realistic haptic feedback should be distributed over a broad area providing good spatial resolution and measuring the magnitude of the pressures applied normal to the tangent of the colonoscope wall, around 360° of its shaft, and in different points along the scope length.

Usually, the first $10cm$ of the colonoscope tube from its tip are commonly an active bending section controlled by the up/down and left/right control knobs. If inserted to its maximum limits, the $50cm$ of a colonoscope most proximal to the colonoscopist is rarely involved in looping. So, the haptic feedback should be provided by a sensing technology

covering the colonoscope region over a length of 100cm, intervening between the 10cm from the tip and the 50cm on the other end. This region of the scope is most likely to be involved in loop formation and thus will also likely be responsible for significant pressures between the colonoscope shaft and colon wall, causing discomfort and introducing risks for the patient [17]. So, the haptic feedback technology has to cover at least the endoscope sheath section related to this area.

Due to the colonoscope flexibility, even loops as small as 10cm in diameter can occur [94], with maximum pressure located at the apex of such loops. Thus, the distance between the sensing points of the haptic feedback device needs to be minimised to avoid this maximum pressure falling in a “dead area” between sensing points.

The range of pressures necessary to injure the colon can vary based on the patient and their anatomy. However, data regarding maximum intraluminal pressure during routine colonoscopy range between 4 and 20kPa, while bursting pressures have values from about 7kPa in the cecum to 30kPa in the sigmoid colon [95]. The critical pressure value around 30kPa is also confirmed by cadaveric studies, providing evidence of muscle and serosa tear at a pressure of 27.5kPa and full thickness perforation occurring at 28.1kPa [96]. So the haptic technology should be able to extensively cover the range of interest [0 – 30]kPa.

Among the main requirements of an haptic feedback device, it is good to mention its compatibility and adaptability to commercial colonoscopes, since re-learning new methods of performing surgery would not be cost-effective. Therefore, it needs to be subtle, flexible and integrated to not impede the endoscopist’s ability to manipulate the scope, adding as little to the diameter of the endoscope tube as possible. Also, it must be considered that the mechanical stiffness related to the number of wires to be incorporated in the tether, its external diameter, the weight and the friction against the colonic mucosa, produce a drag force that needs to be overcome to move the colonoscope forward. So, beside the overall colonoscope diameter, also the introduction of wires inside the endoscope sheath should be minimised.

Other fundamental requirements are robustness, biocompatibility, chemical inertness, and sterilizability. The MRI compatibility is also important. In fact, the detection of a disease in colonoscopy is limited to the visualisation of the surface mucosa, while the extent of invasion beneath the surface requires biopsy, which may introduce complications due to sampling errors or lesions. MRI provides high quality imaging to visualise soft tissues without need of tissue withdrawal as in the biopsy [97]. For this reason, the materials used

for the haptic feedback device need to be carefully selected to prevent the generation of artifacts which may obscure the image details and interfere with the imaging.

The main requirements of an haptic technology for endoscopy can be summarised as follows:

1. Compatibility with commercial endoscopes, including flexibility, miniaturisation and limited introduction of wires inside the sheath.
2. Adaptability to non planar geometry to detect pressures applied normal to the tangent of the colonoscope wall.
3. High spatial resolution to be able to cover a wide surface minimising the "dead zones".
4. Sensing range of pressures between $[0 - 30]kPa$.
5. Biocompatibility and chemical inertness.
6. Sterilizability.
7. MRI compatibility.
8. Low cost and easy manufacturing process to facilitate mass production.

1.6 Objective Of The Work

The development of an haptic feedback technology for endoscopic interventions, able to satisfy the technical requirements as detailed in section 1.5, is still an open challenge. This work suggests some design strategies employing optical based sensors to address this need.

With respect to their electric counterparts, optical sensors present several advantages particularly interesting for the development of haptic technologies for endoscopy. They are durable, flexible, compact, biocompatible, easily sterilisable non presenting electronic components in their main body, electromagnetically immune, and their manufacturing process is generally simple and low cost. However, some also relevant drawbacks need to be overcome.

Since the light in optical fibers travels parallel to the optical axis it is difficult to detect pressures perpendicular to the axis of the fiber. When an optical fiber is employed to detect

pressures, the sensing functionality usually involves just its tip, while the longitudinal surface of the fiber is not able to return any sensing feedback. This aspect limits the possibility of miniaturisation of the sensing technology, because the fibers require space where their longitudinal extension can be placed.

One of the aim of this work is investigating strategies to employ optical fibers and waveguides to detect pressures not applied on their tip, but perpendicular to their longitudinal axis. This allows to develop compact array sensors and sensing skins adaptable to the non planar external surface of the colonoscope and able to measure pressures applied normal to the tangent of the scope wall, around 360° of its shaft. With this configuration, a more spatially distributed sensing feedback can be reached, compared to several devices presented in literature where the sensing area is limited to the only fiber tip as previously mentioned. The spatial resolution can be further enhanced by the capability to distinguish the application point of the pressure along the endoscope length, as also presented in this work.

Furthermore, as previously mentioned, the great majority of optical force sensors are designed to measure the force applied on the tip of a surgical tool. The optical fiber tip can move in one dimension or pivot in 3 dimensions, but the sensing capability is limited in space to a single point or to a limited area. To improve the spatial resolution, fiber bundles are often employed. This introduces complications in terms of light coupling into multiple fibers. Additionally, in the scenario of application to an endoscope, the additional fibers introduced should be embedded into the endoscope shaft. The introduction of these additional wires may compromise its flexibility, adding mechanical stiffness to the shaft. Or, it may be even required to enlarge the endoscope external diameter and altering its weight, compromising the endoscopist's ability to manipulate the scope. In this work, different strategies are presented to provide spatial resolution while minimising the number of channels, as this can be definitely of interest for future applications in MIS.

Finally, the combined study between materials selection and sensor design can lead to cover the pressure range of interest between $[0 - 30]kPa$, thus satisfying all the main requirements as listed in section 1.5.

The next chapters of thesis follow the below structure:

- Chapter 2: some physical concepts are introduced here as they will be recalled along the entire work to analyse the different designs.
- Chapter 3: the possibility of controlling 8 optical channels with only one light

source is explored to provide a compact design with effective spatial resolution. The pressure is applied directly on each channel perpendicularly to the light propagation. The need to detect light losses due to the optical channel deformation required the development of lab-made waveguide instead of using off the shelves optical fibers.

- Chapter 4: the rigid substrate is replaced by a completely flexible one. The spatial resolution is provided by off the shelves fibers. The particular chisel shape is conferred on the fiber tip as an expedient to measure forces at 90° with respect to the fiber optical axis. By increasing the number of fibers distributed sensing is also made possible, although the overall number of fibers is halved by using the same fiber as both emitter and receiver. The signal to noise ratio of the sensor is also improved with respect to the imaging algorithm of Chapter 3, by decoupling input and output signal wavelength thanks to the use of fluorescent dyes as dopants.
- Chapter 5: the fluorescent dyes are replaced by quantum dots to explore the design flexibility and advantages provided by these nanomaterials. A flexible polymer waveguide doped with QDs is presented. The joint analysis of intensity and wavelength modulation under compression is employed to get information regarding the pressure magnitude and its application point along the waveguide length.
- Conclusion: a comparison between the different design strategies is presented. The design of a flexible sensor employing the findings of all previous chapters is presented as a plan for future work.

Chapter 2

Background

In this chapter, an explanation of the main theoretical concepts used in this dissertation is reported.

First of all, the rules that govern the light transmission in a medium are presented, with a particular focus on the light transmission through optical fibers, since all the sensing strategies presented in this work employ optical fibers and waveguides.

A brief discussion presents the light interaction with a sample material, that ends with the derivation of the equation showing how the intensity decreases exponentially while the light travels along a medium and its drop is proportional to the medium thickness. This relationship was applied to simulate the light attenuation through a waveguide.

Since the sensor setups presented in Chapters 3 and 5 employ a laser source, the properties of a Gaussian laser source are presented to provide basic equations which have been used in the cited chapters to simulate the experimental setups.

Later, a section explaining how fluorescent dyes work was introduced. A particular focus has been devoted to how the light properties change after absorption due to fluorescence emission, in order to understand the working principle of the fluorescence based sensor presented in Chapter 4.

Finally, a brief introduction to nanomaterials is reported, also including quantum dots (QDs). The unique properties of these nanoparticles are described, with a particular focus on their piezoelectric effect on which the operating principle of the sensor presented in Chapter 5 is based.

2.1 Light Interaction

2.1.1 Total internal reflection

Assuming that light passes through an interface between two perfectly transparent media, the light absorption through the materials is neglected, therefore the incident light can be partially reflected and partially transmitted through the second medium (figure 2.1a). This phenomenon is described by the well known *Snell's law*:

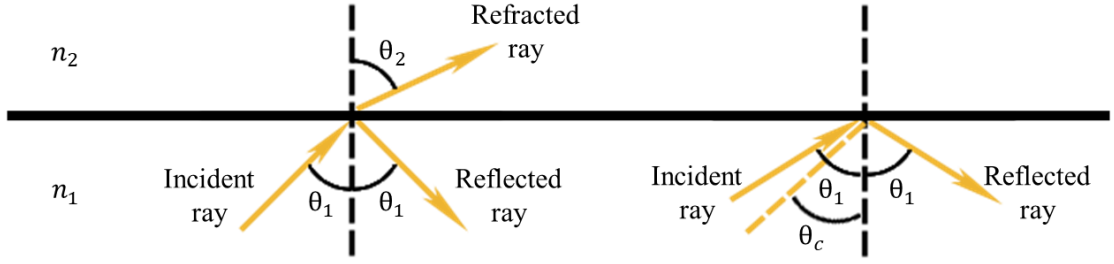


Figure 2.1: **Total internal reflection.** (a) Light transmission through an interface between two media (readapted from [98]). (b) When the incidence angle is higher than the critical angle, total internal reflection (TIR) occurs (readapted from [98]).

$$n_1 \sin(\theta_1) = n_2 \sin(\theta_2) \quad (2.1)$$

where n_1 and n_2 are the indices of refraction of the two media, θ_1 angle of incidence and θ_2 angle of refraction.

In the specific case of $n_1 > n_2$, θ_2 can reach its limit value of 90° , corresponding to the condition $\theta_1 = \theta_c$ where θ_c is called *critical angle* and is defined as follows:

$$\theta_c = \arcsin\left(\frac{n_2}{n_1}\right) \quad (2.2)$$

For values of $\theta_1 > \theta_c$, refraction does not occur anymore and the light is totally reflected into the first medium (figure 2.1b). This phenomenon is known as *total internal reflection* (TIR).

2.1.2 Light transmission in optical waveguides

Optical waveguides consist of a core and a cladding, or substrate surrounding the core. The refractive index of the core n_1 is higher than that of the cladding n_2 , therefore the light beam that is coupled to the end face of the waveguide is confined in the core by total internal reflection. The condition for total internal reflection at the core–cladding interface is given by:

$$n_2 \leq n_1 \sin\left(\frac{\pi}{2} - \theta_1\right) \quad (2.3)$$

where θ_1 is the propagation angle between the direction of the ray travelling along the core and the optical axis of the waveguide (see figure 2.2a) [99].

Considering the refractive index of the air $n_0 = 1$, the relation between θ_1 and the incident

angle on the air-core interface θ_0 is deduced by the Snell's law as

$$\sin(\theta_0) = n_1 \sin(\theta_1) \leq \sqrt{n_1^2 - n_0^2} \quad (2.4)$$

We obtain the critical condition for the total internal reflection as

$$\theta_0 \leq \sin^{-1} \sqrt{n_1^2 - n_0^2} \equiv \theta_{max} \quad (2.5)$$

where θ_{max} denotes the maximum light acceptance angle of the waveguide and is known as the numerical aperture (NA) [99].

A particular configuration corresponds to an optical waveguide with the tip trimmed to an angle equal or higher than the critical angle. In this condition, considering the refractive index of the air n_0 is lower than the one of the core n_1 , because of the TIR, the light reaching the cut surface is reflected at 90° and it can get out from the fiber. Similarly, light coming from outside can be reflected at 90° by the cut surface and then it can be transmitted through the fiber (figure 2.2b).

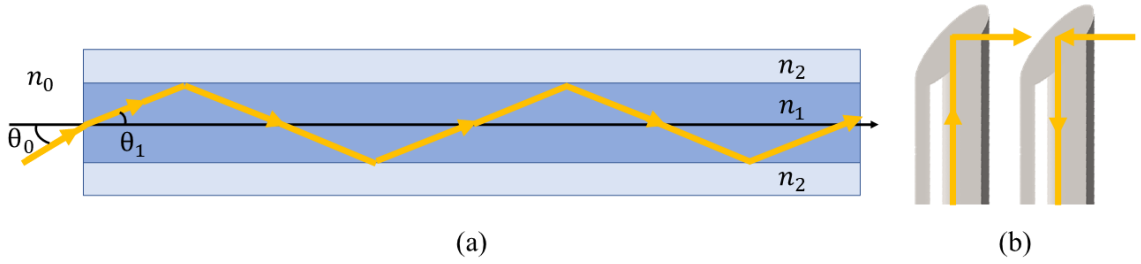


Figure 2.2: **Refractive-index profile in a waveguide.** (a) Basic structure of a refractive-index profile of the optical waveguide. (b) This configuration allows to change the propagation direction of 90° .

2.1.3 Role of the cladding

A waveguide made by just core and suspended in air would be able to transmit light without need of any cladding. However the latter, besides to protect the core from damage, leads to further advantages. In a waveguide (with or without cladding), the angle θ can be defined as the angle between the direction of the ray travelling into the core and incident on the cladding and the perpendicular to the core-cladding interface. If the cladding is absent, a higher number of multiple reflections occurs because the angle θ is small (see fig. 2.3a). In a waveguide equipped with a cladding layer, θ is larger, then rays travel closer to

its axis, there are fewer reflections and the distance travelled is smaller, therefore there is less energy loss and the time of transmission is shorter (see fig. 2.3b).

This effect can be mathematically explained using the equation of the critical angle (2.2). Considering the values of the proposed waveguide, $n_1 = 1.52$ for the core and $n_2 = 1.37$ mean typical value for the cladding, the critical angle is $\theta_c \sim 64^\circ$. In the case no cladding is applied, the critical angle would be lower ($\theta_c \sim 41^\circ$), causing more multiple reflections along the waveguide favouring light losses.

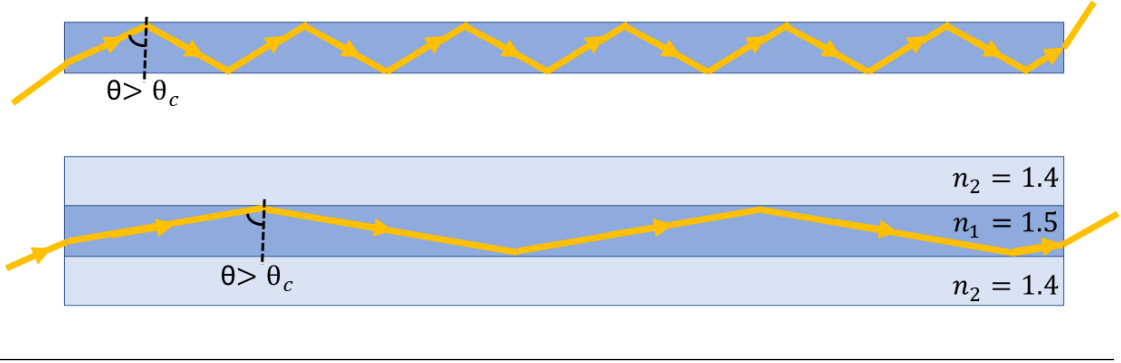


Figure 2.3: **Role of the cladding.** Comparison between light transmission in a waveguide without cladding (a) and with cladding (b).

2.1.4 Reflectance, absorbance and transmittance

Considering a monochromatic light interacting with a material sample, the light will be partially reflected, absorbed and transmitted (fig. 2.4). These quantities can be expressed in terms of radiant flux (or radiant power), which is the radiant energy per unit time. Reflectance is defined as the ratio of the radiant flux reflected from the material sample surface (ϕ_r) to the incident radiant flux (ϕ_i):

$$R = \frac{\phi_r}{\phi_i} \quad (2.6)$$

The reflectance R at the interface between two media (such as sample surface and air) can be calculated at normal incidence according to the *Fresnel equation* [100]:

$$R = \left| \frac{n_1 - n_2}{n_1 + n_2} \right|^2 \quad (2.7)$$

where n_1 and n_2 are the refractive indices of the two media. The remaining light will be partially transmitted and partially absorbed by the material while travelling through its

thickness.

The transmittance T of the material sample is defined as the ratio of the transmitted intensity I over the incident intensity I_0 and takes values between 0 and 1.

$$T = \frac{I}{I_0} \quad (2.8)$$

However, it is more commonly expressed as a percentage transmittance:

$$T(\%) = 100 \frac{I}{I_0} \quad (2.9)$$

The absorbance A of the solution is related to the transmittance and incident and transmitted intensities through the following relations:

$$A = -\log_{10}(T) = \log_{10}\left(\frac{I_0}{I}\right) \quad (2.10)$$

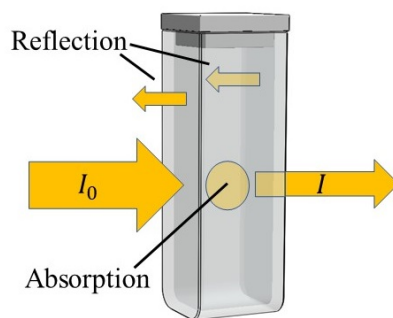


Figure 2.4: **Light interaction with a substance.** A monochromatic light interacting with a sample is partially reflected, absorbed and transmitted. The emergent light I has lower intensity than the incident light I_0 .

In case of homogeneous attenuation, the variation of intensity dI along the propagation direction x can be expressed as

$$dI = -\alpha I dx \quad (2.11)$$

This linear differential equation states that the intensity drop of the light propagating through a material is proportional to the thickness of the material, the initial light intensity, and the attenuation coefficient α which contains the optical properties of the material as set out by the equation:

$$\alpha = \frac{A}{d} = \epsilon c \quad (2.12)$$

where A absorbance, d optical path length, ϵ molar absorption coefficient and c molar

concentration of the material. By integrating equation 2.11, it is possible to obtain:

$$I(x) = I_0 e^{-\alpha x} \quad (2.13)$$

The attenuation coefficient α generally depends on wavelength and has units of inverse length.

2.2 Properties Of A Laser Source

A laser beam is usually assumed to have an irradiance profile that follows an ideal Gaussian distribution. Gaussian irradiance profiles are symmetric around the centre of the beam and decrease as the distance from the centre of the beam perpendicular to the direction of propagation increases (fig. 2.5a). This distribution is described by the equation [101]:

$$I(r) = I_0 \exp\left(-\frac{2r^2}{w_z^2}\right) = \frac{2P}{\pi w_z^2} \exp\left(-\frac{2r^2}{w_z^2}\right) \quad (2.14)$$

where I_0 is the peak irradiance at the centre of the beam, r is the radial distance away from the axis, z is the distance propagated from the plane where the wavefront is flat, w_z is the radius of the laser beam at the propagation distance z where the irradiance is $1/e^2$ (13.5%) of I_0 , and P is the total power of the beam.

This irradiance profile does not stay constant as the beam propagates through space along z . Due to diffraction, a Gaussian beam will converge and diverge from an area called beam waist (w_0), which is where the beam diameter reaches a minimum value. The beam converges and diverges equally on both sides of the beam waist by the divergence angle θ_d (fig. 2.5b). The beam waist and divergence angle are both measured from the axis and their relationship can be seen in the following equation [101]:

$$\theta_d = \frac{\lambda}{\pi w_0} \quad (2.15)$$

In the above equations, λ is the wavelength of the laser and θ_d is a far field approximation. Therefore, θ_d does not accurately represent the divergence of the beam near the beam waist, but it becomes more accurate as the distance away from the beam waist increases. Due to the inversely proportional relation between θ_d and w_0 , decreasing the beam diameter implies the increase of the beam divergence.

The variation of the beam radius in the beam waist region is defined by:

$$w(z) = w_0 \sqrt{1 + \left(\frac{\lambda z}{\pi w_0^2}\right)^2} \quad (2.16)$$

The Rayleigh range of a Gaussian beam is defined as the value of z where the cross-sectional area of the beam is doubled respect to its value at the propagation distance $z = 0$. This occurs when $w(z)$ has increased to $\sqrt{2}w_0$. Using eq. 2.16, the Rayleigh range (z_R) can be expressed as:

$$z_R = \frac{\pi w_0^2}{\lambda} \quad (2.17)$$

This allows $w(z)$ to also be related to z_R , so eq. 2.16 becomes:

$$w(z) = w_0 \sqrt{1 + \left(\frac{z}{z_R}\right)^2} \quad (2.18)$$

From fig. 2.5b the following trigonometric relation can be immediately obtained:

$$z = \frac{w_z}{\tan\left(\frac{\theta_d}{2}\right)} \quad (2.19)$$

with z distance propagated from the plane where the wavefront is flat, w_z radius of the laser beam at the propagation distance z where the irradiance is $1/e^2$ (13.5%) of I_0 , and θ_d divergence angle.

The wavefront of the laser is a function of the distance from the beam waist z defined as follows:

$$R(z) = z + \frac{z_R^2}{z} \quad (2.20)$$

From this relation, it is possible to observe that the wavefront is planar at the beam waist and approaches that shape again as the distance from the beam waist region increases. This occurs because the radius of curvature of the wavefront begins to approach infinity. The radius of curvature of the wavefront decreases from infinity at the beam waist to a minimum value at the Rayleigh range, and then returns to infinity when it is far away from the laser; this is true for both sides of the beam waist.

All actual laser beams have some deviation from the ideal Gaussian behaviour. The laser beam quality is assessed on the basis of the beam parameter product (BPP) defined as follows:

$$BPP = w_0 \theta_d \quad (2.21)$$

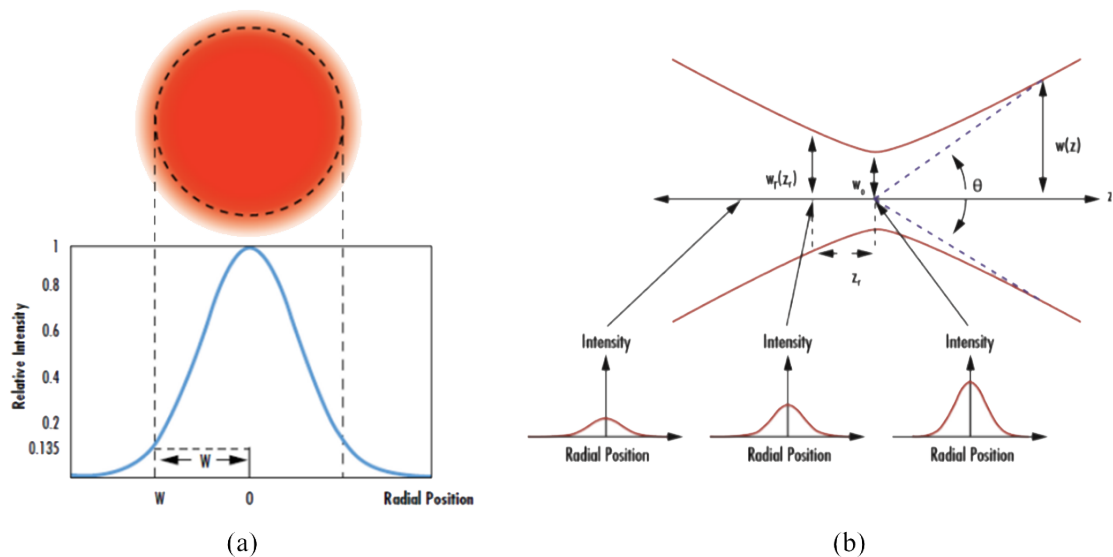


Figure 2.5: **Gaussian source.** Gaussian irradiance profile. The emergent light I has lower intensity than the incident light I_0 .

The performance of a real laser beam are compared with that one of a diffraction-limited Gaussian beam, which is a laser beam with the smallest possible BPP.

The relationship of inverse proportionality between the divergence angle θ_d and the beam waist w_0 must be considered when a laser beam reduction is required to couple light in an optical waveguide. The higher beam divergence resulting from this may introduce not negligible light losses due to the fact that some light rays may be expelled from the waveguide core because the condition for total internal reflection are not satisfied anymore.

2.3 Fluorescence

When photons hit a species containing a fluorescent material, they can get absorbed. The species is then excited by the incident photons and the distribution of electrons and holes is consequently affected within the fluorescent molecules.

The Jablonski diagram shown in fig. 2.6 is a partial energy diagram that represents the energy of a fluorescent molecule in its different energy states. The lowest group of horizontal lines represent the ground-state electronic energy of the molecule labelled as S_0 . At room temperature, the majority of the molecules in a solution are in this state. The upper lines represent the energy state of the first excited electronic state S_1 . Within each state, the thinner lines are different vibrational levels. If an incoming photon (yellow line) has energy higher than the band gap between S_0 and S_1 , it can be absorbed and

followed by the transitions (green line in the figure) from the ground electronic state S_0 to any of the vibrational levels in the excited state S_1 . A vacancy is then left in the ground electronic state S_0 . Absorption transitions (green line in the figure) can occur from the ground electronic state S_0 to various vibrational levels in the excited vibrational state S_1 . After the electron has been promoted to an excited state by absorption, it is in a non-equilibrium state, and it will eventually dissipate the energy that it has gained. This energy is first lost through vibrational relaxation (wavy arrow in the figure) within either the same molecule (intramolecular) or to surrounding molecules (intermolecular) until the lowest vibrational level of the excited electronic state is reached. Vibrational relaxation is non radiative, occurs on a rapid time-scale of 10^{-14} – 10^{-12} s and outcompetes all other transitions [102].

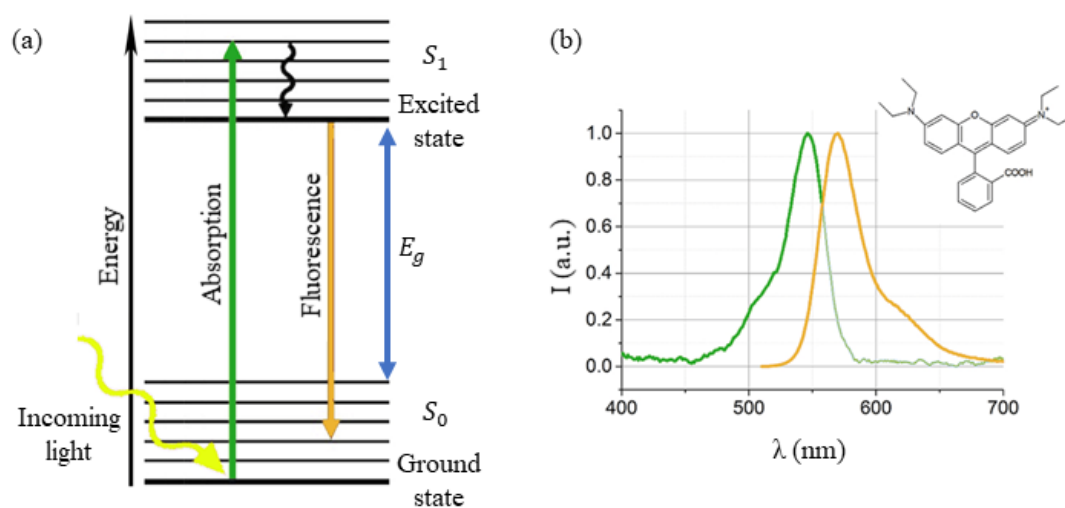


Figure 2.6: **Fluorescence.** (a) Excitation light is absorbed causing an electron of a molecule to leave the ground state and reach a higher energy level. Fluorescence occurs when the electron relaxes again to its ground state by releasing energy in the form of visible light (fluorescence). (b) Typical absorption and emission spectra of Rhodamine B (readapted from [103]).

Secondly, from the lowest vibration level of the excited state S_1 , the electron can radiatively decay back to S_0 , leading to the emission of a photon which is called *fluorescence*. The emitted photon has wavelength within the visible range and energy lower than the incident photon because part of the initial energy may have been dissipated through vibrational relaxation. Since energy is related to wavelength by

$$E = hc/\lambda \quad (2.22)$$

where E energy, h Planck's constant and λ wavelength. Since the emitted photon has lower energy than the incident one, it must also have longer wavelength. This phenomenon is known as *Stokes shift*.

The average time lapse τ between the excitation and the return to the ground state S_0 by the fluorescence emission is the *fluorophore lifetime* [104], which is usually in the order of magnitude of $10ns$.

2.4 Nanomaterials

Materials that extend, at least in one dimension, for less than 100 nm are usually classified as nanomaterials [105, 106]. They are divided in four major categories: zero, one, two and three dimensional nanomaterials [107].

Zero-dimensional (0D) nanomaterials represent materials wherein all the dimensions (x,y,z) are measured within the nanoscale of 1 – 100nm. The most common representation of 0D nanomaterials are nanoparticles [108].

One-dimensional (1D) nanomaterials possess nanometer size in two directions but larger length ($> 100nm$) in the third which leads to needle-like shaped nanomaterials. Carbon nanotubes (CNT), metals or metal oxides nanowires, polymer nanowires or nanofibers, and hybrid materials are the common representatives of 1D nanomaterials [109].

Two-dimensional (2D) nanomaterials are atomically thin sheets of materials with one dimension at the nanoscale, and the other two of the dimensions are not confined to the nanoscale [110].

Three-dimensional (3D) nanomaterials are materials that are not confined to the nanoscale in any dimension. They possess three arbitrarily dimensions above 100nm. However, 3D nanomaterials have a nanocrystalline structure or involve the presence of features at the nanoscale. In terms of the nanocrystalline structure, bulk nanomaterials can be composed of multiple arrangements of nanosize crystals in different orientations. With respect to the presence of features at the nanoscale, 3D nanomaterials can contain dispersions of nanoparticles, bundles of nanowires, and nanotubes as well as multilayers. All these nanomaterials with four different sizes and shapes are depicted in fig. 2.7.

Bulk and nanomaterials with the same molecular structure are chemically identical. However, the same substance in the nanoform is substantially different from its bulk form. When particle size are reduced, the percentage of atoms at the surface of a material becomes more significant. Interior atoms of any material are more coordinated and stable

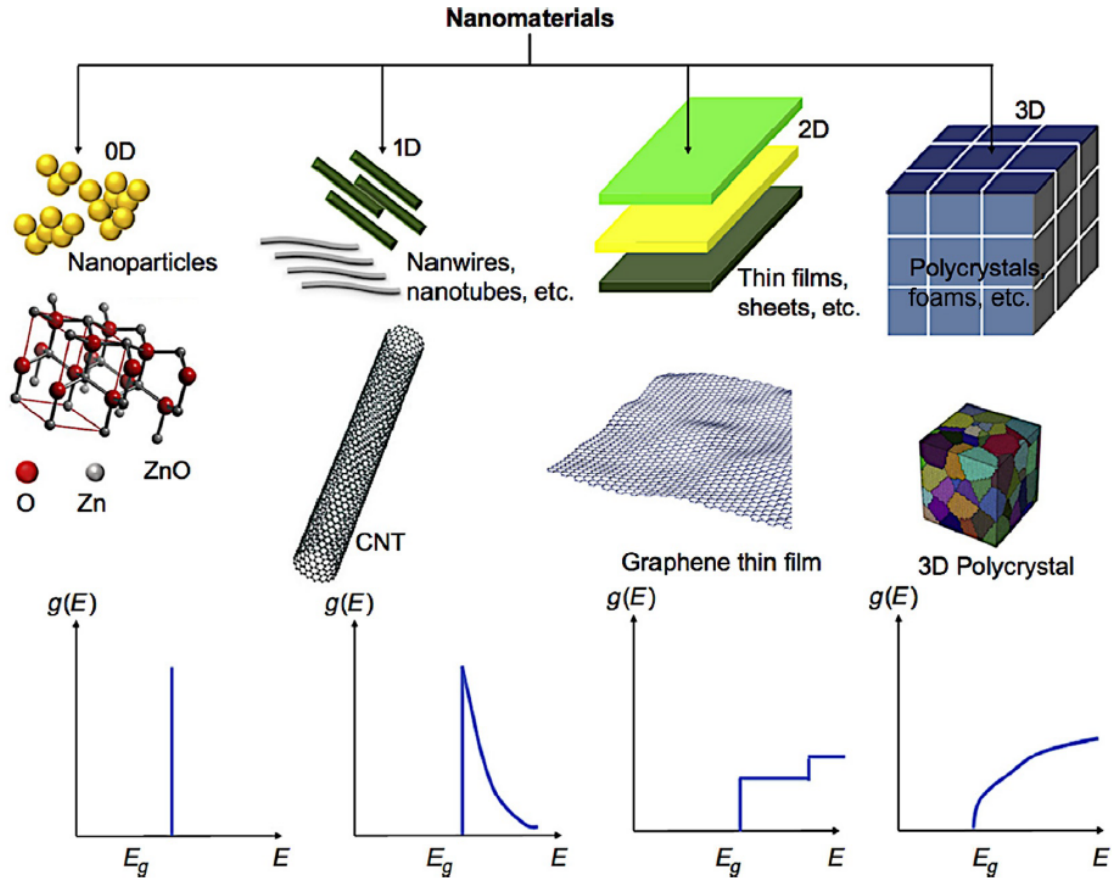


Figure 2.7: **Nanomaterials and their density of electron states.** Schematic representation of zero-dimensional (0D), one-dimensional (1D), two-dimensional (2D), and three-dimensional (3D) nanomaterials and density of electron states of a semiconductor by varying dimension, where $g(E)$ is the density of states (fig. from [111]).

than surface atoms which instead have lesser available bonds and therefore lesser stability [111]. For these reasons, surface atoms are highly reactive and more liable than inner atoms to interact with the environment. This increase in the ratio between surface and interior atoms drastically change the physical, chemical and optical properties of the materials [112, 106].

Optical properties are mostly effected by the electronic structure of the material. In a bulk semiconductor there is a large number of atoms, and the overlap of this high number of atomic orbitals creates a continuum of closely spaced energy levels that form the valence and conduction bands. By reducing the size of the semiconductor to the nanoscale, in the order of $10nm$, this situation changes: fewer atomic orbitals overlap, the valence and conduction bands are no longer continuous, and the bandgap between the valence and conduction bands becomes wider (fig. 2.8) [113]. The smaller the dimensions of the nanostructure, the wider is the separation between valence and conduction bands and the

electronic structure tend to be more discrete getting closer to the single atom electronic levels.

This effect is called quantum confinement. It describes electrons in terms of energy levels, valence and conduction bands, electron energy band gaps and it is only observed when the size of the particle is in the range of the tens of nanometer or smaller [114]. By tuning the particle dimension is possible to change the material properties [115]. Recently it has been seen that the shape of the nanomaterial also plays a role in controlling its properties [116].

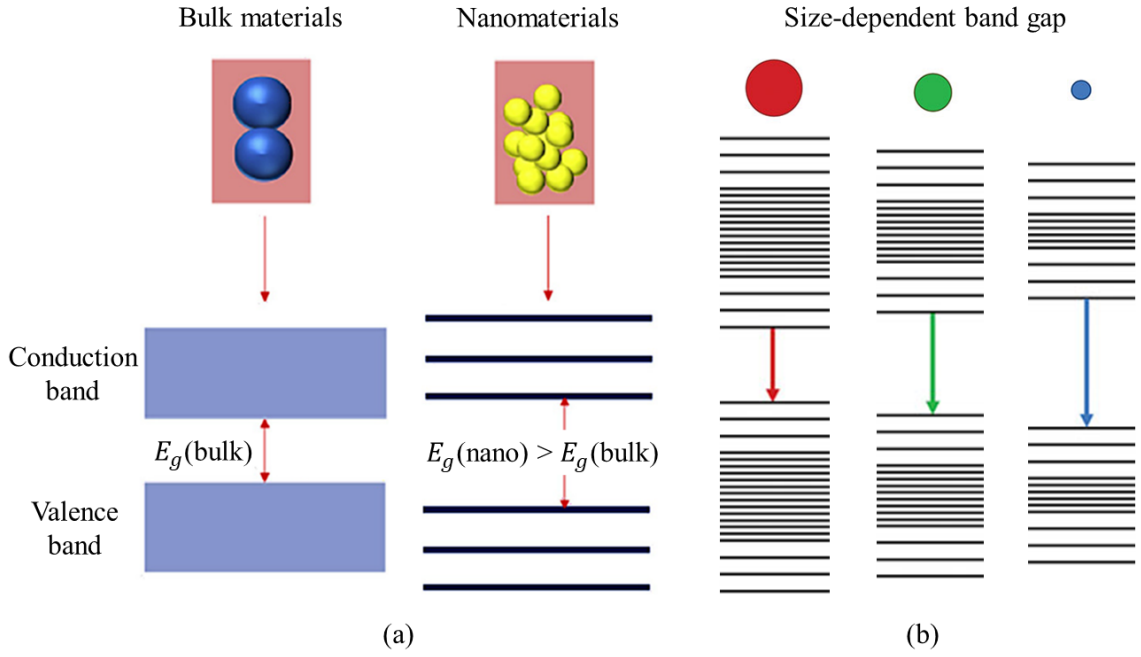


Figure 2.8: **Band gap tunability.** (a) Valence and conduction bands of bulk materials are continuous, while nano-scale materials present discrete energy levels (fig. readapted from [111]). (b) The band gap increases by decreasing the material size.

2.4.1 Optical properties

Optical properties such as emission and adsorption occur when electron transition occurs between valence and conduction bands. This optical bandgap increases with the decrease in particle size, especially for semiconductor nanomaterials. When an electron drops from higher energy state to lower energy state, a quantum of light (photon) with wavelength $\lambda = \frac{hc}{\Delta E}$ will be emitted where h , c , ΔE are Plank's constant, speed of light, and energy difference between allowed electron energy levels, respectively. The larger the ΔE the shorter the wavelength.

Thus, semiconductor nanomaterials absorb and emit light at certain wavelengths that

depend strongly on both particle size and shape due to these quantum confinement effects. By changing the size and composition of the nanomaterials, their emission wavelengths can be tuned from the UV through the visible to the near-infrared regions of the spectrum. For example, by tuning the size of colloidal CdSe/CdS core-shell nanoparticles from 2 to 6nm in diameter, the emission wavelength can be shifted across the visible spectrum, with the smaller particles emitting in the blue and the larger particles emitting red light (fig. 2.9) [117].

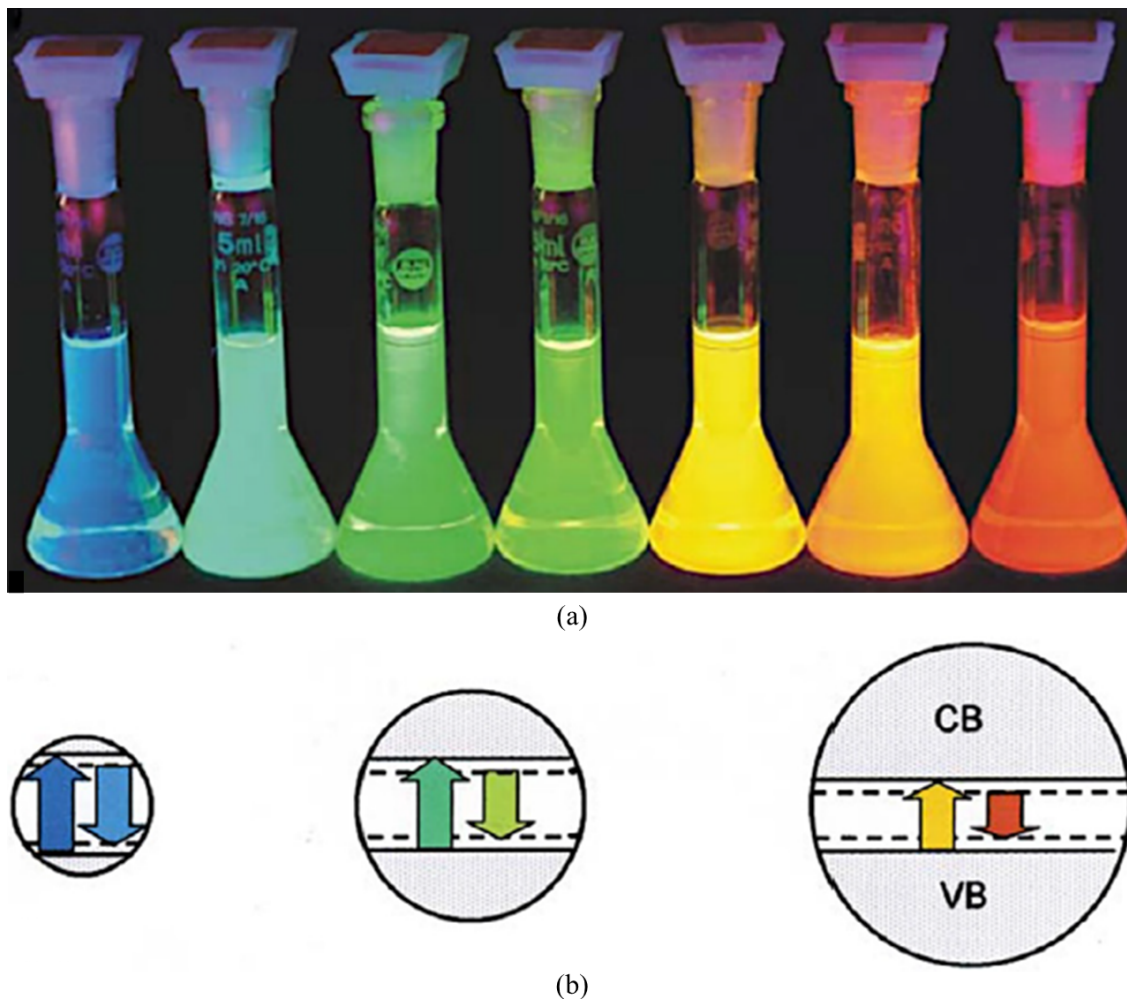


Figure 2.9: **Fluorescence modulation across the nanoparticle size.** (a) Fluorescence of CdSe-CdS core-shell nanoparticles with a diameter of 1.7nm (blue) up to 6nm (red), giving evidence of the scaling of the semiconductor bandgap with particle size. (b) Schematic representation of the size effect on the gap between the valence band (VB), the conduction band (CB), the absorption (up arrow) and fluorescence (down arrow). Smaller particles have a wider band gap (fig. readapted from [117]).

2.4.2 Core-shell QDs

The extremely small size of QDs can result in a very high surface-to-volume ratio and lead to a highly sensitive surface region, wherein the lower coordination of surface atoms is prone to induce the formation of the surface defects. These surface defects can work as "traps" and become a place for non-radiative recombination of photogenerated charge carriers, thereby reducing the photoluminescence efficiency and photo/chemical/thermal stability of QDs, which are detrimental for the relevant optoelectronic applications [118, 119, 120].

The growth of another semiconductor shell on core QDs to form core/shell QDs is one of the most promising approaches to efficiently passivate the surface traps, leading to enhanced PLQY, suppressed photobleaching, and photoblinking as well as largely improved photo/chemical/thermal stability with respect to bare QDs [121, 122]. More importantly, the band structure of core/shell QDs can be tailored via tuning the core and shell compositions and the shell thickness.

Depending on the band gap of the bulk material that composes the core and the shell, three types of core-shell systems can be distinguished: Type I, Reverse Type I and Type II [123], as shown in fig. 2.10 . In Type I (CdSe/ZnS) the band gap of the shell is bigger than the one of the core, being both electrons and holes confined in the core [124]. In this case the shell acts as a protection of the core, giving rise to the significantly enhanced PLQY and photostability that are favorable for light-emitting applications [118, 125, 126, 127]. In Inverse Type I (ZnSe/CdSe) the opposite situation is presented: the band gap of the core is bigger than the band gap of the shell [128]. In this case the position of electrons and holes depends on the thickness of the shell being partially or entirely confined in the shell. Finally, in Type II core-shell QDs (CdTe/CdSe) either the valence band or the conduction band of the shell is situated in the band gap of the core. Consequently, the electron and the hole are separated and situated in different parts of the final structure [129].

The type I core/shell CdSe/ZnS QDs have been employed in this work.

2.4.3 Piezoelectric effect

Piezoelectricity is a phenomenon of strain induced electric polarization in certain crystals [130]. It is a reversible physical phenomenon, as there is the direct piezoelectric effect and the reverse piezoelectric effect. The direct piezoelectric effect is given by the

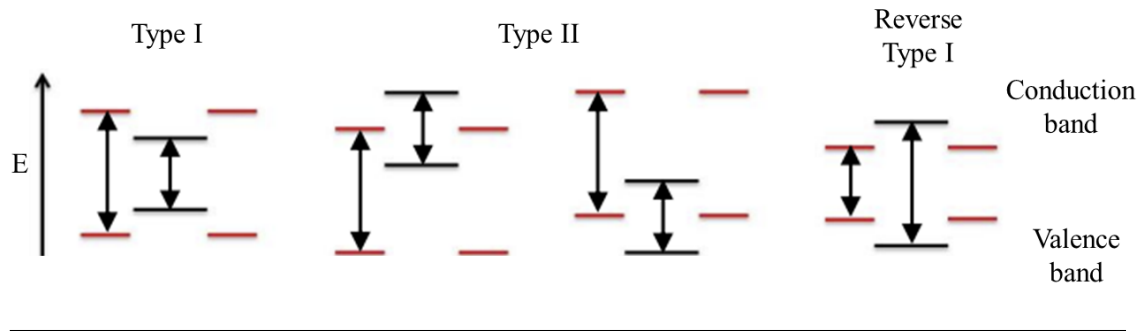


Figure 2.10: **Bandgap alignment in core/shell QDs.** Scheme of the bandgap alignment between the core (black) and the shell (red) material in a core-shell system. From left to right: Type I, Type II (two cases) and Inverse Type I. Fig. readapted from [123].

electric polarization produced by mechanical strain, the polarization being proportional to the strain and changing sign with it. The reverse (or inverse) piezoelectric effect occurs when a piezoelectric crystal is electrically polarised by applying an external voltage and becomes strained [131].

The nature of piezoelectricity comes from the lack of centrosymmetry/inversion symmetry in the crystal related to the atomic structure of the material. The two most important classes include perovskite structure, which occurs in ceramics such as Lead Zirconate Titanate (PZT) and Barium Titanate (BaTiO_3); and wurtzite structure, which occurs in semiconducting materials such as Cadmium Selenide (CdSe), Zinc Oxide (ZnO), Gallium Nitride (GaN), Indium Nitride (InN), and Zinc Sulfide (ZnS) [130].

In a wurtzite structure, each of the two individual atom types forms a sublattice where the atoms have a tetrahedral coordination with each other [132].

Taking as an example the wurtzite-structured CdSe QDs, the tetrahedrally coordinated Cd and Se atoms are accumulated layer-by-layer as depicted in fig. 2.11a. At its original state, the charge center of the anions and cations in each tetrahedral unit of the lattice coincides with each other 2.11b. When an external force is applied, the structure is deformed (stretched or compressed). Therefore, the negative and positive charge centers are displaced and not coincident anymore. So, the structural symmetry is broken and the ionic charges cannot freely move and cannot recombine without releasing the strain. Consequently, an electric dipole is generated, leading to a piezoelectric potential 2.11c. This is called piezoelectric potential or piezopotential [133].

The application of an external mechanical strain induces a bandgap change which alters fluorescence intensity and wavelength of the affected QD. Therefore, the photoluminescence is a direct way to monitor the pressure-dependent lattice variation through

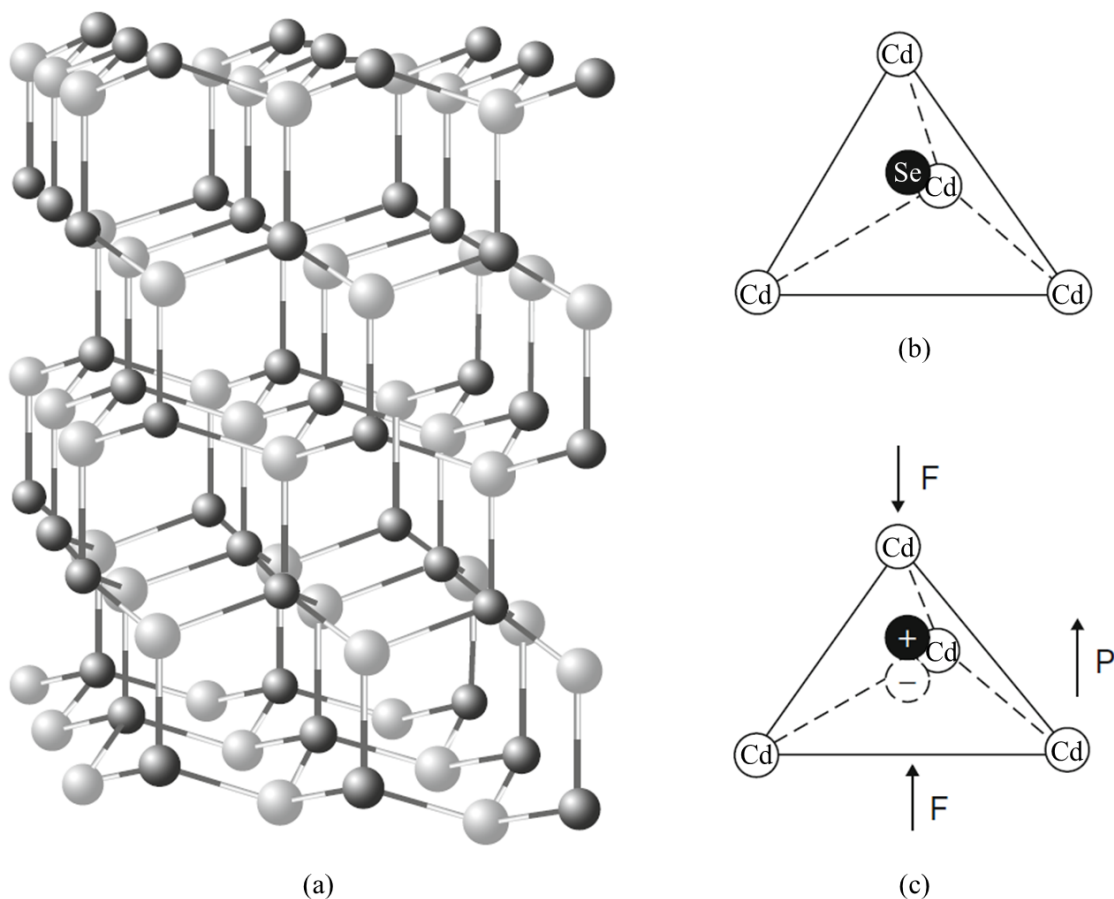


Figure 2.11: **Wurtzite structure.** (a) Wurtzite structure of semiconducting materials such as CdSe. (b) Sublattice of Cd and Se atoms with tetrahedral coordination between each other, in the resting condition. (c) Generation of dipoles and piezo-potential when the sublattice is under compression (fig. readapted from [130]).

spectral shifts, and further determines the pressure dependence of carrier confinement energy [134, 135, 136]. The photoluminescence pressure dependence in CdSe QDs was studied and a blueshift was observed under high pressure [137, 138, 139]. The rate of blueshift is an important signature to reveal the pressure dependence of the electronic properties of these QDs.

The blueshift rate of QD photoluminescence is size-dependent [140], and for some structure the photoluminescence undergoes a slower blueshift rate at higher pressure [136, 139]. Moreover, the photoluminescence properties of QDs exhibit different pressure dependence for different capping agents and pressure mediums [137, 134]. For instance, epoxy matrix can highly increase the pressure sensitivity of CdSe/ZnS QDs in a very low pressure regime (<1 MPa) [134], which provides an important view in the development of sensitive optical strain sensors.

Chapter 3

Optical Waveguide Channels For 3D Distributed Tactile Sensing

As discussed in the introduction, current tactile sensing solutions struggle to provide high-spatial density tactile sensors adaptable to non-planar surfaces such as the sheath of a colonoscope, able to detect pressures applied normally to its sheath, maintaining compact dimensions and lightness to allow the probe movement in spatially constrained environments and, at the same time, satisfying the need of simple manufacturing process and low cost.

To deal with these challenges, an optical sensor based on lab-made soft polymer waveguides is proposed. The fabrication of lab-made waveguides was preferred respect to the use of commercial optical communications fibers, because the latter undergo deformation for pressures in the order of magnitude of *few GPa* [141]. Since the typical pressures in colonoscopy are in the range of *tens of kPa*, it would not be possible to observe light modulation in the range of interest by using commercial optical fibers.

In addition, the lab-made manufacturing of the waveguides confers the freedom to design complex configurations where the light is guided from a single input optical channel and then is split into multiple output channels. This is convenient to avoid the use of fiber bundles which may require to be placed in the endoscope body, potentially compromising its miniaturisation, flexibility and lightness. In addition, the possibility to obtain customised optical channels design also allows to minimising the cost of the final device by using a single light source in front of the input channel which powers all the output channels.

The soft waveguides were fabricated on a rigid substrate to facilitate the fabrication method. In fact, by a proper selection of materials used, the substrate could take on, first, the role of mould to welcome the integration of the core channels by injection moulding and, secondly, the role of cladding to ensure light transmission through the core channels.

The light injected by the optical source propagates through the waveguide channels. Pressures can be applied normally respect to the light propagation direction along each output waveguide channel. When the latter is pressed, the conditions required for light transmission may not be satisfied anymore, determining a light modulation measurable

at the output of the channel. Each one of the multiple output channels works as an independent sensing element providing a light modulation in response to a pressure, which allows to increase the spatial resolution of the sensor.

Although the study presented in this work focuses on a flat rigid substrate, the research team has also demonstrated the possibility to confer a curved shape to the substrate, making this approach adaptable to non-planar surfaces [142]. However, further advancements on this sensing strategy would be required to be able to cover a colonoscope section through 360°. Also, the current thickness of the substrate limits the flexibility of the sensing device.

The sensing strategy described in this chapter offers important characteristics required to be employed as haptic technology for endoscopy as presented in section 1.5 and summarised below.

- The replacement of commercial optical fibers with lab-made waveguides avoids the introduction of wires to be placed inside the endoscope sheath (requirement 1).
- The sensing principle proposed allows the use of optical waveguide configurations to detect pressures applied normal to light propagation direction (the sensing area is not limited to the fiber tip as commonly presented in literature), satisfying the requirement 2.
- The spatial resolution (requirement 3) is enhanced by the development of lab-made waveguide channel configurations leading to multiple sensing output channels.
- The use of lab-made waveguide channels instead of commercial optical fibers confers the possibility to detect pressures in the range of interest (requirement 4), although also materials selection and sensor design were taken into account to confirm this.
- The absence of electrical component in the main body of the sensor ensures biocompatibility, sterilizability and MRI compatibility (requirements 5, 6 and 7).
- The simple fabrication process and the use of a single light source help to reduce the costs and facilitate an eventual mass production (requirement 8).

Although this work is focused on the roof of concept of the presented working principle on a flat geometry, the design can also be adapted to non-flat rigid substrates as shown in fig. 3.1, where the sensing elements follow a curved geometry such as the external surface of an endoscope [143, 144].

The missing points of the proposed sensing approach are the flexibility and the integration

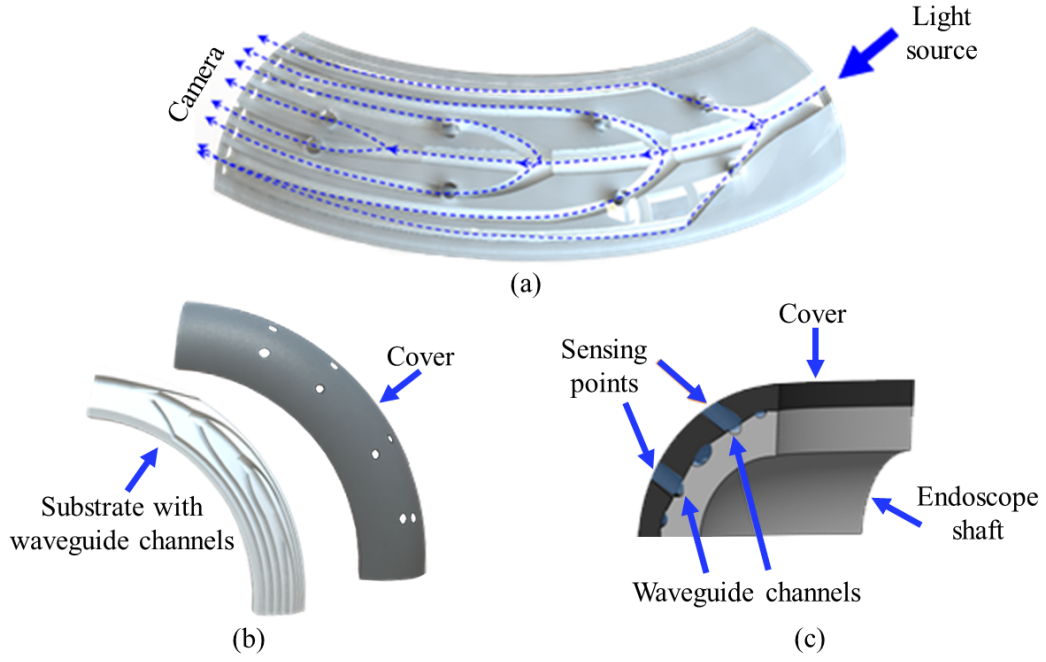


Figure 3.1: **Distributed pressure sensing based on optical waveguides.** The light travels through the channels of the waveguide structure and it is measured by a camera [143].

into commercial endoscopes (requirement 1). These limitations will be overcome by the sensing technologies proposed in Chapters 4 and 5, which are fully flexible and the possibility of miniaturisation was also investigated.

The first challenge faced in this chapter was ensuring that the waveguide channels have a good light transmission efficiency. For this purpose, the optical properties of the material used for the waveguide core have been investigated. A theoretical model was developed to distinguish the different effects leading to light loss through a waveguide. A joint approach involving a simulation in Optic Studio and experimental measurements was employed to quantify the different light losses and validate the theoretical model.

3.1 Sensing Principle

The working principle of the proposed sensing technology uses bending loss technique where deformations of an optical waveguide trigger a modulation in the light propagation detectable at the output. Light losses due to bending can be distinguished in macro and micro bending. Macrobending losses are generated when the curvature radius of a waveguide become so small that total internal reflection is no longer valid for all admitted propagation angles. Microbending is an attenuation increase caused by high frequency

longitudinal perturbations to the waveguide leading to a deviation of its section from its ideal geometry. The small radius bends that cause microbending are typically $< 1\text{mm}$ radius [145]. Perturbations can be caused by manufacturing imperfections (such as core diameter and refractive index variation) or the application of external pressures. The last case refers to the working principle of the proposed sensor. Microbending is most critical when external pressures are such that the optical core is deformed [146]. In this case, the conditions for light transmission through the core may not be satisfied anymore and some light is lost leading to a detectable intensity modulation at the output of the waveguide (fig. 3.2).

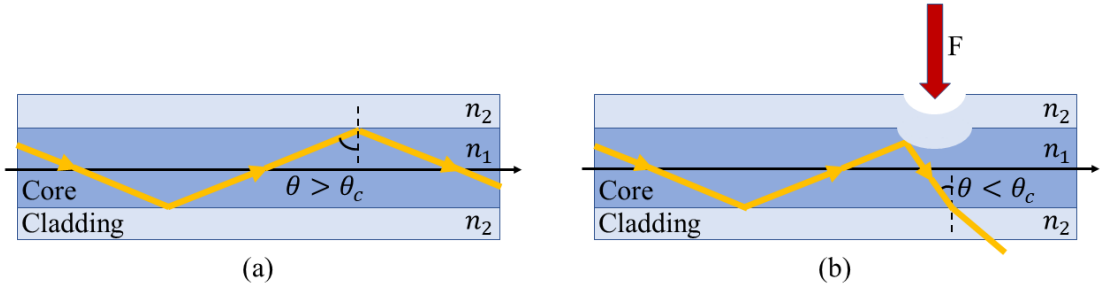


Figure 3.2: **Sensing principle of microbending.** (a) Optical waveguides use TIR to transmit light through the core. (b) When a force is applied on the waveguide, a deformation of the core may occur and the conditions for TIR may not be satisfied anymore, determining light attenuation detectable at the output of the waveguide.

3.2 Waveguide Losses

In order to achieve a good signal to noise ratio, light transmission through the waveguide must be maximised and light losses must be contained.

A characterisation study was carried out on a waveguide realised as explained in subsection 3.3.2 to determine the light transmission properties obtainable from the suggested materials and manufacturing method.

A theoretical model can be used to define the different effects leading to light loss in a waveguide [147].

Insertion losses (IL) are defined as the total losses induced by the device, with respect to the case of absence of the device itself. They are typically expressed in deciBel (dB). In order to measure the IL, light is injected in the input-facet of the waveguide, while the

output-facet is imaged on a power meter head. IL is calculated as follows:

$$IL = 10 \log_{10} \frac{P_{out}}{P_{in}} \quad (3.1)$$

with P_{in} power emitted by the light source and P_{out} power coming out from the output facet of the waveguide. In case of straight waveguides IL can be decomposed in the sum of different terms:

$$IL = CL + FL + PL \times l \quad (3.2)$$

where

- CL (Coupling Losses) occur when optical power is transferred from free propagation to a guiding medium or from one guiding medium to another. When the optical power is transferred from a light source to a single-mode waveguide, the problem of matching the mode of the incident laser light into the mode of the waveguide must be considered. Instead, when a source is coupled into a highly multi-mode waveguide, the mode of the light source will be supported by the waveguide and the power loss due to the mode coupling is negligible. In this case, the coupling losses are mostly caused by one of the alignment problems shown in fig. 3.3. An axial displacement occurs when the propagation axis of the light source is placed at a distance d from the optical axis of the waveguide core (fig. 3.3a). An angular misalignment happens when the propagation axis of the light beam creates an angle θ with the optical axis of the waveguide core (fig. 3.3b). Lastly, also an imperfect finish of the the waveguide facets determines coupling losses. In fact, irregular surfaces or non-flat cut with an angle respect to the optical axis of the waveguide can increase the percentage of light back reflected and not transmitted through the core (fig. 3.3c). Since the experimental setup was designed to get a good positioning of the waveguide respect to the laser beam as detailed in section 3.3, an effective coupling can be considered accomplished and the coupling losses can be regarded as negligible.
- FL (Fresnel Losses) originate at the interface of two media with different refractive indices, where a fraction of the incident optical power travelling though the first medium does not pass the interface with the second medium, but it is reflected back toward the light source. In a waveguide, Fresnel reflections occur at the core-air interface. At normal incidence, the fraction of reflected power is expressed by the

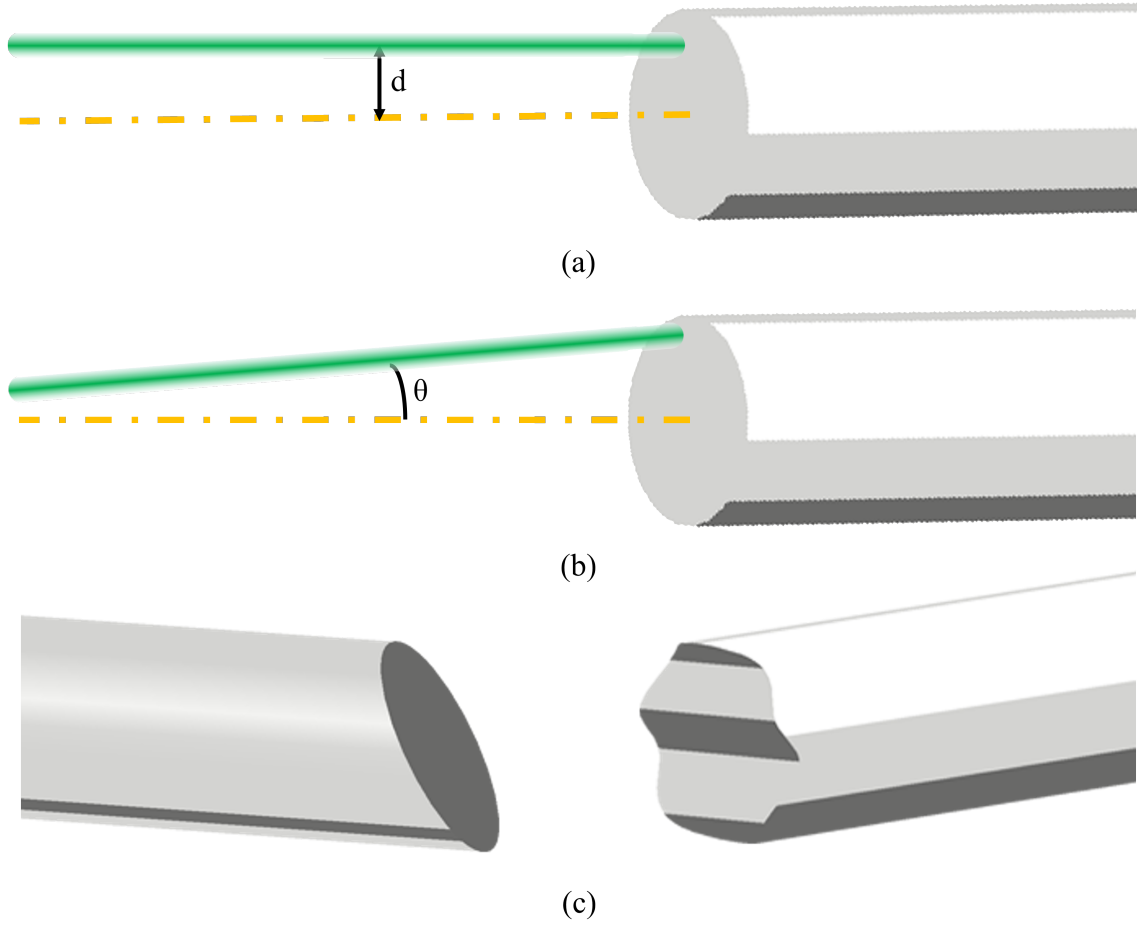


Figure 3.3: **Light coupling from a collimated laser source to a multi-mode waveguide.** Coupling losses are mainly due to a beam displacement with respect to the waveguide optical axis: axial displacement, when the beam propagates parallel to the optical axis but it is not collinear to it (a), angular displacement when the laser doesn't propagate parallel to the optical axis (b) and imperfect finish of the waveguide surfaces resulting in the beam not being perpendicular to the waveguide tip (c).

Fresnel equation as discussed in section 2.1.4 and Fresnel losses can be defined as follows:

$$FL = -10\log_{10}(T) = -10\log_{10}\left[1 - \frac{(n_{core} - n_{air})^2}{(n_{core} + n_{air})^2}\right] \quad (3.3)$$

considering that the transmittance T is equal to the portion of the incident power that isn't reflected, as a consequence of conservation of energy.

The insertion of the waveguide involves two core-air interfaces, namely the input and output waveguide facets, so the contribution of FL is doubled.

- PL (Propagation Losses) are the losses suffered per unit length of propagation in the waveguide, with l total waveguide length. They are due to roughness and non-uniformity in the waveguide structure. In fact, theory predicts no propagation losses

for a waveguide with perfect translational symmetry (i.e. uniformity) along the optical axis direction. They can be calculated from eq. 3.2 once the other terms have been estimated.

In case of a bent waveguide, insertion losses can be calculated as follows:

$$IL = CL + FL + PL \times l + BL \times l \quad (3.4)$$

where the term BL takes into account the losses due to bending.

Insertion losses measured as given in eq. 3.4 are also defined as the power attenuation of the light travelling through the waveguide, since it takes into account the overall optical loss as a result of reflection, absorption, scattering, bending, and other loss mechanisms as just discussed. The total attenuation follows the Beer-Lambert law (see section 2.1.4) and it is a function of the wavelength λ of the light. The attenuation coefficient or attenuation rate is given by $\frac{\alpha}{L} [\frac{dB}{cm}]$ where L is the distance travelled by the light between the points X and Y where P_{in} and P_{out} are measured.

3.3 Manufacturing Process Of Polymer Waveguides On A Rigid Substrate

The proposed sensor design is based on soft optical channels that develop following as multiple splitters connected in cascade. This optical channel configuration required an optimisation process which is detailed in section 3.6.

The optical channels, which assume the role of core, are integrated into a rigid substrate, which absolves the role of cladding. The requirements for the light transmission through the soft channels impose a material selection such that the refractive index of the core is higher than the refractive index of the cladding, as shown in fig. 3.4.

The process of material selection and manufacturing are detailed in this section.

3.3.1 Selection of materials

Materials and manufacturing methods were selected to ensure light transmission through the device. Since the sensing principle is microbending, a soft material was preferred for the waveguide core fabrication to facilitate the channel deformation. A tough material was suitable as substrate instead. It was also considered that if the substrate material had a refractive index lower than the one of the core material, this could take on

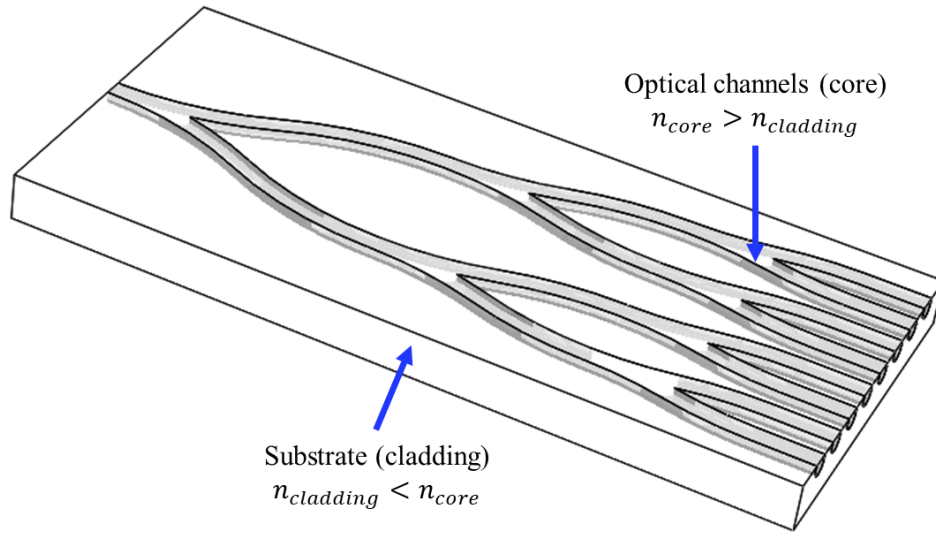


Figure 3.4: **Polymer waveguide channels on rigid substrate.** Multi-splitter configuration of soft core channels (refractive index of ~ 1.5 for commercial plastic optical fiber) integrated on a rigid cladding substrate fulfilling the role of cladding (refractive index of ~ 1.4 for commercial plastic optical fiber).

the role of cladding and welcome the integration of the core channels, without need to use any other additional material (see section 2.1.1). The approximate refractive index values of core (~ 1.5) and cladding (~ 1.4) of a commercial plastic optical fiber (Edmund Optics, 02-536) were taken as reference value to give an initial direction to the materials search. The definition of the manufacturing process and the selection of suitable materials were challenging aspects.

Injection moulding was initially considered as fabrication method of both core and cladding. In this respect, some materials used as coating for optical fibers with refractive index ~ 1.4 have been considered for the cladding. They were provided in the form of a viscous liquid resin, they needed to be poured in a mould and required a UV light source to cure. However, the need to develop a proper mould where to pour this material in and all the subsequent actions required for the core integration would have added several steps to the overall manufacturing process of the sensor, increasing its complexity and duration. Considering that this was a project in collaboration with Huawei with possible commercial perspectives, it was particularly important to keep the manufacturing process as simpler and faster as possible to facilitate a potential future mass production.

It was also considered the possibility to fabricate the core first and then coat it by using dip coating techniques or spraying the cladding material on it. But, considering that the core fabrication was based on injection moulding, these processes presuppose the extraction of

the core channel from the mould after curing. Since it was intended to use a soft material for the core, the extraction of the soft core from the mould was not practicable without deforming, elongating or even breaking the soft core. The use of silicone easy removal products was tested but it was not enough to avoid the alteration of the core shape.

Another not negligible aspect was the high cost of these resins commonly used for optical fiber claddings, quoted for more than one thousand pound for a 500g bottle by the suppliers contacted. For these reasons, the use of these resins and the injection moulding method for the cladding manufacture were excluded.

It was considered, instead, to 3D print or CNC (Computer Numerical Control) machine the substrate in a way to get the hollow channels ready to welcome the soft material of the core to be poured in. The requirement to use the substrate as cladding was finding a material for the cladding with refractive index lower than the material for the core to ensure total internal reflection.

The typical refractive index of some of the main polymers used for 3D printing and CNC machining has been investigated and it was found that materials such as acrylonitrile butadiene styrene (ABS), polycarbonate, polypropylene and nylon have refractive index ~ 1.5 , quite high for the aim to create a cladding layer. The polymer Polytetrafluoroethylene (PTFE) instead presents a refractive index ~ 1.4 measured at $530nm$ [148]) which was considered interesting for the purpose at hand. Designs made of this material can be both 3D printed and CNC milled. So, this polymer was providing a good option to fabricate a substrate able to first assume the role of mould to welcome a suitable soft material for the core and then assume the role of cladding to ensure light transmission through the core. In addition, PTFE is a plastic with unusually high thermal stability and chemical resistance. Both these properties are very interesting for injection moulding procedures, allowing the eventual use of the oven to speed up the curing process and avoiding any chemical reaction when the PTFE substrate gets in contact with the soft material of the core.

On the other end, several suppliers, such as Bentley Advanced Materials or Smooth-On Inc., have been contacted to provide information regarding their silicone rubber materials to find a soft material for the core with proper refractive index and well suitable for injection moulding. In most of the cases, the refractive index was not provided by the suppliers, in other cases the value provided was ~ 1.4 .

Since the requirement to ensure light transmission through the core was not satisfied by these options of materials, for the core the search was moved towards materials specifically

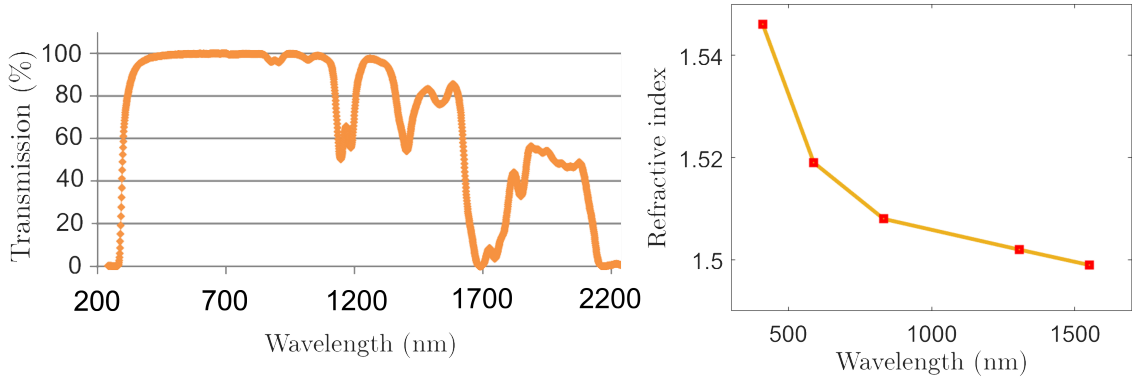


Figure 3.5: **Optical characterisation of the core material.** (a) Transmission rate relative to air considering a 1cm path length. (b) Dispersion diagram measured at 25°C. Plots re-adapted from product data sheet (Nusil, LS1-3252).

produced for optical applications such as LEDs and display assembly. A soft transparent polymer gel (Nusil, LS1-3252) was selected because of its refractive index of ~ 1.5 in the wavelength range of interest (around 530nm), and its low viscosity ($360\text{mPa} \cdot \text{s}$) when uncured. Since the core manufacturing process is based on injection moulding, a material with low viscosity can be easily poured and it naturally follows the shape of the mould reducing voids in the assembly to fill in, and permits time for any trapped air bubbles to float to the fluid surface and escape. These are very important properties to reduce irregularities in the geometry of the moulded core and inclusions and impurities within its volume, which affect the transmission efficiency of the resulting waveguide causing light loss.

Fig. 3.5 shows some data of the soft gel as provided by the supplier. The transmission rate of the light passing through a 1cm layer of the polymer gel surrounded by air, over the range $[200 - 2200]\text{nm}$ is shown in fig. 3.5a. It can be observed that the transmission rate is close to 100% on the whole visible range. This is fundamental to minimise signal losses due to absorption for a waveguide designed to operate in the visible range. The dispersion diagram shows a refractive index n_{core} between $[1.5 - 1.55]$ in the visible range. This value is higher than the typical refractive index of common transparent silicone materials (usually around 1.4) and for this reason it is well suited to be used as core material in order to guarantee total internal reflection.

3.3.2 Manufacturing process

Once the design of the waveguide channels is done (this will be detailed later) and the materials selected, 3D printing and CNC machining techniques have been considered to fabricate the sensor substrate equipped with the waveguide channels. The main challenge of manufacturing these channels is obtaining a well defined geometry and very smooth surfaces. These are fundamental requirements because the presence of irregularities and asymmetries in the waveguide structure leads to power loss of the light transmitted (transmission losses). To prevent the occurrence of this type of transmission losses, the surface roughness should be lower than the wavelength of the light to be transmitted, so generally in the range of few hundreds of *nm* or lower. In order to take these needs into consideration, standard CNC-milling, with a typical resolution of $\pm 0.1\text{mm}$, was preferred over 3D printing techniques, commonly characterised by resolution of $\pm 0.3\text{mm}$ or higher.

The milled parts were outsourced and, once received, they have been used as mould as explained in the following steps:

1. input and outputs of its machined channels were temporarily closed with some melted wax;
2. the soft material was injected into the channels using a syringe equipped with a thin needle to minimise the presence of air bubbles (which causes absorption and scattering effects leading to light loss);
3. the surplus material on the upper surface, which is not enclosed by the mould but remains exposed to air, can be simply levelled using a smooth blade edge;
4. the filled mould was left in a vacuum pump for about 15 minutes to further remove air bubbles and then left to dry;
5. after a three hours dry time at room temperature, a thin PTFE sheet (thickness of 0.1mm , Amazon, MAGT Film Sheet) was placed over the mould and left to adhere during further 48 hours of curing.

The curing process can be reduced to 4 hours by placing the mould in a oven at 65° . The manufacturing process is outlined in fig. 3.6 where the multi-splitter channel configuration is taken as an example, although same materials and procedures were used for every prototype with rigid substrate presented in this chapter. Under a visual inspection, the sensors

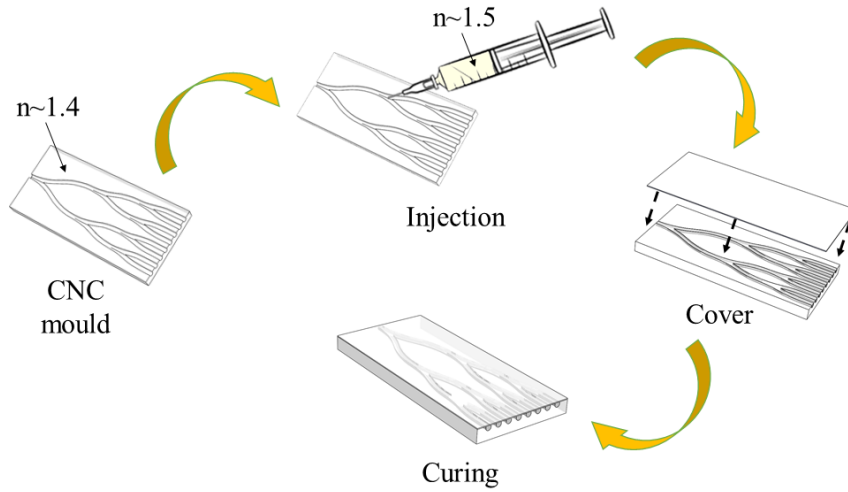


Figure 3.6: **Manufacturing process.** A CNC machined PTFE part is used as mould, a soft material with refractive index higher than PTFE is injected into the machined channels, a PTFE sheet is used as cover and the mould is left drying.

obtained following this method appeared homogeneous, without evident air bubbles or cavities.

It should be noted that CNC machining on PTFE is quite expensive, because the drill must rotate very slowly to allow the polymer to cool down and avoid melting it during the process. However, each PTFE part can be re-used multiple times, while the part of the sensor more subject to wear is the core. When the core needs to be replaced, the soft material that constitutes it can be thoroughly removed and the PTFE substrate can be accurately cleaned using a cloth damped with some alcohol.

3.3.3 Absorption of the core material

In order to study the light losses for a waveguide manufactured as described in section 3.3, a preliminary measurement was done to quantify the light absorption on the range $[350 - 550]nm$ through a sample made of the transparent polymer gel LS1-3252 used as core material for the waveguide. The sample was realised by using materials and methods analogous to those of the waveguide manufacturing process presented in section 3.3, to ensure consistency between this experiment and the followings carried out on multi-channel waveguide designs.

A PTFE mould was CNC machined and was made by two parts, a lower plate and an upper plate equipped with a slot milled from side to side, where the soft material is placed. Upper and lower plates were screwed together, creating an enclosed mould suitable for

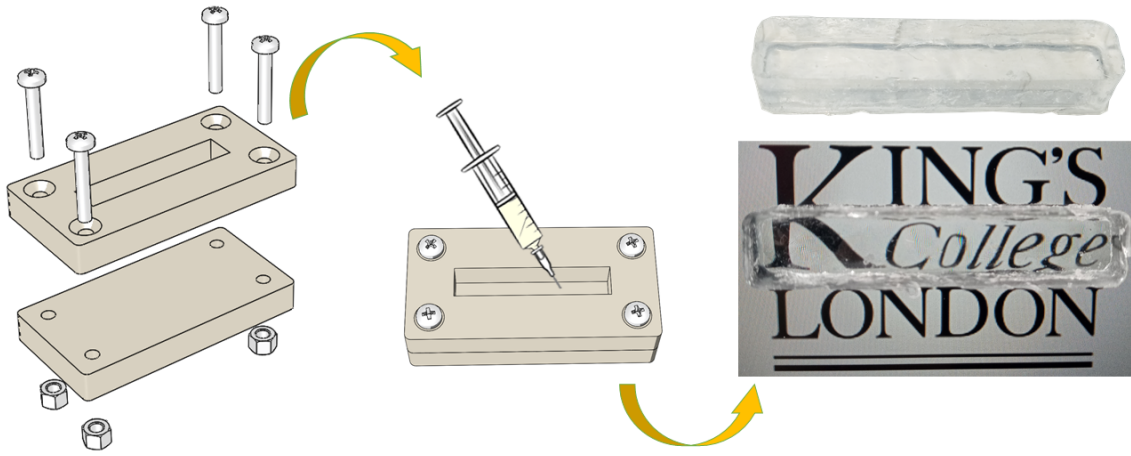


Figure 3.7: **Fabrication of the core material sample.** A CNC machined mould made by two parts which can be unscrewed facilitates the removal of the sample, once cured. The resulting sample seems to have pretty smooth surfaces and good transparency.

injecting the gel material. A syringe equipped with a thin needle was used for injection and the filled mould was left in a vacuum chamber for about 15 minutes to minimise the presence of air bubbles as shown in fig. 3.7. After curing, the sample was pulled out unscrewing the the two parts of the mould and pushing the soft material out of the slot. The resulting sample was a slab with squared section having sides of 9mm . From a qualitative inspection, the resulting sample appears to have good transparency (fig. 3.7).

Absorption measurements along a broad wavelength range are usually performed by multiple acquisitions illuminating the sample with different small bands of wavelengths for each measurement, rather than by a single acquisition illuminating the sample with the full wavelength range. This allows to avoid effects that may occur if the sample is fluorescent for specific wavelengths [149]. Another point to consider is that effects of heating and thermochromism (colour change of a substance due to a temperature variation) may affect the all measurement when the sample is directly irradiated with the full wavelength range of the source [150]. By splitting the full spectrum in small bands it is possible to identify the wavelength sub-range where any fluorescence effect occurs. In addition, the total power irradiating the sample is way lower than the one of the full spectrum, therefore any temperature rise due to eventual absorption effects will be lower as well, affecting the measurement in a minor way and allowing a more reliable absorption measurement.

The full experimental setup is presented in fig. 3.8a. To prevent the effects just explained, the spectrum of a broad range lamp (Thorlabs, SLS205, range $[240 - 1200]\text{nm}$) was splitted in wavelength subranges by the alternation of a series of band-pass filters at

355nm, 405nm, 450nm (FWHM bandwidth of 10nm) and 532nm (FWHM bandwidth of 4nm) placed in front of the lamp beam. The soft polymer gel sample, moulded as previously explained, follows the filter and it is placed vertically so that the light path within the sample is equal to its width of 9mm. The outgoing spectral distribution was measured by a spectrometer (Thorlabs, CCS200/M, range 200 – 1000nm, FWHM spectral accuracy $< 2nm$ at 633nm). The spectrometer in use was not provided with a radiometric power calibration and the spectral output was displayed in terms of normalised intensity. The normalisation to the range [0-1] was performed by dividing the whole spectral distribution by the highest peak in the spectrum. To convert the spectral emission in terms of output power, an additional measurement was carried out using a power meter (Ophir Photonics, PD300R-3W, spectral range 350 – 1100nm, resolution 0.1nW). Then, for each filtered wavelength range, the normalised intensity spectrum given by the spectrometer was divided by the power measured by the power meter.

For each filtered wavelength range, the spectral distribution and the power were acquired without sample and with sample. The power measured in the first configuration corresponds to P_{in} (area filled with darkest colour in fig. 3.8b), while the one measured in the second configuration corresponds to P_{out} (area filled with lightest colour in fig. 3.8b). The insertion losses of the sample were calculated following eq. 3.1. IL correspond to the sum of coupling losses CL , Fresnel losses FL and propagation losses PL multiplied by the light path l through the sample (9mm), according to eq. 3.2. CL are considered negligible, assuming that the rays of the lamp present a small divergence and they travel through the sample pretty much parallel to each other. Considering $n_{core} \sim 1.53$ for a wavelength of 532nm referring to the dispersion data provided by the supplier (fig. 3.5a), FL can be calculated from eq. 3.3 giving $FL = -0.39dB$. Then it is possible to obtain the propagation losses for each wavelength range, which gives information regarding the light transmitted through the sample. The value complementary to the unity gives the absorption, which is expressed in terms of percentage in fig. 3.8c. The error on each measurement was calculated to be lower than 1%.

For the specific case of wavelength $\lambda = 532nm$, $P_{in} = 41.60\mu W$ and $P_{out} = 23.02\mu W$, leading to $IL = -2.57dB$. Subtracting FL and dividing the result by the light path l , the resulting propagation losses per unit length are $PL = -2.43\frac{dB}{cm}$, corresponding to a percentage transmission $\frac{P_{out}}{P_{in}} = 58\%$.

The average absorption rate of the soft gel on the range [350 – 550]nm is approximately

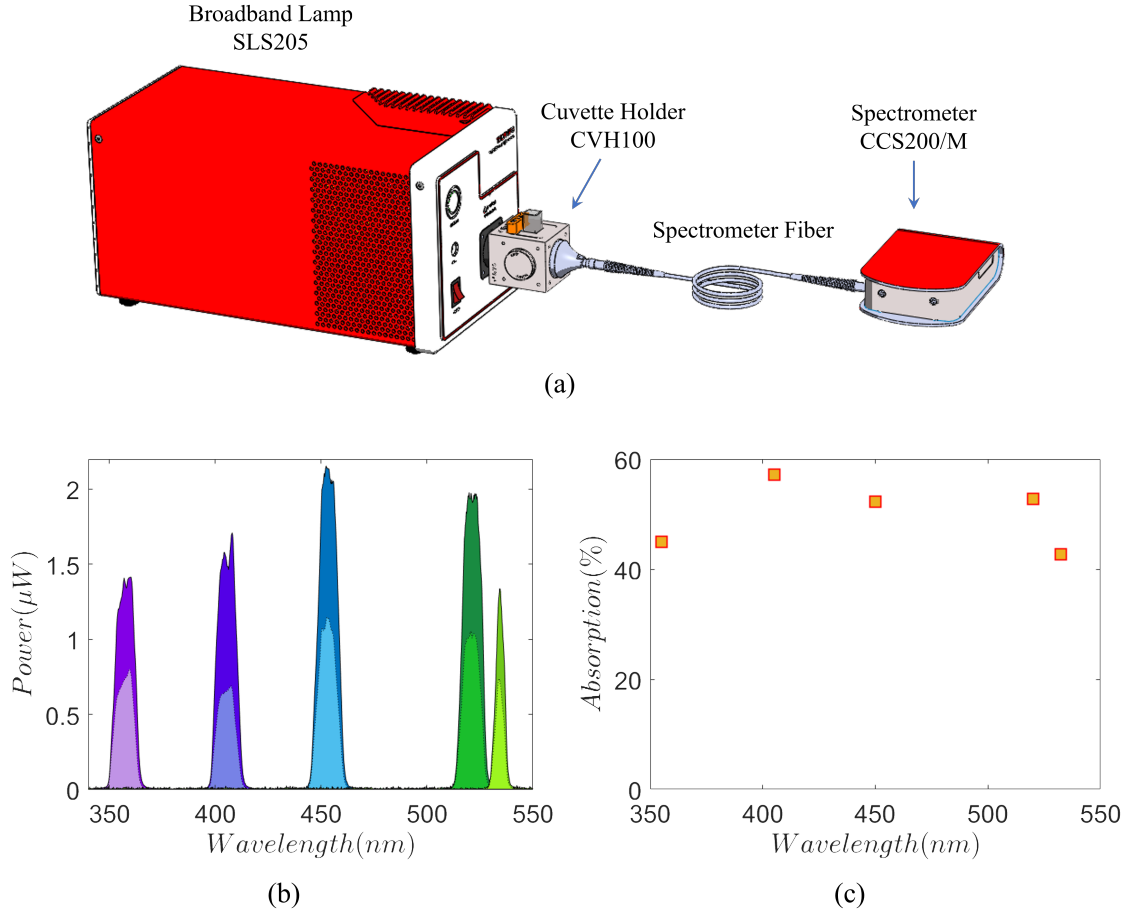


Figure 3.8: **Absorption rate of core material.** Measured through a sample of $9mm$ thickness over the visible range between $[350 - 550]nm$. The error on each measurement is lower than 1%.

between 40% and 60%. The consequent transmission rate is much lower than the one provided by the supplier, which is close to 100% on the same range (fig. 3.5). By observing the sample carefully, it was possible to see the presence of inclusions and impurities within the sample. So, beside the absorption of light from the soft gel, the power detected at the output may be mostly reduced by scattering effects of the light on dust particles, air bubbles or other kind of inclusions entrapped in the volume of the soft gel sample. This may be the main reason of the disparity between the transmission rate measured and the one provided by the supplier of the material.

3.3.4 Absorption measurement through a straight waveguide

The measurement done by using the broad band lamp was compared to a measurement done on a straight waveguide channel of length $l = 4.85cm$ with semi-circular section of $1.5mm$ radius manufactured as detailed in section 3.3.

The light source used in this case is a collimated laser diode with emission at 532nm (Thorlabs, CPS532). The light is injected into the input facet of the waveguide, while the output facet is imaged on a power meter head (Ophir, PD300R-3W). The output power was measured without using any optical component, but just placing the photodiode attached to the output surface of the waveguide (fig. 3.9).

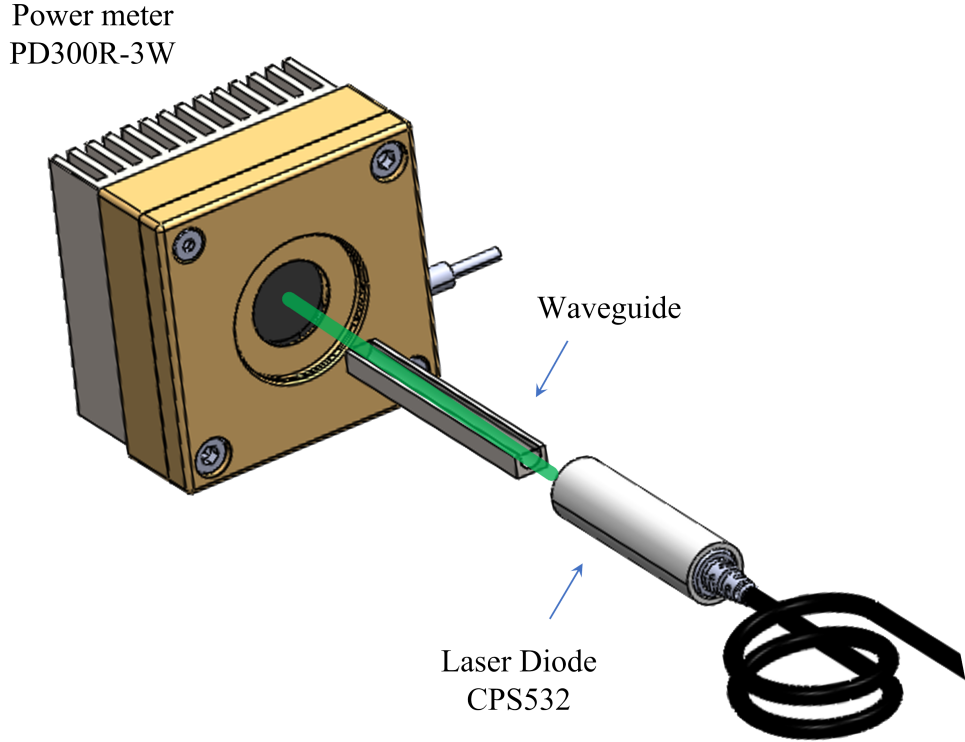


Figure 3.9: **Experimental setup.** The laser light is coupled into the waveguide and measured at the output by the detector.

For good coupling efficiency into a multi-mode waveguide, the focused beam of the light source should be comparable to the core size of the waveguide, and the incident cone angle should not exceed the arcsine of the NA of the waveguide to ensure that total internal reflection is granted. In case of a collimated laser beam, the divergence angle should be considered in this regard.

Since the beam diameter of the laser as provided by the supplier is $\sim 2.95\text{mm}$, the overall beam dimension was higher than the area of the input facet of the waveguide. A beam reducer made by a 4f system with suitable demagnification factor can be used to get a beam fully contained within the input surface of the waveguide core. As explained in section 2.2, reducing the beam dimension leads to increasing the beam divergence which may raise the transmission losses by compromising the conditions of TIR for the most

divergent rays within the beam. Therefore, a simulation in Optic Studio was carried out, as presented in section 3.3.5, to determine which effect was predominant between the reduction of the injection losses and the eventual increase of transmission losses. The convenience of using the beam reducer in this case was confirmed by the simulation result. Coupling losses were minimised ensuring a good alignment between the laser beam and the waveguide. A couple of iris was employed to ensure that the light coming from the laser was travelling straight forward. This was performed placing a power meter directly after the second iris. The laser was mounted on a tilt and tip system which allowed to correct the beam direction. The tilt and tip setting which maximises the power measured with both the iris completely close is the configuration ensuring that the light is travelling straight forward. Then the power meter was replaced by the waveguide. A system of stages where the laser was mounted on was permitting to move the beam in the plane X-Y and point it at the centre of the input facet of the waveguide. The waveguide was fixed on a horizontal plate as straight as possible along the laser beam direction, with its input facet perpendicular to the beam. The power meter was placed in front of the output facet of the waveguide. The latter was slightly moved on the plate to find the alignment with the laser beam which maximise the power at the output of the waveguide.

The power sent on the input facet was $P_{in} = 4800\mu W$, while the power measured at the output was $P_{out} = 336.67\mu W$, resulting in $IL = -11.54dB$. Following the same steps as done in section 3.3.3 and according to eq. 3.2, IL is equal to the sum of coupling losses CL , Fresnel losses FL , and propagation losses PL multiplied by the light path l corresponding to the length of the waveguide in this case. CL are considered negligible, because the light source is a collimated laser and the effect of the beam reducer on the divergence is considered very small (this is confirmed by the simulation presented in section 3.3.5). Knowing that $FL = -0.39dB$, it is possible to obtain $PL = -2.30\frac{dB}{cm}$ corresponding to the transmission percentage $\frac{P_{out}}{P_{in}} = 59\%$. This result is in accordance with the one obtained for the sample in section 3.3.3 differing by just 1%.

The Lambert-Beer law (eq. 2.13) can be used to calculate the absorption coefficient α of the waveguide. Considering that the power ratio related to the propagation losses per unit length is equal to $\frac{P_{out}}{P_{in}} = 59\%$ as previously obtained, then $\alpha = 0.53cm^{-1}$. The variation of $\frac{P_{out}}{P_{in}}$ as a function of the waveguide length is plotted in fig. 3.10. It can be observed that the power ratio decreases drastically and the propagation losses overcome the 90% for a waveguide with length higher than 5cm.

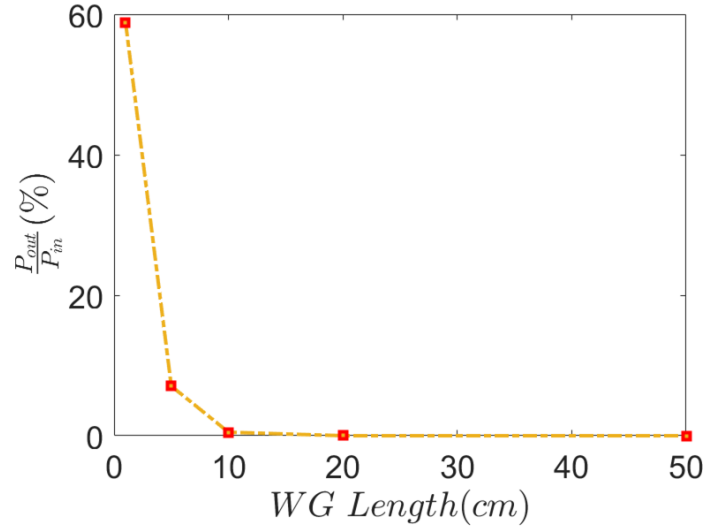


Figure 3.10: **Absorption coefficient.** Light propagation through the waveguide across its length.

3.3.5 Simulation

Material properties

In order to define a custom material in OpticStudio, two sets of measurements must be provided: dispersion and transmittance data.

Dispersion data show the variation of the refractive index resolved in wavelengths. Optic Studio employs dispersion models, which use mathematical relations called dispersion formula to evaluate the optical properties of the material by adjusting specific fit parameters. For a given set of dispersion data, OpticStudio selects, among a series of dispersion models, the one which best fits the data set. The parameter values optimised by the fit are then stored within Optic Studio and are used to calculate the index of refraction for any given wavelength. Transmittance data, instead, take into account the light attenuation through the material and the properties of the latter. This is modelled by OpticStudio following the eq. 2.13.

Transmittance and dispersion data of the cladding material (PTFE) have been obtained referring to the literature (fig. 3.11). The transmittance rate of $\sim 10\%$ corresponding to $532nm$ (fig. 3.11a) was used in the simulation. Fig. 3.11b shows dispersion data of PTFE for three different grades, i.e. different molecular weight, composition and/or molding temperatures. The average value of ~ 1.3 corresponding to $532nm$ was considered for

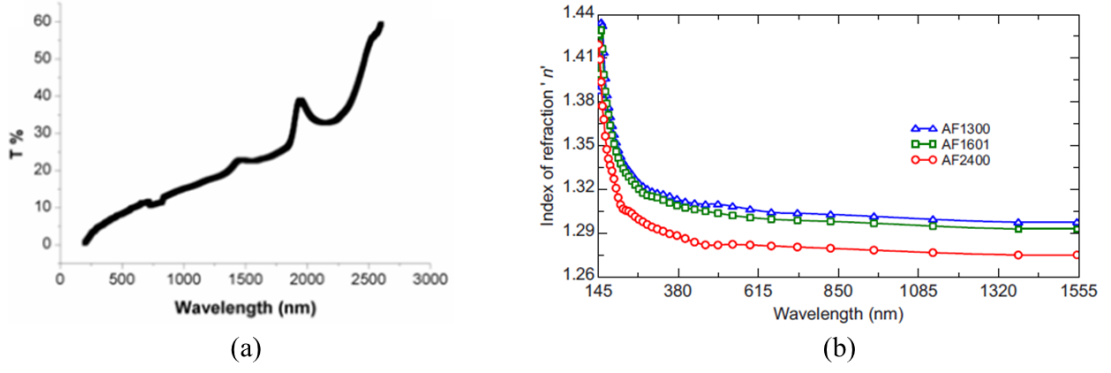


Figure 3.11: **PTFE optical properties.** Transmittance rate (readapted from [151]) and dispersion data (readapted from [152]).

the simulation. For the core material (LS1-3252), dispersion data as provided by the supplier (fig. 3.5a) were taken as a reference, so a value of 1.53 corresponding to a wavelength of 532nm was used in the simulation settings. Instead, since the transmission percentage does not depend just on the refractive index of the pure polymer, but it is also strongly affected by the manufacturing process and the presence of any inclusions and impurities, an experimental measurement was carried out as presented in section 3.3.4. The transmission ratio per unit length through a waveguide channel with semi-circular section of 1.5mm radius was $\sim 57\%$, therefore this value was used in the simulation.

Light source

As explained in section 2.2, it is commonly assumed that the irradiance profile of a laser beam follows an ideal Gaussian distribution. In the simulation, the laser source used in the experimental setup was modelled as a gaussian beam with emission centred at 532nm in accordance with the data provided by the supplier. The laser beam was oriented perpendicular to the input facet of the waveguide. A detector (a photodiode or a camera depending on the measurement carried out) was placed perpendicular to the output facet of the waveguide.

Divergence angle of the light source

The laser beam radius at the propagation distance z where the irradiance is $1/e^2$ (13.5%) of I_0 , as provided by the supplier, is $w_z = 1.48mm$. Since the waveguide channels have semi-circular section of 1.5mm radius, even in the case where the laser is perfectly aligned to the waveguide, just half of the laser beam interacts with the input facet of the waveguide

core, while the remaining half overfills the section of the waveguide core leading to light loss. As anticipated in the setup description of section 3.3.4, a beam reducer was applied to the laser to get the beam fully contained within the input surface of the waveguide core. The effective advantage of using a beam splitter in this case was verified by simulation.

The divergence of the beam is inversely proportional to the magnification of the optical system, and the product between divergence and dimension of the beam is constant as assessed by the following relations:

$$\begin{aligned}\theta_{d1} &= \frac{\theta_{d0}}{M} \\ \theta_{d0}w_{z0} &= \theta_{d1}w_{z1}\end{aligned}\tag{3.5}$$

where θ_{d0} , w_{z0} , θ_{d1} and w_{z1} are divergence angle and radius at the propagation distance z where the irradiance is $1/e^2$ of I_0 respectively of the original beam (without beam reducer) and the reduced beam, and M is the magnification factor. Consequently, if the radius of the beam is reduced, the divergence increases. A higher divergence may cause light loss, because the incidence angle of the most divergent rays in the beam may become lower than the critical angle θ_c , leading to refraction into the cladding and then light loss (see section 2.1.1).

A simulation was done to verify which light loss effect is predominant between the beam not fully contained in the input facet of the waveguide in the configuration without beam reducer, or the rise of divergence in the case where the beam reducer is applied.

The beam reducer used was made by a couple of lenses giving a magnification factor of $M = 0.024$. Of course a much lower beam reduction would have been enough to ensure that the beam was geometrically fully contained into the section of the input facet of the waveguide core. However, it was decided to use a couple of lenses already available rather than outsourcing some new ones.

The simulation setup is presented in fig. 3.12. A straight waveguide core with semi-circular section of radius $1.5mm$ and length $10cm$ is surrounded by cladding material on three sides and air on the upper side. The properties of core and cladding were defined in the simulation software as detailed in section 3.3.5.

A Gaussian source injects light on one side of the waveguide core. Given laser beam radius w_z and divergence angle θ_d as provided by the supplier, it was possible to obtain the distance z using the eq. 2.19. The same parameters were calculated for the case where the beam reducer is added in front of the laser using the relations in eq. 3.5 and the resulting

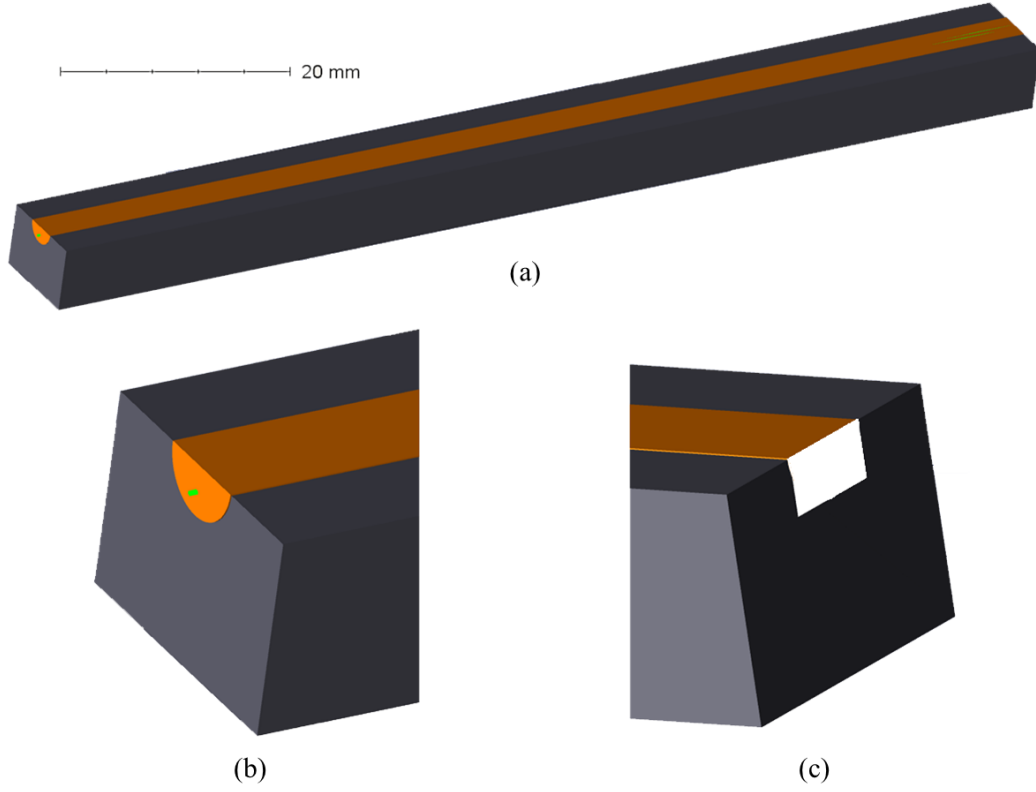


Figure 3.12: **Simulation setup.** (a) Straight waveguide with semicircular section with radius of 1.5mm and length of 10cm . (b) Light injected perpendicularly into the input facet. (c) Light collected by a detector (white rectangle) placed right in front of the output facet.

values are reported in tab. 3.1. The simulation was run for the case of not reduced beam and reduced beam, using these parameters. Simulation results of power ratio and insertion losses are reported in tab. 3.1.

	$w_z(\text{mm})$	$\theta_d(\text{mrad})$	$z(\text{mm})$	$\frac{P_{out}}{P_{in}}(\%)$	$IL(\text{dB})$
Not reduced beam	1.48	0.50	5920.00	0.28	-25.58
Reduced beam	0.04	20.83	3.84	0.47	-23.30

Table 3.1: **Beam reducer effect.** Laser beam parameters and simulated output power with and without using the beam reducer.

The overall power ratio is quite low in both the cases, and this is mainly due to the length of the waveguide (10cm) considered for this simulation as discussed in section 3.3.4. However, the output power is almost doubled when the beam is reduced. This means that any light loss due to the divergence increase is lower than the light gained by narrowing

the beam dimension and allowing the beam to be fully contained into the input facet of the waveguide core. In this way, injection losses are reduced.

The beam ellipticity of the laser considered can be neglected and the beam can be considered circular. The beam has radius of 1.48mm and the radius of the semicircular core of the waveguide is 1.5mm , so just half of the beam intersect the section of the core. However, the power ratio of the not reduced beam is higher than the half of the power ratio of the reduced beam. This can be explained considering that the laser beam is gaussian, which means that the most of the power is concentrated in the middle of the beam and gradually decreases moving away from the centre. Fig. 3.13 shows the Gaussian intensity profile within the waveguide core, detected $20\mu\text{m}$ from the input facet.

A further consideration can be deduced comparing the values of the angles involved in the light transmission along the waveguide when the beam is reduced. Considering the reference values for the refractive index of core and cladding (respectively, 1.5 and 1.3), from eq. 2.2 the critical angle can be calculated as $\theta_c \sim 60^\circ$. From simple trigonometric considerations, this relation can be deduced for the incident angle $\theta_i = 90^\circ - \theta_d$. Since θ_d of the reduced beam is $\sim 1.19^\circ$, then $\theta_i \sim 88.85^\circ$. As a result, the direction of the beam rays is $\theta_i > \theta_c$, so the condition for total internal reflection is granted.

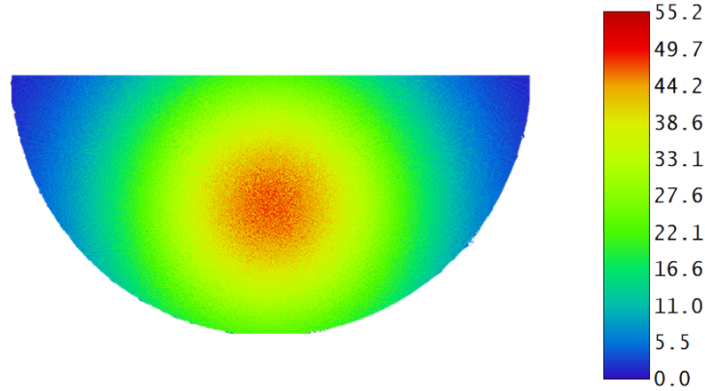


Figure 3.13: **Section of the waveguide core $20\mu\text{m}$ after the input surface.** The intensity is not uniform but more intense at the centre, because a laser beam is gaussian.

Using the same simulation setup as shown in fig. 3.12, a series of simulations were run increasing the divergence of the laser beam, while still being fully contained into the input facet of the waveguide. All the parameters used to simulate the divergence of the laser and the results obtained are reported in table 3.2. It can be observed that the power ratio decreases by increasing the divergence angle following the trend shown in fig. 3.14.

$\theta_d(\text{degree})$	$\theta_d(\text{rad})$	$w_z(\text{mm})$	$z(\text{mm})$	$\frac{P_{out}}{P_{in}}(\%)$	$IL(\text{dB})$
1.19	0.02	0.04	3.84	0.47	-23.30
5.00	0.09	0.04	0.92	0.47	-23.31
15.00	0.26	0.04	0.30	0.46	-23.34
30.00	0.52	0.04	0.15	0.45	-23.47
60.00	1.05	0.04	0.07	0.40	-23.94
90.00	1.57	0.04	0.04	0.33	-24.80

Table 3.2: **Study of divergence modulation.** Simulated light loss due to the increase of beam divergence.

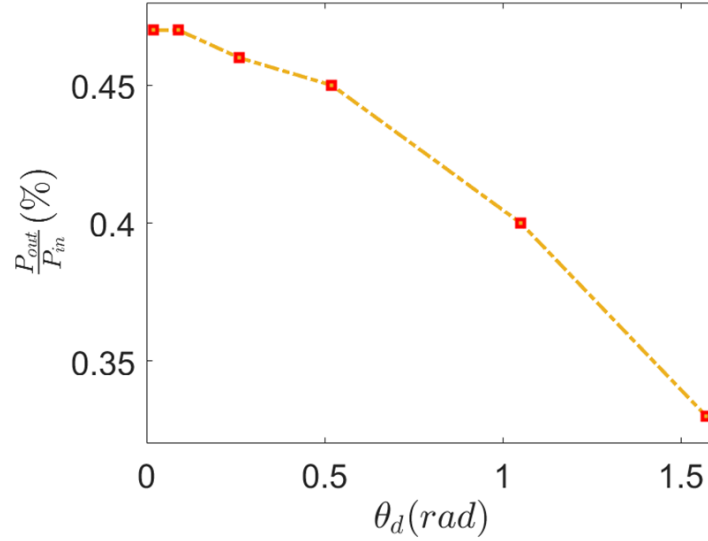


Figure 3.14: **Divergence angle of the light source.** Dependence of the power ratio across the divergence angle θ_d .

Roughness study

The roughness on the surface of CNC-machined PTFE parts has been studied in [153] and the microscope image reported in (fig. 3.15a) shows it like a pattern of channels in relief with a thickness between $[0.69 - 3.5]\mu\text{m}$. Based on this observation, the roughness has been modelled as channels with a semi-circular section of $5\mu\text{m}$ radius separated by a distance of $50\mu\text{m}$ from each other. Since the Solidworks files to be imported in

OpticStudio were pretty heavy due to the high number of small features corresponding to the roughness channels, just the Solidworks model of the core was considered while the cladding was not imported into the simulation. If no surrounding material is defined, OpticStudio consider that the objects are suspended in air with refractive index equal to 1. Moreover, since the aim of this analysis is studying the contribution of the roughness on the output power of waveguides with different lengths, the absorption of the core material as measured in section 3.3.3 was neglected and a 100% transmission was considered in this case. Also reflection on the input and output facets of the waveguide was not considered in this analysis to isolate the roughness contribution.

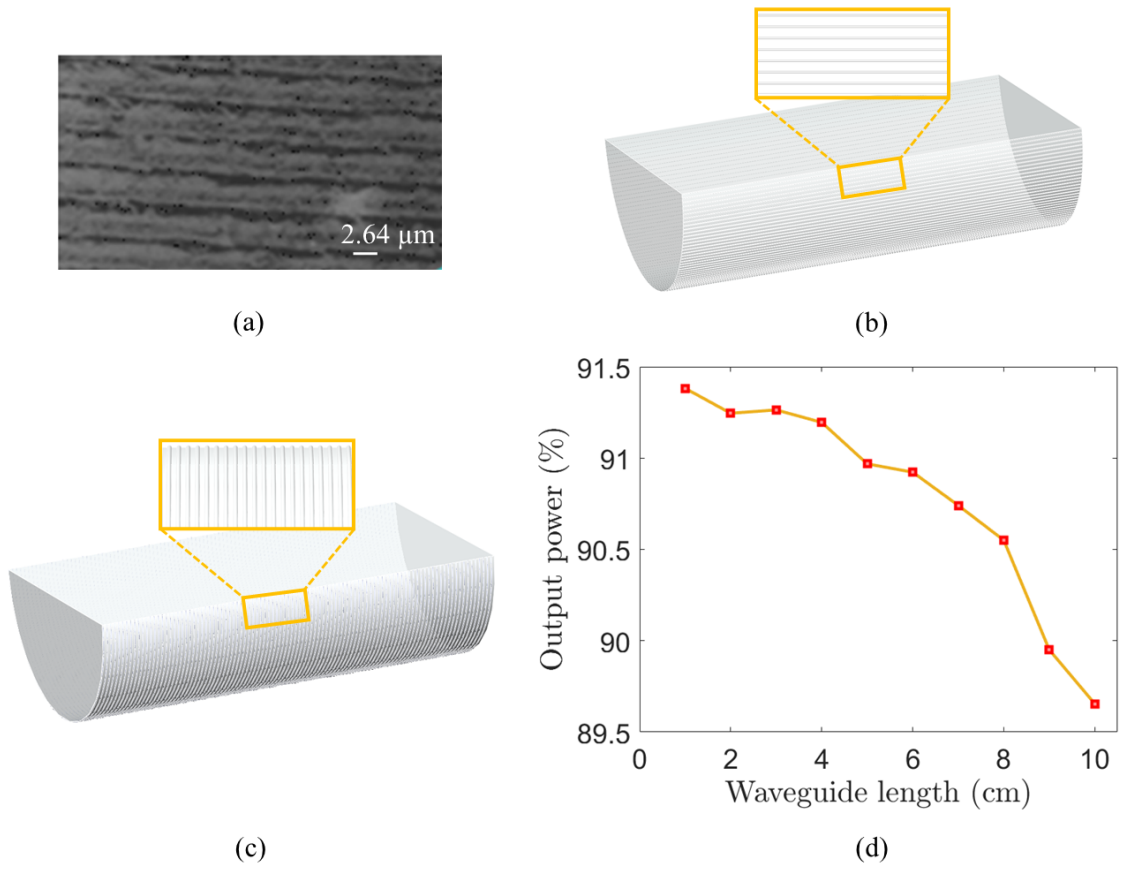


Figure 3.15: **Roughness on a CNC-machined PTFE part.** (a) Image re-adapted from [153]. (b) Component parallel to the light propagation direction. (c) Perpendicular component. (d) Output power across the length of a waveguide with perpendicular component of roughness.

The roughness contribution is evaluated in the case where the channels travel parallel to the light propagation direction (fig. 3.15b) and perpendicular (fig. 3.15c).

In case of roughness parallel to the light propagation direction, a light loss of just 2% is obtained considering a waveguide of 10cm length. It was verified that the roughness has

higher contribution on the light transmission when it has a component perpendicular to light propagation direction. This case was evaluated for different values of waveguide length. Results in fig. 3.15d show that the output power is within $[89.5 - 91.5]\%$ for waveguide lengths between $[1 - 10]cm$, so it can be assumed a light absorption ratio due to the perpendicular roughness component of $\sim 10\%$.

It should be noted that the light is lost due to roughness when it bounces on the interface between core and cladding. Therefore, this kind of losses may rise in the case of a bent waveguide, since the number of bouncing would increase in that case.

3.3.6 Bending losses

Four bent waveguide channels with semi-circular section of $1.5mm$ radius were manufactured as detailed in section 3.3. They have bending radius respectively of 6.0, 4.0, 2.5 and $1.5cm$ and length of 9.42, 6.28, 3.93 and $2.36cm$ (see fig. 3.16).

The experimental setup was analogous to the one described in section 3.3.4.

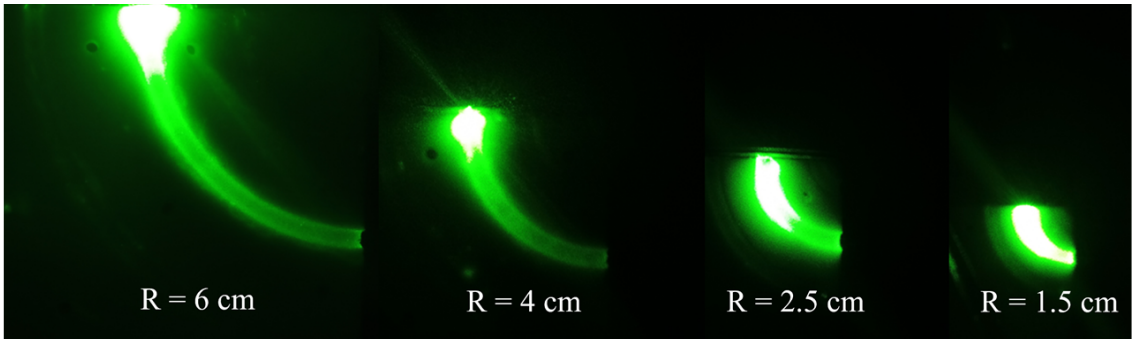


Figure 3.16: **Bending losses measurement.** Moulded waveguides with different curvature radius. Light is injection onto the input facet and collected from the output facet by a power meter.

Power input and output were measured using the power meter and the IL were calculated following the eq. 3.1. Fresnel Losses can be calculated by eq. 3.3 as $FL \sim -0.39dB$ for both the interfaces. Considering eq. 3.4, it was possible to calculate the bending losses, knowing all the other terms. Propagation losses per unit length were measured on a straight waveguide as presented in section 3.3.4 and they are equal to $PL = -2.30 \frac{dB}{cm}$. So bending losses can be obtained consequently. Results are presented in tab. 3.3.

A simulation was set up as explained in section 3.3.5 with reduced beam of radius $0.04mm$. The roughness was neglected. Results are presented in tab. 3.4.

$R(cm)$	$l(cm)$	$\frac{P_{out}}{P_{in}}(\%)$	$IL(dB)$	$BL(\frac{dB}{cm})$
6.0	9.42	0.16	-27.87	-0.62
4.0	6.28	1.21	-19.17	-0.69
2.5	3.93	5.00	-13.01	-0.91
1.5	2.36	7.36	-11.33	-2.34

Table 3.3: **Bending losses.** Experimental results.

$R(cm)$	$l(cm)$	$\frac{P_{out}}{P_{in}}(\%)$	$IL(dB)$	$BL(\frac{dB}{cm})$
6.0	9.42	0.60	-22.22	-0.02
4.0	6.28	3.14	-15.03	-0.03
2.5	3.93	10.97	-9.60	-0.05
1.5	2.36	24.84	-6.05	-0.10

Table 3.4: **Bending losses.** Simulation results.

The simulation was repeated adding a cladding layer with thickness of $300\mu m$ on the upper surface of the core. Analogous results were obtained also in this configuration.

A disparity between bending losses given by simulation and experimental data can be observed, as graphically shown also in fig. 3.17. It can be also noted that such discrepancy rises while the bending radius decreases. In a waveguide with lower bending radius, the number of interactions of the light rays with the interface between core and cladding are higher than in a waveguide with a smaller bending. This observation leads to think to a possible light loss phenomenon happening when the light rays hit the interface between core and cladding.

To verify this intuition, the number of interactions of the light rays on the core surface was counted through simulation for each waveguide with the four curvature values. These values per unit length n_{hits} are reported in table 3.5. Then the difference between BL_{exp} obtained experimentally and BL_{sim} given by the simulation was weighted on the number of interactions n_{hits} to verify how much these values vary from each other. From table 3.5, it is possible to see that the resulting ratio are very similar and diverge from each

other by 1% to 8%. Therefore a correlation between the bending losses and the number of interaction of the rays along the waveguide is very likely and one of the possible reasons, which is not modelled in the simulation, may be related to losses due to the roughness of the core surface.

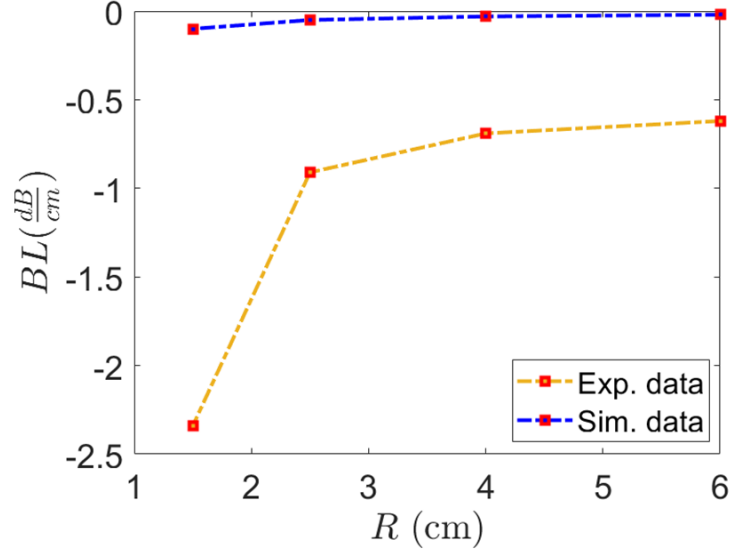


Figure 3.17: **Light loss in bent waveguides.** Bending losses across the curvature radius of the waveguide were obtained experimentally (yellow trend) and by simulation (blue trend).

$R(cm)$	$n_{hits}(cm^{-1})$	$\frac{BL_{exp}-BL_{sim}}{n_{hits}}(dB)$	$\frac{BL_{exp}-BL_{sim}}{n_{hits}}(\%)$
6.0	1.04	-0.58	87
4.0	1.43	-0.46	90
2.5	1.65	-0.52	89
1.5	2.55	-0.88	82

Table 3.5: **Curvature losses.** P_{out} ratio and absorption coefficient α across the waveguide curvature radius.

3.4 Single Splitter

A single splitter waveguide was realised as preliminary study to get light equally split between two output branches and then start increasing the spatial resolution from one to

two output channels.

The configuration starts with an initial straight channel 10mm long, which bifurcates into two branches of length 9mm each, separated by an angle $\alpha \sim 15^\circ$ (see fig. 3.18).

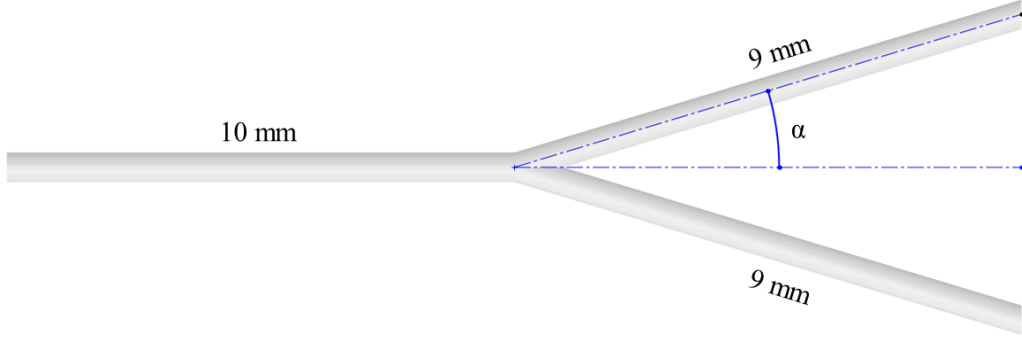


Figure 3.18: **Single splitter design.** An initial straight channel divergences in two output channels.

3.4.1 Experimental setup

This design was manufactured and tested before running any simulation or performance study, with the purpose to start increasing the spatial resolution and prove the concept of the proposed sensing principle. The waveguide channels have semi-circular geometry with radius of 1.5mm. Same manufacturing process and materials as described in section 3.3.2 were used.

At this time the only light source available was a digital fiber optic sensor (Keyence FS-N40). This module can be employed for both sending and receiving light. However, it was considered that the power meter could be more accurate as detector, therefore this was used just as light source. This digital fiber opti sensor is equipped with an LED emitting red light and the light coupling is based on optical fibers. An optical fiber was connected to the emitter slot of the unit on one side and it was fixed in front of the facet of the input channel of the splitter on the other side. The optical fiber was selected to have a core dimension similar to the dimension of the waveguide core to minimize the injection losses. Another optical fiber was fixed to the output facet of the waveguide to lead the light to the power meter for detection. This configuration allowed to measure one output branch at a time. A 6-axes force/torque sensor (ATI Nano-17, resolution 0.003N) was mounted on a manual translation stage (Thorlabs PT1/M, resolution 10 μm), which was moved by steps of 50 μm forward (backward). An equivalent width compression (relaxation) was applied

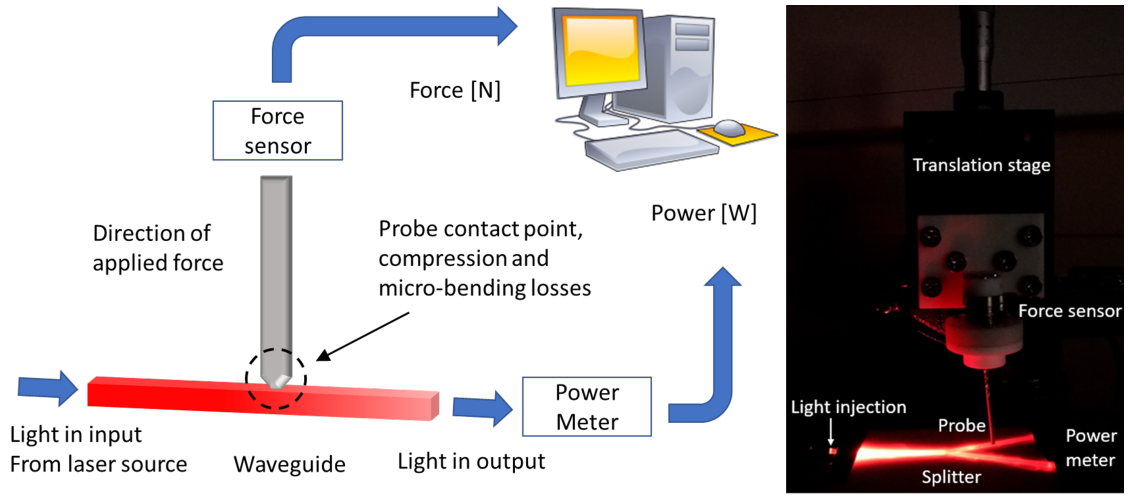


Figure 3.19: **Single splitter setup.** The force is applied by a metal probe mounted on a translation stage.

to the soft material channels of the prototype by a metal rod mounted on the calibration force sensor with diameter of 2.2mm . The setup is shown in fig. 3.19.

3.4.2 Results

Calibration and hysteresis experiments were carried out on each of the two branches of the single splitter configuration. The translation stage was moved by steps of $50\mu\text{m}$ for compression and decompression of each of the two soft sensing channels corresponding to the splitter branches.

To obtain the calibration curve, each one of the two output channels of the prototype was compressed and relaxed with steps of $50\mu\text{m}$ by the tip of the metal rod. Each measurement was repeated three times. The force values were recorded by the calibration force sensor, and the power was detected by the power meter. Calibration results for channel 1 and 2 are shown in fig. 3.20a-b. The compression-decompression loop was fitted using a 3rd degree polynomial equation. The fitting curve was used as calibration trend to determine a correspondence between the light power detected and the force applied on each sensor channel in compression and decompression. For each compression (or decompression) step of the force sensor (displacement), the force applied on each channel was determined considering the correspondence between the light power detected by the power meter and the force as given by the calibration curve. The force values plotted in fig. 3.20c-d were obtained in this way for each sensing channel. Loading and unloading curves give the hysteresis of each channel. The black line shows the mean force for each displacement

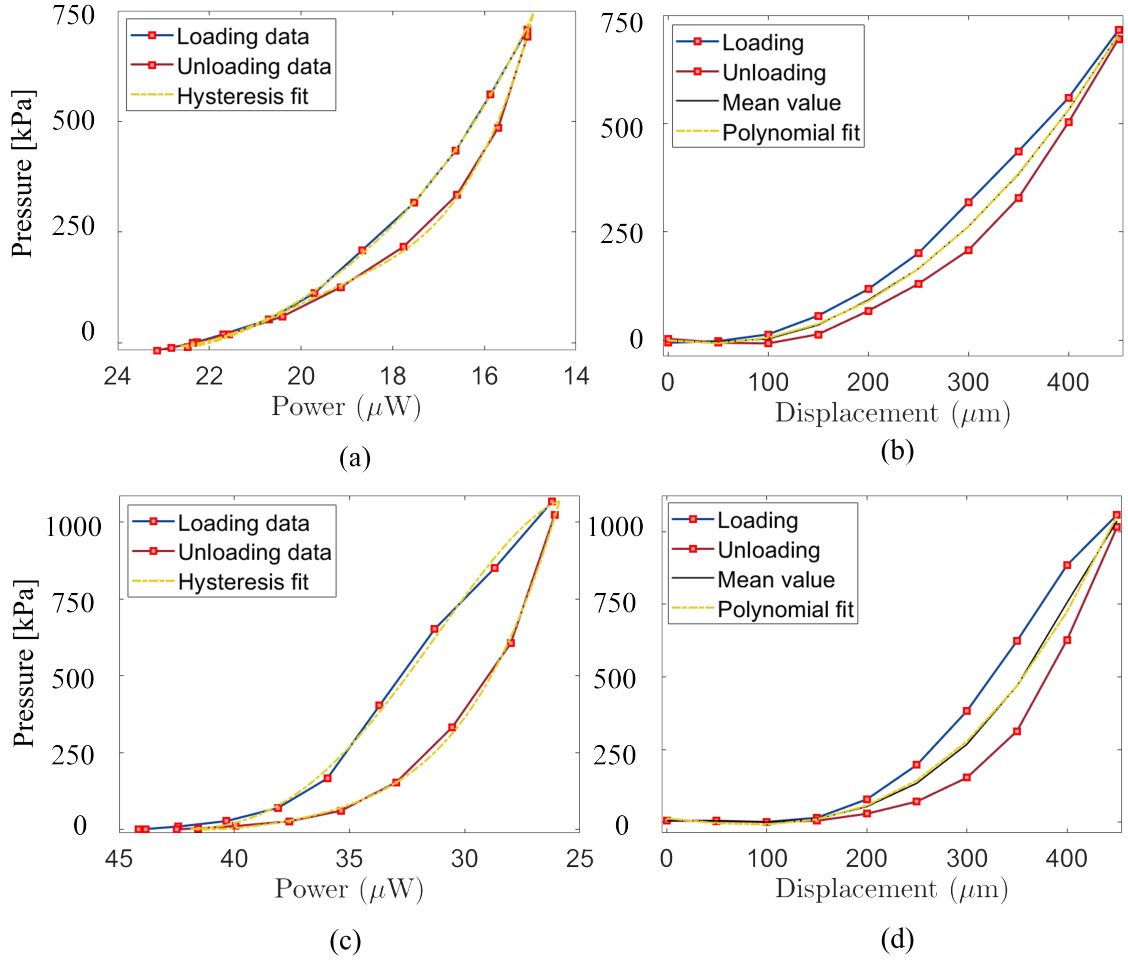


Figure 3.20: **Evaluation experiments.** (a-b) Calibration results for channel 1 and 2 of the splitter. (c-d) Hysteresis results for channel 1 and 2 of the splitter.

value.

Looking at fig. 3.20a-b, it can be observed that the power at the output is not equally split on the two channels. In particular, the power on channel 2 for the starting condition of not compressed channel is almost doubled compared to channel 1. This may be due to a problem in the coupling light method. In fact, the use of the optical fiber to inject light into the input waveguide channel does not ensure that the light travels straight forward. Even if the output facet of the optical fiber was placed parallel and right in front of the input facet of the waveguide channel, this configuration does not allow a proper alignment procedure as previously done in the case of the laser source.

Also the sensing range is slightly more extended for channel 2, with values between $[0 - 750]kPa$ for channel 1 and between $[0 - 1000]kPa$ for channel 2. Channel 2 present higher hysteresis than channel 1.

However, it was possible to observe a power modulation across the force applied on the

two output channels of the splitter, providing a prove of concept of the suggested sensing principle.

To reduce the hysteresis and extend the range of detectable forces, the proposed soft gel can be replaced with a different stretchable material with higher toughness and fatigue resistance, provided that the optical requirement regarding the refractive index is still met. Due to the limitations in getting a different type of soft material with the optical properties of interest as explained in section 3.3, the presented one is the only core material tested in this work.

3.4.3 Simulation for design optimisation

The single splitter design is the first step towards a multi-splitter configuration, where the design is further developed by adding further branches at the output of the previous ones. In this way, the number of output channels assuming the role of sensing elements is incremented and consequently the spatial resolution of the final device is increased.

However, the sensing part of the sensor is the bottom part where the output channels are placed. Instead, the upper part has the function to develop the branching of the core channels but it is not the part where the forces are expected to be applied. For this reason, it is important to keep the design compact as much as possible, such that the upper part which does not absolve any sensing role takes up as little space as possible.

To decrease the overall dimension of the device, the diameter of the core was decreased from 1.2mm to 0.5mm. The U-shape design as shown in fig. 3.21 was used at first instance. It was verified by simulation if it was possible to optimise the value for the angle α between the two branches of the splitter such that the output power is maximised. The same design as shown in fig. 3.18 was used, and the following values for the angle have been tested: 5°, 10° and 15°. The output power ratio for the three cases is presented in tab. 3.6. It can be observed that increasing the angle, the output power dramatically drops down and the best value among those considered is $\alpha = 5^\circ$.

For this angle value, three different section shapes have been investigated: U-shape, semicircular and rectangular section. The details of the geometry is presented in fig. 3.21. Results are shown in tab. 3.7 and it can be observed that the output power ratio has the lowest ration for the semicircular section, while it is more than 5% higher for the U-shape and it is increased by a further 3% in the case of the rectangular section.

The conditions which would optimise the design are the angle of $\alpha = 5^\circ$ between

α	5°	10°	15°
Channel 1	21.325%	1.268%	0.004%
Channel 2	21.344%	1.270%	0.004%

Table 3.6: **Splitter configuration.** P_{out} ratio at the output of each one of the two channels varying α .

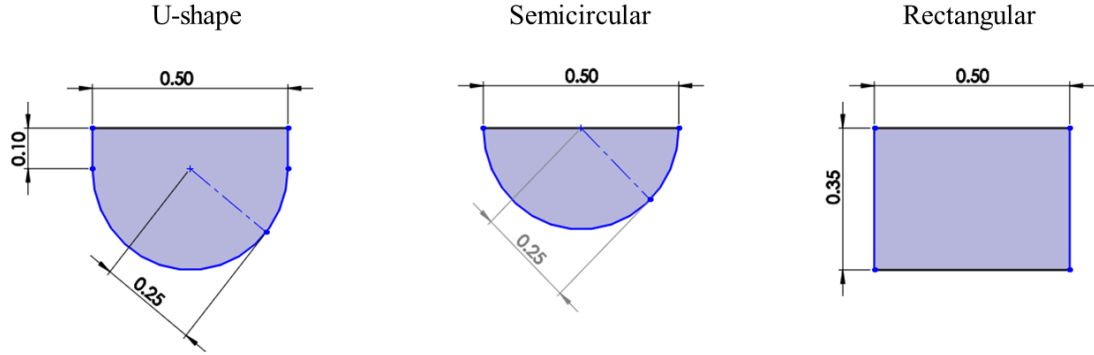


Figure 3.21: **Section geometry of the waveguide core.** Three section geometry have been considered: U-shape, semicircular and rectangular section.

$\alpha = 5^\circ$	U-shape	Semicircular	Rectangular
Channel 1	21.33%	14.55%	24.36%
Channel 2	21.34%	14.56%	24.36%

Table 3.7: **Splitter configuration.** P_{out} ratio at the output of each one of the two channels varying the section shape.

the two branches of the splitter and the rectangular section. However, with such a small angle, the two branches would be very close to each other and this may present some limitations in the CNC milling. Furthermore, the only way to develop this design with additional output channels would be applying a similar V-shape to each of the two output branches. However, this configuration would take up a lot of space in the transverse direction, precluding the possibility to get a compact design.

For these reason it was considered to move to a different design, as presented in the next paragraph.

3.5 Optimisation Process For A Multi-splitter Design

The study of a multi-splitter configuration was aimed to equally split the light in the output channels and maximize the overall light transmission. Getting a similar light transmission on the output branches is relevant to create an optical based sensor where the channels have similar response to an applied force. In the case of a single splitter, this requirement can be easily reached imposing the symmetry between the two branches. This aim is not easily achieved anymore in the case of a higher number of output channels instead. Also the need to maximise the light transmission through the device requires a deeper study.

As seen in the previous paragraph, a design presenting sharp edges does not favour the light transmission and, in addition, present some limitations for the CNC milling of the core channels into the PTFE substrate and prevent the development of a compact design. The significant light loss of the design presented in section 3.4 is most probably due to the presence of small radii of curvature in the design, which do not allow the rays of the beam to satisfy the Snell's law at the interface with the cladding. In fact, if the angle of incidence of a ray is higher than the critical angle, that ray is not guided into the core anymore, but it gets lost in the cladding.

To reduce this phenomenon, the branches of the single splitter were designed using smooth curvature radii. The U-shape section with the geometry described in fig. 3.21 was employed as first instance.

3.5.1 Curvature optimisation

The use of gentle curves to replace any sharp edge avoids the presence of discontinuities in the light path, minimizing the light loss. However, a higher curvature radius requires to enlarge the sensor in terms of width and length. A simulation study was carried out to determine the best trade-off between the light loss introduced by the presence of curvatures and the sensor dimension. Since in the case of a single splitter the aim to equally split the light into the two output channels can be easily reached by a symmetrical design, the analysis was focus on a single branch first, to optimise the curvature. The waveguide channel starts and ends with a couple of straight segments (blue dotted lines in fig. 3.22). Then a curvature starts following the path defined by two construction circumferences (red dotted lines in fig. 3.22) which are tangent between each other and tangent with the

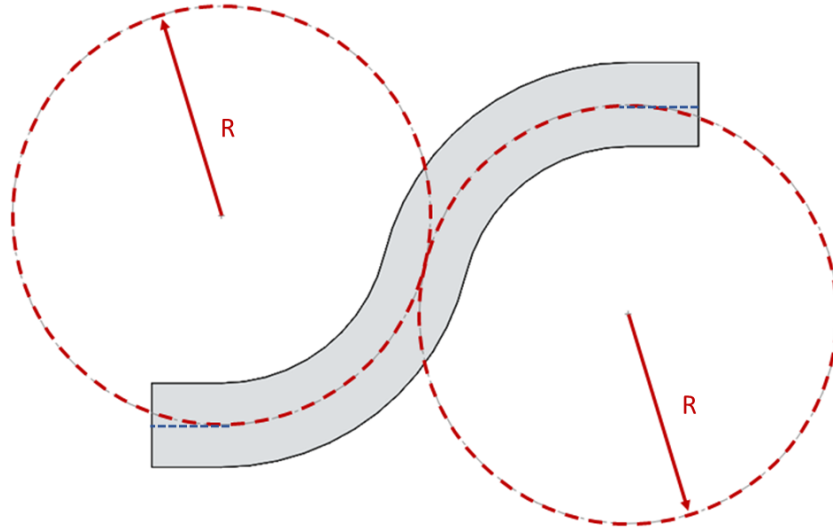


Figure 3.22: **Curvature study.** Optimisation of the curvature of a single branch of a multi-splitter design.

ending point of the first straight segment (first circumference) and the starting point of the second straight segment (second circumference). The two circumferences have equal radius R , and this curvature radius was kept constant along the entire waveguide for each splitter branch.

The output power was measured for the values of circumference radius $R = 0.3, 0.45, 0.6, 1.5, 2.4 \text{ cm}$. However, the overall waveguide length was kept constant (0.8 cm) so that the overall path for the light to travel was always the same: this ensures to have the same transmission loss for each simulation measurement and makes the results comparable between each other.

The bending losses per unit length were calculated from eq. 3.4 as done previously in the chapter: insertion losses were given by the simulation, coupling losses were neglected, and Fresnel losses are $FL \sim 0.38 \text{ dB}$ considering both input and output interfaces. A simulation of a straight waveguide with a U-shape section with dimensions as shown in fig. 3.21 was run to get the propagation losses per unit length, which differ just of 5% from the one obtained for the semicircular section, and they are equal to $PL = -2.30 \frac{\text{dB}}{\text{cm}}$. The consequent results are shown in fig. 3.23.

The lowest values of bending losses correspond to larger curvature radii. In particular, the curvature losses drastically increase for a curvature radius lower than 0.6 cm . Instead, the trend moves toward a plateau for a curvature radius higher than 1.5 cm . The blue dashed line represents the propagation losses on the straight waveguide, which is the limit value

of the trend, in absence of bending. Based on this result a curvature radius of 2.4cm was chosen for the construction circumferences of the waveguide design, because any further improvement would have elongated the device too much.

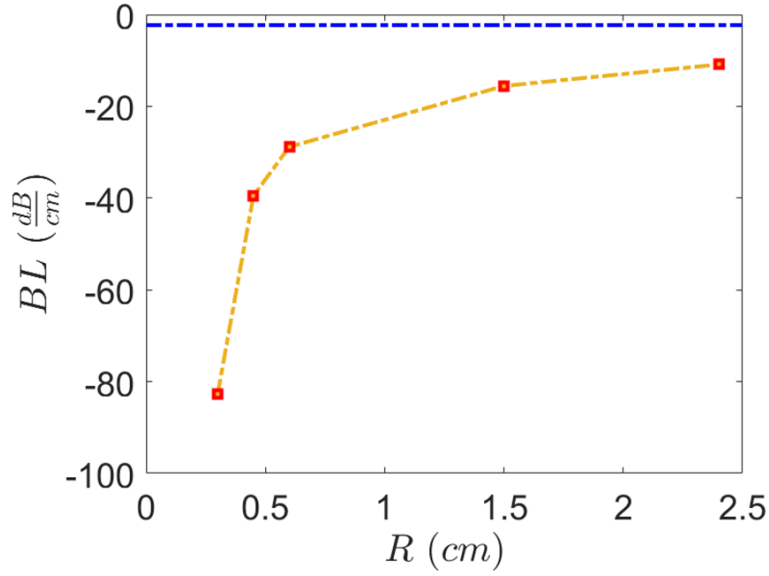


Figure 3.23: **Curvature study.** Optimisation of the curvature of a single branch of a multi-splitter design.

The same design of a single splitter branch satisfying the constraint of 24 mm curvature radius was tested for different section geometry: semi-circular, with a U-shape and rectangular. The details of the geometry of each section are presented in fig. 3.21. The output power ratio for the three section types are reported in tab. 3.7. The results are analogous to those obtained in tab. 3.8 for the previous design, with the lowest output power ratio in the case of semicircular section, more than 5% of rise in the case of U-shape section and an increase a further 2% in the case of rectangular section.

However, the rectangular geometry is complex to be CNC milled, due to its sharp edges. An alternative to this is machining the channels with a U-shape section which does not differ much from the optical rectangular one in terms of output power ratio. Therefore, the U-shape was selected to define the section geometry of the waveguide.

U-shape	Semicircular	Rectangular
7.26%	1.77%	9.33%

Table 3.8: **Splitter configuration.** P_{out} ratio at the output of each one of the two channels varying the section shape.

3.6 Multi-splitter Design

The design of the single branch was extended to a single splitter first and then to a series of splitters connected in cascade: the design starts with a single channel for the light injection which is splitted in two branches; then each branch is further splitted in other two, and so on. Rising the number of the output channels means increasing the spatial resolution of the sensor, since compression and decompression of each output channel causes a light modulation correlated to the force applied on the channel. However, increasing the number of the output channels affects the width and length of the design. In particular, more separation is needed between the two branches of the first splitter at the input to provide enough space to place the remaining branches belonging to the following cascade splitters. To limit the overall dimension of the sensor, a maximum of eight output channels was reached.

The definition of some geometrical constraints allows the light to reach the eight output branches and be equally split in them. Such a configuration leads to the manufacture of a compact sensor array where each sensing element presents a similar force range and gives similar information regarding the applied force. The displacement between the eight output branches defines the spatial resolution of the sensor.

The single branch with a curvature radius of 24 mm and a U-shape section was mirrored to create a 50/50 waveguide splitter. Another couple of splitters, satisfying the same geometry constraints, were connected to each branch of the first splitter. Then, another series of four similar splitters were connected (fig. 3.24b). The symmetry of each couple of branches helps the light to be equally split at every bifurcation.

The final configuration based on a U-shape section with dimensions as shown in fig. 3.21 was tested. However, the transmission efficiency of the device was very low and it was not possible to obtain any result. This issue was related to the small dimension of the core channels which make the manufacturing process more challenging.

For this reason, the section was enlarged as shown in fig. 3.24a. The rest of the design was updated consequently and the separation between the outputs of each of the three splitters starting from the input one was set at 8.0mm, 4.0mm and 2.0mm as shown in fig. 3.24b.

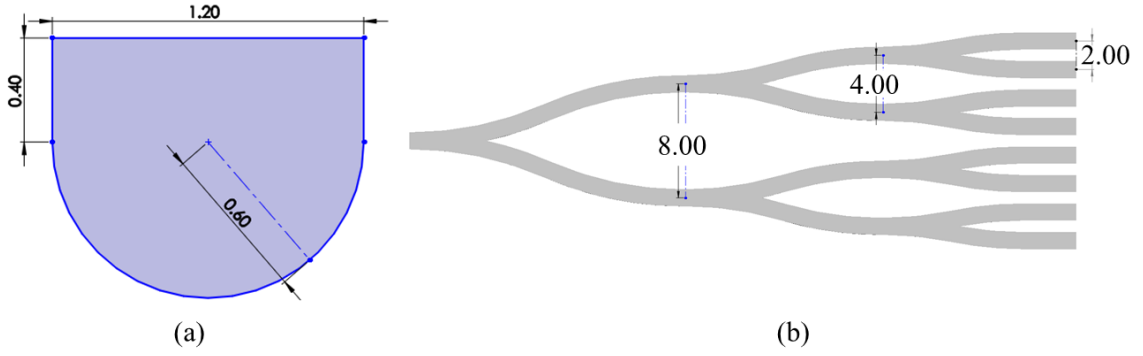


Figure 3.24: **Multi-splitter configuration.** (a) Enlarged U-shape section. (b) Final design with detail of channels separation.

3.6.1 Simulation

An optimization process through simulation was carried out on the design of the multi-splitter made by three sub-splitters connected in cascade. A simulation was run for the two sub-splitters first and then for the final configuration to get the power transmission across the design.

The first step of the optimization process focused on the design of a single splitter. Getting a similar output power on the two branches is relevant to create an optical based sensor where channels have similar response to an applied force. In the case of a single splitter, this requirement can be easily reached forcing symmetry between the two branches. However, this becomes more challenging when the number of output channels is increased. The first splitter shows a power percentage higher than 16% at the output of each branch (fig. 3.25a). In the second splitter, the branches 2 and 3 transmit more than 7% of power; however, the power transmission on branches 1 and 4 is lower and close to 0.1% (fig. 3.25b). The third histogram shows the power percentage transmitted by the eight final branches (fig. 3.25c).

A symmetrical behaviour can be observed between channels 1-4 and 5-8. However, the light is mainly transmitted through the output channels 3 and 6, while the power ratio is much lower on the rest of the channels.

Although in section 3.3.5 it was seen how increasing the divergence was causing a reduction of light power transmitted by a straight waveguide, in the case of a multi-splitter configuration a higher divergence angle can facilitate the light to follow the bifurcation right after the light injection in the input channel, and then be split in a more uniform way on the all output channels. This intuition was verified through an additional set of

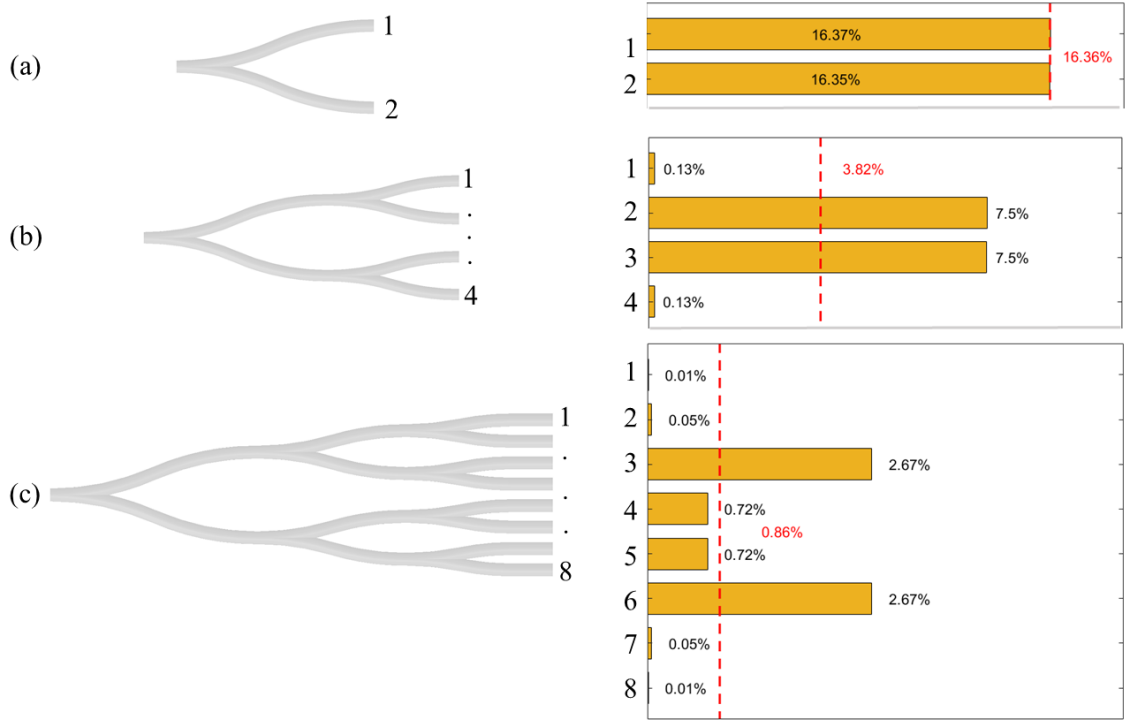


Figure 3.25: **Simulation results.** (a) Sub-splitter configuration simulated individually. (b) Output power ratio for each sub-splitter.

simulations where the divergence angle of the laser beam was varied as reported in table 3.9. Since the symmetric behaviour of the two sets of output channels 1-4 and 5-8 was previously verified, in this case just the output ratio of the channels 1-4 are considered. Results are shown in fig. 3.26 confirming that a divergence increase improved the light splitting on the output channels.

Looking at the results shown in fig. 3.25, corresponding to a divergence angle $\theta_d = 0.02\text{rad}$, the maximum deviation from the average value is given by channels 3 and 6 and it is equal to 1.81%. Looking instead at the results shown in fig. 3.26d, corresponding to a divergence angle $\theta_d = 0.21\text{rad}$, the maximum deviation from the average value is given by channels 1 (and 8, assuming it has an analogous behaviour) and it is reduced to 0.57%.

Finally, the case of total absence of impurities within the core (i.e. air bubbles due to injection, dust, etc), and irregularities/asymmetries in the channel geometry was considered, and a simulation was repeated assuming 100% transmission through the core. In such ideal conditions, the proposed design shows an overall high transmission of 86.8%. Therefore, the main problem of the poor transmission efficiency of the multi-splitter is related to the fabrication method. The requirement of small channel diameter poses several challenges for both the CNC milling of the substrate and the soft material injection and

$z(mm)$	$w_z(mm)$	$\theta_d(rad)$
3.84	0.08	0.04
3.84	0.16	0.08
3.84	0.24	0.12
3.84	0.40	0.21

Table 3.9: **Simulation parameters.** Divergence modulation on a multi-splitter configuration.

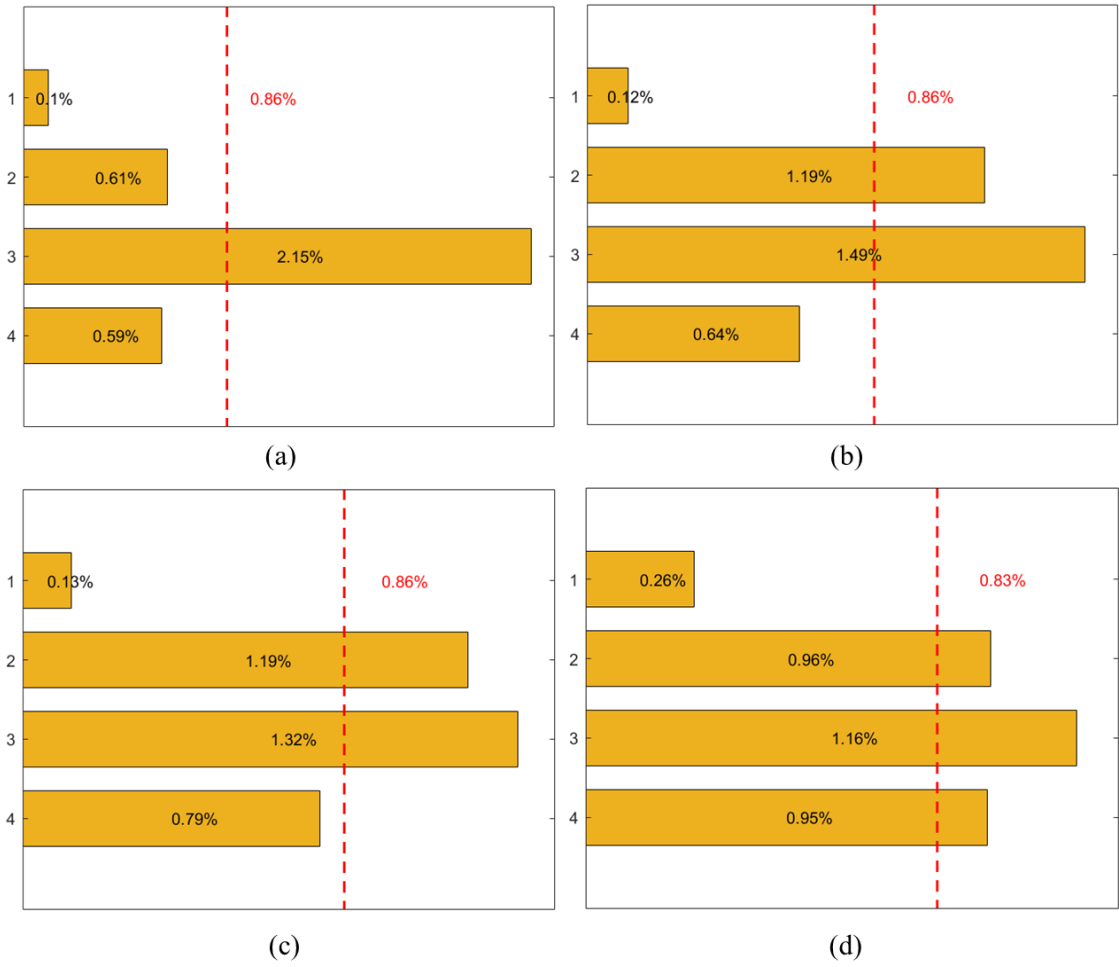


Figure 3.26: **Simulation results.** (a) Output ratio modulation for the divergence angle of the beam equal to $\theta_d = 0.04rad$, (b) $0.08rad$, (c) $0.12rad$ and (d) $0.21rad$.

drying. However, the prototype was tested as prove of concept as presented in the next section.

3.6.2 Evaluation experiments

The final prototype is shown in fig. 3.27a. The sensor has an 18 mm height, a 48 mm length and a 3.0 mm depth. The output channels are 2 mm distant from each other, providing a good spatial resolution. The eight sensing elements are red circled in fig. 3.27b. The experimental setup is presented in fig. 3.27b. The light transmission through the splitter is shown in fig. 3.27c. The light source is a laser nominally centered at 532 nm (Thorlabs CPS532, Collimated Laser-Diode, 4.5 mW). The light is transmitted through the soft material channels following the multi-splitter structure, as shown in fig. 3.27b. An optical fiber transmits the light signal from the output of each channel to the camera (Blackfly USB3, 2.3 MP, 41 fps). The acquired picture was analyzed through an image processing algorithm for the recognition of the region of interest (ROI), corresponding to the tip of the fiber. For each measurement, the average intensity was calculated considering the intensity value of the pixels belonging to the ROI, while all the other pixels were ignored. A 6-axes force/torque sensor (ATI Nano-17, resolution 0.003 N) was mounted on a manual translation stage (Thorlabs PT1/M, resolution $10\mu m$), which was moved by steps of $50\mu m$ forward (backward). An equivalent width compression (relaxation) was applied to the soft material channels of the prototype by a metal rod mounted on the calibration force sensor. The metal rod had a rounded flat head with diameter of 0.8 mm.

To obtain the calibration curve, each one of the eight output channels of the prototype was compressed and relaxed with steps of $50\mu m$ by the tip of the metal rod. Each measurement was repeated three times. The pressure values were recorded by the calibration force sensor, and the intensity values were detected by the camera, analysed by the image processing algorithm, and then normalised in the range [0-1]. Results for each soft channel are presented in fig. 3.28. The compression-decompression loop was fitted using a 3rd degree polynomial equation. The respective R^2 values are reported on each plot to demonstrate the goodness of the fit. Since the calibration force sensor is subject to fluctuation, 50 values of force were recorded for each measurement, converted to pressure and the error was calculated as standard deviation of these 50 values. The maximum error is lower than 16% across all channels. The fitting curve was used as calibration trend to determine a correspondence between the light intensity detected by the camera and the force applied on each sensor channel in compression and decompression. For each compression (or decompression) step of the force sensor (displacement), the force applied on each channel was determined considering the correspondence between the light

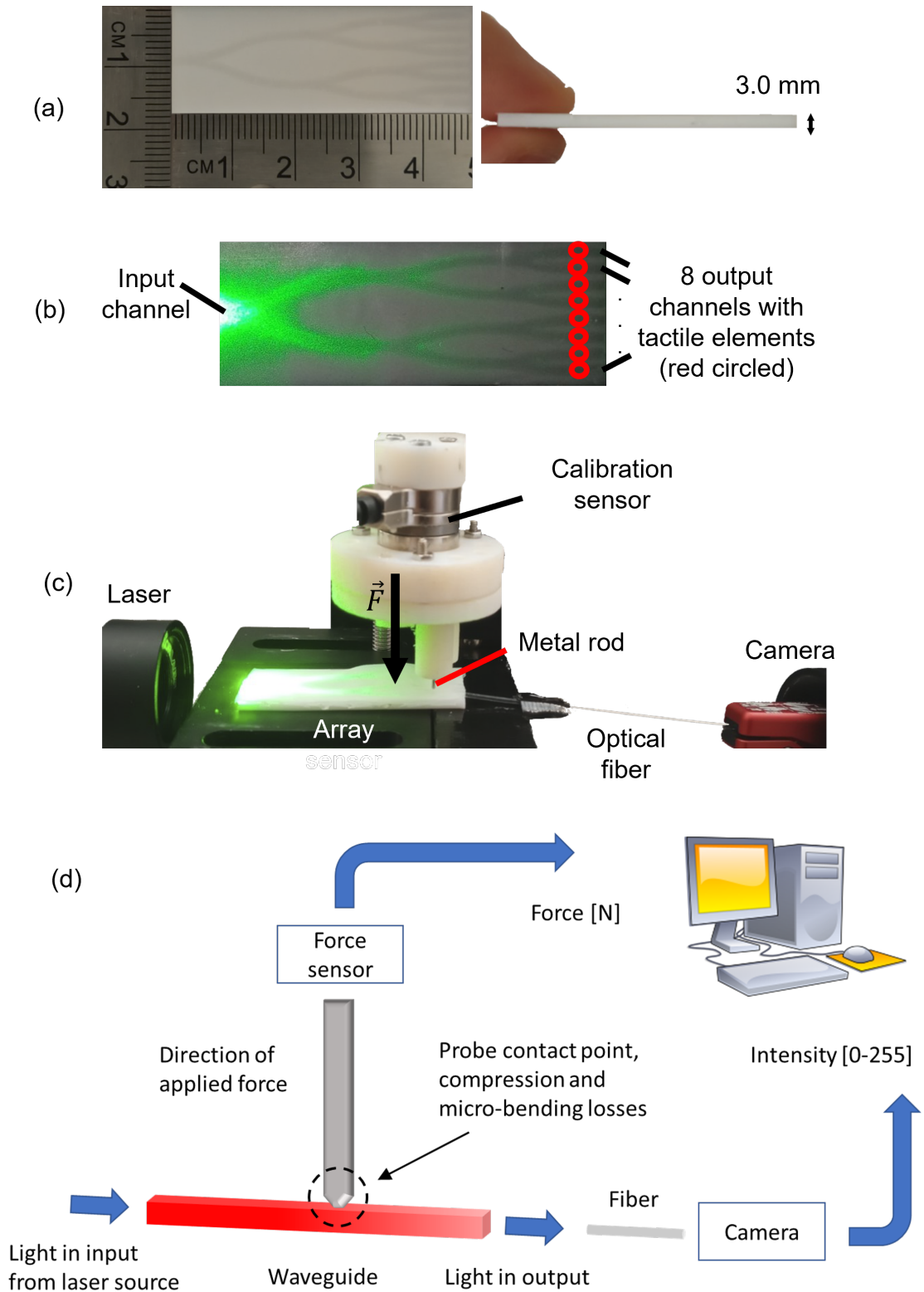


Figure 3.27: **Experimental setup.** The laser light is coupled into the device and an optical fiber carries the light from the output to the camera for detection. The core is compressed by a metal rod mounted on a calibration force sensor.

intensity detected through the camera and the force as given by the calibration curve.

Looking at the channels, the most of them stretch on the pressure range $[0 - 800]kPa$, apart

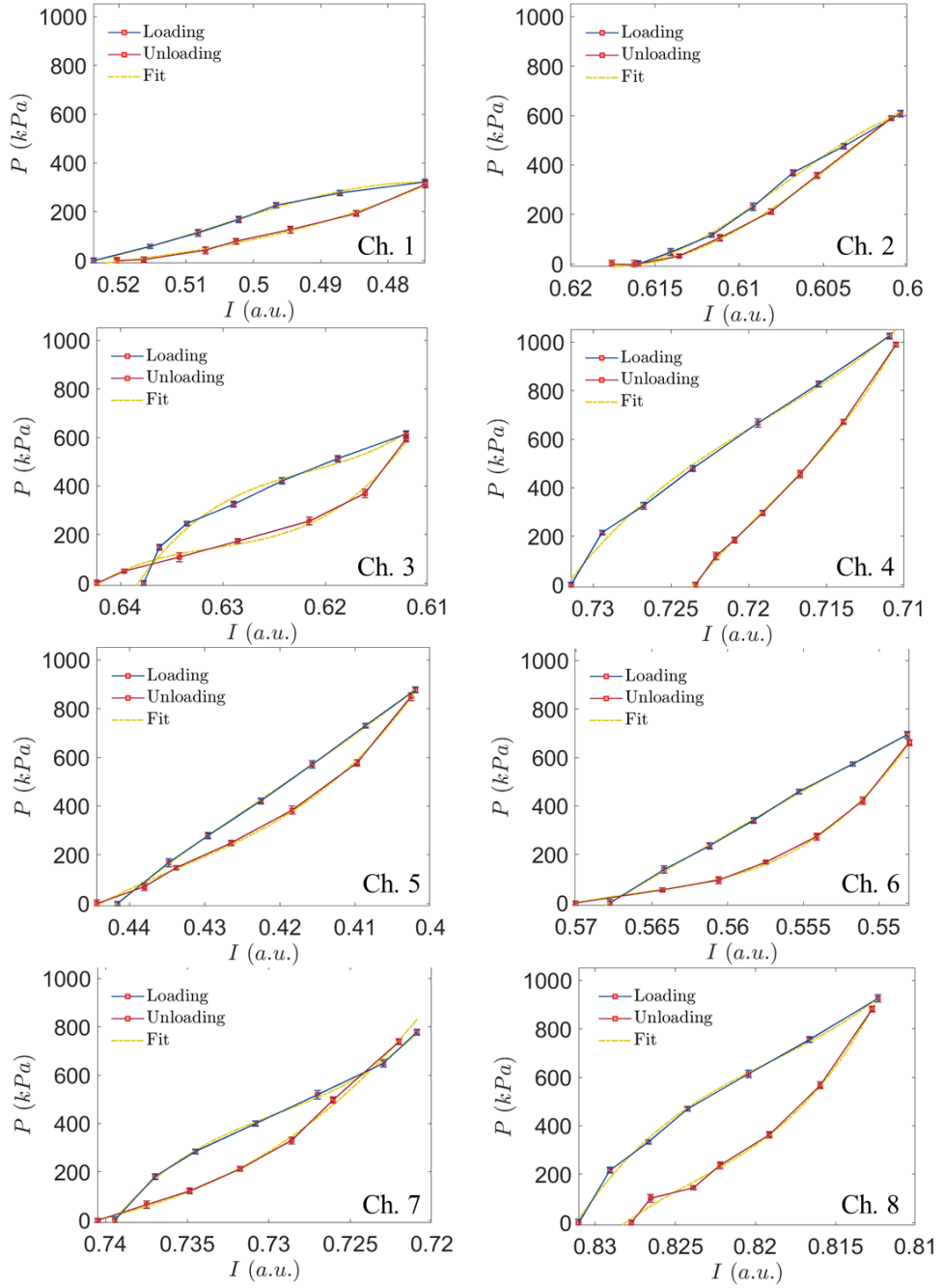


Figure 3.28: **Evaluation results.** Calibration curve of the force across the intensity measured by the camera.

channels 4 and 8 reaching almost 1000kPa , and channel 1 which presents a much lower maximum sensed pressure lower than 400kPa . This effect can be due to a manufacturing problem affecting this channel or to the preliminary tests carried out on this channel before starting the final data acquisition, causing a plastic deformation of the soft material. Also the signal-to-noise ratio present high variability on the basis of the channel considered, with minimum value of ~ 15 and maximum value of ~ 30 . To reduce the hysteresis and extend the range of detectable pressures, the proposed soft gel can be replaced with a

different stretchable material with higher toughness and fatigue resistance, provided that the optical requirement regarding the refractive index is met.

3.7 Conclusion

The proposed array prototype is an optic-based sensor made by polymer materials. The light is transmitted from the source to the detector passing through a multi-splitter structure of channels filled with a soft material. The presence of a single input channel avoids the use of multiple light sources, favouring the miniaturisation and reducing the cost of the full device. A multi-splitter configuration is used to gradually divide the light in different channels, to reach eight output channels corresponding to eight independent sensing elements. A simulation study helped determining the best channel design to minimise light loss and overall dimension of the sensor. The presented prototype offers the key advantages of optical sensors, such as the immunity to electromagnetically induced noise, provides greater safety than electrical sensors when used in hazardous environments and enjoys long life.

In this chapter it was demonstrated how the suggested method and materials can be successfully used to implement an array sensor. Each channel of the array can detect pressures in a similar range between $0kPa$ and $700 - 1000kPa$, widely covering the range of interest for endoscopic interventions. The difference among the channels can be due to a limit of the proposed manufacturing method, which should be further investigated also through the use of more advanced instrumentation. The presence of air bubbles formed during the injection of the soft material into the channels or any irregularities and asymmetries in the manufacturing process can affect the light transmission and therefore determine a different force response of each channel. Additionally, simulation analysis highlighted how the roughness of the waveguide surface should be further improved in order to enhance the light transmission efficiency.

The signal-to-noise ratio is highly variable on the different channels of the array sensor and its average value is ~ 22 . The sensitivity is $\sim 0.008kPa^{-1}$.

The rigid substrate of course prevents the adaptability to the non-planar surface of an endoscope and the sensing area is currently limited to the terminal part of the device, while the most of the sensor occupied by the development of the splitters cascade does not provide any pressure feedback.

The sensing strategy presented in the next chapter proposes an alternative approach to

address the limitations of this design.

Chapter 4

Soft Tactile Skin Employing Fluorescence Based Optical Sensing

Although the sensing strategy addressed in the previous chapter presented important characteristics for the application to colonoscopy, the combination between simulation analysis and experimental validation highlighted some disadvantages.

Since the fabrication of lab-made waveguides presented some challenges and the rigid substrate constituted a not negligible limitation, for this design it was considered to use commercial optical fibers embedded in a flexible polymer pad leading to the fabrication of a tactile skin.

Each optical fiber tip corresponds to an independent sensing element and the distribution of a number of optical fibers integrated into the pad can lead to an extended sensing area. The pressure can be detected not just when it is applied exactly in correspondence of a fiber tip location; also the areas of the skin included between different fibers provide sensing feedback, thanks to the centre of mass calculation as explained later in the chapter, limiting the "dead zones". This enhances the spatial resolution of the previous sensor which was limited just to the terminal part of the device while the most of the sensor was not providing any pressure feedback.

The expedient to confer a chisel shape to each fiber tip allows to detect pressures applied normal to the light propagation direction as required by endoscopic applications.

An important innovation of the technique presented in this chapter is the use of the properties of fluorescent dyes for the development of tactile sensors. Fluorescence applications are mainly focused on the biochemical and medical field, and involve imaging, drug targeting, and therapeutic agents for real-time observations.

The typical absorption and emission spectra of fluorescent dyes can be distinguished based on the *Stokes shift*, as explained in section 2.3. This effect allows to filter out the excitation signal and isolate the emission signal on the basis of the wavelength. Because of this characteristic, fluorescence has been extensively used in the applications as mentioned above, where the signal-to-noise ratio is particularly critical [154].

In this chapter, it was verified how the use of fluorescence improved the signal-to-noise ratio respect to the design presented in the previous chapter. Moreover, fluorescence

also allowed to use the same optical fiber as emitter and receiver at once, thanks to the possibility to decouple emission and excitation light travelling in the same fiber. This permits to halve the number of optical fibers used, optimise the overall size of the sensing skin and free up space which can be occupied by additional optical fibers increasing the number of sensing elements and therefore the spatial resolution of the tactile skin. In the proposed design, the integration of additional optical devices such as couplers or bifurcated bundles is also prevented, getting a simplified manufacturing process.

The proposed design satisfies several requirements for its application to the external surface of an endoscope. Referring to section 1.5 a summary is presented below.

- The proposed skin is soft and flexible, so it can be adapted to the non-planar surface of an endoscope. The thickness of the skin can be optimised for miniaturisation. Fluorescence is used to decouple the light coming from the light source and the signal emitted by the pad under compression, allowing to use the same fiber as emitter and receiver and so halving the overall number of fibers to be embedded into the skin and eventually partially placed inside the endoscope sheath (requirement 1).
- Chisel shaped fiber tips allow to detect pressures applied normal to the light propagation direction (requirement 2).
- The spatial resolution (requirement 3) is enhanced by integrating multiple optical fibers in the flexible skin. Each fiber works as an independent sensing element. Pressure magnitude and application point on the skin can be measured, leading to an extended sensing area.
- The materials selection and sensor design were studied to realise a sensing skin able to measure pressures in the range of interest (requirement 4).
- Biocompatible fluorescent dyes can be adopted to guarantee chemical inertness and non-toxicity (requirement 5).
- The absence of electrical components in the main body of the skin lends the proposed design to sterilizability and MRI compatibility; the low costs can even make this sensing skin disposable (requirements 6 and 7).
- The simple fabrication process and low costs can facilitate an eventual mass production (requirement 8).

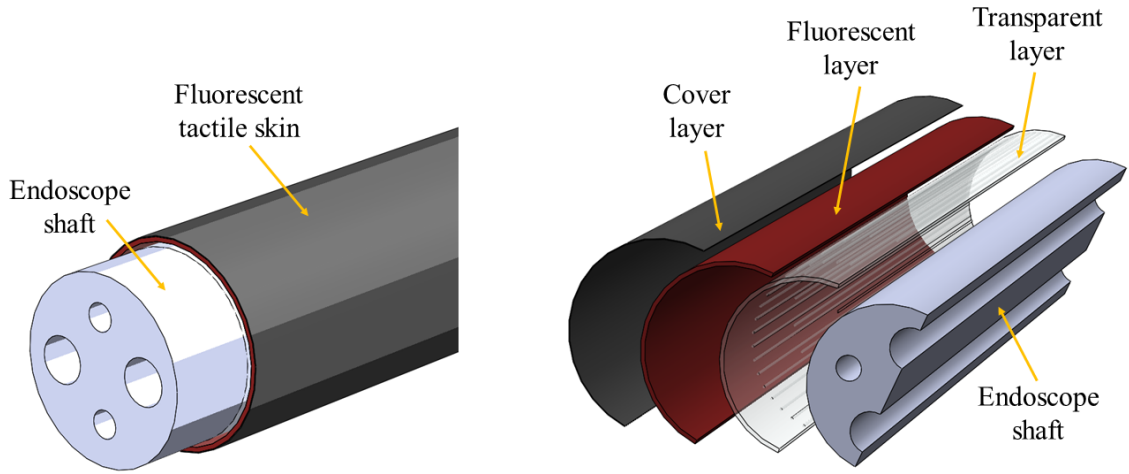


Figure 4.1: **Tactile skin for medical tools.** The design is adaptable to non-planar surfaces such as the outer surface of an endoscope [155].

A graphical representation of the application of the proposed flexible skin to a commercial endoscope is presented in fig. 4.1. The tactile skin can be wrapped around the outer surface of the instrument shaft, layer by layer: a transparent layer, a layer dopped with fluorescent dyes and a covering layer. The fiber tips, corresponding to the tactile elements of the sensing skin, are embedded in the transparent layer, while the rest of the fiber body would be embedded into the endoscope shaft [155].

The sensing principle was first validated using a single optical fiber. Then a prototype of soft skin pad was made as feasibility study. In this case, four optical fibers were embedded into the soft material composing the skin, but the design can be further extended. The combination of multiple sensing elements can provide information not only about the magnitude of the applied pressure, but also about the position of its application point on the pad.

4.1 Sensing Principle

As shown in fig. 4.2a, the sensor is made by a transparent layer and a fluorescent layer which absorbs light matching the absorption spectrum of Rhodamine B and emits light with a longer wavelength according to its emission spectrum, as a result of fluorescence. Typical spectra of Rhodamine B are presented in section 2.3 (fig. 2.6b).

The excitation light is transmitted by the optical fiber embedded into the transparent layer. When the light reaches the angled tip of the fiber, it is reflected at 90° due to total internal reflection, as explained in section 2.1.2. The light hits the lower surface of the fluorescent

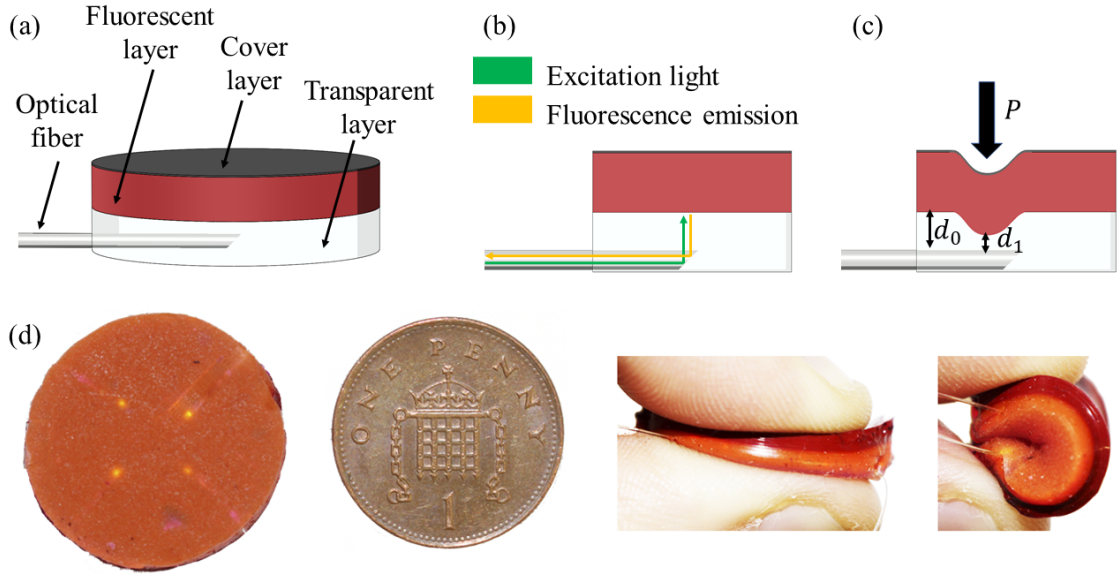


Figure 4.2: **Tactile skin.** (a) Design of the sensor. (b) The same fiber is used as emitter and receiver thanks to the combined effect of fluorescence and the angled tip optical fiber. (c) When a pressure is applied, the deformation causes the enhancement of the fluorescent emission measured. (d) The prototype of tactile skin equipped with four tactile elements has a compact geometry, it is compressible and flexible.

layer and gets absorbed by the fluorescent molecules, then the fluorescence light with longer wavelength is emitted (fig. 4.2b). This is the signal to detect which is transmitted back through the fiber towards the acquisition system.

When a force is applied on the sensor, the fluorescent layer is deformed and the distance between the lower fluorescent surface and the optical fiber changes from d_0 to $d_1 < d_0$ (fig. 4.2c). Since now the fluorescent layer is closer to the fiber, the latter emits light which reaches the fluorescent layer with a higher intensity. Consequently also the intensity of the fluorescence emission increases and it can be transmitted back through the fiber and detected. The expected result is detecting an increasing light intensity as a function of the pressure applied on the sensor.

4.2 Manufacturing Process

4.2.1 Angled tip realisation

The proposed tactile skin is based on light transmission through one or more optical fibers to a silicone pad doped with fluorescent dyes. Each fiber has an angled tip that is cut at an angle higher than the critical angle. Because of the Snell's law (see section 2.1.1)

such an angled tip fiber is able to emit/receive light signals at normal incidence with respect to its optical axis without the use of rigid optics such as mirrors. This configuration can be employed in medical applications where flexibility and miniaturisation are important requirements [156, 157, 158].

A plastic optical fiber (Edmund Optics, Acrylic substrate, fiber diameter 1mm) was used. The core of this fiber is made of PMMA (polymethylmethacrylate) and its typical refractive index is around 1.49 measured at 530nm [159]. The critical angle can be calculated as explained in section 2.1.1, eq. 2.2, considering $n_1 = 1.49$ and $n_2 = 1$ (refractive index of the air). Then, the critical angle is around 42° . To fulfil the total internal reflection requirements, the tip of the fiber was cut at 45° , value higher than the critical angle.

A rudimentary fiber cleaver was designed and 3D-printed to cut the tip of the optical fiber (fig. 4.3a). Then a polishing procedure was followed to get a very smooth surface and a

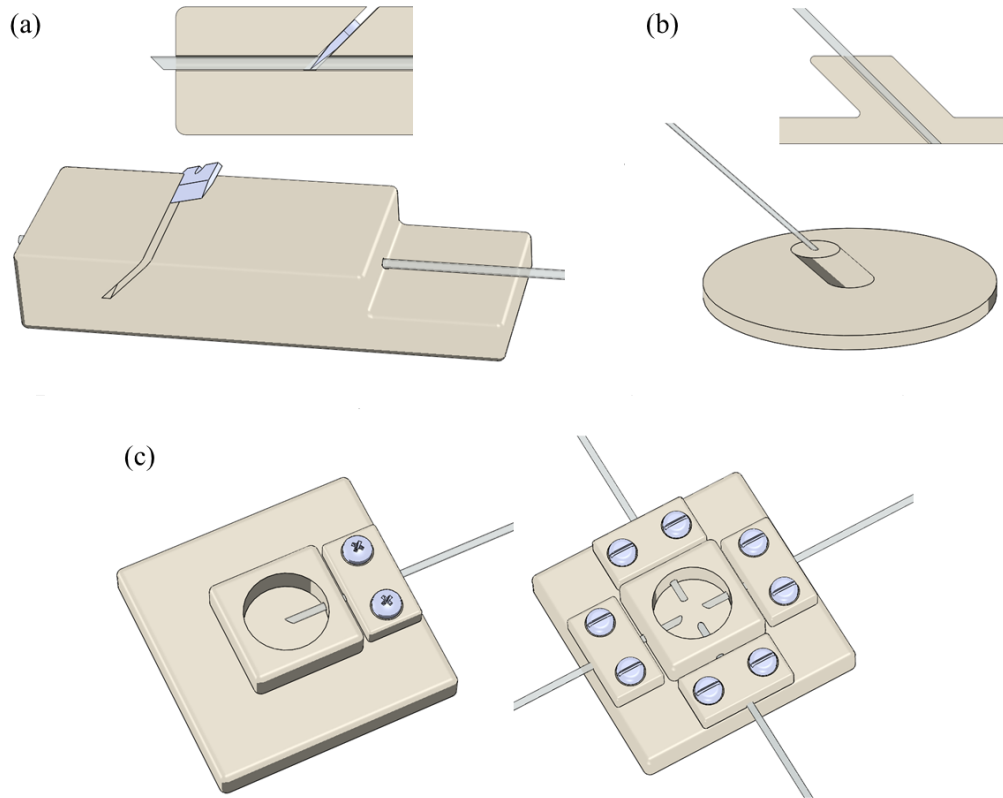


Figure 4.3: **Angled tip fiber fabrication and integration.** (a) The fiber is cut with a cleaver equipped with a sharp blade. (b) A polishing disc with the same cut angle of the fiber is used for lapping. (c) Once the fiber has a very clean and smooth surface, it can be placed and fixed into the mould where the soft material of the sensor body will be poured in. This ensures that the fiber is integrated into the sensor body after curing.

specific polishing disc was designed for the purpose (fig. 4.3b). A rounded shape was chosen for the sensor prototype. So, two different moulds with this shape were designed and 3D-printed: the first one for the single fiber sensor; the second one for the four fibers sensor (fig. 4.3c). In both the design, the mould presents the appropriate hole(s) where the fiber(s) can be placed. The plaquette(s) with screws allows(allow) the fiber(s) to be firmly fixed during the soft material injection and curing.

Although the cleaver was equipped with a pretty sharp blade, after the cut the fiber, still with its black outer jacket, presents an irregular surface, with many PMMA scraps (fig. 4.4a). An accurate polishing procedure was required to get a smooth surface and allow the light to be reflected as described by the Snell's law. About 1cm of black outer jacket of the fiber was removed to facilitate the polishing using a fiber optic stripper. Three different types of lapping films were used for the polishing: the first one with a granularity of $3\mu m$, the second one of $1\mu m$ grit and the last one of $0.3\mu m$ for very fine polishing (Throlabs, Aluminum Oxide Lapping Sheets). After each polishing phase, the fiber was cleaned with a lintfree cloth moistened with methanol alcohol to remove any scraps. Fig. 4.4b,c,d shows the surface of the fiber after being polished by the three different lapping sheets. It can be observed how the surface becomes much more defined in shape and smoother during the procedure. Fig. 4.4d shows the final result with the sharp angle at 45° (fig. 4.4e,f).

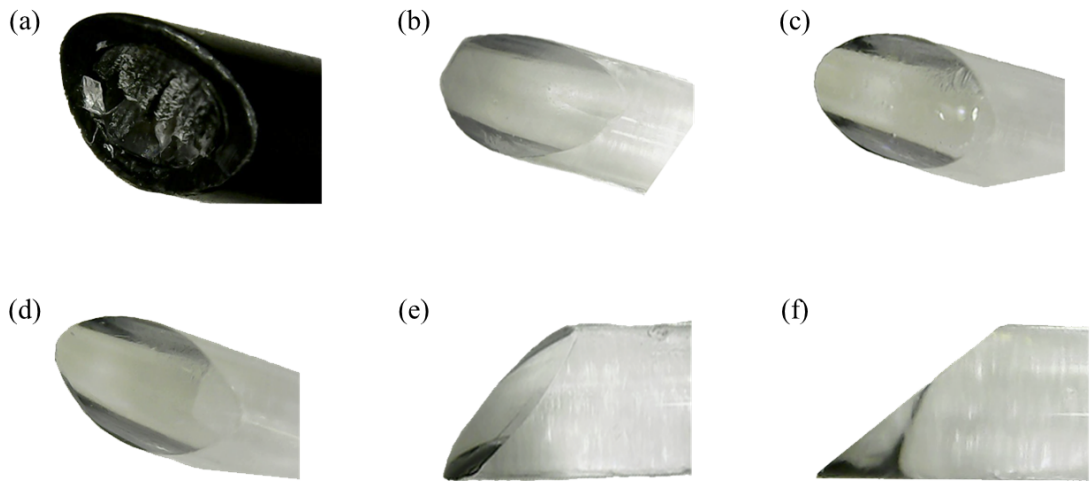


Figure 4.4: **Polishing procedure.** (a) After the cleaver cut, the fiber presents a broken surface. Fiber surface after being polished using a sheet with granularity of $3\mu m$ (b), $1\mu m$ (c) and $0.3\mu m$ (d). The fiber looks very smooth (e) and the cut at 45° well defined (f).

4.2.2 Sensor fabrication

The sensor is shown in fig. 4.2a. It has a round shape with diameter of 11.50mm and is characterised by three layers: the first one is a transparent silicone layer (thickness of 2mm), the second one is a silicone mixture containing the fluorescent dye (thickness of 2mm), finally a black paint was sprayed as third layer to prevent environmental light from interfering with the sensor.

The clear silicone used (Sorta-Clear™ 12, Bentley Advanced Materials) is made by two parts, A and B, to be mixed in a ratio of 1 part A to 1 part B by volume. After the angled optical fibers are placed into the mould, the clear silicone mixture can be poured until the mould is half filled. Then it is left for drying for few hours. As a result, the fiber is fixed inside the cured transparent layer, at the distance of about 1mm from the upper surface of the transparent layer.

The transparent silicone is also used as host material for the fluorescent dye Rhodamine B (Sigma-Aldrich, maximum absorbance 542 – 554nm, fluorescence emission 570nm).

The dye appears as a fine powder and it is diluted in methanol with 1:10 weight ratio. The solution is mixed with the clear silicone previously used with 1:10 weight ratio. The mixture is poured into the mould upon the transparent layer, until it is fully filled. Then it is left for drying for 48 hours.

Once cured, a thin layer of black paint was sprayed on the sensor to prevent the external light to reach the fluorescent layer and/or the optical fiber and interfere with the measurements. The final sensor with four tactile elements presents a compact size, is compressible and flexible (fig. 4.2d).

4.3 Imaging System

Typically, experimental setups for spectroscopy measurements are characterised by a particular configuration where any fluorescence emitted by the sample is detected at 90° to the incident light beam. This geometry, pioneered by Stokes in the 1850s, is still used in virtually all commercial and laboratory-built fluorescence instruments, inevitably with many additions, variations, and accessories for individual applications [160]. Its crucial advantages are that photons coming from the excitation light source and transmitted by the sample are not detected, and that Rayleigh scattered light has a minimum intensity in the 90° direction [160]. The key optical elements of the design are the light source, the

excitation monochromator or filter, the sample cell, the emission monochromator or filter, and the detector.

The imaging system is presented in fig. 4.5 and follows the same configuration as traditional fluorescence spectroscopy and imaging systems where only the fluorescence light is imaged. The purpose to have the fluorescence emission detected at 90° to the incident light beam is achieved by using a dichroic mirror, which spectrally separate light by transmitting or reflecting it as a function of wavelength. Longpass dichroic mirrors have a transmission and reflection band that are divided by a cut-on wavelength: the mirror is highly reflective below the cut-on wavelength and highly transmissive above it [161].

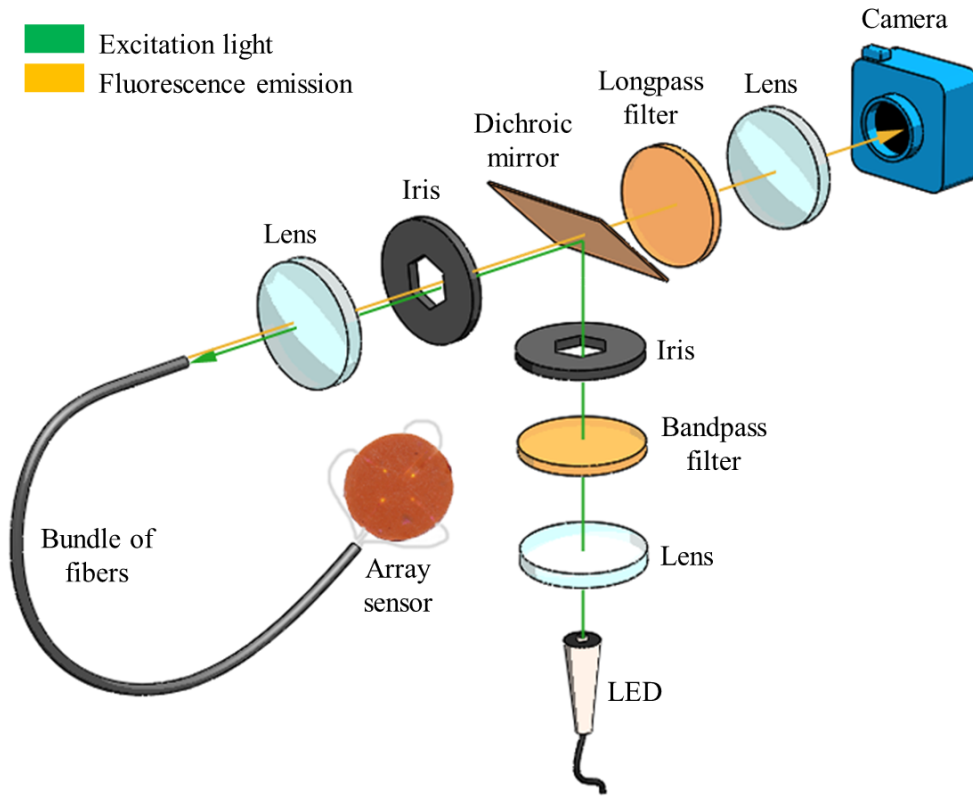


Figure 4.5: **Fluorescence imaging system.** The excitation light (green arrow) is reflected at 90° and reaches the sensor. Then, fluorescence emission is released by the doped silicone layer and transmitted back to the camera (yellow arrow).

The light source is an LED with nominal wavelength of 530nm (FWHM bandwidth 33nm , 350mW , Thorlabs, M530L4). To minimise the high divergence of the LED (full viewing angle at half maximum 80°) and maximise the light power reaching the sample, a lens with proper numerical aperture NA is placed in front of the light source. A bandpass filter (CWL = 532 nm , FWHM = 4 nm , Thorlabs, FLH532-4) has the role to narrow the spectrum of the LED, so that the excitation spectrum does not overlap with the

fluorescence emission spectrum. An iris is used to modulate the intensity reaching the sample. A longpass dichroic mirror (567nm Cut-On wavelength, Thorlabs, DMLP567R) placed at 45° respect to the initial light propagation direction is able to reflect the incident LED light at 90°. A second iris is used to block any divergent ray which may compromise the sharpness of the image acquired by the camera and therefore worsen the signal-to-noise ratio. The light is then focused and coupled into a bundle of optical fibers. The fibers, equipped with an angled tip and embedded into the sensor pad, can transmit the excitation light and receive back the fluorescence signal. The latter follows the path backwards and, stretching on wavelengths longer than the cut-on wavelength of the dichroic mirror, it is transmitted forward. Since in general the blocking efficiency of a dichroic mirror is not 100% effective [161], one additional filter adapted to the emission properties of the fluorescent dye is required. In this case, a longpass filter (cut-on $\lambda = 550nm$, Thorlabs, FEL0550) is used. The fluorescence signal can then be focused on the camera (Blackfly USB3, 2.3MP, 41fps).

4.4 Results

4.4.1 Spectral acquisition

A series of spectra were acquired to show the effect of the filters used in the experimental setup.

The LED spectrum covers the range [450 – 600]nm (fig. 4.6a). After the bandpass filter, its spectrum is narrowed between [530 – 540]nm (fig. 4.6b). The dichroic mirror does not affect the wavelength distribution and, after it, both excitation signal and fluorescence emission are observed. However, the excitation light peak is more than 60% lower than the higher peak belonging to the fluorescence emission thanks to the 90° acquisition system configuration (fig. 4.6c). Finally, the longpass filter completely removes the contribution of the excitation light, so that only the fluorescence signal reaches the camera improving the signal-to-noise ratio (fig. 4.6d).

4.4.2 Calibration

Evaluation experiments were carried out using the single fiber fluorescence sensor. One end of the optical fiber was embedded into the sensor; while the other end was connected to the imaging system to detect the fluorescence light. The aim of the experiment is getting

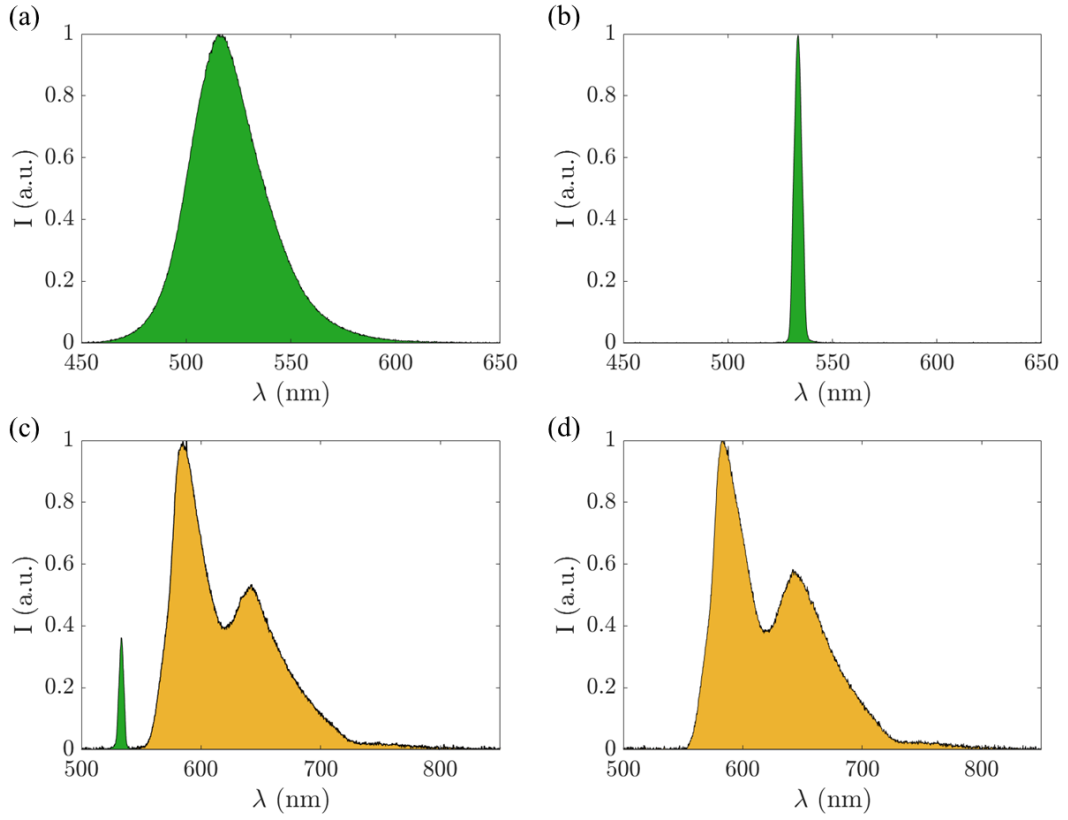


Figure 4.6: **Acquired spectra.** (a) Original light source spectrum. (b) Narrowed light source spectrum. (c) Coexistence of excitation light and fluorescence emission. (d) Light source is completely filtered out. Thus, the camera of the imaging system just detects the fluorescence signal.

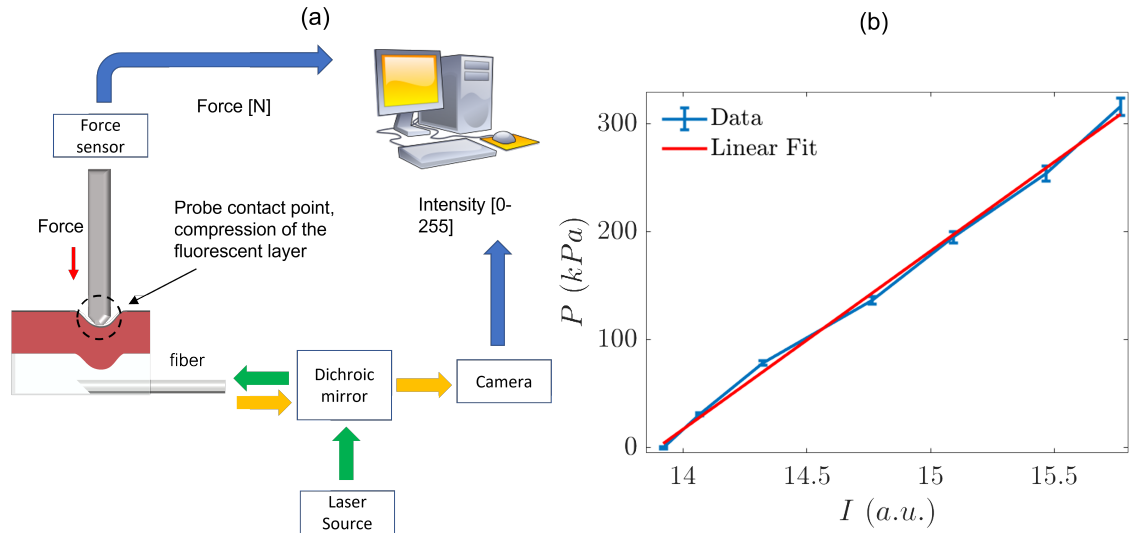


Figure 4.7: **Experimental evaluation.** (a) scheme of the experimental setup employed for pressure measurements (b) Calibration curve: 30 measurements for each point were acquired to carry out the repeatability experiment.

a calibration curve which relates the fluorescence intensity modulation with the pressure applied on the sensor.

A 6-axes force/torque sensor (ATI Nano-17, resolution $0.003N$) was mounted on a motorized linear guide. The linear guide moved at steps of $20\mu m$ forward (backward), causing an equivalent sensor width compression (relaxation).

The resulting fluorescence signal variation was transmitted by the angled tip optical fiber to the imaging system and then detected by the camera.

For each position, the force applied on the sensor was recorded by the calibration force sensor while an image was acquired by the camera. The region of interest (ROI), corresponding to the tip of the fiber, was detected by an image processing algorithm based on a threshold method. The intensity values associated with the pixels included in the ROI were considered to calculate the average intensity at each fiber tip.

To obtain the calibration curve, the silicone pad was compressed and relaxed in the same position for thirty times. A probe of $3mm$ of diameter was used for the compression (fig. 4.7a). Fig. 4.7b is a plot of the acquired pressure readings versus the recorded average intensity. The sensor compression increment was about $130\mu m$ for each point. Force data were later converted to pressures to be comparable with typical values measured during colonoscopy as reported in literature. Data regarding maximum intraluminal pressure during routine colonoscopy range between 4 and $20kPa$, while bursting pressures have values from about $7kPa$ in the cecum to $30kPa$ in the sigmoid colon [95].

As shown by the calibration curve (fig. 4.7b), the presented sensor is able to measure pressures in the range of interest for this specific application. Moreover, as expected, an increase of pressure applied on the sensor corresponds to an increase of fluorescence intensity. Data are characterized by a linear correlation with $R^2=0.986$. The error bars represent the standard deviation, equal to 3% of the fluorescence signal readings at a specific pressure value. Based on this, an average signal to noise ratio of 117 has been calculated. This is more than a factor 5 higher than the result obtained with the previous design and confirms the hypothesis that wavelength separation can provide a more efficient sensor.

4.4.3 Photobleaching

When excited, fluorescent dyes face a constant and progressive decay that eventually, with time, makes them unable to further fluoresce. Such phenomenon is called photo-

bleaching [162] and represents one of the major limitation to the sensor life time. To measure the fluorescence signal decay caused by photobleaching, the sensor has been continuously exposed to excitation light for 8 hours, sampling the fluorescence signal every second. The resulting data are shown in fig. 4.8.

It is possible to observe that after two hours the photobleaching causes an intensity decrease lower than 1%.

Considering that the mean duration of endoscopic interventions is around 30minutes [163], photobleaching can be neglected.

The photobleaching experiment was prolonged for a further 24 hours. After that, the experiment was interrupted for one hour and resumed for another hour. The decrease of the intensity can be considered constant along time and it is not sensibly affected by interruptions of the sensor operations.

The experiment was also repeated keeping the sensor compressed by a constant force of about 15N for eight hours. In this case the light intensity seems to decrease slightly faster. However the slope of the signal intensity decay remains linear and of the same order of magnitude.

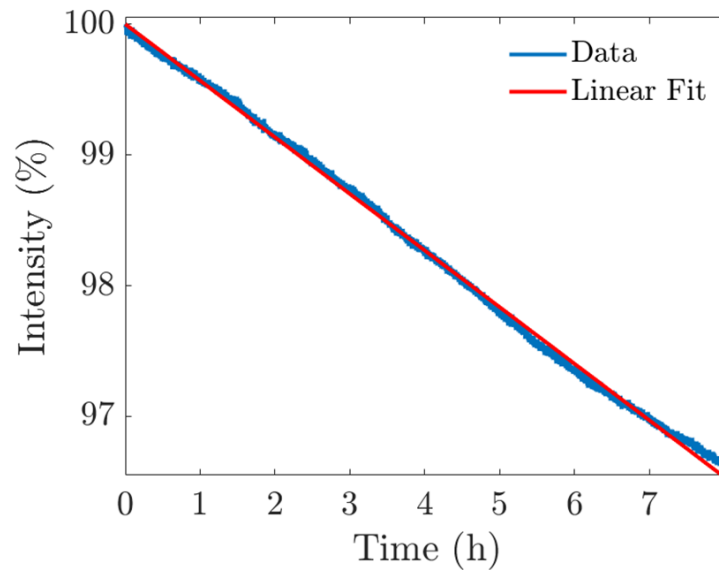


Figure 4.8: **Measure of photobleaching.** The slope of the intensity decay over 8 hours was measured three times, giving values within the same order of magnitude.

4.5 Extension To A Soft Tactile Array Sensor

A multi-fiber fluorescence sensor was developed to demonstrate the feasibility of a soft tactile array sensor employing fluorescence. The array pad presents the same layers structure as the single fiber prototype, but aims to provide the coordinates of the application point of the pressure over the sensor area. In this case, a bundle of four fibers was used and the fibers were embedded into the flexible pad at the distance of $7mm$ between each other, going to design a square.

These fibers present similar diameter and same optical properties (refractive indices and materials of core and cladding) than the fibre used in section 4.4.2. Thus, the calibration curve (figure 4.7b) obtained for the single fiber sensor is assumed valid with good approximation for each fibre of the array sensor.

4.5.1 Image processing algorithm

An image processing algorithm was developed to identify the ROI corresponding to the output surface of the four fibers of the bundle.

The starting image shown in fig. 4.9a is cropped in four sub-images to restrict the areas where the four fiber outputs are contained (fig. 4.9b). For each sub-image, the histogram of the occurrences for each intensity value was studied and the threshold was evaluated by eye looking at the peaks. For example, looking at the histogram and the related sub-image in fig. 4.9c, the highest peak stretching on intensity values lower than 0.1 corresponds to the dark background; the central small peak refers to the edge of an adjacent fiber circled in red in the figure; while the peak with intensity values between [0.25-0.40] corresponds to the fiber output of interest (circled in white in the picture). In this case, a lower threshold of 0.28 is set up and all the pixels with intensity $I > 0.28$ are considered. Since more than one pixel region may satisfy the lower threshold condition (e.g. bright spots or blurry regions around the fiber output contour), all the regions formed by less than 50 pixels are removed from the selection. Then, any gaps of the selected regions are filled and just the region with the highest number of pixels is considered as ROI (fig. 4.9d). The final result of the identified pixels belonging to the fiber output of interest is shown in (fig. 4.9e). In the case of the other three fibers, a combination of an upper and a lower threshold may have been necessary. The four fiber outputs identified by the algorithm are shown in fig. 4.9f. Once the ROI is identified, it is possible to calculate the light intensity of each fiber

and evaluate the application point of the force.

A flow chart describing the algorithm for the detection of the ROI of a fiber and the source code with comments which refer to the steps of the flow chart are reported in Appendix E. The same code is iteratively applied to find the ROI of each fiber in the starting image.

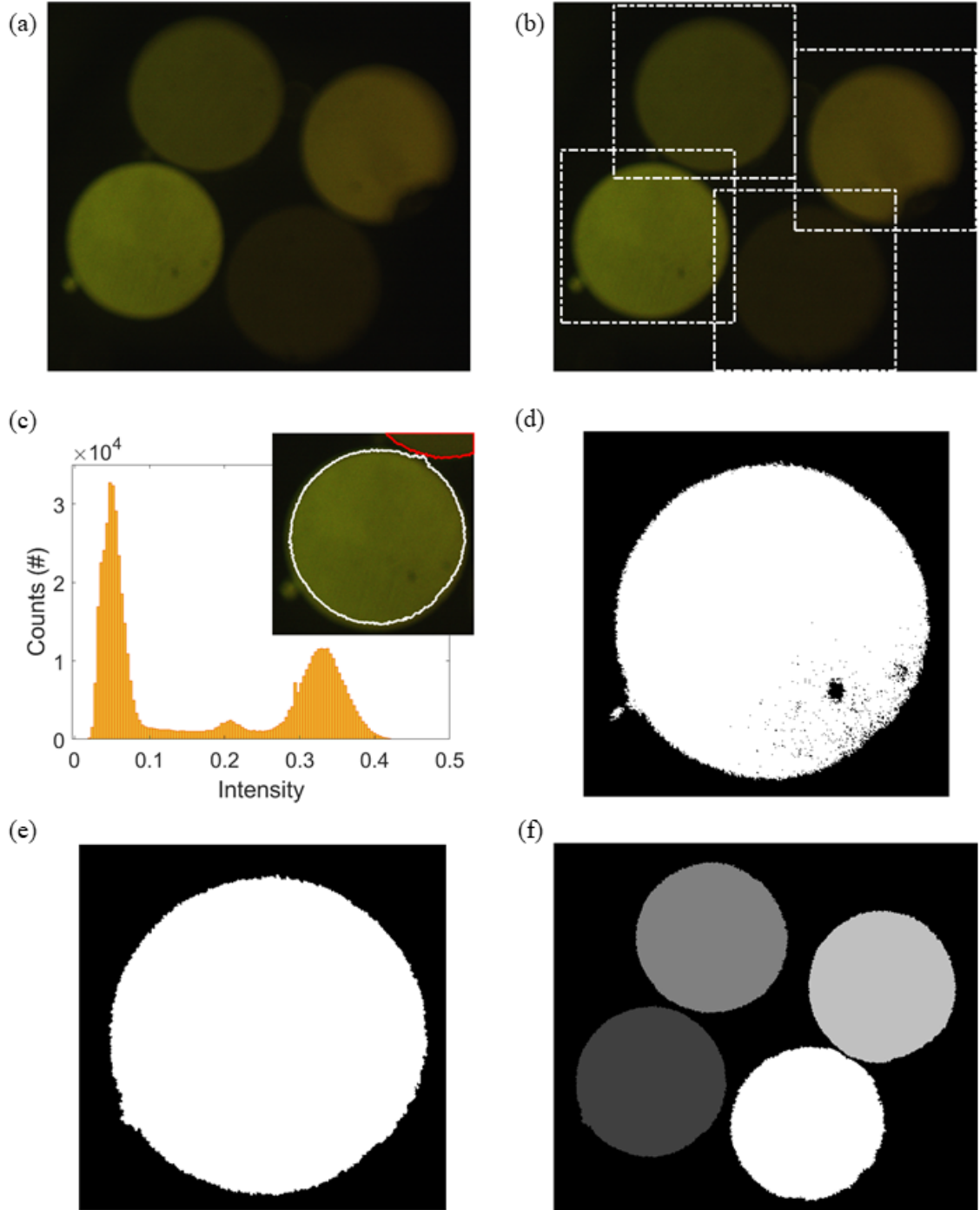


Figure 4.9: **ROI identification.** (a) Starting image. (b) The image is cropped in four sub-images. (c) Selection of the intensity threshold. (d) Presence of multiple selected regions and gaps. (e) Identification of pixels belonging to the fiber output. (f) ROI identification of the four fibers.

4.5.2 Position calculation

Each fiber was compressed and released 10 times and a picture of the output of the four fibers was acquired at every step of compression and decompression. The four regions of interest identified by the image processing were considered to calculate the mean intensity of the four fiber output for each image, so that just the pixels belonging to the ROI corresponding to each fiber have been involved in the calculation. The mean intensity of each fiber in decompression was subtracted to its mean intensity in compression. In this way, the modulation of intensity on each fiber was measured. The average intensity modulation values of each fiber $f_{1,2,3,4}$ were then calculated on the 10 repeated measurements.

The application point of the pressure on the sensor was considered corresponding to the center of mass calculated as follows:

$$x_{CM} = \frac{\sum_{i=1}^4 (x_i f_i)}{\sum_{i=1}^4 f_i} \quad y_{CM} = \frac{\sum_{i=1}^4 (y_i f_i)}{\sum_{i=1}^4 f_i} \quad (4.1)$$

where x_i and y_i are the coordinates of the center of each fiber tip and f_i the corresponding average intensity. The values x_i and y_i were calculated on the basis of the graphical representation shown in 4.10 where the four dark-green dots represent the real position of the fibers inside the sensor array.

In all the four cases of pressure applied in correspondence of one fiber tip, the measured location falls within the blue circle representing the pressure application probe. When the middle of the sensor is pressed, the calculated position is slightly outside of the blue circle. It should be noted that a correct detection of the position requires at least 3 fibers surrounding the application point of the pressure. Thus, due to its specific design, the sensing area of the proposed sensor corresponds to the square defined by the four fiber tips. Considering the highest uncertainty experimentally obtained (fig. 4.7), it can be concluded that the proposed sensor is able to detect the application point of the pressure with an error lower than 10% of the sensing area.

Regarding the potential application of this sensor, a further design improvement is required to create a flexible covering skin for the external surface of medical tool shafts. The increase of both the flexible pad surface and the number of sensing elements, in addition to a non-planar geometry, will lead to an extension of the sensing area. In fact, more fibers would be surrounded by other fibers and it will be possible to define the application point

of a pressure on a more extended surface.

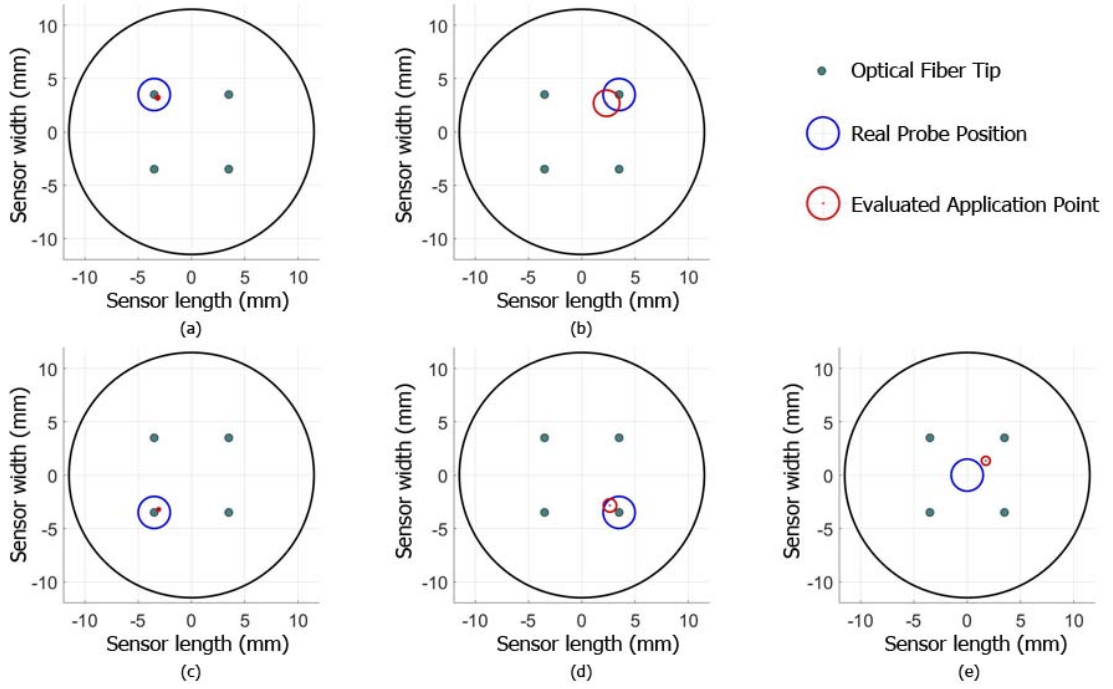


Figure 4.10: **Measurement of the application point of the pressure on the sensor.** A pressure was applied on five different locations of the flexible array sensor: on the tip of each of the four fibers (grey circles) and at the center of the sensor. The sensor was pressed 10 times for each location, using a probe with a diameter of 3mm . The blue circles represent the real position of the probe. An algorithm calculates the centre of mass on the basis of the intensity of the four fibers to evaluate the point of the pressure application (red dot). The error is the standard deviation of the repeated measurements and corresponds to the radius of the red circles.

4.6 Conclusion

The introduction of fluorescence for the development of force sensors present various advantages. Fluorescence offers the possibility to distinguish between excitation and emission light on the basis of the different wavelengths. This characteristic plays a fundamental role in improving the signal-to-noise ratio. By using fluorescence in combination with an angled optical fiber tip there is no need to deploy mirrors or other rigid components favoring the flexibility of the structure and simplifying the manufacturing process. Moreover, the same optical fiber can be used both as emitter and receiver allowing further design miniaturization.

In this chapter we have demonstrated how fluorescence can be successfully used to implement both single and multi-fiber array pressure sensors. The single fiber sensor is

able to detect pressures between $[0 - 300]kPa$ widely covering the range of interest, with a repeatability of 3%. The use of fluorescence contributed to improve the signal-to-noise ratio, which is ~ 117 , so over 5 times better than the design presented in the previous chapter. The sensitivity is $\sim 0.006kPa^{-1}$.

The development of a multi-fiber array sensor allowed to measure the application point of the pressure with an uncertainty lower than 10% of the sensing area. The unwanted effect of photobleaching is negligible considering the typical duration of a single endoscopy. The relatively simple manufacturing process and its low cost can make this sensor disposable. Finally, this sensor is immune to electromagnetic interference, making it MRI compatible.

In order to apply the proposed sensor to the external surface of an endoscope shaft, the thickness should be further reduced while the area of the sensing skin should be extended with the possibility to embed an higher number of fibers, enhancing the spatial resolution of the tactile skin. It should be mentioned that the increase of number of fibers leads to significant practical challenges. For this reason, the proposed array sensor presents just four sensing elements. However, the results presented in figure 4.10 show that the contact location can be identified with relatively small margin of error using the proposed method. Thus, the feasibility of the practical use of this sensor for flexible endoscopes is demonstrated.

To make the presented sensing skin applicable to a commercial endoscope, the manufacturing process for the multi-fiber array sensor should be further improved to allow the integration of a higher number of optical fibers in a larger and thinner tactile skin.

The effect of photobleaching presents a limitation since it can potentially compromise the sensing performance when an endoscopic intervention takes longer than its typical duration and prevent the re-use of the same skin for multiple interventions on different patients, since the sensing capability of the skin may deteriorate over the time.

Lastly, the fluorescent dyes employed in this study are not biocompatible. Although they are embedded into a silicone layer to prevent the direct contact with the patient body, an accurate toxicology study should be carried out to ensure the biocompatibility of the final device, Alternatively, the fluorescent dyes selection should be limited to the class of biocompatible dyes only.

Chapter 5

Design Of Polymer/QDs Composites For Waveguide Applications

The sensing strategy described in the previous chapter presented important characteristics for the application to colonoscopy, however some important limitations still needed to be addressed.

Fluorescence dyes are subject to photobleaching and have a limited biocompatibility. In this chapter, fluorescent dyes have been replaced by QDs. A detailed comparison is presented in the next section. However QDs, based on the same fluorescence principles as the dyes, are characterised by a higher photostability and their toxicity is largely reduced in the case of core-shell QDs. The latter also offer a higher QY, which is particularly important for the development of sensing technologies because it can lead to an enhancement of the signal-to-noise ratio respect to technologies employing fluorescent dyes.

The sensing strategy presented in the previous chapter required the use of a large number of fibers to improve the spatial resolution. The design was allowing to halve the overall number of fibers using each of them as emitter and receiver, the required amount of fibers would be still considerable. Considering that the sensing skin needs to cover all-round the external surface of an endoscope (typical diameter of 15mm) over a length of at least 1m as explained in section 1.5, and assuming to place the fibers at a distance of $\sim 7\text{mm}$ from each other as done in the prototype presented in the previous chapter, the number of fibers required would exceed 280. Only the tip of these fibers was involved in the fluorescence signal detection, while the rest of the fiber was just transmitting the signal to the camera for the measurement. Then the tip of these fibers was embedded into the soft skin but the main part of the fiber body was going out of the skin from its bottom layer and was supposed to be placed into the endoscope shaft. Assuming that the inner diameter of the endoscope shaft is $\sim 13\text{mm}$, the fibers should have a diameter lower than $\sim 470\mu\text{m}$ to fit inside the endoscope. The use of fibers with a diameter more than halved respect to the fibers used in the prototype previously presented would introduce additional challenges in the manufacturing process and signal detection efficiency. In addition, the insertion of a so high number of fibers, even if thin, into the endoscope shaft may substantially compromise its flexibility.

In this chapter the development of lab-made polymer waveguides doped with QDs was investigated. QDs integrated in polymer optical fibers (POF) or planar waveguides are already widely employed for thermometry applications [164, 165, 166, 167, 168, 169, 170], as well as fluorescent fiber probes for monitoring of heavy metal pollution [171], and for intracellular sensing and medical diagnostics [172]. The use of QDs-polymeric waveguides for the development of pressure sensors is an innovative application.

Beside the advantages respect to the fluorescent dyes, QDs are particular interesting for sensing applications because of their piezoelectric effect, which determines a modification of the optical properties of the material as a result of an applied pressure, as explained in section 2.4.3. The simultaneous modulation of intensity and wavelength of the QDs fluorescence emission under pressure was employed to develop a QDs doped waveguide where the multi-parameter variation is used to detect the magnitude of the pressure and its location along the waveguide itself. In this way, not just the tip of the waveguide is involved in the signal detection, as it was for the fibers in the previous design, but all of its body is sensitive to pressure. These waveguides can be fixed one next to each other over the external surface of an endoscope, parallel to its axis, without need to be inserted into its shaft at any point. It is important to fabricate waveguides with a small diameter, to avoid to excessively increase the outer diameter of the endoscope. For this purpose, waveguides with different diameters have been tested.

Referring to section 1.5, it can be observed that the design proposed in this chapter satisfies several requirements for its application to the external surface of an endoscope as summarised below.

- The proposed waveguides are flexible and their diameter can be miniaturised so they can be adapted to the non-planar surface of an endoscope. They do not need to be embedded into the endoscope sheath (requirement 1).
- The waveguides are able to detect pressures applied normal to the light propagation direction (requirement 2).
- The spatial resolution (requirement 3) is enhanced by employing the piezoelectric effect of QDs which allows the simultaneous detection of magnitude and location of the applied pressure along the waveguide. The all body of the waveguide is sensitive to pressure.
- The materials selection and sensor design were studied to realise a sensing waveguide

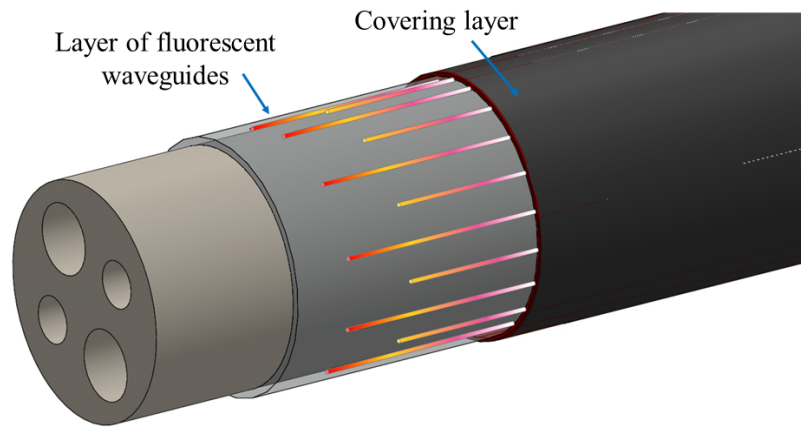


Figure 5.1: **Skin of waveguides doped with QDs.** The application of multiple fluorescent waveguides to the external surface of an endoscope constitutes a sensing skin able to return pressure feedback.

able to measure pressures in the range of interest (requirement 4).

- Core-shell QDs integrated into a polymer matrix confined into a PTFE tube ensure the biocompatibility of the device (requirement 5).
- The absence of electrical components in the main body of the sensing technology lends the proposed design to sterilizability and MRI compatibility (requirements 6 and 7).
- The simple fabrication process can facilitate an eventual mass production (requirement 8).

A graphical representation of the application idea of the proposed flexible waveguides to a commercial endoscope is presented in fig. 5.1 [173].

In this study, the integration of CdSe/ZnS QDs in the core of a polymer waveguide has been investigated. Specifically, intensity modulation and wavelength shift have been employed to measure both magnitude of the applied force and position of the application point along the waveguide. Simulation and experimental results are used as proof of concept of the proposed principle for multi-parameter pressure sensing.

The simulation results presented in this chapter are the result of a joint collaboration with the team of Dr Cedric Weber, Reader at Department of Physics, King's College London. The team focused on the study of the theoretical model describing the luminescence modulation of a single QD subject to an external mechanical force. The team also developed a ray tracing simulation to study the application of this principle to a QDs-

PMMA composite waveguide. Simulation results obtained by the theoretical team were compared with the experimental results on which I focused my work in the collaboration.

5.1 Comparison Between Fluorophores And QDs

For a given fluorophore, the QY defines its emission efficiency and it can be formally expressed as:

$$QY = \frac{\# \text{ photons emitted}}{\# \text{ photons absorbed}} \quad (5.1)$$

For its wide-spread use, a luminescence based sensing technology needs to address the following challenges:

1. high PLQY of fluorescent material in its synthesis batch;
2. high quantum efficiency (QE) of them in host matrix;
3. low overlap between the absorbance and photoluminescence of the fluorophore;
4. being free of toxic elements;
5. scalable production for wide-spread use

The points (1)–(3) are fundamental in order to enhance the photoluminescence emission and get a good signal-to-noise ratio. In addition, point (4) ensures the application of the technology to biomedical applications and minimise the adverse effects on environmental sustainability, in addition to facilitate the processes of storage, handling and disposal. Point (6) shows the suitability for large-scale production. Therefore, fulfilling the requirements (1)–(6) are prerequisites to a practical technology for safe and effective sensing.

The sensing prototype presented in Chapter 4 was employing fluorophores embedded into a silicone matrix. However, the use of fluorophores is accompanied with major challenges for the fabrication of sensing technologies involving the integration of fluorophores into host materials such as soft polymers. Organic dyes generally present limited photostability [174, 175, 176]. Moreover, optical stability and PLQY of organic dyes in host materials undergo further reduction when they are integrated into host materials [177, 178]. Alternatively, colloidal quantum dots (QDs) offer exceptional optoelectronic properties compared to fluorophores and their integration into a polymer matrix presents several advantages.

QDs are prone to degradation of their surface that leads to a loss of their properties; examples of this are the photooxidation effects when they are exposed to air [179]. Another important aspect is the toxicity of QDs due to the heavy metals composition. Therefore, protecting quantum dots using polymers can help overcome the drawbacks listed above and facilitate their use in optoelectronic and biological applications. QDs dispersed in polymer would be protected against possible degradation, so against loss of their optical properties. Furthermore, the working environment would be protected and the impact of their toxicity notably reduced [180].

As detailed in section 2.4, they allow the control of the optical properties by tuning their size, shape, and chemical composition. In addition, by using different inorganic core/shell structures, high PLQY can be reached to decrease the optical losses. Furthermore, the ability of precisely tailoring absorption and emission spectra of the QDs by engineering Stokes shift can enable low reabsorption losses, which is important to minimize the propagation losses of the down-converted luminescence travelling along an optical waveguide. Also, the typical absorption spectra with steady increase toward UV wavelengths allows the proper selection of the excitation wavelength for a straightforward separation of excitation and emission [181].

Regarding the photo-stability, both fluorescent dyes and QDs are affected by photobleaching and blinking effects which cause unstable signals and performance degradation [182, 183, 184]. The blinking is the fluorescence intensity intermittency affecting continuously illuminated single QDs or dye molecules [185]. These limited dark periods constitute a considerable disadvantage for single-molecule spectroscopic applications, but they are not observed for an ensemble of many quantum dots [179], like the one presented in this work. After a number of cycles of excitation and back relaxation to the ground state, both fluorescent dyes and QDs undergo irreversible modifications in the energetic structure such that the electronic transitions leading to fluorescence do not occur anymore. This permanent loss of capacity of fluorescence is called photodegradation or photobleaching [162]. QDs are highly resistant to bleaching compared to typical organic fluorophores [186] and their photo-stability can be optimized for long-term use [187, 188, 189, 190].

In particular, core-shell CdSe/ZnS quantum dots (QDs) are highly fluorescent systems compared with organic dyes [125]. The ZnS shell plays a crucial role in their emission properties; it decreases non-radiative pathways associated with the trapping of the electron or the hole generated after the absorption of light by the CdSe core [191]. Fluorescence QY

of properly surface-passivated CdSe QDs are in most cases high in the visible light range (400 – 700nm) with values of [0.65 – 0.85] [192, 193]. In addition, the shell enhances the chemical- and photo-stability of the QDs. CdSe/ZnS nanoparticles are further passivated with organic ligands to allow them to remain stable when diluted in organic solvent or mixed within host materials [125].

5.2 Selection Of Materials

The materials selection and the development of the manufacturing process to realise flexible waveguides with the integration of QDs into their core required a deep study. The first step involved the selection of QDs. Semiconductor quantum dots (SQDs) have emerged as potential candidates for many optoelectronic and photonic applications [194, 195]. Among several types of SQDs, CdSe has been widely studied because of its tunable luminescence can cover the full visible wavelength range and because of advances in synthetic methods [196, 197].

The quantity to be analysed in the current application is the photoluminescence spectrum and its modulation in response to a force applied. In order to obtain a good signal-to-noise ratio, it is fundamental to have high QY which consequently allows to get high photoluminescence intensity.

In this regard, it should be noted that the quality of the QDs surfaces influences their performance, as detailed in section 2.4. In particular, surface defects that include dangling bonds can create sites where non-radiative recombinations can occur, deteriorating optical properties such as QY. In order to overcome these detrimental effects, it has been found that the encapsulation of QDs by shells improve their performance with respect to bare QDs. This is the case of CdSe/ZnS core/shell QDs, for which the shell has been reported to enhance the QY and photoluminescence intensity with respect to CdSe QDs [191, 198, 199].

The formation of a shell has additional advantages, such as preventing the release of the non-environmentally-friendly heavy metals [126], which is a fundamental aspect to ensure biocompatibility and suitability of the proposed sensing technology to MIS applications. For all of these reasons, the attention was focused on this type of QDs. Further considerations were done for the selection of the photoluminescence emission of these QDs.

The light source available at that time for the experiments was a laser with emission centred at 532nm. Optical properties, lead time and costs have driven the choice to the

company PlasmaChem focused on nanomaterials production and related technologies. The supplier suggested to select the photoluminescence emission at least 30 nm longer than the excitation wavelength. Therefore, photoluminescence emission around 560nm were considered.

In addition, as explained in section 2.4, the QDs luminescence emission is size-tunable, i.e. it can be modulated by controlling the nanocrystal size. However, the sizing can compromise the QDs efficiency in converting the excitation light into fluorescence, i.e. QY.

In the specific case of CdSe/ZnS QDs produced by the selected supplier, QDs with photoluminescence emission peak included in the range [530 – 580]nm usually have higher QY (from 30% up to 80% depending on the batch); while QDs with emission peak outside of the previous range, i.e. < 530nm or > 580nm, typically have lower QY. In particular, the supplier assessed that their CdSe/ZnS QDs with the highest QY are usually those with photoluminescence emission at 550 – 560nm. Therefore, CdSe/ZnS QDs with photoluminescence emission centred at 560nm were selected. The same type of QDs with emission centred at 610nm were also tested and used when the previous type ran out and was not available in stock from the supplier.

Important requirements for the core material selection are the optical properties needed to ensure light transmission, such as transparency and suitable refractive index. But in addition to this, it should be a proper matrix material, i.e. a component that holds the filler (QDs in this case) together. Polymer materials can be suitable hosts for QDs integration because of their easy processability, in addition to presenting other advantages such as light weight, flexibility, biocompatibility, low cost and high optical transparency [200, 201, 202]. The compound resulting by the combination of two constituent materials, which are the QDs mixed into the polymer, forms a so called composite material.

Initially, the soft polymer material (Polymer System Technologies Ltd, LS1-3252) used for the core of the waveguide structures presented in Chapter 3 was considered as matrix material. However, a deeper study has revealed the chemical incompatibility of this material with the QDs.

Polymers are macromolecules built up by linking a large number of much smaller molecules together. The small molecules that combine with each other to form polymer molecules are termed monomers, and the reactions by which this combination process occurs are termed polymerisations [203]. Polymerization catalysts are substances used

to regulate the incorporation of one or more monomers into a polymer chain [204]. The material LS1-3252 was polymerised using Platinum as catalyst. The presence of this element makes this polymer incompatible with QDs, because Platinum reacts chemically with the QDs destroying them.

Alternative materials were searched in the literature and it was found that composite films were produced by using CdSe/ZnS QDs integrated into a Polymethyl methacrylate (PMMA) matrix [205]. Even if this publication was focused on the realisation of thin films, the use of PMMA was found particularly interesting because this material is widely used for the production of commercial plastic optical fibers (POFs). POFs are extensively employed in local area networks and automotive applications, due to their advantages comparing to glass (silica) optical fibers (GOFs), namely low production costs, ease of optical coupling and flexibility [206, 207].

For these reasons, the process for the manufacture of QDs-PMMA composite films was taken as starting point and re-adapted to the manufacture of optical waveguides.

PTFE was used as cladding material, analogous to the waveguide structures presented in Chapter 3. In this case, clear and flexible PTFE sleeves with circular section were employed as cladding for the realisation of flexible optical waveguides. These PTFE hollow pipes lend itself to the core material injection into their central bore. Different bore diameters have been selected and tested: 0.71mm, 1.01mm, 1.91mm and 3.05mm.

5.3 Manufacturing Process

The main material being used to create the core was PMMA powder (Polymethyl methacrylate, average M_w 120,000 by GPC, Sigma-Aldrich). The typical refractive index value is around 1.50 at 500nm for PMMA and 1.38 at 500nm for PTFE. The PMMA powder was diluted in the organic solvent DMF (N,N-Dimethylformamide, anhydrous, 99.8%, Sigma-Aldrich) at 22wt%. The solution was mixed with a stirrer at 1100rpm for about 5 hours. The core-shell CdSe/ZnS QDs with emission wavelength of 560nm (powder form, PlasmaChem GmbH) were diluted in toluene (Anhydrous, 99.8%, Sigma-Aldrich) with a mass concentration of 5mg ml^{-1} . QDs were added to the polymer solution in the concentration of 0.06wt% and mixed for 30min using the stirrer. The final solution was placed in the ultrasonic bath for 15 minutes to degas. Then the polymeric composite material was injected into a PTFE tube using a syringe. The filled tube was left to dry for 24 hours at room temperature and then for 72 hours at 60°C in the oven. The steps of the

manufacturing process are outlined in fig. 5.2.

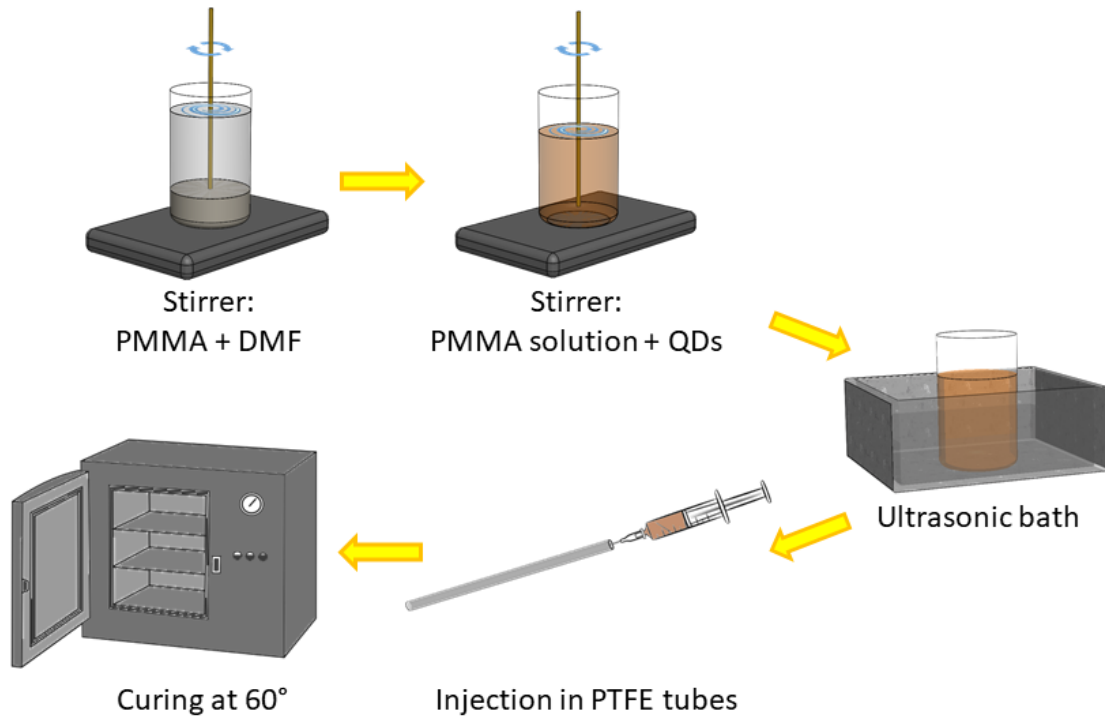


Figure 5.2: **Waveguide manufacturing process.** The PMMA powder is diluted, QDs are added and mixed together, the solution is left in a ultrasonic bath for air bubbles removal and then injected into PTFE tubes. The waveguide is left curing at 60°.

PMMA is a tough material; however, part of the solvent was still not evaporated within the PTFE sleeves after the curing process. The resulting polymeric composite material containing QDs has a low viscosity soft gel-form, which allows to get flexible waveguides. To prevent any further evaporation effect of the solvent and to confer stability to the core material composition, two optical fibre pieces of 1cm length was inserted at the input and output of the PTFE tube and they were tightly fixed into the PTFE bore using some thread sealant tape. The fibre was selected so that core diameter and refractive index were similar to the waveguide core to minimise the light losses due to the refractive index changes at the interface between the optical fiber and the waveguide core. The resulting prototype is shown in fig. 5.3.

Due to the low concentration of QDs embedded into the waveguide core, it can be assumed that the nanoparticle integration does not affect macroscopically the refractive index of the core, therefore the requirements for the light transmission through the waveguide are satisfied.

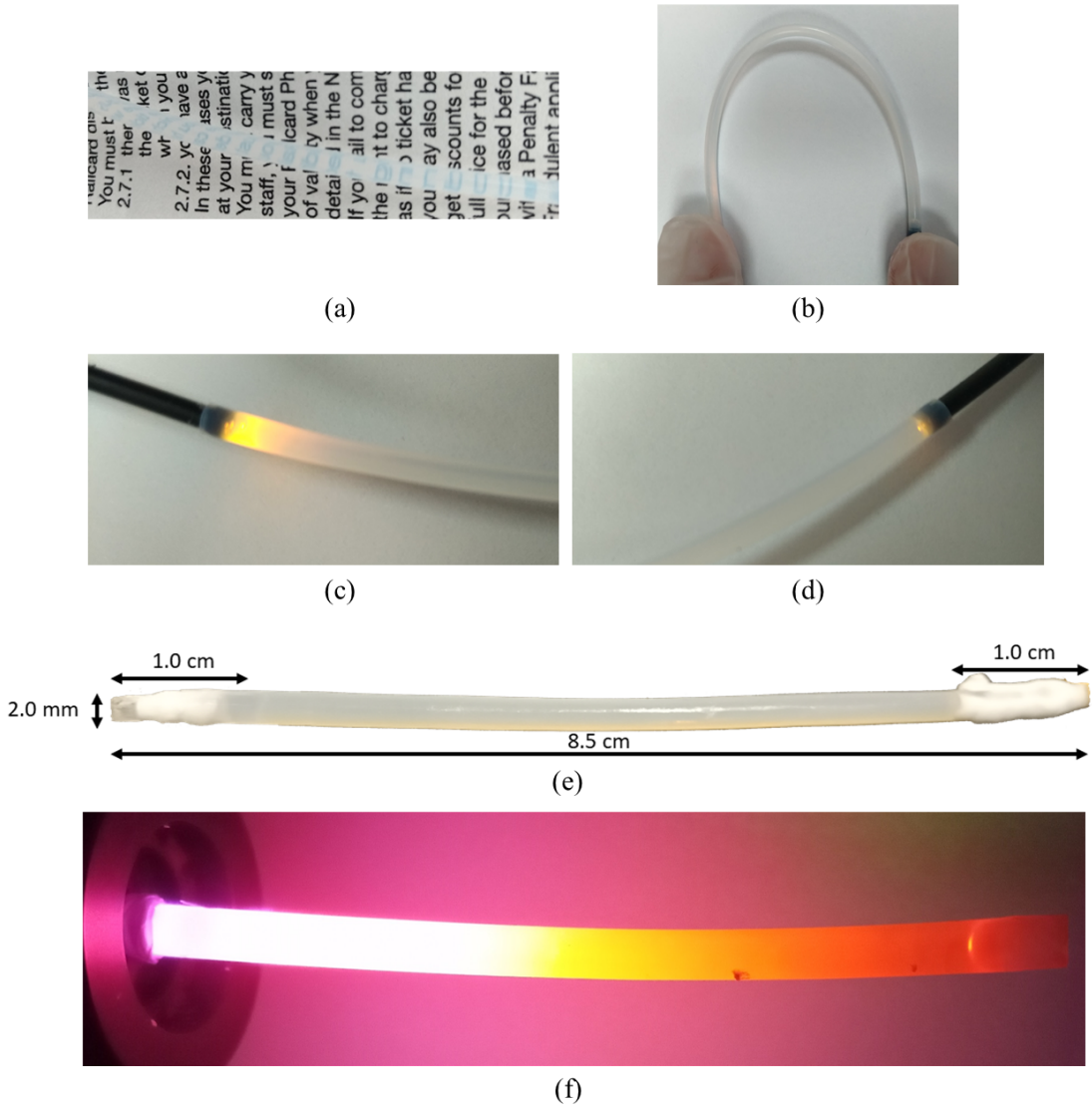


Figure 5.3: **Waveguide prototype.** The plain waveguide (without QDs integration) is (a) transparent and (b) flexible. (c) The light injected at the input is transmitted through the waveguide and (d) reaches the output. (e) Final design of QDs-PMMA composite waveguide. (f) Fluorescence emission of the composite waveguide irradiated with UV light.

The fabrication process of the plain optical fibre (not containing QDs) follows the same procedure as described above, except the phase of QDs integration. The final QDs-PMMA composite waveguide is presented in fig. 5.3e-f.

5.4 QDs-PMMA Composite Waveguide Photostability

The output spectrum of a plain waveguide was compared with the output spectrum of a PMMA-QDs composite waveguide fabricated as described in section 5.3. The acquisition

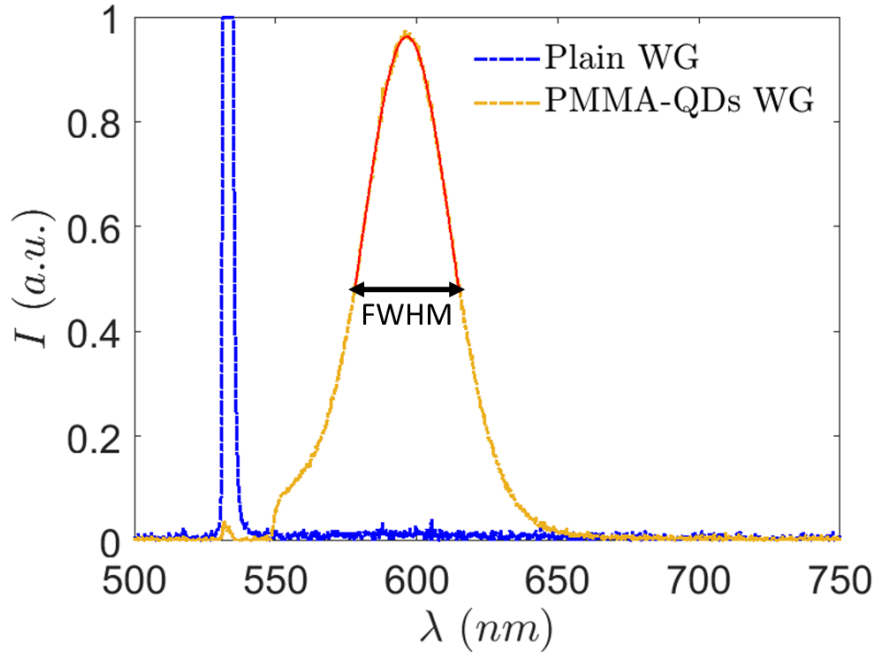


Figure 5.4: **Plain VS QDs-PMMA waveguide (WG).** Output spectrum of a plain waveguide (without integration of QDs) and a QDs-PMMA composite waveguide. The photoluminescence emission is clearly visible in the latter (yellow peak stretching over the range $[550 - 650]nm$).

was performed using a collimated green laser with emission peak at $532nm$ (Thorlabs, CPS532). A proper lens was placed in front of the output facet of the waveguide to collimate the beam and a longpass filter (Thorlabs, FELH0550) with cut-on wavelength at $550nm$ was used to filter out the light source. A second lens was used to focus the light which was collected by a spectrometer (Thorlabs, CCS200/M). For both the acquisitions, the same integration time of $1s$ was set on the spectrometer to get a good QDs signal-to-noise ratio.

In the case of the plain waveguide (not containing QDs), some laser light (peak around $532nm$) still reaches the spectrometer despite the presence of the long-pass filter, since scattering and absorption effects related to QDs do not occur in this waveguide. Also, the long integration time, required to detect the QDs signal, brings the laser peak to saturation, while the rest of the spectral profile on the range $[540 - 750]nm$ is flat (blue spectrum in fig. 5.4).

In the doped waveguide instead, the most of the laser light is absorbed by the QDs and eventually re-emitted at longer wavelength. The result is a spectral distribution stretching on the range $[560 - 640]nm$ (yellow spectrum in fig. 5.4).

As mentioned in section 5.1, photobleaching is the permanent disappearance of the

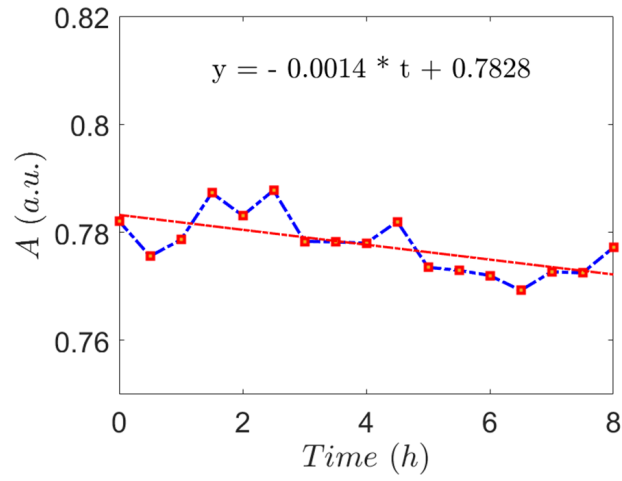
luminescence emission. To quantify this effect and determine its influence on the photostability and performance of the proposed technology, the QDs-PMMA composite waveguide was continuously irradiated by the green laser for 8 hours. The output spectra were acquired at intervals of 30min. Since the spectrum does not follow a perfect Gaussian distribution because the left tail is cut off by the long-pass filter, while the QDs emission is typically slightly asymmetric with a longer tail on the right hand side, the full width at half maximum was determined and a Gaussian fit was applied on the part of the spectrum above this value as shown in fig. 5.4 (red line). The amplitude values of these Gaussian fitting curves are plotted in fig. 5.5a. The amplitude decreases over the time following a linear trend. Looking at the photobleaching measurement obtained for the sensing prototype employing fluorescent dyes presented in section 4.4.3, it could be observed an amplitude decrease of about 1% after two hours. Following the linear fitting curve obtained for the QDs-based waveguide, instead, the amplitude reduction after two hours is $\sim 0.36\%$, that is almost 3 times lower than the one obtained for the fluorescent dyes.

A direct comparison with the literature was not possible because the photostability critically depends on the environmental and excitation conditions [208]. However, typical behaviours of the PL signal from CdSe/ZnS QDs integrated in PMMA films under continuous irradiation by $80\text{kW}/\text{cm}^2$ of a laser of 514.5nm in a vacuum are presented in [209]. In this particular conditions, the photoluminescence intensity drops by more than 40% in the first 10min of illumination and then continues to drop on a slower rate over the time of exposure.

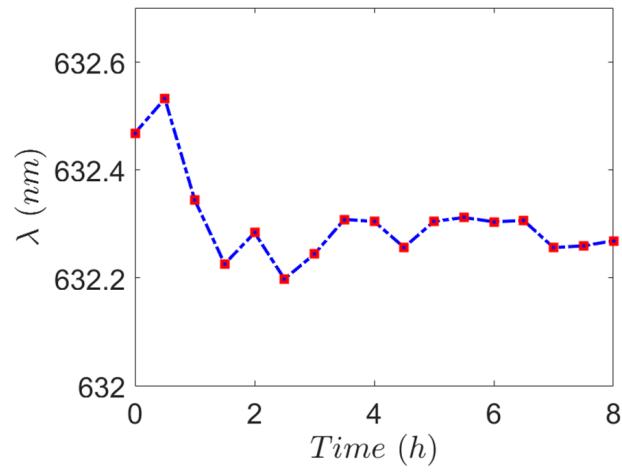
Among the conditions affecting the photobleaching time, one of them is the excitation intensity: QDs photobleach faster if the excitation intensity is increased. The light used to irradiate the waveguide is $\sim 65 * 10^{-6}\text{kW}/\text{cm}^2$ which corresponds to 6 order of magnitude lower than the irradiation flux used in [209]. This can be one of the main reasons of the much longer photobleaching time measured on the waveguide respect to the one reported in literature.

From the same spectra acquired every 30min by continuously irradiating the QDs-PMMA composite waveguide for 8 hours, also the centroid location values of the Gaussian fitting curves of the spectra were analysed and reported in fig. 5.5b. The trend presents an initial blue-shift (lower than 0.4nm) over the first hour and a stable behaviour over the lasting 7 hours of acquisition.

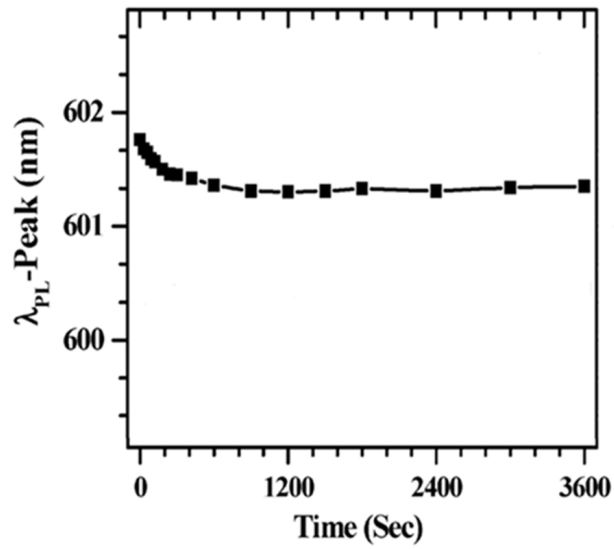
The trend reported in literature [209] and shown in fig. 5.5c looks very similar to the one



(a)



(b)



(c)

Figure 5.5: **Photobleaching of QDs-PMMA composite waveguide.** (a) Amplitude and (b) wavelength decrease across the time. (c) Measure of wavelength decrease across the time from literature [209].

measured on the QDs-PMMA polymer waveguide as shown in fig. 5.5b. In fact, data obtained for CdSe/ZnS QDs polymer films continuously irradiated and kept under inert atmosphere show that the photoluminescence wavelength is insignificantly shifted to the blue side (less than 0.4nm , in accordance with the initial shift obtained for the waveguide) over the first phase of acquisition and then stabilises over the course of the experiment.

At ambient conditions surface oxidation effects usually happen on the CdSe/ZnS QDs even without intense excitation leading to a photo-induced oxidation effect [208]. This is caused by oxygen diffusion through the ZnS shell, determining the size reduction of the CdSe core because of the oxidation. Because of the size-dependent effect, the photoluminescence emission shows a continuous blue shift due to the fact that the core became smaller. This photooxidation process is accelerated by laser irradiation. It was verified that oxidation effects in quantum dots can be removed with the use of PMMA as a host [210]. When QDs are embedded in PMMA, there are no oxidation effects and there are no spectral shifts caused by illumination [179, 211]. Looking at the result in fig. 5.5b, it was verified that no photooxidation effects were observed on the PMMA-QDs composite waveguide.

5.5 QD Luminescence Modulation Under Compression

A force applied on a QD determines the displacement of the carriers within the atomic structure of the material, as explained in section 2.4.3. This carrier displacement generates a piezoelectric potential E_p , which alters the luminescence of the QD. The model describing this effect follows the quantum mechanical analysis of piezoelectric effect from Zhang et al [212]. Since the ZnS shell of the quantum dots do not drastically alter the energy level structure [213], the model developed considering bare CdSe QDs was considered applicable also to CdSe/ZnS QDs.

The strain-induced piezoelectric potential E_p causes the electron states to shift to lower (or higher) energies and the hole states to shift to higher (or lower) energies, so the bandgap is increased (or reduced) due to the Coulombic repulsion (or attraction) between the electron-hole pair of the exciton [212]. This bandgap variation leads to a redshift (or blueshift) in the luminescence. E_p can be defined as follows:

$$E_p = 24 \left(\frac{2}{3\pi} \right)^6 \frac{e^2 E^2 m_{e,h} (2r)^4}{\hbar^2} \quad (5.2)$$

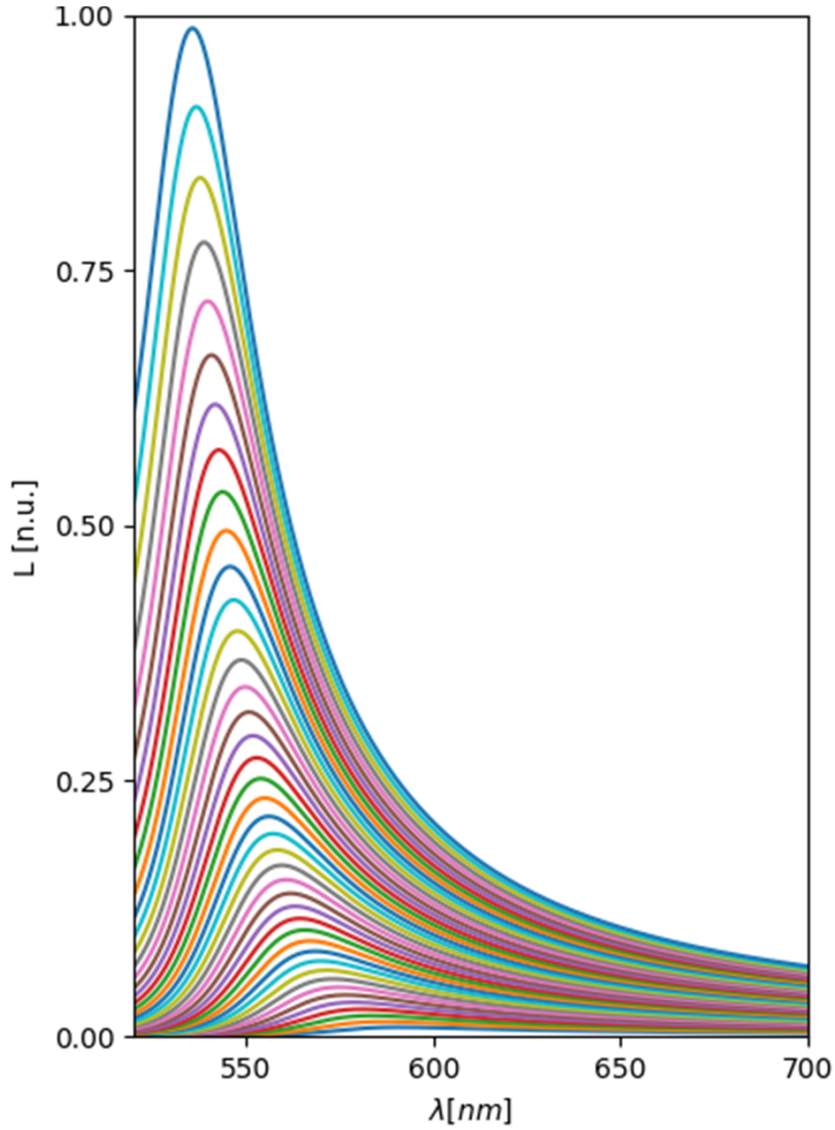


Figure 5.6: **Single QD photoemission spectra.** Normalised emission spectra of a single QD: the feature blue-shifts and increases in amplitude under compression.

where e is the electron charge, E denotes the piezoelectric field, \hbar is the reduced Planck's constant, $m_{e,h}$ represents the effective masses of the electron and hole, respectively, and r is the approximate radius.

The normalised single QD emission spectra resultant from the model are illustrated in fig. 5.6, showing the increase in emission amplitude and the blue shift in wavelength as the compressive force increases. The general trend of amplitude modulation and wavelength shift over the force is expressed as arbitrary unit.

5.6 Ray Tracing Simulation

The light transmission in the PMMA-QDs composite waveguide was modelled through a ray tracing simulation developed using the open source software pvtrace [214]. The emission spectrum associated to each QD contained in the waveguide was deduced by the results obtained for the single QD. The ray tracing approach was already employed in the literature to model absorption and scattering effects of light travelling within a matrix of QDs [215, 216, 217].

The waveguide was split into three separate simulation segments, dimensions $50 \times 50 \times 50 \text{ nm}$ each with refractive index of $n_{PMMA} = 1.50$ (measured at 425 nm[218]). Each segment was surrounded by a cladding layer along the length of the waveguide, with refractive index of $n_{PTFE} = 1.38$ (measured at 425 nm[148]) and thickness of 10nm. Each segment also contains spherical structures of refractive index[219] $n_{CdSe} = 2.64$ (radius = 1.5nm, consistent with the manufacturer values, PlasmaChem, PL-QD-O-560) distributed in a cubic mesh manner with inter-QD distance of 10nm. These spherical structures play the role of the QDs suspended in the waveguide, and contain absorption and emission spectra corresponding to the resting condition where the only force sensed by the QDs is due to their integration in the PMMA matrix. These spectra were calibrated through matching the simulation results with experimental observations. The second and third segments contain simulated QDs with different spectra, consistent with a further externally applied force. The rays are generated in a spherical cone distribution of 30° at the beginning of the first segment, with wavelength of 425nm.

The ray tracing simulation takes several types of events into account as a ray approaches any interface between objects; the ray could be reflected and adopt a new direction of propagation, or transmitted at angle due to the difference of refractive indices at the interface. The ray could also be absorbed, corresponding to the absorption spectrum of a QD. Finally after being absorbed into a QD, the ray has a likelihood of being emitted from a QD with a new wavelength and propagation direction.

The percentages of final outcome of the rays for a sample ray tracing simulation of five million rays, at ambient waveguide conditions, are shown in fig. 5.7a. The outcomes are split into four categories: all rays that have not been absorbed or emitted by a QD, and are transmitted through the detector-end interface between the simulated waveguide core and vacuum are shown as a part of the 'Detector' category in blue. Rays that have not been absorbed or emitted by a QD, and are not transmitted through the waveguide core/

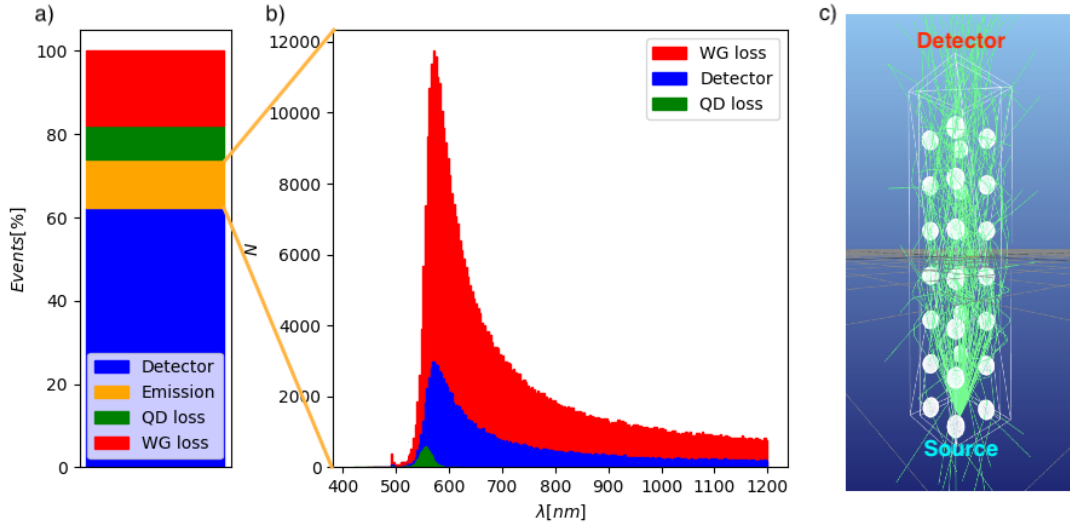


Figure 5.7: **Ray-tracing outcomes.** a) Stacked bar chart illustrating the breakdown of ray tracing events. b) Stacked histograms resolved in wavelengths showing the further split of the 'Emission' events in a) with a force of 6 nN applied on the quantum dots of the middle waveguide segment. c) Wireframe structure diagram of a scaled down example of the ray tracing simulation.

detector interface are depicted in the 'WG loss' category in red, indicating that the rays have been lost due to transmission through the waveguide cladding into simulated vacuum. The rays that have been absorbed by a QD, and are not re-emitted due to the QY of the QDs (estimated at 60%) are shown in green as 'QD loss'. Lastly, all rays which have been emitted by a QD are classified in the 'Emission' category in orange.

The 'Emission' rays are further split into three wavelength resolved outcome categories in fig. 5.7b, where the classification of ray categories follow those of fig. 5.7a, but all rays have been emitted by a QD.

A comparison between the ratio of 'Detector' rays in fig. 5.7a and 'Detector' rays in fig. 5.7b informs us that we are in the regime where the detector senses an order of magnitude more light-source wavelength rays than QD emitted (or signal) rays, consistent with the experimentally observed ratios where the light-source wavelength is detected as a saturated peak. Moreover, a significant amount of simulated rays are lost through the 'WG loss' categories. This is due to ray being scattered or emitted by QDs at angles with large perpendicular components with respect to the length of the waveguide. This allows for the possibility where rays propagate to the cladding at an angle greater than the critical angle θ_c , whereby the ray is transmitted through the cladding and are lost. This phenomena also explains the significantly larger ratio of 'WG loss' in fig. 5.7b, where the rays have been

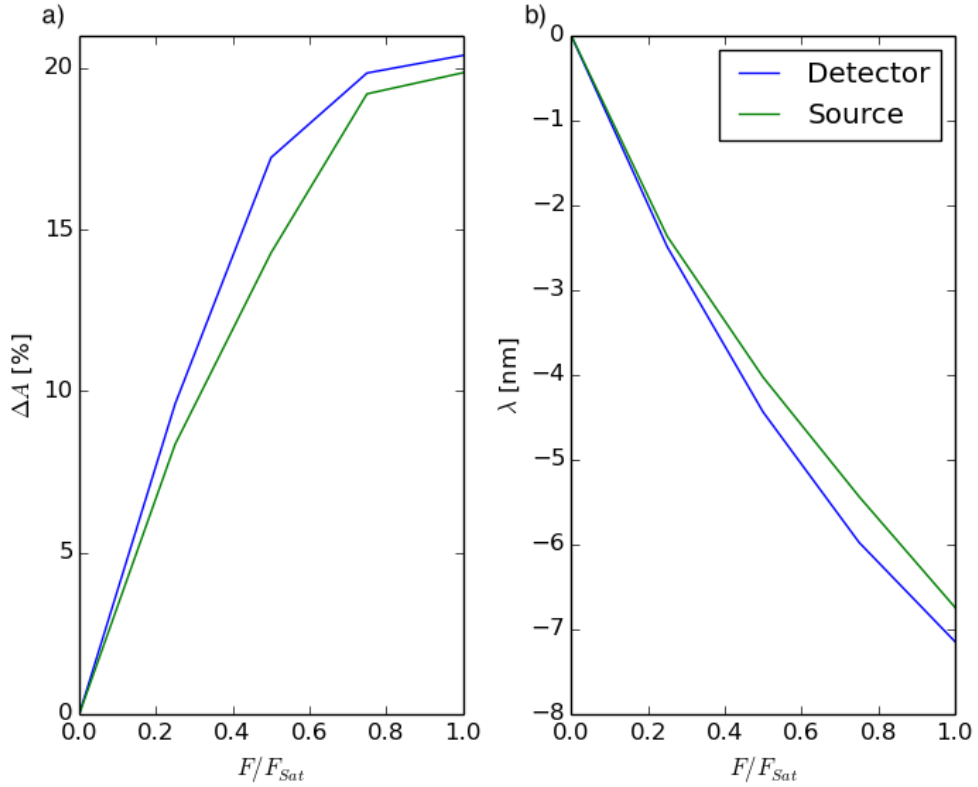


Figure 5.8: **Simulated trend of the intensity and wavelength.** a) Theoretical amplitude of the photonic distribution measured at the detector as a function of the applied force, where the latter is applied near the detector (source) and labelled in blue (green). The applied forces (F) are normalised by the saturation limit (F_{sat}). b) Wavelength shift of the maxima of the distribution's peak, as a function of waveguide compression.

emitted by QDs, compared to 'WG loss' in fig. 5.7a, where the rays have not been emitted by QDs and are likely to propagate with a large parallel component with respect to the length of the waveguide.

The simulated piezoelectric driven emission was fitted using a skewed Gaussian trend. The corresponding amplitude and wavelength shift of the fitting curve are shown in fig. 5.8a-b as a function of compressive force applied onto the middle waveguide segment (green) and last waveguide segment (blue). The percentage increase (ΔA) of the amplitude is evaluated with respect to the resting condition (no force applied on the waveguide). The range of forces considered are normalised to a saturation force F_{sat} , where the amplitude increase of the signal saturates.

Intensity and wavelength trends are more pronounced for the 'Detector' simulations. This effect may be related to the likelihood of a QD emitted ray to become scattered out of the waveguide (WG loss), or be absorbed (QD loss) and re-emitted by a subsequent QD;

the closer to the detector this compressive force is applied, the less likely that the signal information is overwritten by these effects from a subsequent QD.

5.6.1 Experimental setup

A sketch of the experimental setup is shown in fig.5.9.

The optical fibres, firmly fixed inside the PTFE tube using some thread sealing tape, were further anchored to the experimental desk using some metal plates. When a force is applied on the waveguide, the two optical fibres assume the role of stoppers and keep the soft material of the waveguide under compression.

A collimated laser diode ($\lambda_{em} \sim 532 \text{ nm}$, 4.5 mW, Thorlabs) injects light into a cylindrical polymer waveguide of 8.5 cm length and diameter of 2.5 mm. A long-pass filter ($\lambda_{cut-on} \sim 550 \text{ nm}$, Thorlabs) was placed at the output of the waveguide to filter out the light coming from the laser and isolate the signal emitted by the QDs. The output signal is collected by a lens telescope and sent to the spectrometer (Thorlabs, CCS200/M). A 6-axes force/torque sensor (ATI Nano-17, resolution 0.003 N) was mounted on a manual translation stage (Thorlabs, resolution 10 μm) which was moved downwards to progressively compress the waveguide. A circular probe of 8 mm diameter mounted on the calibration force sensor was used as compression probe (fig. 5.9).

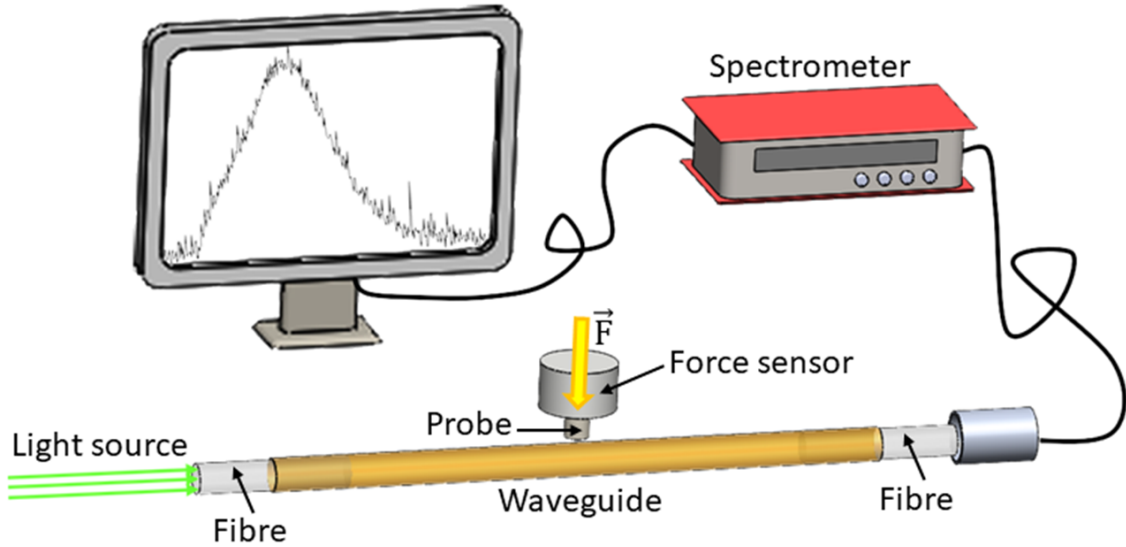


Figure 5.9: **Schema of the experimental setup.** A probe mounted on a calibration force sensor apply a pressure on the waveguide at different distances from its input surface. The modulation of photoluminescence emission is detected by a spectrometer.

5.6.2 Experimental results

The emission observed in fig. 5.4 for the PMMA-QDs composite waveguide is identifiable as the piezoelectric emission, showing its characteristic properties as predicted by the single QD model: skewed blue with a trailing edge towards red.

A calibration experiment was carried out to determine the characteristic trend of intensity and wavelength modulation as a function of the force applied on two different locations of the waveguide: 3 cm and 4 cm from the input surface of the waveguide. The force applied covers the range [0-12] N, with a step of 1 N. The maximum value of 12 N is the mechanical limit imposed by the experimental setup in use and the amplitude corresponding to this force value was used as normalisation factor. The integration time of the spectrometer was set to 5 s. For each force value, 10 repeated spectra were acquired. A Gaussian fit was applied on each one of the 10 spectra, then the mean of the coefficients was calculated to get the final Gaussian fit for each force value. The amplitude coefficient of the final averaged Gaussian trend was considered to get the modulation of the peak amplitude of the signal (fig. 5.10a), and the wavelength shift as a function of force (fig. 5.10b). The error bars were calculated as standard deviation on the 10 repeated measurements for each force value. Results in fig. 5.10a show a linear trend between [0-5] N with $R^2 \sim 0.98$; the rest of the trend still presents a linear behaviour with a different slope. Also in fig. 5.10b a linear trend is observed: although the standard deviation error bars are quite large with a maximum value of ± 0.03 nm, the mean values follow the fit line pretty well with $R^2 > 0.97$. Both intensity modulation and wavelength shift corresponding to the pressing location at 4 cm are more pronounced and this is in accordance with the simulation results. This result is related to the likelihood for a QD emitted ray to be scattered out of the waveguide or absorbed (but not re-emitted) or absorbed and re-emitted by a subsequent QD. For QDs further from the waveguide output, these effects are more likely, causing light loss and then a lower light intensity detected at the output, as well as a less pronounced blue-shift. The different slopes obtained for both amplitude and wavelength suggest the possibility to distinguish between the two pressing positions along the waveguide combining the measurement of the two parameters. The black error bars take into account the signal drift occurring during the acquisition time for each force value.

An additional experiment was carried out to measure the signal drift under a constant pressure over the time. The waveguide was kept compressed for 90 minutes and the output spectrum was acquired every 5 minutes. The exponential decay of the amplitude over the

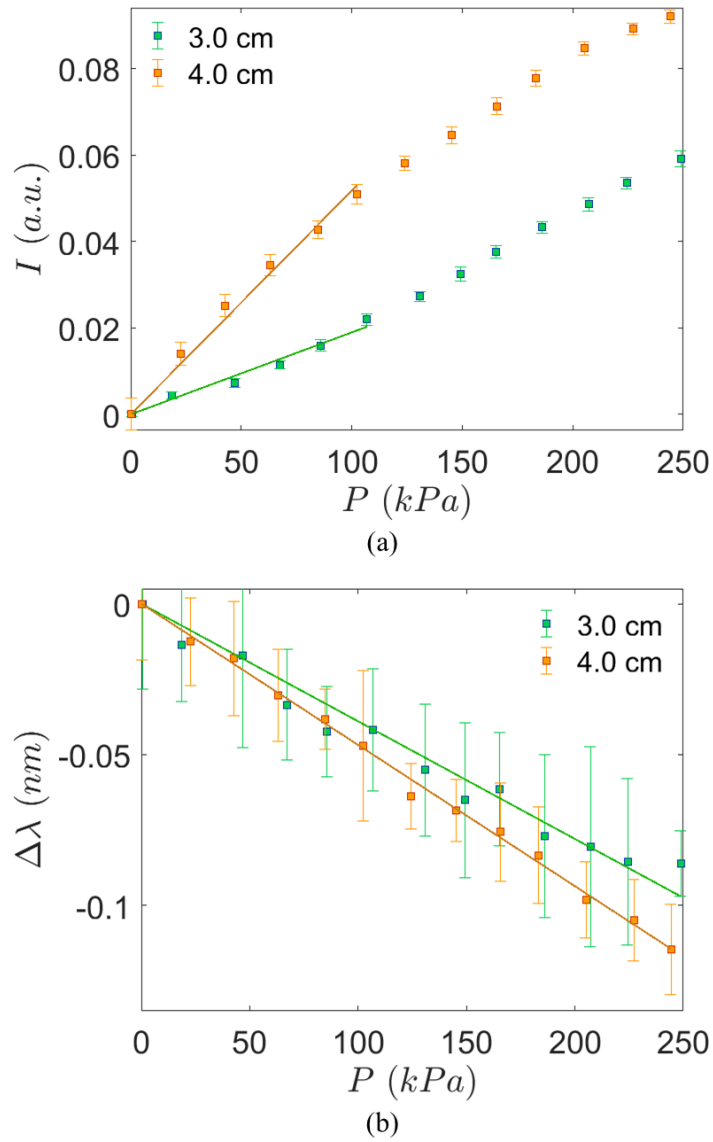


Figure 5.10: **Amplitude modulation and wavelength shift calibration.** The waveguide was compressed on two different locations: 3 cm and 4 cm from its input surface. For each force value, amplitude modulation a) and wavelength shift b) were measured.

time suggests that the polymeric soft material of the waveguide core is subject to a stress relaxation effect. The time dependency of amplitude and wavelength of the output signal has been measured applying a constant pressure on the waveguide and the spectrum was monitored for 90 minutes. Results (fig. 5.11) show that both amplitude and wavelength move towards a plateau after about one hour and an half of acquisition. The black error bars were added to fig. 5.10 to take into account this relaxation effect occurring during the acquisition time for each force value.

The exponential decay observed in fig. 5.11a can be explained by the viscoelasticity of polymer materials which show a combination of elastic and viscous behaviour. An

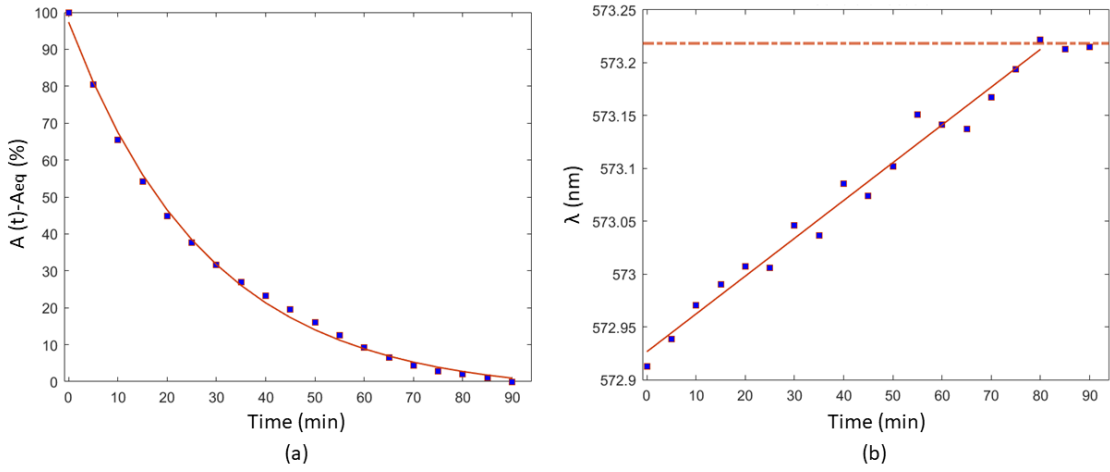


Figure 5.11: **Time-dependent relaxation of the polymer waveguide.** a) The amplitude modulation $A(t)$ shows a negative exponential behaviour, typical of stress-relaxation in viscoelastic materials. b) The wavelength shift presents a linear fashion.

immediate consequence of viscoelasticity is that deformations under stress are time dependent. If a constant deformation is imposed then the induced stress will relax with time. Several polymeric materials show a linear viscoelastic behaviour, such that the stress (at a constant strain) decreases in time as a simple exponential Debye function:

$$\sigma(t) = \sigma_0 \exp^{-t/\tau} \quad (5.3)$$

The time constant τ is the relaxation time at which $\sigma(t)$ decays to the value $1/e$ of its initial value σ_0 [220].

Although it was not possible to determine how the force applied on the waveguide translates to the force sensed by each single QD in the waveguide, the overall phenomenon described by the simulation analysis is confirmed by the experimental results, leading to the same modulation effect of the analysed light properties.

Both in the experimental and simulation results, the trends are more pronounced when the force is applied closer to the detector. This can be explained by the fact that the closer to the detector this compressive force is applied, the less likely for a QD emitted ray to be scattered out of the waveguide, or absorbed and not re-emitted (these two events would reduce the amplitude variation), or to be absorbed and re-emitted by a subsequent QD (this event would reduce the wavelength variation). This observation suggests that not only the pressure can be detected, but also the location of the applied force can be obtained, as both light amplitude and wavelength are affected differently through the scattering process.

5.7 Spectral Characterisation

A preliminary measurement was done to study the light absorption on the range $[350 - 550]nm$ through a sample of QDs diluted in toluene. CdSe/ZnS QDs with photoluminescence emission centred at $610nm$ were used for this particular purpose. The solution was obtained as described in section 5.3 (a concentration of $5mg\ ml^{-1}$ of QDs in toluene). For the same reasons explained in section 3.3.3, absorption measurements along a broad wavelength range were performed by multiple acquisitions illuminating the sample with different small bands of wavelengths for each measurement, rather than by a single acquisition illuminating the sample with the full wavelength range, to minimise the influence of fluorescence, heating and thermochromism effects on the spectral measurements.

The full experimental setup is presented in fig. 5.12a. The spectrum of a broad range lamp (Thorlabs, SLS205, range $[240 - 1200]nm$) was splitted in wavelength subranges by the alternation of a series of band-pass filters at $355nm$, $405nm$, $450nm$ (FWHM bandwidth of $10nm$) and $532nm$ (FWHM bandwidth of $4nm$) placed in front of the lamp beam. The QDs-toluene solution contained into a cuvette was placed in front of the filter and the light path within the solution is $10mm$ (equal to width of the cuvette). The outgoing spectral distribution was measured by a spectrometer (Thorlabs, CCS200/M, range $200 - 1000nm$, FWHM spectral accuracy $< 2nm$ at $633nm$). The spectrometer in use was not provided with a radiometric power calibration and the spectral output was displayed in terms of normalised intensity. The normalisation to the range $[0 - 1]$ was performed by dividing the whole spectral distribution by the highest peak in the spectrum.

For each filtered wavelength range, a first set of measurements was acquired with the empty cuvette, while the cuvette was filled with the QDs solution for the second set of measurements.

In the first configuration (empty cuvette), the light measured by the spectrometer at each wavelength sub-range corresponds to the intensity emitted by the lamp and filtered out by the related filter. The normalised intensity measured in the first configuration is shown in fig. 5.12b). The coloured areas in the figure represent the excitation light sent on the QDs solution in the second configuration (filled cuvette) for each spectral sub-range. For each wavelength sub-range, the excitation light was absorbed according to the absorbance spectrum of the QDs at hand and the photoluminescence (red-shifted) spectrum was emitted consequently. This emission was acquired by the spectrometer and is shown in fig. 5.12c.

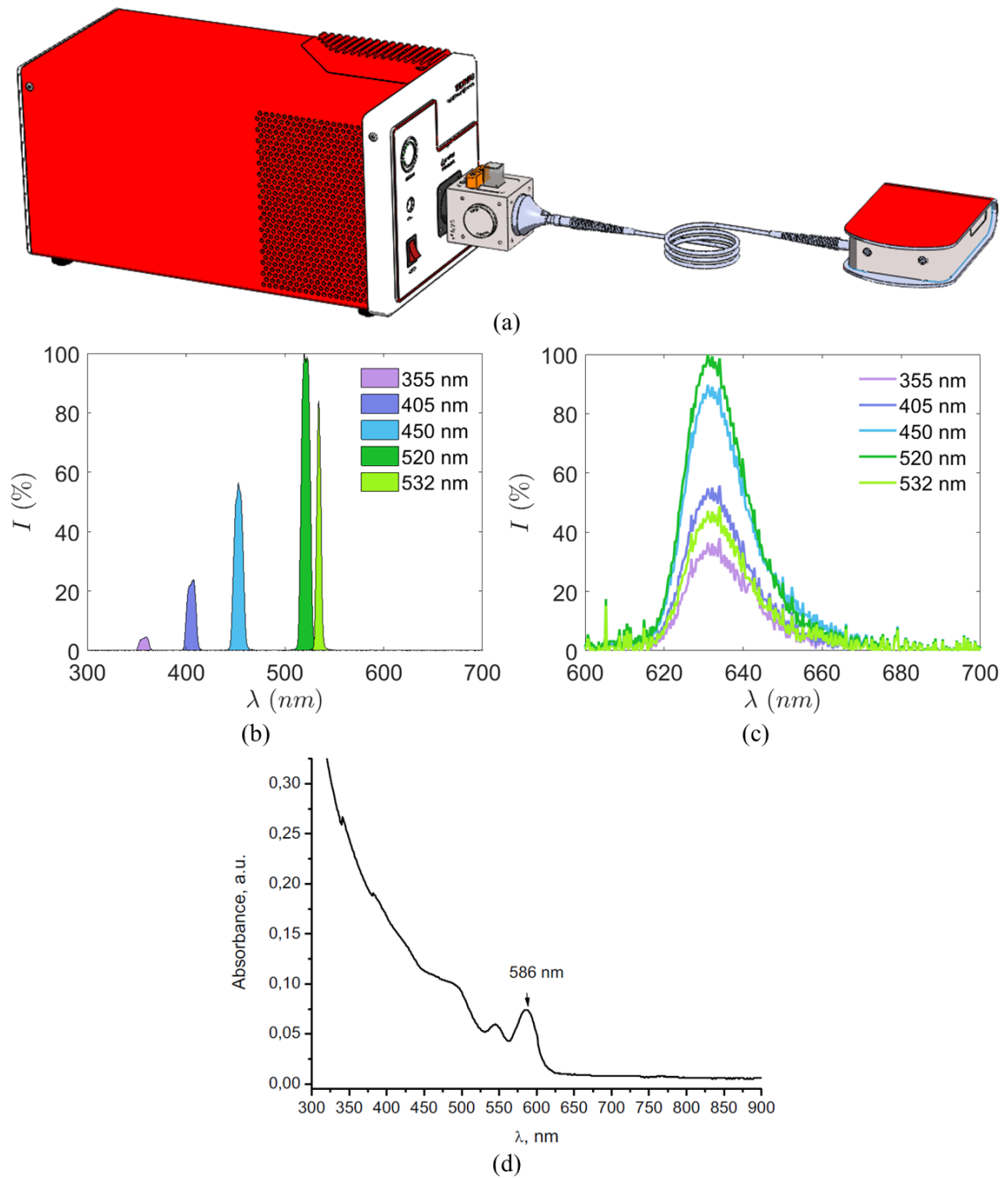


Figure 5.12: **Spectral characterisation of CdSe/ZnS QDs diluted in toluene.** (a) Experimental setup. (b) Normalised excitation spectra and (c) normalised emission spectra for each wavelength sub-range. (d) Absorbance spectrum of CdSe/ZnS QDs as provided by the supplier.

It can be observed that the emission spectrum corresponding to excitation light centred at 520nm shows the highest intensity respect to the others. However, it should be considered that the excitation light sent at 520nm has intensity higher than all the other wavelength sub-ranges. This is because the lamp emission is not uniform on its whole range ([240 – 1200]nm). In addition, the probability of light absorption across the wavelength should also be taken into consideration. In this regard, the supplier provided the

absorbance spectrum of the CdSe/ZnS QDs used and this is shown in fig. 5.12d.

Looking at the excitation spectra in fig. 5.12b, the intensity at 520nm is $\sim 98\%$, while it is $\sim 4\%$ at 355nm. Therefore, the intensity sent at 520nm is ~ 24.5 higher than the one sent at 355nm. However, considering the graph in 5.12d, the absorbance at 520nm is $\sim 0.04a.u.$ while the one at 355nm is $\sim 0.26a.u.$. This means that the probability for the light to be absorbed is ~ 6.5 times lower at 520nm than at 355nm.

Consequently, it can be expected to have an emission intensity $\frac{24.5}{6.5} = \sim 3.7$ times higher at 520nm than at 355nm. Looking at the emission spectra in 5.12c, the ratio between the peak at 520nm and the one at 355nm is ~ 3 , which is comparable with the expected value. It can be concluded that the measured emission spectra are in accordance with the expected absorbance spectrum for the considered type of QDs.

The absorbance spectra for CdSe/ZnS QDs with emission at different wavelengths were also provided by the supplier. However, they do not differ substantially from each other. Therefore, the considerations just made on CdSe/ZnS QDs with emission centred at 610nm regarding the absorbance are assumed applicable also to the same type of QDs but with emission peak centred at different wavelength.

A further experiment was carried out to verify how the wavelength of the excitation light affects the photoluminescence emission at the output of a waveguide containing QDs. The light was injected in waveguide with diameter of 3mm and 1cm length. Two collimated lasers were used alternatively, one with emission peak at 405nm (Thorlabs, CPS405) and one with emission peak at 532nm (Thorlabs, CPS532). The typical output power is $\sim 4.5mW$ in both the cases. The spectrum at the output of the waveguide was measured using a spectrometer (Thorlabs, CCS200/M) with an integration time of 10ms for both the light sources. The experimental setup is depicted in fig. 5.13a.

Results are shown in fig. 5.13b. The first sharp peak at 405nm for the first trend and at 532nm for the second trend corresponds to the amount of light source reaching the waveguide output, without being absorbed or scattered by the QDs (or any other impurity present in the waveguide). It can be noted that a much lower intensity of UV light reaches the waveguide output compared to the green light. This is because UV light is much more absorbed than green light by the QDs within the waveguide, according with the absorbance spectrum as reported in fig. 5.12d. So, it would be natural to think that if the absorption probability is higher in the case of UV light, consequently also the re-emission at longer wavelengths should be higher.

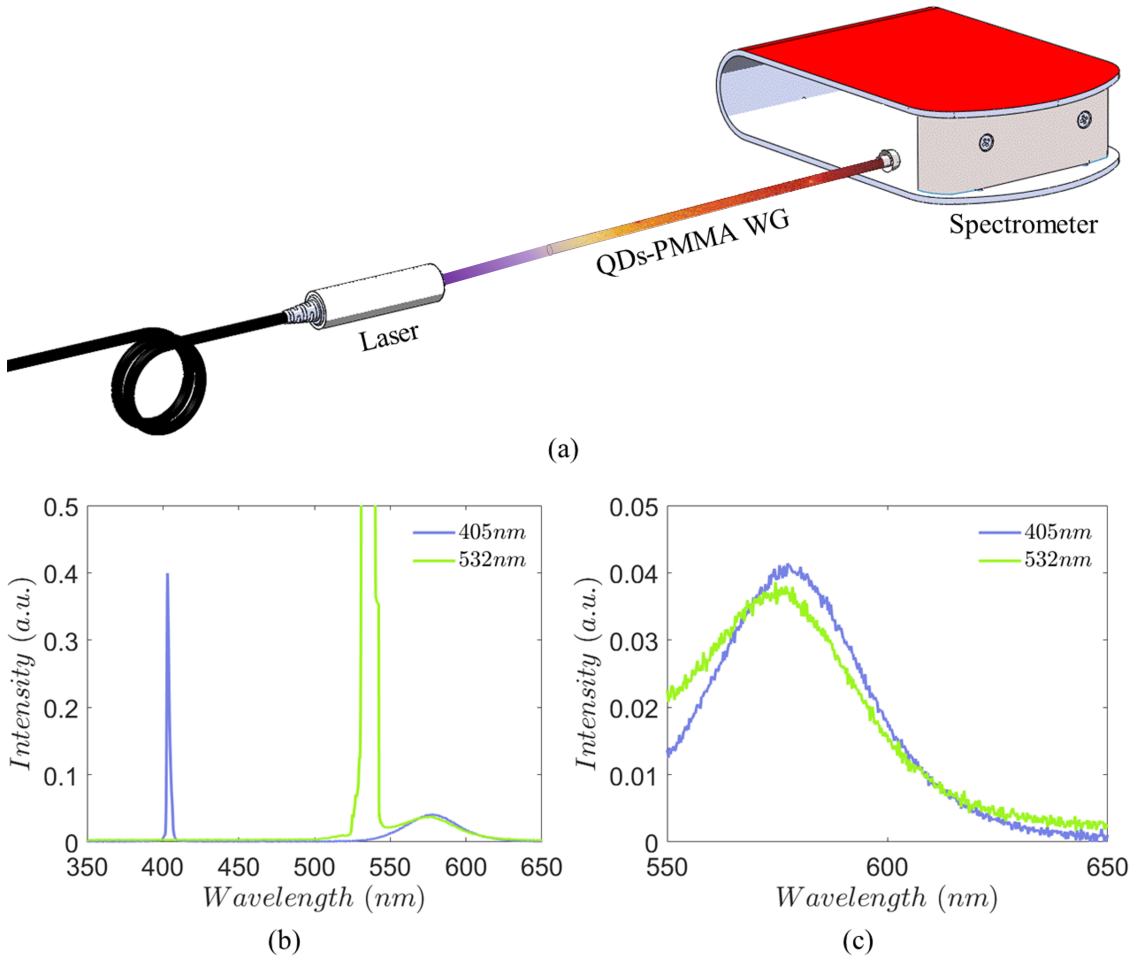


Figure 5.13: **Excitation light wavelength.** (a) Light is injected into the PMMA-QDs composite waveguide by a collimated laser and the spectrum is acquired by a spectrometer. (b) Output spectra obtaining by exciting the waveguide using two laser with different wavelength emission (at 532nm and at 355nm). (c) The photoluminescence peak is slightly higher when the UV light source is used.

Actually, this conclusion is not obvious, because, even if the UV light tends to be more likely absorbed after a shorter light path respect to the green light, the down-converted photoluminescence would be emitted by the QDs contained in the initial section of the waveguide and then this light signal should travel through the remaining part of the waveguide, avoiding scattering effects and not-radiative absorption effects from all the other QDs, before being detected at the output. Instead, in the case of green excitation source, the light is progressively absorbed through a longer light path and a larger quantity of down-converted photoluminescence is emitted closer to the output of the waveguide, and it can be scattered or lost less likely.

Looking at the zoomed sub-range [550 – 650]nm shown in fig. 5.13c, for this specific case of a waveguide of 1cm, the intensity of the emission spectrum corresponding to excitation

light at 405nm is higher than the case of excitation light at 532nm , presenting a difference of $\sim 7.5\%$. However, further experiments on waveguides with different length should be made to deduce additional considerations on this. For sure, wavelength of the excitation light, waveguide length and QDs concentration are quantities strongly related to each other and they are important design parameters to consider to optimise the emission signal and therefore the sensing efficiency of the proposed technology.

5.8 QDs Concentration In A Waveguide

Using a larger waveguide facilitates the light injection, and the signal at the output can be easily enhanced because, under the same QDs concentration, a larger waveguide contains a higher number of QDs per unit transversal cross-sectional area respect to a thinner waveguide. However, the ability to use a thinner waveguide can be relevant in order to miniaturise the single sensing unit (the waveguide itself) and have to possibility to add multiple waveguides and multi-channel waveguide structures to enhance the spatial resolution of the device. For this reasons, waveguides with different diameters have been tested.

As detailed in section 5.2, PTFE sleeves with circular section were employed as cladding for the realisation of flexible optical waveguides with length of 5cm each. These PTFE hollow pipes were selected with different bore diameters: 0.7mm , 1.0mm , 1.9mm and 3.0mm . The one of 0.71mm presented challenges in injecting the core material inside due to the small dimension of the inner channel and, once fabricated, no signal could be detected by the spectrometer at the output of this waveguide. So no further tests were carried out on waveguides of this size.

Instead, for each one of the other three diameter dimensions, four waveguides were fabricated with different levels of QDs concentration.

Specifically, the core-shell CdSe/ZnS QDs with emission wavelength around 560nm (powder form, PlasmaChem GmbH) were diluted in toluene (Anhydrous, 99.8%, Sigma-Aldrich) with a mass concentration of 5mg ml^{-1} . Then, QDs were added to the polymer solution in the concentration of 0.01wt\% , 0.05wt\% , 0.10wt\% and 0.20wt\% and mixed for 30min using the stirrer. The manufacturing process was followed as explained in section 5.3 for all the remaining phases.

The experimental setup employed was analogous to the one presented in fig. 5.13a. In this case, the light source used is the UV collimated laser diode (Thorlabs, CPS405). The

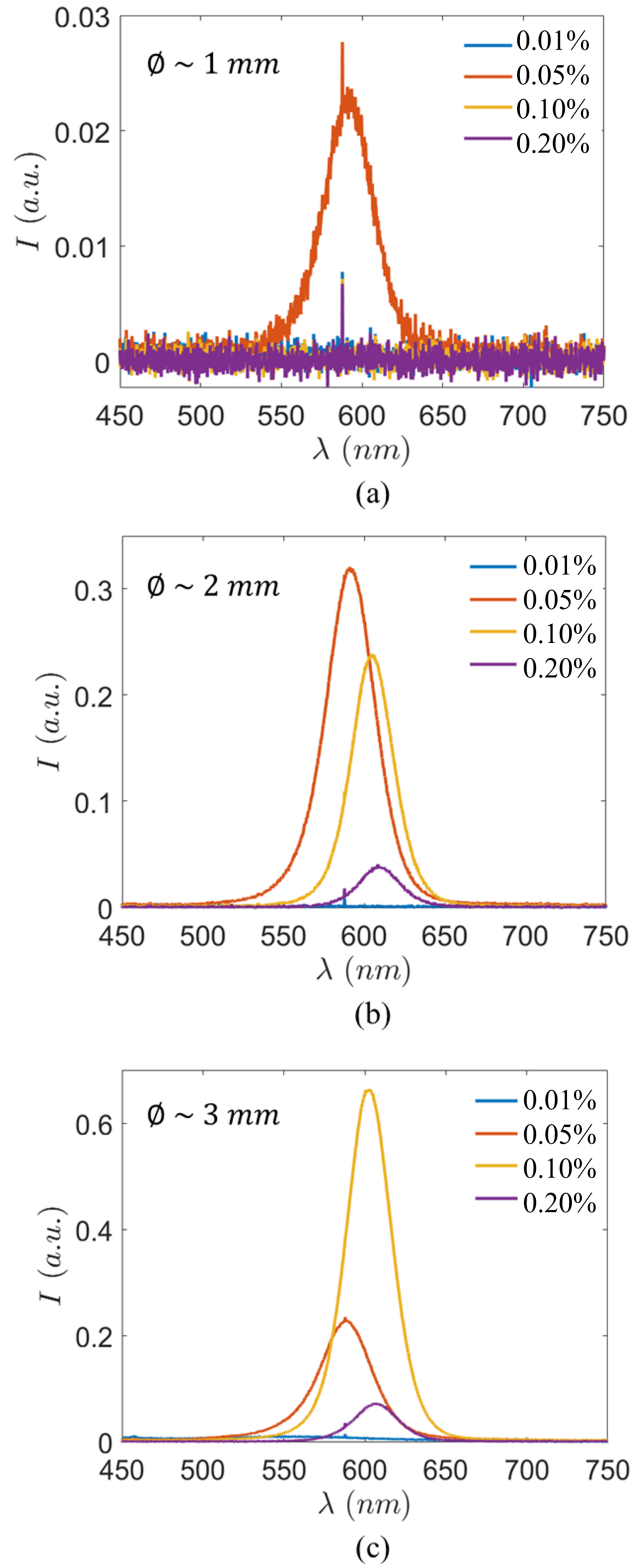


Figure 5.14: **Relation between QDs concentration and waveguide diameter.** Emission spectrum across different QDs concentrations for a waveguide with diameter of (a) $\sim 1 \text{ mm}$, (b) 2 mm and (c) 3 mm .

collimated beam was injected alternatively into the waveguides with different diameter dimension and QDs concentration. The spectrum at the output of the waveguide was measured using a spectrometer with an integration time equal to 100ms for all the measurements. For each waveguide, with specific diameter dimension and QDs concentration, the spectrum was acquired three times and the average was considered as final measurement. Fig. 5.14a shows the results for the waveguide with bore diameter of 1.0mm. The signal at the output is quite noisy for all the concentration values. The photoluminescence peak is clearly distinguishable from the noise just for 0.05wt%. For this particular diameter value, 0.01wt% of QDs solution is a too low concentration to get some signal at the output, while 0.10wt% and 0.20wt% are too high concentration which causes scattering effects and non-radiative re-absorption determining the loss of the photoluminescence signal along the waveguide.

Fig. 5.14b shows the results for the waveguide with bore diameter of 1.9mm and fig. 5.14c shows the results for the waveguide with bore diameter of 3.0mm. In both the cases, the profile appears completely flat for 0.01wt% and the trend starts being well defined for 0.05wt%, even if not very intense with absolute intensity value of ~ 0.3 in both the cases. In the case of the waveguide with diameter of 2.0mm, the output signal is maximised for 0.05wt%, while it is about $\frac{1}{6}$ lower for 0.10wt%. In the case of the waveguide with diameter of 3.0mm, instead, the output signal is maximised for 0.10wt%, while it is about $\frac{2}{3}$ lower for 0.05wt%. Comparing the two curves for a concentration of 1.0ml, the absolute intensity for the waveguide with diameter of 3mm is 3 times higher than the one with diameter of 2mm. In a thinner waveguide the number of bouncing of the light on the cladding is higher than in a thicker waveguide. In section 3.3.5, it was seen that the light is lost due to roughness when it bounces on the interface between core and cladding. One reason of the lower emission signal in the case of waveguide with diameter of 2mm may be the greater light loss due to the higher number of reflections of the light on the cladding respect to the waveguide with diameter of 3mm. So, due to the lower light losses in a larger waveguide, the latter can support a higher concentration of QDs in order to maximise the photoluminescence signal at the output.

For both the waveguides with diameter of 2mm and 3mm, increasing the concentration causes a red-shift in the luminescence emission of the waveguide.

This can be intuitively explained considering the partial overlap between absorption and emission spectra of the QDs considered (see fig. 5.12), which introduces the possibility

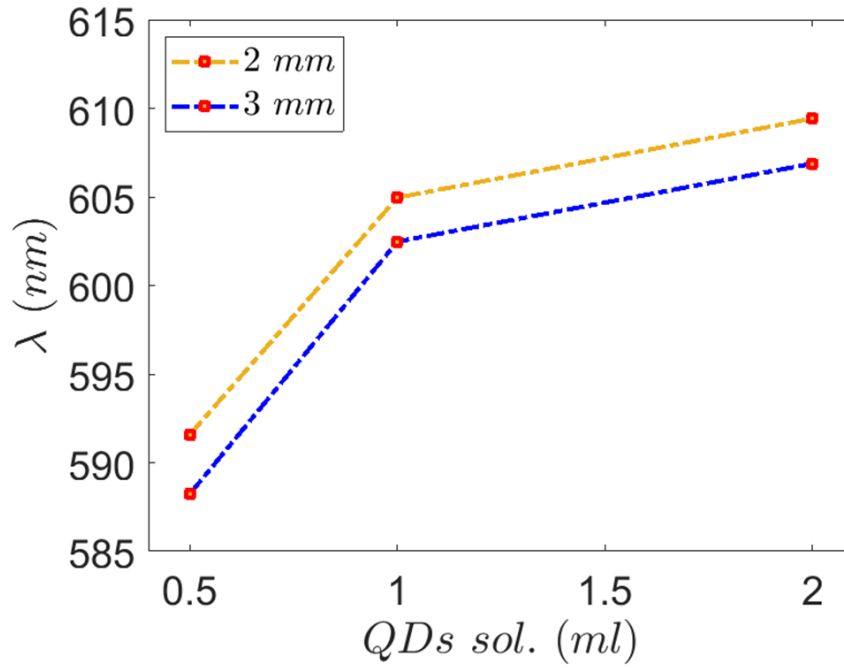


Figure 5.15: **Wavelength shift across the QDs concentration.** Photoluminescence red-shift across the concentration increase.

of multiple luminescence effect for each single photon. Rising the number of QDs the same photon can be absorbed and re-emitted multiple times by different QDs along the waveguide. For each absorption and re-emission process, the emitted photon is red-shifted respect to the absorbed one and this is reflected by the overall luminescence emission acquired at the output of the waveguide.

In addition, it was observed in the literature that CdSe/ZnS QDs integrated in PMMA layers tend to aggregate with an aggregate size depending on the average QD concentration [221]. Since the photoluminescence is size-dependent and bigger QDs present red-shifted emission spectra, the aggregation effect can lead to a red-shift of the emission with increasing QDs concentration.

This aggregation gives also rise to radiationless energy transfer due to the close packing of the QDs [221], which can further justify the intensity drop over a certain concentration value for all the three waveguides considered. The QDs aggregation affecting luminescence intensity and wavelength can be inhibited in a PMMA copolymer for QDs concentrations below a certain threshold.

Looking at fig. 5.15, it can be noted that the red-shift is slightly higher for the waveguide with diameter of 2 mm respect to the one of 3 mm. The reason causing this effect is not clear and further experiments would be needed to confirm this trend on additional waveguide

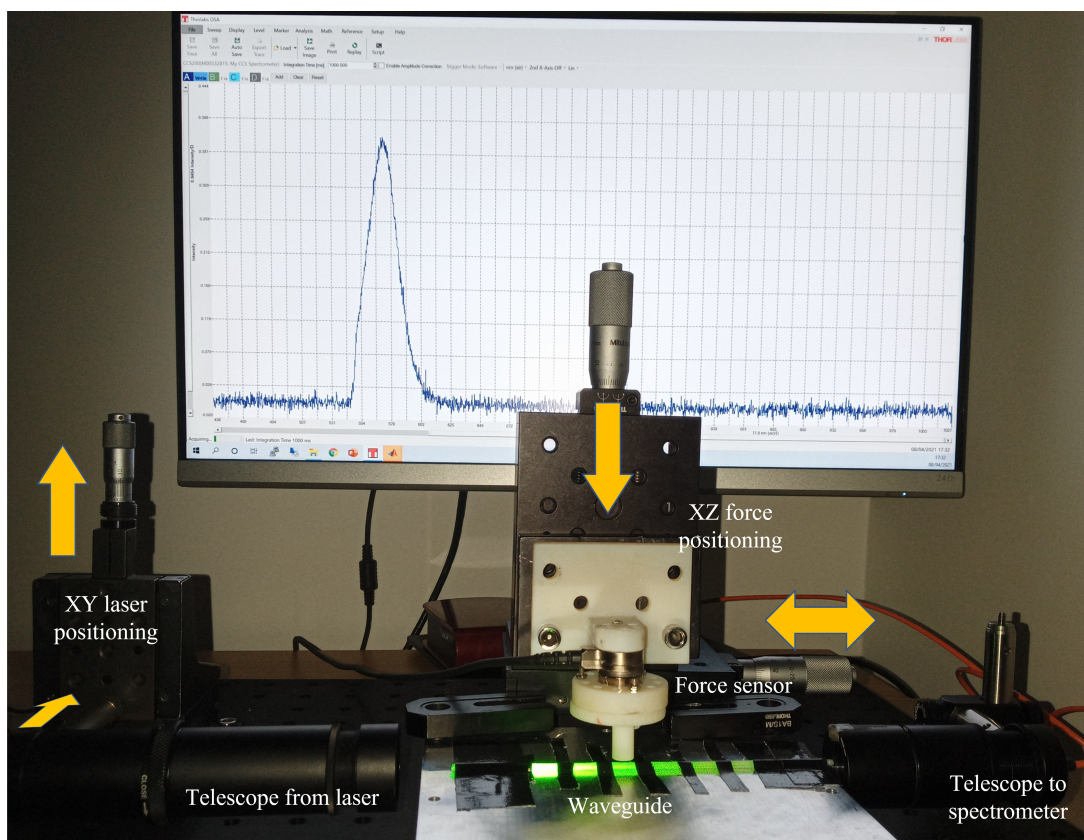
diameter values.

5.9 Reduction Of Acquisition Time

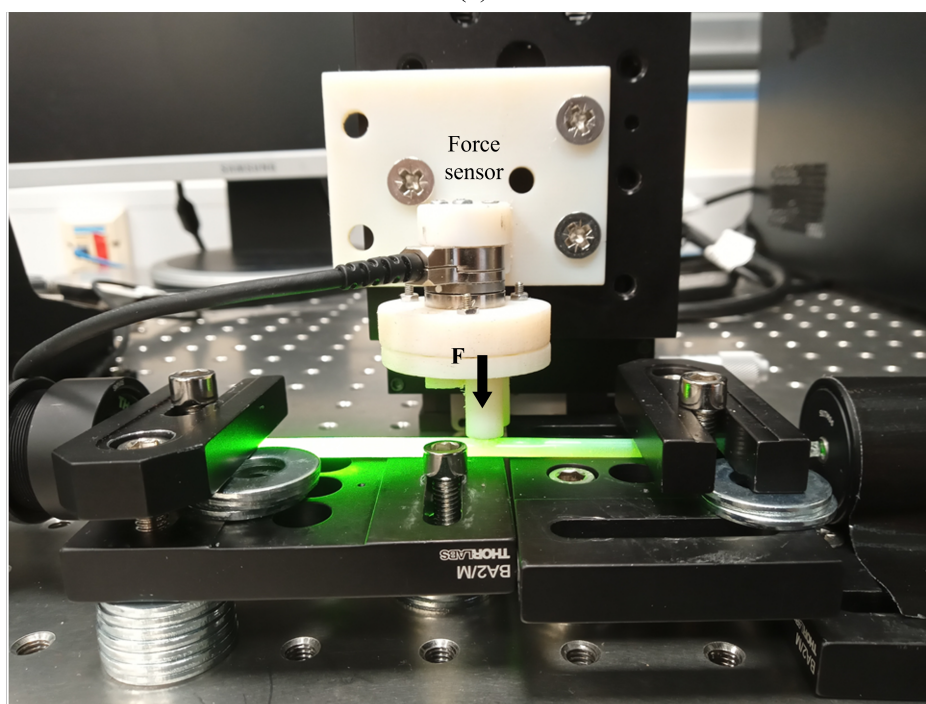
In section 5.6.2, the experimental results showed the increase of intensity and blue-shift of the wavelength across the pressure applied on the waveguide. The two trends appear more pronounced in the case of pressure applied closer to the spectrometer, confirming the behaviour predicted by the theoretical model and ray tracing simulation.

The main limitation of this sensing prototype is the extremely long acquisition time (50s) for the single measurement, required to measure the extremely small wavelength shift (full range variation $\sim 0.1nm$). To verify if a better alignment strategy can help addressing this limitation, the experimental setup was improved. For the same purpose, the considerations regarding the QDs concentration as discussed in section 5.8 were also employed.

The experimental setup used to obtain the results presented in section 5.6.2 is shown in fig. 5.16a. The green laser is mounted on a stage allowing the translation of the laser in the plane X-Y as shown by the yellow arrows in the figure. A beam reducer system is mounted in front of the laser to ensure that the beam is fully contained into the waveguide and minimising the coupling losses. The light travels along the waveguide and it is collected by a telescopic system which focuses it on the input facet of an optical fiber connected to the spectrometer. The alignment between the waveguide and the spectrometer telescopic system was found without the help of any translation stage; the alignment was found manually and the position fixed by using some screws. This operation was requiring long time and was not easy, also because once the optimal position was found, the movement caused by screwing the screws was affecting the alignment which sometimes needed to be repeated again. The spectrum acquired by the spectrometer was recorder on the PC. The pressure was applied on the waveguide through a circular probe of 8mm diameter, mounted on a couple of translation stages: the vertical one to allow the movement of the probe upwards and downwards to compress the waveguide on a single location, the horizontal one to move the probe along the waveguide and change pressing location. The detail of the waveguide compression is presented in the zoomed fig. 5.16b. The waveguide is firmly fixed to the breadboard using a metal post holder on each side. The force sensor mounted between the probe and the translation stage detects the force applied on the waveguide, converted in pressures in the post-acquisition analysis.



(a)



(b)

Figure 5.16: **Experimental setup.** (a) The laser injects light into the waveguide. The output signal is collected by the spectrometer and recorded by the PC. (b) The waveguide is firmly fixed to the breadboard at its two tips and is pressed by a circular probe with diameter of 8.0mm.

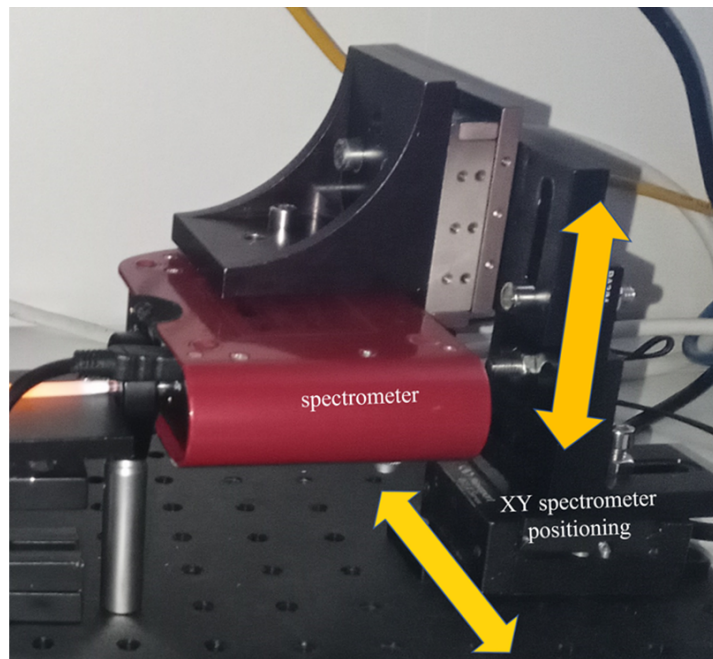


Figure 5.17: **Experimental setup: alignment improvement.** Light collected by the spectrometer without use of any lens. The alignment was improved introducing two degree of freedom for the spectrometer to translate in the plane X-Y.

The experimental setup was improved and the main change was done on the spectrometer alignment as shown in fig. 5.17. The telescopic system and the optical cable connected to the spectrometer were removed. This permitted to remove any light loss contributions due to the previously used optical components. The spectrometer was placed directly in front of the output facet of the waveguide. The alignment, in this case, was based on the use of two translation stages allowing the spectrometer to move in the plane X-Y.

The spectra obtained from the two versions of the experimental setup are presented in fig. 5.18. For both the acquisition, the green laser was injecting light into a waveguide with a diameter of 2mm and the QDs concentration used to fabricate the waveguide was $0.05\%_{\text{wt}}$. The difference consists of the integration which was 5s in the case of fig. 5.18a, while it was 500ms in the case of fig. 5.18b. Although the integration time was reduced of a factor 10, the maximum intensity of the photoluminescence emission is more than doubled respect to the acquisition done on the first version of the experimental setup and the signal-to-noise ratio is improved from ~ 17 to ~ 118 . This result confirms that the a proper alignment helps to consistently reduce the acquisition time and improve the signal-to-noise ratio.

Looking at fig. 5.18b, it was observed that still a consistent amount of light was

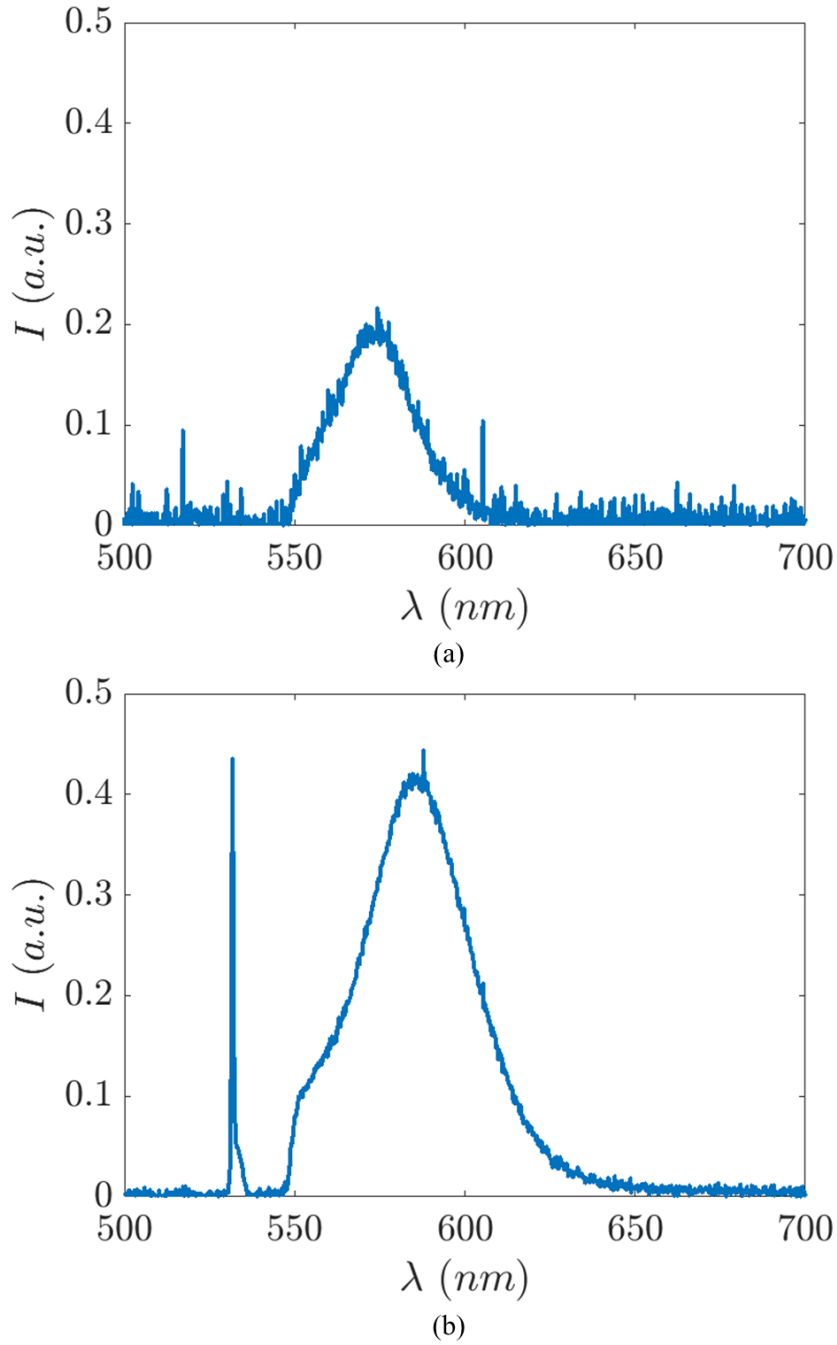


Figure 5.18: **Photoluminescence signal enhancement.** (a) Photoluminescence signal obtained using the first presented version of the experimental setup. (b) Photoluminescence signal obtained using experimental setup with improved alignment capability. The integration time is reduced up to a factor of 10.

reaching the spectrometer (narrow peak around 532nm). So, the waveguide with same dimensions but higher concentration ($0.10\%wt$) was tested in the same conditions to see if increasing the number of QDs and then the likelihood of absorption and re-emission effects was further enhancing the photoluminescence emission. Results are presented in fig. 5.19 and show that in the case of concentration $0.10\%wt$ the amount of excitation

light reaching the spectrometer is ~ 10 times lower respect to the concentration $0.05\%wt$ and the maximum intensity of the photoluminescence emission is ~ 2.25 times higher. The signal-to-noise ratio is improved from ~ 118 to ~ 281 .

Since the signal for concentration $0.10\%wt$ is close to saturation, the integration time could be further reduced; some tests have been done demonstrating that a further reduction of factor 4 on the photoluminescence maximum intensity would not compromise the measurement. Due to the linear relation between the integration time and the maximum intensity of the photoluminescence emission, a reduction of a factor 4 on the latter would lead to an integration time of $\sim 125ms$. Respect to the initial case of integration time of $\sim 5s$, an improvement of 40 times can be achieved.

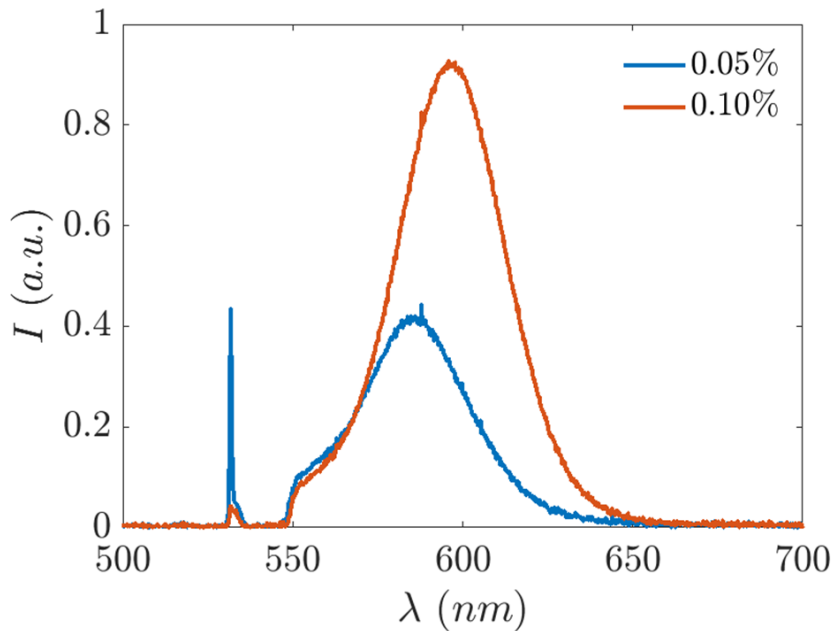


Figure 5.19: **Photoluminescence signal enhancement.** The photoluminescence signal is increased of a factor of ~ 2.25 by doubling the QDs concentration in the waveguide.

5.10 Conclusion

Respect to the design presented in the previous chapter, fluorescent dyes have been replaced by QDs. The enhancement of the photostability respect to the fluorescent dyes based sensor was demonstrated. The photoluminescence emission was measured at the output of the waveguide under resting condition (no pressure applied) over a time period of 8 hours. The signal has shown an intensity reduction of $\sim 0.36\%$ after two hours, which is almost 3 times slower than the intensity drop obtained for the fluorescent dyes.

The wavelength variation under the same conditions was also analysed, showing a stable behaviour over 8 hours of acquisition.

QDs were embedded into a flexible pressure sensing waveguide. The combined approach of theoretical simulation and experimental results confirmed the possibility to detect intensity and wavelength variation due to a pressure applied, as a result of the piezoelectric effect of the QDs placed in the compressed section of the waveguide.

The photoluminescence modulation due to a pressure applied on a single QD was studied, applying a theoretical model from the literature readapted to the type of QDs used for the waveguide fabrication (CdSe/ZnS QDs). A ray tracing simulation was developed to study the light propagation along the waveguide. The modulation of photoluminescence intensity and wavelength of a QD subject to compression, as predicted by the theoretical model, was applied to the distribution of QDs contained into the waveguide, as simulated by the ray tracing. The waveguide was divided by three segments from the light source to the detector, and the simulation was run for the case of pressure applied to the second and third segment. The simulation results showed that intensity and wavelength trends are more pronounced when the force is applied closer to the detector (corresponding to the case of pressure applied on the third waveguide segment in the simulation). This behaviour was confirmed by the experimental results.

Because of the simultaneous detection of two parameters, intensity modulation and wavelength shift, the ability of this sensing approach to detect magnitude and position of the applied pressure along the waveguide was verified. In this way, the proposed QDs based waveguide can sense the pressure in different points along its length and the sensing capability is not limited to its tip only as it was in the design presented in the previous chapter.

The sensing concept has been proved testing a QDs dopped waveguide with length of 85.0mm and diameter of 2.0mm, which was able to detect pressures between $[0 - 250]kPa$, widely covering the range of interest for endoscopic interventions. The sensitivity of $\sim 0.02kPa^{-1}$ is from 2.5 to over 3 times better than the sensors in the previous chapters.

The first experiments carried out on the PMMA-QDs waveguide required an extremely long acquisition time of 50s, unacceptable for any pressure sensing application. The reason for that was related to the challenges in measuring the very small wavelength shift under pressure, hardly distinguishable from the noise. The measurements result in a signal-to-noise ratio of just ~ 17 over 10 times lower than the fluorescent dyes based

sensor.

An experimental study focused on QDs concentration and waveguide diameter showed how these two parameters can be modulated to optimise the signal-to-noise ratio and then reduce the acquisition time. The improvement of the experimental setup also contributed to a consistent improvement of the acquisition time. The optimisations altogether can reduce the acquisition time up to $\sim 1.25s$, so 40 times lower respect to the original design. The signal-to-noise ratio can be improved up to ~ 281 , almost 2.5 times higher than the fluorescent dyes based sensor.

Experimental results have demonstrated the possibility to reduce the acquisition time by improving the setup alignment and controlling the QDs concentration into the waveguide. However, the obtained acquisition time of $1.25s$ should be further improved to get a performing sensing device able to provide a real-time pressure feedback. A QDs dopped waveguide satisfying all the optimisation factors should be tested to determine how intensity and wavelength modulation would be enhanced respect to the tested non-optimised waveguide.

Chapter 6

Conclusion And Future Work

The possibility to provide a sensing feedback to the surgeon during endoscopic interventions conducted with robotic tools is highly desirable. For such purpose, the sensing technology should be able to measure pressures perpendicular to the tool surface and not be limited to its tip. Optical sensors can potentially fulfil important requirements for endoscopic applications, such as flexibility, miniaturisation, sterilisation and MRI compatibility.

In this work three design strategies employing optical technologies relying on different working principles have been explored. Prototypes have been developed and tested as prove of concept of the proposed strategies.

The first design is based on light transmission through a multi-splitter structure made by soft channels integrated on a rigid substrate. When the channels are pressed a light intensity modulation can be detected at the output of the device.

The second design is a completely flexible array sensor employing fluorescent dyes. When a pressure is applied on the sensor, the fluorescence signal is enhanced leading to a higher light intensity measured by the camera.

The third design is a flexible polymer waveguide doped with QDs. When a section of the latter is pressed, a combined modulation of intensity and wavelength can be detected at the output as a result of the piezoelectric effect of the QDs contained in the volume of the compressed waveguide section.

For all the three approaches, the attention has been placed on (i) the reduction of number of optical channels, (ii) the sensing of pressures perpendicular to the tool surface, (iii) the developing of a simple and scalable manufacturing process and (iv) the spatial resolution enhancement. Characteristics such as sensing range, signal-to-noise ratio and sensitivity have been quantified to compare the different prototypes.

All the designs are able to measure pressures normal to the endoscope external surface. The biocompatibility can be ensured in all the three approaches by a proper selection of the materials involved in the fabrication (biocompatible fluorescent dyes or core-shell QDs). Since no electrical components are contained in the main body of the sensors, they

can be sterilised and the MRI compatibility is also guaranteed.

The lack of flexibility due to the rigid substrate of the first design proposed is certainly an important limitation for the application to endoscopy. Another drawback is that each output channel has just one sensing point located in the final section of the splitter configuration, close to its output facet. All the rest of the sensor body, where the splitter cascade develops, is not used for pressure detection. The manufacturing process involves the use of CNC milling on PTFE, which is an expensive machining technique. This was preferred respect to cheaper 3D printing techniques to reduce the roughness, which plays a role in the light transmission losses. The manufacturing process presented some challenges in the channel fabrication and requires some improvements.

The second design is fully flexible and any point of its area can return a pressure feedback. The use of fluorescent dyes may limit the usage time of the sensor because of the photobleaching effect. The sensing performances should not be compromised during a single endoscopic intervention, since it was observed an intensity decrease lower than 1% over two hours, while the mean duration of endoscopic interventions is around 30minutes. However, the photobleaching may prevent the re-use of the same sensor for several interventions on different patients, while a replacement of the all sensing skin may be more convenient, also considering that the manufacturing costs are low. Also in this case, the manufacturing process should be improved especially considering the need to reduce the thickness of the device and further extend the overall area of the sensing skin to cover the most of the endoscope body.

The third sensor is also fully flexible. The replacement of fluorescent dyes with QDs allows to extend the usage time of the sensor of at least 3 times, thanks to the better photostability of the nanoparticles respect to the dyes. The multi-parameter detection permits to measure the pressure and identify its application point, providing longitudinal spatial resolution along the waveguide. However, multiple waveguides are required to cover the endoscope and provide transversal spatial resolution at 360° around its axis. An efficient solution to deliver the light to the input of the multiple waveguides employing a single light source should be developed. The high cost of QDs is a limitation of this design. The smallest waveguides tested have a diameter of 1mm. The manufacturing process may need to be improved for further miniaturisation and to reduce the acquisition time which was measured to be 1.25s in the last presented experiments.

All the sensors are able to detect pressures over the range of interest. The most extended

range, between $[0 - 1000]kPa$, is given by the first design. The other two sensors have similar sensing range, one stretching over $[0 - 300]kPa$ and the other over $[0 - 250]kPa$. The first design has a quite low signal-to-noise ratio of ~ 22 , much improved by the second design which reaches ~ 117 employing the possibility to distinguish between excitation and emission light offered by the fluorescence. The expected effect of replacing fluorescent dyes with QDs was a further improvement of the signal-to-noise ratio because of the better photostability and photoefficiency of QDs respect to fluorescent dyes. Initial results returned a signal-to-noise ratio of just ~ 17 , but additional analysis and experiments highlighted the possibility to reach a value up to ~ 280 , almost 2.5 times higher than the fluorescent dyes based sensor.

The first two sensors show similar sensitivity of $\sim 0.008kPa^{-1}$ and $\sim 0.006kPa^{-1}$. The third one provides a sensitivity of $\sim 0.0020kPa^{-1}$, between 2.5 to 3 times better than the other optical based sensors presented in this work, although it is still lower than the most flexible pressure skins based on piezoresistive, capacitive and piezoelectric sensors [40]. A schematic comparison of the three design strategies is presented in the table 6.1.

Several sensing requirements have been enhanced by the third design respect to the previous two. The proposed sensing waveguide offers promising characteristics for the development of a sensing skin able to measure pressures applied during endoscopic interventions. The waveguides tested in this work presented a quite limited length of $85.0mm$. Much longer waveguides, of at least $1m$ length, would be required for the application to a commercial endoscope. A QDs dopped waveguide should be fabricated satisfying the conditions maximising the photoluminescence emission as presented in Chapter 5 and its sensing performance should be tested. Since the endoscope skin would be made by a series of waveguides placed parallel to the endoscope axis, next to each other, an efficient solution to deliver the light to the input of the multiple waveguides should be developed. The use of a fiber bundle may be beneficial: a single light source placed in front of the bundle would deliver light to all the individual fibers, each one of them connected to a waveguide input facet, so that the light would travel along all the QDs dopped waveguides covering the endoscope. As future work, a deeper study of the most suitable materials to fabricate the proposed prototype could be beneficial to enhance the light transmission through the waveguide and ensure the chemical compatibility of the core material with the QDs embedded in it, in order to preserve their unique optical properties.

	Design 1	Design 2	Design 3
Compatibility with comm. endoscopes	Limited flexibility and miniaturisation	Flexible, but limited usage time and miniaturisation	Extended usage time; acquisition time to be further enhanced.
Pressures normal to the endoscope	✓	✓	✓
Spatial resolution	Limited sensing area	Area fully sensitive but it should be extended	Waveguide fully sensitive, but multiple waveguides to cover extended areas
Biocompatibility	✓	Limited to the use of biocompatible fluorescent dyes	Limited to the use of core-shell QDs embedded in polymer matrices
Sterilisation	✓	✓	✓
MRI compatibility	✓	✓	✓
Mass production	Costs should be reduced; manufacturing process to be improved	Low costs; manufacturing process gets more complex if sensing area is extended and thickness reduced	QDs are expensive; manufacturing process gets more complex in case of miniaturisation
Sensing range	✓ $[0 - 1000]kPa$	✓ $[0 - 300]kPa$	✓ $[0 - 250]kPa$
Signal-Noise ratio	~ 22	~ 117	~ 17 , but improvable up to ~ 280
Sensitivity	$\sim 0.008kPa^{-1}$	$\sim 0.006kPa^{-1}$	$\sim 0.020kPa^{-1}$

Table 6.1: **Design strategies comparison.** Advantages and disadvantages in relation to the requirements for the application to endoscopy.

Appendix A

Touch Sensing Device, Electronic Device, Earphones, And Watch

Wang Steven, Liu Hongbin, Hu Jian, De Chiara Federica, Ni Gang

A.1 Abstract

Disclosed in the embodiments of the present application is a touch sensing device, comprising a light source, an optical waveguide, a photoelectric sensor, and a housing. The optical waveguide comprises a waveguide layer and a cladding layer; the waveguide layer is covered with the cladding layer; the refractive index of the waveguide layer is greater than that of the cladding layer; the waveguide layer comprises a plurality of paths; the input end of each path is provided with the light source, and the output end of the path is provided with the photoelectric sensor; the light source, the optical waveguide, and the photoelectric sensor are accommodated in the housing; a plurality of contact points are distributed on the housing; when one contact point is pressed, the contact point is in contact with one path, and the path consequently deforms; when any two contact points are pressed, the contacted paths are different; and the photoelectric sensor obtains an optical signal transmitted by the path, and the optical signal obtained by the photoelectric sensor is used for determining the degree of pressure of a contact force. The solution provided by the present application can achieve multi-point pressure sensing, and provides a reliable data basis for the completion of an accurate operation. Description Tactile sensing device, electronic device, earphone and watch

A.2 Technical Field

This application relates to the field of sensor design, in particular to a tactile sensing device, electronic device, earphone and watch.

A.3 Background Technique

With the development of science and technology, intelligent machinery has gradually replaced manual precision control in many fields. Accurate tactile information plays a vital role in the realization of the overall functions of intelligent machinery. The tactile sensor can restore tactile information to a large extent, improve the decision-making efficiency of the entire system, and ensure an orderly and safe interaction process. Currently, tactile sensors generally include capacitive tactile array sensors, inductive tactile sensors, piezoresistive tactile sensors, piezoelectric tactile sensors, and so on. However, these tactile sensors have complicated wiring, limited work scenarios, insufficient adaptability, and difficulty in high-density integration. Therefore, how to realize multi-point pressure sensing and provide a reliable data basis for the completion of precise control needs to be solved urgently.

A.4 Summary Of The Invention

The embodiment of the present application provides a tactile sensing device that realizes multi-point pressure sensing and provides a reliable data basis for the completion of precise control. In order to achieve the foregoing objectives, the embodiments of the present application provide the following technical solutions. The first aspect of the present application provides a tactile sensing device, which may include: a light source, an optical waveguide, a photoelectric sensor device, and a housing. The optical waveguide may include a waveguide layer and a cladding layer, the cladding layer envelops the waveguide layer, and the refractive index of the waveguide layer is higher than the refractive index of the cladding layer. This is to ensure that the transmission of the optical signal from the light source in the waveguide layer meets the condition of total reflection. The waveguide layer may include multiple paths, each path is provided with a light source at the input end, and each path is provided with a photoelectric sensor device at the output end. The light signal emitted by the light source is transmitted to the photoelectric sensor device through multiple paths. The light source, the optical waveguide and the photoelectric sensor are contained in the housing. There are multiple contacts distributed on the housing. Each of the multiple paths corresponds to a contact. When a contact is pressed, it will only contact one path, and the other paths will not be affected. When a contact is pressed, it will come into contact with a path, and the path will be deformed. When the path is

deformed, the path will no longer meet the condition of total reflection, that is, the optical signal transmitted by the path will have loss. When the pressure of the contact force on the contact is greater, the deformation of the path will be greater under the action of the contact, and the loss of the optical signal transmitted by the path will be greater. The photoelectric sensor device acquires the light signal transmitted by the path in real time, and the light signal acquired by the photoelectric sensor device is used to determine the pressure degree of the contact force. From the first aspect, when the path is bent, the total reflection condition of the path will be destroyed, the optical signal generated by the path will be lost, and the optical signal obtained by the photoelectric sensor device set at the output end of the path will change. Specifically, the intensity of the light signal acquired by the photoelectric sensor device provided at the output end of the path will be weakened. From the solution provided in the first aspect, it can be seen that the paths correspond to the contacts one-to-one, for example, the contact A corresponds to the path A, the contact B corresponds to the path B, and the contact C corresponds to the path C. The photoelectric sensor at the output of the path A detects the loss of the optical signal, and it can be determined that the contact A is pressed. The photoelectric sensor devices at the output ends of the path A and the path B both detect the loss of the optical signal, and it can be determined that the contact A and the contact B are pressed. For another example, the photoelectric sensor devices at the output ends of path A and path B and path C sequentially detect the loss of the optical signal, and can determine that there is a sliding force, the direction is from contact A to contact C, or the direction is from contact C To contact A. With the solution provided by this application, since the positions of the contacts are preset, the contacts correspond to the paths one-to-one, and the photoelectric sensor device provided at the output end of the path can obtain the intensity conversion of the optical signal of each path, thereby realising multiple points.

Please refer to the following link for the full version of the patent available at the following link: <https://patents.google.com/patent/WO2021253420A1/en?q=WO2021253420A1>

Appendix B

Design Of Optical Waveguide Channels For 3D Distributed Tactile Sensing

Federica De Chiara, Jian Hu, Stephen Wang, Rong Wang, and Hongbin Liu

B.1 Abstract

High-spatial density tactile arrays equipped on 3D surfaces are highly desirable in various applications. However, current tactile sensing solutions lack the ability to provide high density tactile sensing on a 3D surface and, at same time, satisfying the need of simple manufacturing and low cost. To deal with these challenges, this paper proposes a sensor array based on the light transmission through polymer waveguide branches fabricated on a rigid substrate. Materials and manufacturing methods were selected to maximize the light transmission of the device. The characteristic channel structure made by several splitters connected in cascade allows the light to be transmitted from a single input channel to eight output channels, corresponding to eight independent sensing elements with similar force response. Simulation and experimental results are presented to validate the presented sensing principle.

B.2 Introduction

Within the field of robotics, tactile sensors have experienced, especially in the last two decades, a constantly growing interest in the attempt of providing realistic dexterous artificial manipulation [222, 223, 224, 225]. According to the number of sensing elements, tactile sensors can be divided into two types, including single-point contact sensor and high spatial resolution tactile array [223]. The latter has attracted more attention due to its significant advantages, such as identifying the shape of objects via less manipulation, improving the grasping stability, judging the sliding speed, and providing higher spatial resolution. Several technologies have been exploited to develop performing tactile sensors. The most diffuse working principles are based on an electric signal, such as voltage, resis-

tance, or capacitance, affected by a particular physical quantity [224, 226]. Piezoelectric materials generate voltage when their crystal lattice is deformed because of compression [227]. They exhibit a good high frequency response, and this makes them ideal for dynamic measures such as vibration [228, 229] and they offer very high resolution in the order of sub μN [230]. However, they are not able to measure static forces accurately since the electric signal generated by the compression decay very rapidly [228, 229] and their fabrication methods are still relatively complex [231]. In capacitive tactile sensors, the pressure is detected when the capacitance of the sensor is changed because of a mechanical deformation. Nowadays one of the most common design is flexible thin film based with a layer of elastic dielectric (such as PDMS, air or fluids) between the capacitor electrodes [56]. Capacitive sensors are independent from temperature [224] and they have high frequency response and dynamic range [55]. However, they are affected by noise coming from stray capacitance (i.e. the parasitic capacitance that exist just because two layers of the device are within close proximity) and channel crosstalk [228, 56]. Sensors based on resistive effects behave as an electric resistor whose resistance is affected by a particular physical quantity. The resistance may change according to a change in material properties, a modification of the geometry or a combination of these. Quantities that can easily be measured using resistive effects are temperature (thermistors and metal thermometers), light (LDR or light-dependent resistor), magnetic field strength (magnetoresistors), and deformation (piezoresistors) [232]. The main drawbacks of the above sensing principles are the dependence of materials and device performance on acquisition time and environment conditions. The relatively large time drift and temperature drift make these sensors unsuitable for long-term monitoring. In addition, they present a complex wiring structure, and they are susceptible to electromagnetic disturbance effects and humidity. Optical sensors measure the variation of the light transmitted from a light source to a detector. Compared to the other types of sensors, they are immune to electromagnetically induced noise and provide greater safety than electrical sensors when used in hazardous environments. Among optical sensors, fiber optic sensors characteristically enjoy long life, good accuracy, manufacturing simplicity and high reliability [233, 234, 235]. TacTip family is aimed at developing low-cost optical-based sensors for object exploration [236]. But the thickness, which is not easily reduced, limits its application scenarios. GelSight sensors have been proposed by measuring a 3D topography of a contact surface via photometric stereo [237]. However, the quality of the reconstructed area is strictly

dependent on the performance of the light source, which increases the manufacturing cost. Also, the integration of optical tactile sensors into devices with different shapes is still a huge challenge. At present, tactile sensing elements can only be mounted in a flat or cylinder surface [238, 239]. Consequently, their adaptability is limited in many applications. The proposed device is made by polymer waveguides embedded on a rigid substrate. The light signal from a single source is divided by multiple splitters connected in cascade into eight channels. The final eight waveguide channels can be deformed when an external force is applied causing a variation of light transmittivity on each channel. Knowing the relation between the intensity variation and the waveguide deformation, the applied force can be measured. Although the paper is focused on a flat geometry, the multi-splitters can also be adapted to non-flat rigid substrates as shown in fig. B.1, where the sensing elements follow a curved geometry. This allows the sensor to be adaptable to various application scenarios. The prototype presents a compact size, and the use of a low power laser (5mW, the same as a common laser pointer) reduces the manufacturing cost. A simulation study was conducted to develop the most suitable waveguide design to maximize the device sensitivity ensuring equal response from each of the eight channels within a compact structure. The sensing principle was validated through calibration and hysteresis experiments, demonstrating that the sensor can detect small forces in the range $[0 - 0.5]N$ and the eight sensing elements present similar force response.

B.3 Polymer Waveguides For Sensing

b.3.1 Materials and manufacturing process

Light transmission in waveguides is based on the principle of total internal reflection. If the core of the waveguide has a refractive index n_1 higher than the refractive index of the cladding n_2 , then total internal reflection occurs for those rays being transmitted through the fiber at an angle equal or higher than the critical angle (see fig. B.1), which can be deduced by the Snell's law as follows:

$$\theta_c = \arcsin\left(\frac{n_2}{n_1}\right) \quad (B.1)$$

The materials were selected considering the physical principles which underlie the light transmission in a waveguide. A soft gel (LS1-3252 by Polymer Systems Technology

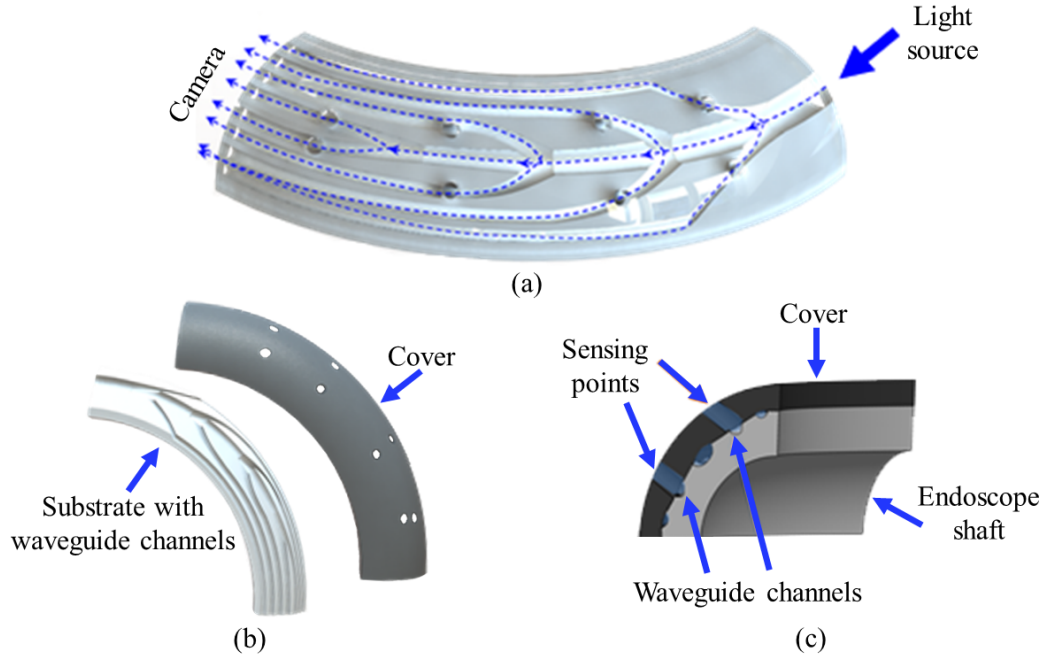


Figure B.1: **Distributed pressure sensing based on optical waveguides.** The light travels through the channels of the waveguide structure and it is measured by a camera.

Limited) was selected as core material because of its refractive index mean value of 1.52 in the visible range (400 – 800nm). The polymer Polytetrafluoroethylene (PTFE) was selected as rigid substrate, assuming the role of cladding with its typical refractive index around 1.37. The soft material was injected into the PTFE mold using a thin syringe needle to minimize the presence of air bubbles, which cause light losses due to absorption and scattering effects. After about three hours, a PTFE layer of 0.1 mm was adhered to the upper side of the channels assuming the role of upper cover of the final device. The soft material, now enclosed between the two PTFE layers, finished drying in 48 hours at room temperature.

b.3.2 Light losses and sensing principle

The main light losses in optical waveguides can be classified as injection/detection, transmission and bending losses. Bending can increase the attenuation of an optical waveguide through two mechanisms: macrobending and microbending. Macrobending occurs when the waveguide is bent or wrapped. In these conditions, the light attenuation happens because the total internal reflection is not satisfied anymore and some light is refracted out of the waveguide. Microbending is an attenuation caused by a set of bends of the fiber core with typical radius lower than 1mm [238]. The proposed sensor exploits

the microbending loss as sensing principle. In fact, the waveguide core made by soft material can be deformed by sub-millimeter structures. This deformation can be regarded as equivalent to a microbending, determining an output power attenuation.

B.4 Optimisation Process For Sensor Design

The first step of the optimization process focused on the design of a single splitter: the light injected through a single input channel must split and reach two output channels. The study of a single splitter configuration was aimed to equally split the light in the two output channels and maximize the overall output power. Getting a similar output power on the two branches is relevant to create an optical based sensor where channels have similar response to an applied force. In the case of a single splitter, this requirement can be easily reached forcing symmetry between the two branches. A deeper study was required to maximize the output power. Several designs have been developed and tested through the simulation software Optic Studio (Zemax) for this purpose. In this paper, just the most performing design is shown (fig. B.2) and the final simulation results are presented. The single branch with a curvature radius of $24mm$ and a U-shape section was mirrored to create a 50/50 waveguide splitter (fig. B.2a). Another couple of splitters, satisfying the same geometry constraints, were connected to each branch of the first splitter (fig. B.2b). Then, another series of four similar splitters were connected (fig. B.2c). The separation between the outputs of each of the three splitters starting from the input one was set at $8.0mm$, $4.0mm$ and $2.0mm$. The symmetry of each couple of branches helps the light to equally split at every bifurcation. A series of simulations were carried out to get the power transmission of each one of the three sub-splitters forming the final design, as shown in fig. B.2. The first splitter shows a power percentage higher than 47% at the output of each branch. In the second splitter, the branches 1 and 4 transmit a slightly higher amount of power. However, each branch deviates from the ideal splitter value (red dotted line in fig. B.2) of less than 3%. The third histogram shows the power percentage transmitted by the eight final branches. The branches present a strong symmetric trend and the output 3 and 6 reach the highest power transmission of about 12.4%, deviating from the ideal splitter trend of around 6%. In ideal condition, i.e. with total absence of impurities within the core (i.e. air bubbles due to injection, dust, etc), and irregularities/asymmetries in the channel geometry, the proposed design shows an overall high transmission of 86.8%.

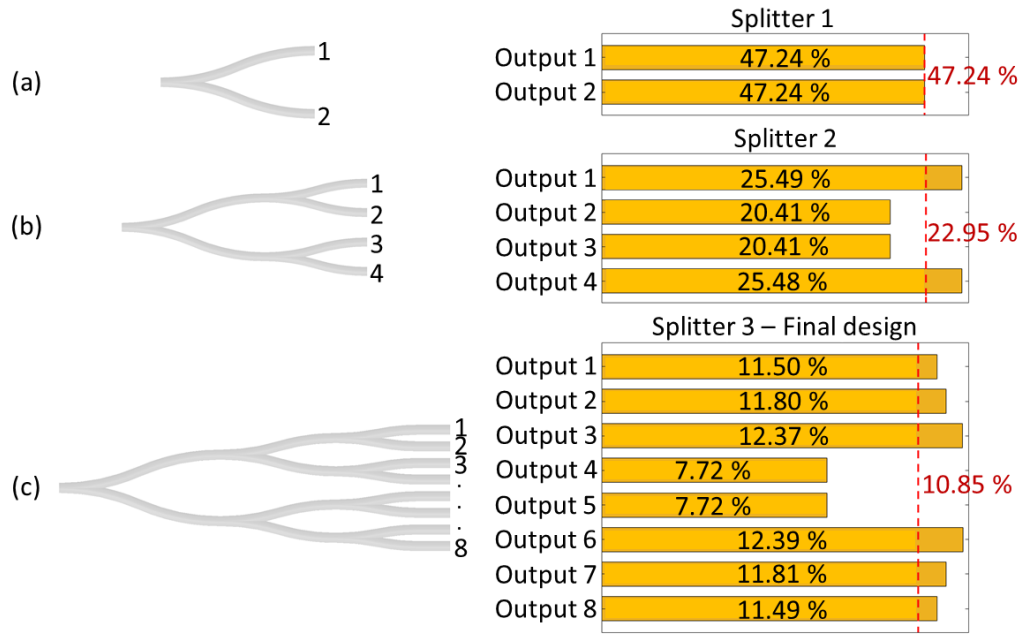


Figure B.2: **Waveguide channels with multi splitter design.** Several splitters have been coupled to create a complex design able to equally split the light at the output of the 8 branches. The power percentage at the output of each branch of the three sub-splitters was obtained through simulation.

B.5 Evaluation Experiments

The final prototype is shown in fig. B.3a. The experimental setup is presented in fig. B.3b. The light source is a laser nominally centered at $532nm$ (Thorlabs CPS532, Collimated Laser-Diode, $4.5mW$). The laser beam was focused on the input channel. The light is transmitted through the soft material channels following the multi-splitter structure, as shown in fig. B.3a. An optical fiber with core refractive index similar to the waveguide refractive index was selected to minimize coupling losses. The fiber, glued in front of each splitter output, transmits the light signal from the output of each channel to the camera (Blackfly USB 3, $2.3MP$, $41fps$). The acquired picture was analyzed through an image processing algorithm for the recognition of the region of interest (ROI), corresponding to the tip of the fiber. For each measurement, the average intensity was calculated considering the intensity value of the pixels belonging to the ROI, while all the other pixels were ignored. A 6-axes force/torque sensor (ATI Nano-17, resolution $0.003N$) was mounted on a manual translation stage (Thorlabs PT1/M, resolution $10\mu m$), which was moved by steps of $50\mu m$ forward (backward). An equivalent width compression

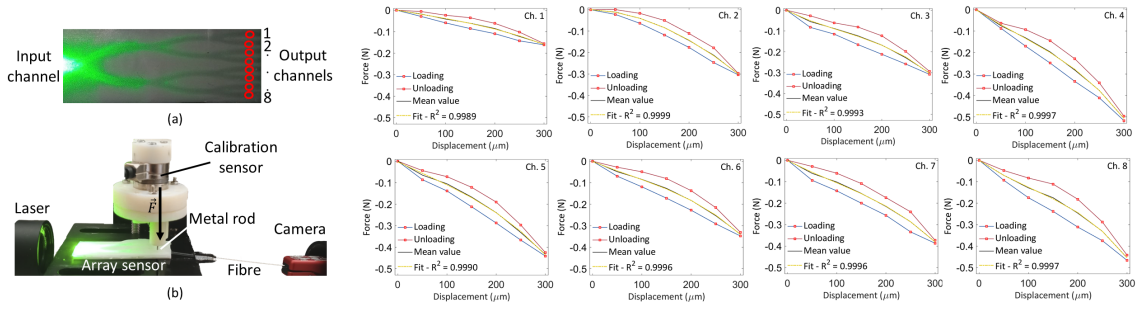


Figure B.3: **Setup and experimental results.** (a) The sensor has an 18 mm height, a 48 mm length and a 3.0 mm depth. The output channels are 2 mm distant from each other, providing a good spatial resolution. The eight sensing elements are red circled. (b) Calibration and hysteresis of the eight output channels.

(relaxation) was applied to the soft material channels of the prototype by a metal rod mounted on the calibration force sensor. The metal rod had a rounded flat head with diameter of 0.8mm . To obtain the calibration curve, each one of the eight output channels of the prototype was compressed and relaxed with steps of $50\mu\text{m}$ by the tip of the metal rod. Each measurement was repeated three times. The force values were recorded by the calibration force sensor, and the intensity values were detected by the camera, analysed by the image processing algorithm, and then normalised in the range $[0 - 1]$. This measurement provided a correspondence between the light intensity detected by the camera and the force applied on each sensor channel in compression and decompression. For each compression (or decompression) step of the force sensor (displacement), the force applied on each channel was determined considering the correspondence between the light intensity detected through the camera and the force as given by the calibration curve. The force values plotted in fig. B.3c were obtained in this way for each sensing channel. Loading and unloading curves give the hysteresis of each channel. The black line shows the mean force for each displacement value. A 3rd degree polynomial was used to get the fit and the respective R^2 values are shown on each graph, demonstrating the goodness of the fit. Looking at the channels from 2 to 8, the force range starts from 0 and reaches a maximum value between $[0.3 - 0.5]N$. Channel 1 deviates from this range with a maximum force value of $0.16N$. This effect can be due to a manufacturing problem affecting this channel or to the preliminary tests carried out on this channel before starting the final data acquisition, causing a plastic deformation of the soft material. To reduce the hysteresis and extend the range of detectable forces, the proposed soft gel can be replaced with a different stretchable material with higher toughness and fatigue resistance, provided

that the optical requirement regarding the refractive index is met.

B.6 Conclusion

The proposed array optic-based sensor is made by polymer materials. The light is transmitted from the source to the detector passing through a multi-splitter structure. The presence of a single input channel avoids the use of multiple light sources, favoring the miniaturization and reducing the cost of the full device. The light is gradually divided into different channels and then reaches the eight outputs corresponding to eight independent sensing elements. Each channel of the array can detect forces in a similar range between $0N$ and $[0.3 - 0.5]N$. The presented prototype offers a compact design, low cost and simple manufacturing, and it is adaptable to 3D surfaces. Future works will involve the improvement of the manufacturing process with the aim to extend the design to an array sensor with higher number of sensing elements and reduced distance between them, to increase the spatial resolution of the device.

Appendix C

Creating A Soft Tactile Skin Employing Fluorescence Based Optical Sensing

Federica De Chiara, Shuxin Wang, and Hongbin Liu

C.1 Abstract

Currently, optical tactile sensors propose solutions to measure contact forces at the tip of flexible medical instruments. However, the sensing capability of normal pressures applied to the surface along the tool body is still an open challenge. To deal with this challenge, this paper proposes a sensor design employing an angled tip optical fiber to measure the intensity modulation of a fluorescence signal proportional to the applied force. The fiber is used as both emitter of the excitation light and receiver of the fluorescence signal. This configuration allows to (i) halve the number of optical fibers and (ii) improve the signal to noise ratio thanks to the wavelength shift between excitation and fluorescence emission. The proposed design makes use of soft and flexible materials only, avoiding the size constraints given by rigid optical components and facilitating further miniaturization. The employed materials are bio-compatible and guarantee chemical inertness and non-toxicity for medical uses. In this work, the sensing principle is validated using a single optical fiber. Then, a soft stretchable skin pad, containing four tactile sensing elements, is presented to demonstrate the feasibility of this new force sensor design.

C.2 Introduction

Tactile sensing allows robotic devices to work efficiently in constrained environments [56]. In minimally invasive surgery (MIS), where the environment is unstructured and space-limited, flexible robotic arms equipped with tactile sensors can significantly improve the perception of the applied force by the physician during surgical or diagnostic interventions. This would prevent the application of excessive pressures with consequent damage or perforation of internal tissues. For this reasons such devices have been increasingly

attracting interest worldwide [240, 241, 242].

During its navigation within the human body the flexible instrument typically applies, to blood vessels or internal organs, pressure and shear forces by two points: its tip and the external surface of its main frame [243]. In order to provide the sense of touch while using flexible MIS tools, numerous methods have been adopted such as piezoresistive or capacitive materials and strain gauges or conductive elastomers where the applied force is measured based on the electrical signals [244, 245, 246, 229]. Magnetic tactile sensors have also been employed to measure applied forces from changes in the magnetic field [247, 248, 249, 250]. The main drawback of the above sensing principles is that they are susceptible to electromagnetic disturbance effects in the environment.

Optical tactile sensing can effectively address the above limitations and presents advantages in miniaturization, therefore it has been successfully applied in clinical practices [234, 251, 235]. Optical based tactile sensing makes use of optical fibers and measure forces by observing changes in the properties of the optical signal carried within the fiber [252]. The probed optical signal properties can be intensity [253], phase [254], frequency [255], or polarization [256]. To date, the optical tactile sensing technology provides adequate solutions for tool tip force sensing. However how to apply this technology to add force sensing capability along the flexible body of the instrument is still an open challenge in the field. The design proposed to overcome such challenge is a fluorescence signal based pressure sensor employing an angled tip optical fiber.

Fluorescent dyes are substances able to absorb light with a certain wavelength and emit light with a longer wavelength known as fluorescence emission. Thus, having different wavelengths, absorption light and fluorescence emission can be distinguished from each other within the same optical fiber that can be used as both emitter and receiver avoiding the need of optical couplers or bifurcated bundles. Such fiber, equipped with an angled tip, can be placed in parallel with the axis of a medical tool shaft. This configuration (fig. C.1c) minimises the thickness of the soft skin applied to the external surface of the tool by halving the number of fibers. Furthermore, an angled tip optical fiber allows the detection of normal pressures applied on the tool body without the use of rigid components such as mirrors [156, 157, 158]. These characteristics can facilitate the fabrication of an extended design with a cylindrical shell shape which can be adapted to the external surface of non-planar medical tools, creating a kind of flexible covering skin doped with fluorescent dyes (fig. C.1e).

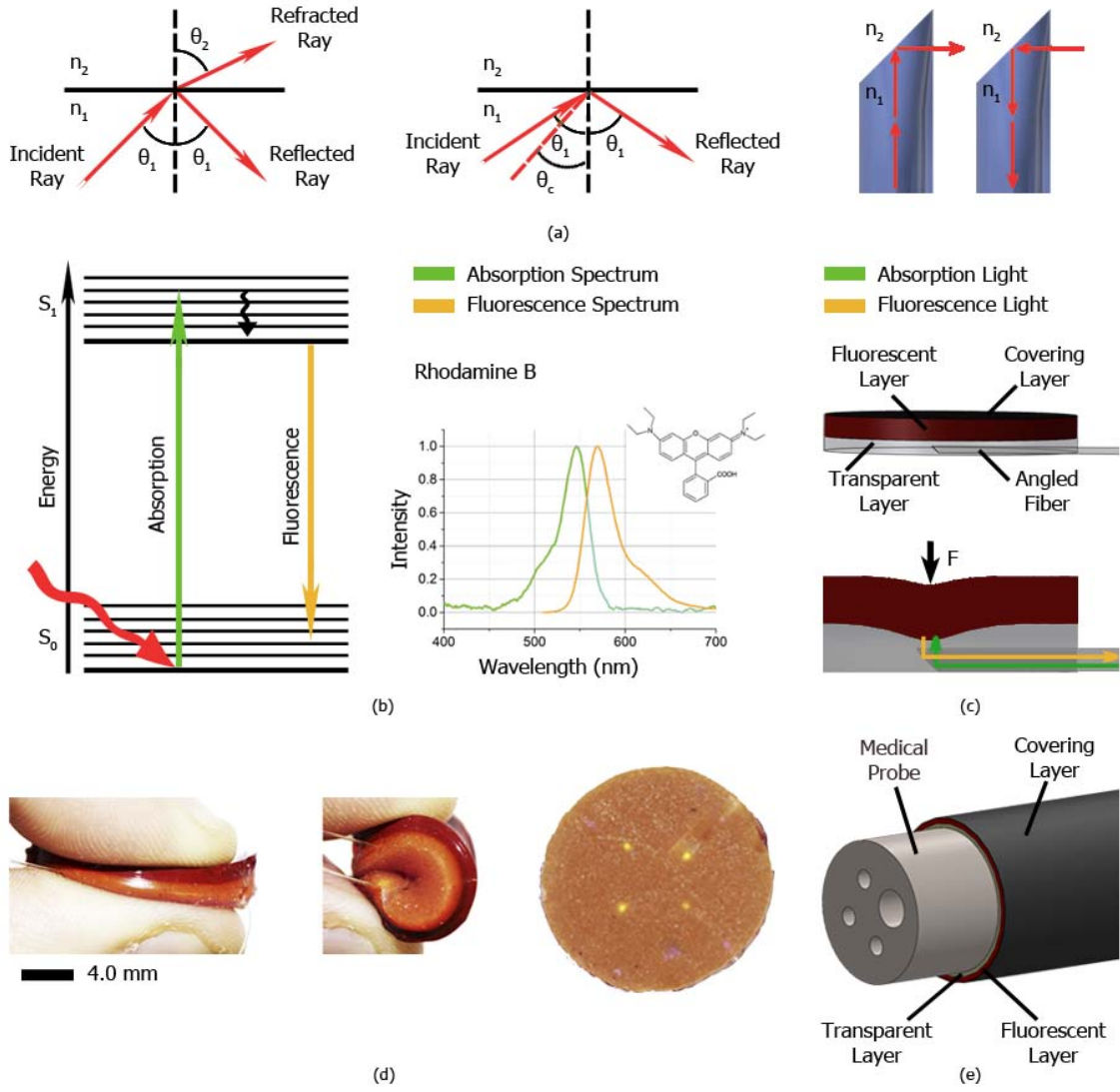


Figure C.1: **Stretchable tactile array sensor based on fluorescence.** (a) Light passing through two transparent media with different refractive indices is totally internal reflected When the incidence angle is higher than the critical angle (readapted from [98]). This is applicable to optical fibers where the tip is cut at an angle higher than the critical angle. (b) Absorption and emission spectra of Rhodamine B are presented (readapted from [103]). (c) The proposed sensor is characterized by a layer structure of soft material. The optical fiber is embedded into the lower transparent layer. Its angled tip implements the TIR principle: the light of the light source (green arrow) reaches the fluorescent layer and the fluorescence emission (yellow arrow) is transmitted by the fiber to the imaging system. When a force is applied to the sensor, the lower surface of the fluorescent layer gets closer to the fiber and a higher light intensity can be detected by the camera. (d) The use of multiple optical fibers can lead to a flexible tactile array sensor. (e) The proposed sensor can be applied to the external surface of medical tool shafts, such as the one of an endoscope.

In the case of multiple fibers embedded into the soft material composing the skin, each fiber works like a tactile sensing element. The combination of multiple sensing elements can provide not only information about the magnitude of the applied pressure, but also about the position of its application point. Moreover, biocompatible fluorescent dyes can be adopted to guarantee chemical inertness and nontoxicity.

The sensing principle was first validated using a single optical fiber. Then a soft and stretchable skin pad, containing four tactile sensing elements, was made as feasibility study for the application of this design to the flexible body of medical instruments. The case study, took as model of the presented sensor, is the measure of pressures applied to the external surface of a catheter during endoscopic interventions.

C.3 Sensing Concepts

c.3.1 Total internal reflection and prismatic-tip optical fiber

Light passing through an interface between two different media may be partially reflected and partially transmitted through the second medium. This phenomenon is described by the well known *Snell's law*:

$$n_1 \sin(\theta_1) = n_2 \sin(\theta_2)$$

where n_1 and n_2 are the indices of refraction of the two media, θ_1 angle of incidence and θ_2 angle of refraction.

In the specific case of $n_1 > n_2$, θ_2 can reach its limit value of 90° , corresponding to the condition $\theta_1 = \theta_c$ where θ_c is called *critical angle* and is defined as follows:

$$\theta_c = \arcsin\left(\frac{n_2}{n_1}\right)$$

For values of $\theta_1 > \theta_c$, refraction does not occur anymore and the light is totally reflected into the first medium. This phenomenon is known as TIR.

An optical fiber works with the same principle. If the core of a fiber has a refractive index n_1 higher than the refractive index of the air n_2 and the tip of the optical fiber is cut with an angle equal or higher than the critical angle, then total internal reflection occurs. The core of the fiber used is made of acrylic polymer PMMA (polymethylmethacrylate) and its refractive index is 1.492. Then the critical angle for the considered fiber is around 42° . To

fulfil TIR requirements we can therefore cut the tip at 45° . Thus, the light transmitted by the fiber is reflected at 90° and it can get out. Similarly, light coming from outside can be reflected at 90° by the 45° cut surface and then it can be transmitted through the fiber (fig. C.1a). For this reason a prismatic tip fiber will be able to receive light signals at normal incidence with respect to its optical axis without the use of rigid optics. This allows the fiber to run parallel and close to the surface of a flexible tool such as an endoscope, making it easily adaptable to non-planar surfaces.

c.3.2 Physical principles of fluorescence

When a photon reaches a material surface it may cede its energy to an electron. If such energy is higher than the energy gap between the initial atomic level of the electron and an adjacent higher one, the electron is promoted to the higher level. The lower energy atomic level is now empty. Such vacancy can be filled with an electron decaying from a higher energy level by the emission of a photon. If this is the case, such photon can be seen as visible light and we call it *fluorescence*. The average time lapse τ between the excitation event and the return to the ground state by the fluorescence emission is the fluorophore lifetime [104]. The lifetime is usually in the order of magnitude of $10ns$.

Fluorescence light is emitted at longer wavelength than the excitation signal. This phenomenon, known as *Stokes shift*, is mainly due to non-radiative relaxation to the lowest vibrational energy level of the excited state, in which the excitation energy is dissipated as heat (black wavy arrow in fig. C.1a).

Thanks to this clear distinction between excitation and signal wavelength, fluorescence has been extensively used in biochemical and medical applications where the signal to noise ratio is particularly critical [154]. The specific fluorescent dye used in this work is Rhodamine B and its absorption and emission spectra are presented in fig. C.1b.

c.3.3 Physical design of the sensor and working principle

The sensor has a round shape with diameter of $11.50mm$ and it is characterized by three layers: the first one is a transparent silicone layer (thickness of $2mm$), the second one is a silicone mixture containing the fluorescent dye (thickness of $2mm$) and finally a black paint was sprayed as third layer to prevent environmental light from interfering with the sensor.

The fluorescent dye (Rhodamine B, Sigma-Aldrich, excitation wavelength $550nm$, fluo-

rescence wavelength $570nm$) was diluted in methanol with 1:10 weight ratio. Then, the solution was mixed with clear silicone (Sorta-Clear™ 12, Bentley Advanced Materials) with 1:10 weight ratio.

A $1mm$ optical fiber was cut and polished to get an angled tip emitting and receiving light at once, based on the total internal reflection (TIR) principle. A mold was designed to keep the fiber in place during the silicone curing process. As result, the fiber is fixed inside the transparent layer, at the distance of about $1mm$ from the fluorescent layer.

The fluorescent layer absorbs light transmitted by the fiber and emits, in turn, light with a longer wavelength as a result of fluorescence. When a force is applied on the sensor the fluorescent layer is deformed and the distance between fiber and fluorescent surface decreases. As a result, the light emitted by the fiber reaches the fluorescent layer with a higher intensity. Consequently also the fluorescence excitation increases, enhancing eventually the fluorescence emission (fig. C.1c).

C.4 Imaging System

The imaging system is presented in fig. C.2a. The excitation light emitted by the LED is reflected at 90° and then reaches the fiber (green arrow). Once the LED light illuminates the sensor, fluorescence is emitted by the dopped silicone layer and transmitted back to the camera through the fiber (yellow arrow).

The employed camera is Blackfly USB3, 2.3MP, 41fps. The excitation spectrum is nominally centered at $530nm$ (green) with a full width at half maximum (FWHM) of $4.5nm$ while the fluorescence spectrum stretches from $555nm$ to $800nm$ (yellow-red). Excitation and emission spectra are shown in fig. C.2b.

To improve the signal to noise ratio the system is equipped with an optical band pass filter matching the fluorescence emission of Rhodamine B.

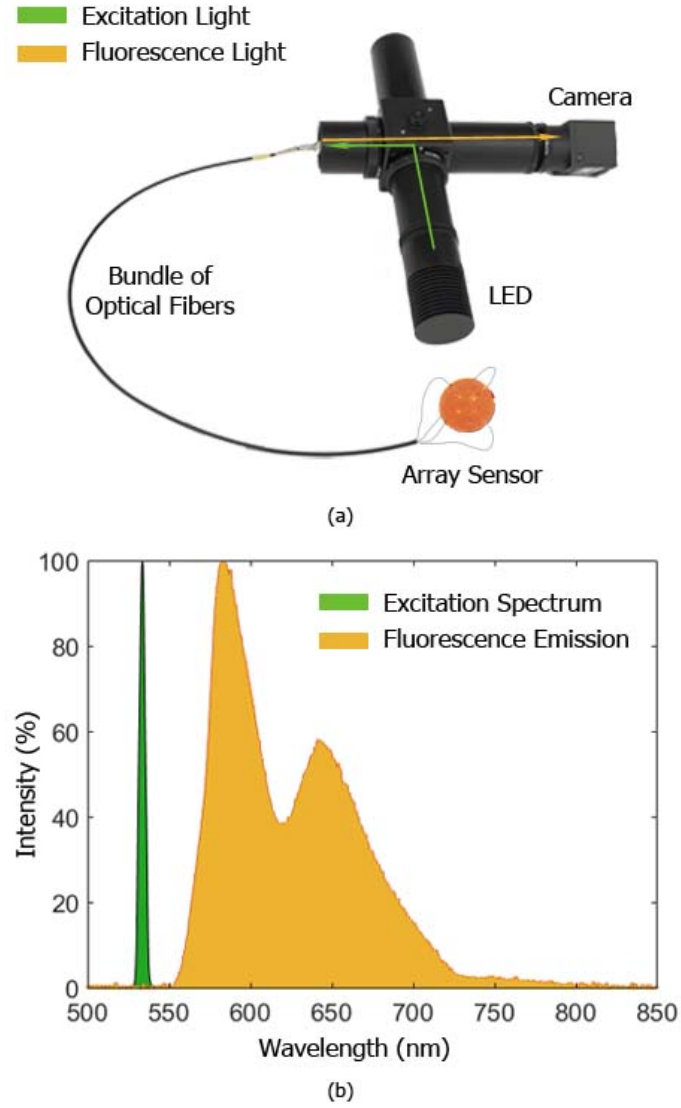


Figure C.2: **Experimental setup and acquired spectra.** (a) The array sensor is connected to the fluorescence imaging system using a bundle of angled tip optical fibers. The light emitted by the LED reaches the sensor which consequently emits fluorescence light. (b) As a result of the applied filtering system, the spectra of the excitation light source and fluorescence emission cover different wavelength ranges. Thus, the camera of the imaging system is able to detect the fluorescence signal filtering out the light source completely.

C.5 Evaluation Experiments

Evaluation experiments were carried out using the sensor design as described previously. One end of the optical fiber was embedded into the sensor; while the other end was connected to the imaging system to detect the fluorescence light and its intensity variation

when a force is applied.

A 6-axes force/torque sensor (ATI Nano-17, resolution $0.003N$) was mounted on a motorized linear guide. The linear guide moved at steps of $20\mu m$ forward (backward), causing an equivalent sensor width compression (relaxation).

The resulting fluorescence signal variation was transmitted by the angled tip optical fiber to the imaging system and then detected by the camera.

For each position, the force applied on the sensor was recorded by the calibration force sensor while an image was acquired by the camera. The ROI, corresponding to the tip of the fiber, was detected by an image processing algorithm. The intensity values associated with the pixels included in the ROI were considered to calculate the average intensity at each fiber tip.

c.5.1 Calibration

To obtain the calibration curve, the silicone pad was compressed and relaxed in the same position for thirty times. A probe of $3mm$ of diameter was used for the compression. Figure C.3a is a plot of the acquired pressure readings versus the recorded average intensity. The sensor compression increment was about $130\mu m$ for each point. Force data were later converted to pressures to be comparable with typical values measured during colonoscopy as reported in literature. Data regarding maximum intraluminal pressure during routine colonoscopy range between 4 and $20kPa$, while bursting pressures have values from about $7kPa$ in the cecum to $30kPa$ in the sigmoid colon [95].

As shown by the calibration curve (fig. C.3a), the presented sensor is able to measure pressures in the range of interest for this specific application. Moreover, as expected, an increase of pressure applied on the sensor corresponds to an increase of fluorescence intensity. Data are characterized by a linear correlation with $R^2=0.986$. The error bars represent the standard deviation, equal to 3% of the fluorescence signal readings at a specific pressure value.

c.5.2 Photobleaching

When excited, fluorescent dyes face a constant and progressive decay that eventually, with time, makes them unable to further fluoresce. Such phenomenon is called photobleaching [162] and represents one of the major limitation to the sensor life time. To measure the fluorescence signal decay caused by photobleaching, the sensor has been

continuously exposed to excitation light for 8 hours, sampling the fluorescence signal every second. The resulting data are shown in fig C.3b.

It is possible to observe that after two hours the photobleaching causes an intensity decrease lower than 1%.

Considering that the mean duration of endoscopic interventions is around 30 minutes [163], photobleaching can be neglected.

The photobleaching experiment was prolonged for a further 24 hours. After that, the experiment was interrupted for one hour and resumed for another hour. The decrease of the intensity can be considered constant along time and it is not sensibly affected by interruptions of the sensor operations.

The experiment was also repeated keeping the sensor compressed by a constant force of about 15N for eight hours. In this case the light intensity seems to decrease slightly faster. However the slope of the signal intensity decay remains linear and of the same order of magnitude.

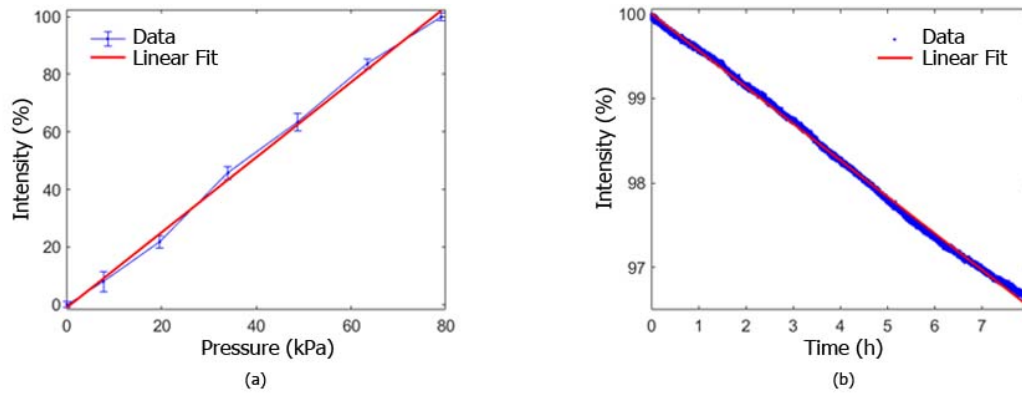


Figure C.3: **Experimental evaluation.** (a) Calibration curve: 30 measurements for each point were acquired to carry out the repeatability experiment. (b) Measure of photobleaching: the slope of the intensity decay over 8 hours was measured 3 times, giving values within the same order of magnitude.

C.6 Extension To A Soft Tactile Array Sensor

The design shown in fig. C.1d was developed to demonstrate the feasibility of a soft tactile array sensor exploiting fluorescence. The array pad presents the same layers structure as the single fiber prototype, but aims to provide the coordinates of the application point of the pressure over the sensor area. In this case, a bundle of four fibers was used.

These fibers present similar diameter and same optical properties (refractive indices and materials of core and cladding) than the fibre used in section IV. Thus, the calibration curve (fig. C.3a) obtained for the single fiber sensor is assumed valid with good approximation for each fibre of the array sensor. The four fibers were embedded into the flexible pad at the distance of $7mm$ between each other, going to design a square.

The five graphs in fig. C.4 are a graphical representation of the sensor when a pressure is applied on five different locations. An image processing algorithm was developed to calculate the light intensity of each fiber of the bundle. Then, the application point of the pressure on the sensor was considered corresponding to the center of mass calculated as follows:

$$x_{CM} = \frac{\sum_{i=1}^4 (x_i f_i)}{\sum_{i=1}^4 f_i} \quad y_{CM} = \frac{\sum_{i=1}^4 (y_i f_i)}{\sum_{i=1}^4 f_i}$$

where x_i and y_i are the coordinates of the center of each fiber tip and f_i is the corresponding average intensity defined as in the single fiber case. The values x_i and y_i were calculated on the basis of the geometry pattern shown in fig. C.4 which is a scheme of the real position of the fibers inside the sensor array.

In all the four cases of pressure applied in correspondence of one fiber tip, the measured location falls within the blue circle representing the pressure application probe. When the middle of the sensor is pressed, the calculated position is slightly outside of the blue circle. It should be noted that a correct detection of the position requires at least 3 fibers surrounding the application point of the pressure. Thus, due to its specific design, the sensing area of the proposed sensor corresponds to the square defined by the four fiber tips. Considering the highest uncertainty experimentally obtained (fig. C.4b), it can be concluded that the proposed sensor is able to detect the application point of the pressure with an error lower than 10% of the sensing area.

Regarding the potential application of this sensor, a further design improvement is required to create a flexible covering skin for the external surface of medical tool shafts. The increase of both the flexible pad surface and the number of sensing elements, in addition to a non-planar geometry, will lead to an extension of the sensing area. In fact, more fibers would be surrounded by other fibers and it will be possible to define the application point of a pressure on a more extended surface.

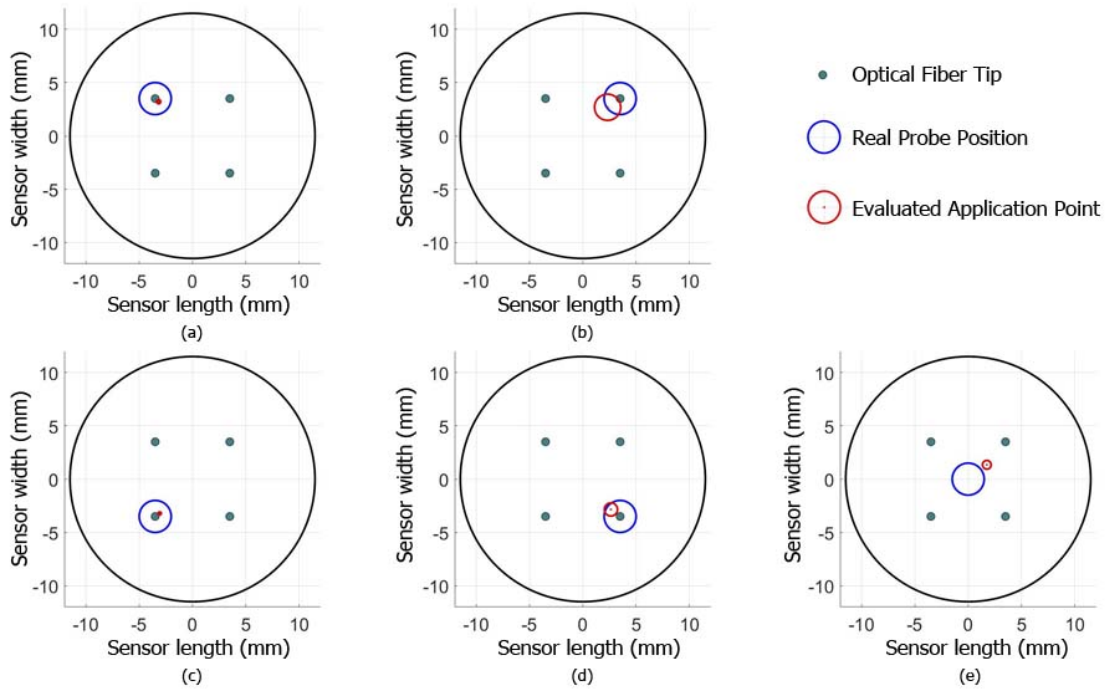


Figure C.4: **Measurement of the application point of the pressure on the sensor.** A pressure was applied on five different locations of the flexible array sensor: on the tip of each of the four fibers (grey circles) and at the center of the sensor. The sensor was pressed 10 times for each location, using a probe with a diameter of 3mm . The blue circles represent the real position of the probe. An algorithm calculates the centre of mass on the basis of the intensity of the four fibers to evaluate the point of the pressure application (red dot). The error is the standard deviation of the repeated measurements and corresponds to the radius of the red circles.

C.7 Conclusion And Future Work

The introduction of fluorescence for the development of force sensors present various advantages. Fluorescence offers the possibility to distinguish between excitation and emission light on the basis of the different wavelengths. This characteristic plays a fundamental role in improving the signal-to-noise ratio. By using fluorescence in combination with an angled optical fiber tip there is no need to deploy mirrors or other rigid components favoring the flexibility of the structure. Moreover, the same optical fiber can be used both as emitter and receiver allowing further design miniaturization.

In this paper we have demonstrated how fluorescence can be successfully used to implement both single and multi-fiber array force sensors. The single fiber sensor is able to

detect pressures with a repeatability of 3%. The development of a multi-fiber array sensor allowed to measure the application point of the pressure with an uncertainty lower than 10% of the sensing area. The unwanted effect of photobleaching is negligible considering the limited duration of endoscopic interventions. The relatively simple manufacturing process and its low cost can make this sensor disposable. Finally, this sensor is immune to electromagnetic interference, making it MRI compatible.

In order to apply the proposed sensor to the external surface of an endoscope shaft, shape and dimensions should be further improved and miniaturized, enabling a design with a higher density of tactile elements. It should be mentioned that the increase of number of fibers leads to significant practical challenges. For this reason, the proposed array sensor presents just four sensing elements. However, the results presented in [fig. C.4](#) show that the contact location can be identified with relatively small margin of error using the proposed method. Thus, the feasibility of the practical use of this sensor for flexible endoscopes is demonstrated.

Future works will involve the improvement of the manufacturing process for the multi-fiber array sensor. Furthermore, a comprehensive study of contact location estimation will be carried out to allow the measurement of magnitude and position of an applied pressure. An extended design presenting a higher number of sensing elements could fit various MIS applications and it could be particularly interesting to monitor pressures applied on the external surface of a catheter during endoscopic interventions.

Appendix D

Sensing Applied Pressure By Triggering Electronic Quantum Many-body Excitations In An Optical Waveguide

Federica De Chiara, Hovan Lee, Cedric Weber, and Hongbin Liu

D.1 Abstract

In the past few decades quantum dots have gained increasing interest. Thanks to their unique properties, a wide variety of optoelectronic devices have been developed, such as light-emitting diodes, solar cells, and photodetectors. In this paper, we exploit emission wavelength tunability of quantum dots for pressure sensor prototyping. The sensor design is based on a flexible polymer waveguide doped with CdSe/ZnS quantum dots. Quantum dots emission is affected by the pressure applied on the waveguide. The modulation of both amplitude and wavelength of the quantum dots emission can be employed as multi-parameter sensing principle. In particular, the simultaneous detection of the pressure magnitude and its application point along the waveguide has been investigated. Theoretical model and simulations describe the sensing principle while experimental evidence is presented for validation.

D.2 Introduction

In the past few decades, quantum dots (QDs) have attracted a growing interest in various scientific and technological areas. Due to their size-related effects leading to unique physical, chemical, optical, electrical, and magnetic properties, these materials can be widely used to develop novel sensors in biomedical and chemical research and clinical diagnosis even with multi-parameter capability [257, 258, 259, 260, 261, 262, 263].

The integration of QDs in optical waveguides can offer attractive advantages for sensor development, inheriting the interesting characteristics of optical fibers such as immunity to electromagnetic interference, miniaturized structures, ability to perform in

high temperature, biocompatibility, as well as more options for signal retrieval from optical intensity, spectrum, phase, and polarization [264, 265, 266, 267, 200]. Polymer optical fibers can be suitable hosts for QDs integration because of their easy processability, in addition to presenting other advantages such as light weight, flexibility, biocompatibility, low cost and high optical transparency [200, 201, 202]. QDs integrated in polymer optical fibers (POF) or planar waveguides are already widely employed for thermometry applications [164, 165, 166, 167, 168, 169, 170], as well as fluorescent fiber probes for monitoring of heavy metal pollution [171], and for intracellular sensing and medical diagnostics [172].

In order to develop pressure and strain sensors, some nanomaterials have attracted particular interest because of their piezoelectric effect [268, 269, 270, 271]. Semiconducting piezoelectric QDs, such as CdSe/ZnS QDs, have also shown piezoelectric properties, generating an electric potential in response to stress or strain. This piezo-potential tunes the band structure of the semiconductor, modulating the generation, separation and recombination of photo-generated electron-hole pairs. The result of this process is a variation of the emission spectrum of the QDs with respect to the resting condition (no stress or strain applied) [272, 273, 274]. Piezoelectric processes that lead to a modification of the optical properties of the material are usually referred as piezo-phototronic.

In this paper, the integration of CdSe/ZnS QDs in the core of a polymer waveguide has been investigated. When a force is applied on the waveguide, thanks to the piezo-phototronic effect, the emission spectrum of the QDs is tuned leading to an intensity modulation and a wavelength shift that can be linked to the applied force. Simulation and experimental results are used as proof of concept of the proposed principle for multi-parameter pressure sensing. Specifically, intensity modulation and wavelength shift have been employed to measure both magnitude of the applied force and position of the application point along the waveguide.

D.3 Results And Discussion

d.3.1 Model of a single qd emission

The evaluation of the set of piezoelectric affected emission spectra from a single QD under a range of compressive forces was analysed. A few difficulties exist in simulating these spectra; the crystalline structure and thickness of the ZnS shell are not specified by

the provider.

ZnS exist in both sphalerite (cubic) and wurtzite (hexagonal) forms, the piezoelectric tensor of the sphalerite form only contain a single unique nonzero element: d_{14} (in Voigt notation), which does not correspond to a uniaxial compressive stress, and therefore can be safely neglected for our calculations. The relevant piezoelectric tensor elements of the wurtzite form are roughly a factor of three smaller than the corresponding CdSe tensor elements ($d_{31}^{ZnS} = -1.1$, $d_{33}^{ZnS} = 3.2$, $d_{31}^{CdSe} = -3.92$, $d_{33}^{CdSe} = +7.8$, all values are in pC/N and are cited from [275]), and thus do not play a significant role in affecting the piezoelectric trend that we wish to showcase as a proof of concept. Moreover, since the ZnS shell of the QDs do not drastically alter the spectral line shape[213], we modelled our QDs as pure CdSe entities following the quantum mechanical analysis of piezoelectric effects from Zhang et al[212].

In the cited work, rate of emission is calculated via the Lorentzian expression of the zero dimensional density of states and a product of Fermi-Dirac distributions:

$$R(\omega) = \frac{\Gamma/2}{(\hbar\omega - E_{QD})^2 + (\Gamma/2)^2} f_c(1 - f_v), \quad (D.1)$$

where Γ is the line width (or full width at half maximum) of the distribution, which describes the coupling between a photon and an electron in the conduction band of the QD. f_c and f_v are the Fermi-Dirac distributions of electrons in the conduction and valence bands of the QD, and E_{QD} is the effective energy of the QD, described as:

$$E_{QD}(r, F, T) = E_g + E_e(r) + E_h(r) - E_{ex} - E_p(r, F) + \alpha_1 T \quad (D.2)$$

with E_g as the band gap of bulk CdSe, $E_{e,h}$ are the electron and hole confinement energies, and are inverse-squarely proportional to the radius of the QD. E_{ex} is the excitonic binding energy, for CdSe the electronic thermal energy (at room temperature and in vivo) exceeds the binding energy of excitons. Therefore, we neglect the excitonic binding energy. E_p is the energy change induced by the piezoelectric potential of the material, it is dependent on both the radius of the QD and the force applied onto the QD. In addition, we have also included the shift in E_{QD} due to temperature; the Debye temperature of CdSe ($\Theta_D = 181K$ [275]) is significantly lower than room temperature, we therefore implemented a linear shift in energy with the trend $\alpha_1 = 0.32MeV/K$ [276].

The calculation of the Fermi-Dirac distributions $f_{c,v}$ require the notion of chemical

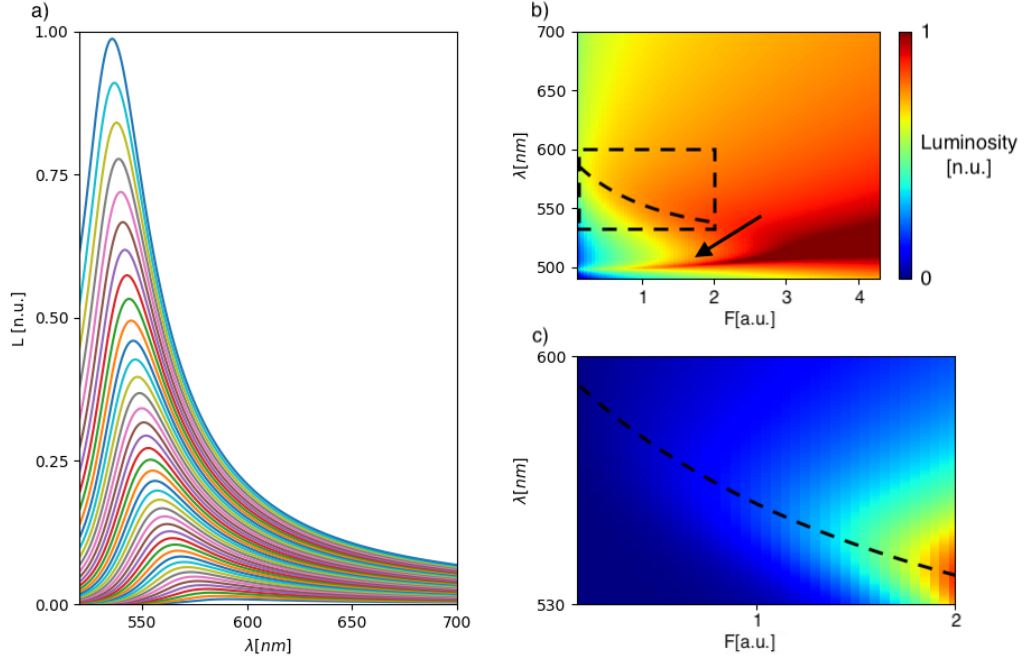


Figure D.1: **Single QD photoemission spectra.** a) Normalised emission spectra of a single QD: the feature blue-shifts and increases in amplitude under compression. b) Heat map of the single QD photoemission effect under compression (in vacuum). The lower wavelength band (pointed out by the black arrow) corresponds to the Lorentzian peak, whereas the upper wavelength band (in the dashed box) corresponds to the piezoelectric dipole emission. Dotted-line box indicates the region shown in c). c) Dotted line as a guide to the eye for the blue shift trend of the piezo-electric feature under compression. The colour scheme for b) is logarithmic whereas c) is linear.

potential $\mu_{c,v}$ in both the conduction and valence bands, which are evaluated by considering the radius and force dependent, piezoelectrically generated charge carriers in the respective bands:

$$n_{c,v}(r, F) = \frac{dF}{V} = \frac{1}{2\pi^2} \left(\frac{2m_r}{\hbar^2} \right)^{3/2} \int \frac{\sqrt{E}}{e^{(E-\mu_{c,v})/k_B T} + 1} dE \quad (D.3)$$

where the charge carrier density is determined from the piezoelectric strain coefficient of CdSe d , the applied force F and the volume of the QD V , this can be further expressed through the notion of reduced mass m_r , with an integral over energy E .

The various parameters of the single QD simulation were obtained from bulk CdSe parameters [277, 278, 137] where possible. The general trend of amplitude modulation and wavelength shift over the force is expressed as arbitrary unit. The normalised single QD emission spectra are illustrated in fig.D.1a where the increase in emission amplitude and the blue shift in wavelength, as the compressive force increases, for the piezoelectric band is shown.

The full single QD emission spectrum under compressive forces is presented as a heat map in fig.D.1b, here we observe two distinct features: the Lorentzian peak corresponding to the effective QD energy gap, and the overlap between the piezoelectric charge Fermi-Dirac distributions, as illustrated in fig.D.1. The two structures are dependent on both the radius of the QD and the force applied. However, the effective QD energy gap peak red-shifts under increasing force, whereas the piezoelectric band blue-shifts. These contrasting wavelength shifts present an upper limit of the operational force range of this technique due to the adjoining of the two features, at least at the single QD emission spectra level.

Moreover, the pair of structures depend differently on the radius of QDs. This therefore permits a rough calibration of the parameters which have been used to simulate the PMMA-QDs waveguide (see next section). The parameter we used to match the experimental setup is a computationally calibrated ambient force of $F = 1 \text{ nN}$, corresponding to an estimation of the force experienced by QDs suspended in PMMA without any other external force applied on the PMMA-QDs composite matrix.

In fig.D.1c we showcase the single QD operational force range (the same region is shown in fig.D.1b in a dotted box). The blue shifting trend is explicitly depicted as a dotted line.

d.3.2 Ray tracing simulation

The light transmission in the PMMA-QDs composite waveguide was modelled through a ray tracing simulation where the emission spectrum associated to each QD contained in the waveguide was deduced by the results obtained for the single QD modelling. The modelling of absorption and scattering of a matrix of QDs using the ray tracing approach has been proven to accurately model similar nano devices [215, 216, 217].

The waveguide was split into three separate simulation segments, dimensions $50 \times 50 \times 50 \text{ nm}$ each with refractive index of $n_{\text{PMMA}} = 1.50$ (measured at 425 nm[218]). Each segment was surrounded by a cladding layer along the length of the waveguide, with refractive index of $n_{\text{PTFE}} = 1.38$ (measured at 425 nm[148]) and thickness of 10 nm. Each segment also contains spherical structures of refractive index[219] $n_{\text{CdSe}} = 2.64$ (radius = 1.5 nm, consistent with the manufacturer values, PlasmaChem, PL-QD-O-560) distributed in a cubic mesh manner with inter-QD distance of 10 nm. These spherical structures play the role of the QDs suspended in the waveguide, and contain absorption and emission spectra corresponding to the ambient condition where the only force sensed

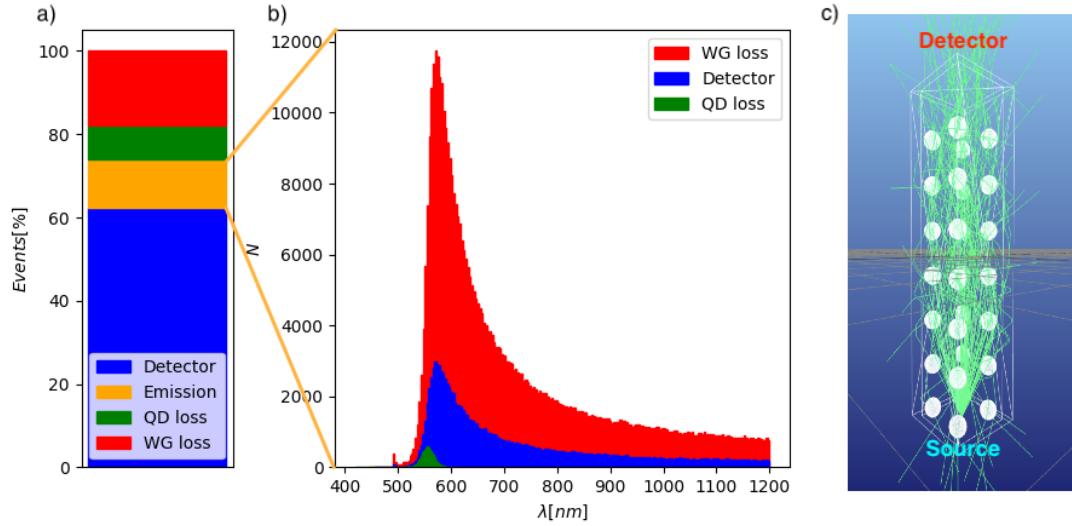


Figure D.2: **Ray-tracing outcomes.** a) Stacked bar chart illustrating the breakdown of ray tracing events. b) Stacked histograms resolved in wavelengths showing the further split of the 'Emission' events in a) with a force of 6 *nN* applied on the quantum dots of the middle waveguide segment. c) Wireframe structure diagram of a scaled down example of the ray tracing simulation.

by the QDs is due to their integration in the PMMA matrix. These spectra were calibrated through matching the simulation results with experimental observations. The second and third segments contain simulated QDs with different spectra, consistent with a further externally applied force. The rays are generated in a spherical cone distribution of 30° at the beginning of the first segment, with wavelength of 425 *nm*.

The ray tracing simulation takes several types of events into account as a ray approaches any interface between objects; the ray could be reflected and adopt a new direction of propagation, or transmitted at angle due to the difference of refractive indices at the interface. The ray could also be absorbed, corresponding to the absorption spectrum of a QD. Finally after being absorbed into a QD, the ray has a likelihood of being emitted from a QD with a new wavelength and propagation direction.

The percentages of final outcome of the rays for a sample ray tracing simulation of five million rays, at ambient waveguide conditions, are shown in fig.D.2a. The outcomes are split into four categories; all rays that have not been absorbed or emitted by a QD, and are transmitted through the detector-end interface between the simulated waveguide core and vacuum are shown as a part of the 'Detector' category in blue. Rays that have not been absorbed or emitted by a QD, and are not transmitted through the waveguide core/ detector interface are depicted in the 'WG loss' category in red, indicating that the

rays have been lost due to transmission through the waveguide cladding into simulated vacuum. The rays that have been absorbed by a QD, and are not re-emitted due to the quantum yield of the QDs (estimated at 60%) are shown in green as 'QD loss'. Lastly, all rays which have been emitted by a QD are classified in the 'Emission' category in orange.

The 'Emission' rays are further split into three wavelength resolved outcome categories in fig.D.2b, where the classification of ray categories follow those of fig.D.2a, but all rays have been emitted by a QD.

A comparison between the ratio of 'Detector' rays in fig.D.2a and 'Detector' rays in fig.D.2b informs us that we are in the regime where the detector senses an order of magnitude more light-source wavelength rays than QD emitted (or signal) rays, consistent with the experimentally observed ratios where the light-source wavelength is detected as a saturated peak. Moreover, a significant amount of simulated rays are lost through the 'WG loss' categories. This is due to ray being scattered or emitted by QDs at angles with large perpendicular components with respect to the length of the waveguide. This allows for the possibility where rays propagate to the cladding at an angle greater than the critical angle θ_c , whereby the ray is transmitted through the cladding and are lost (see Light propagation in a waveguide in Methods section). This phenomena also explains the significantly larger ratio of 'WG loss' in fig.D.2b, where the rays have been emitted by QDs, compared to 'WG loss' in fig.D.2a, where the rays have not been emitted by QDs and are likely to propagate with a large parallel component with respect to the length of the waveguide.

The 'Detector' category in fig.D.2b can be further analysed to obtain the distribution of ray location and propagation directions. For a simulated compressive force of 6 nN on the QDs of the middle waveguide segment, all rays (of a five million ray simulation) that have been emitted by a QD and is transmitted through the detector end of the waveguide is shown in fig.D.3a. Here, the rays are colour coded into three groups ($\lambda \leq 650\text{nm}$ for green, $650\text{ nm} < \lambda \leq 800\text{ nm}$ for orange and $800\text{ nm} < \lambda$ for blue). The position of the ray incident on the simulated waveguide-detector interface is illustrated in fig.D.3b, where r is the normalised uni-dimensional distance of the ray position from the centre of the cross-section of the interface. The normalised component of ray propagation which is perpendicular with respect to the length of the waveguide is shown in fig.D.3c, and the parallel component is shown in fig.D.3d.

We observe in fig.D.3b that there is a slight preference for rays to propagate incident to the interface with r close to unity. In our view, this is due to rays that are consistently

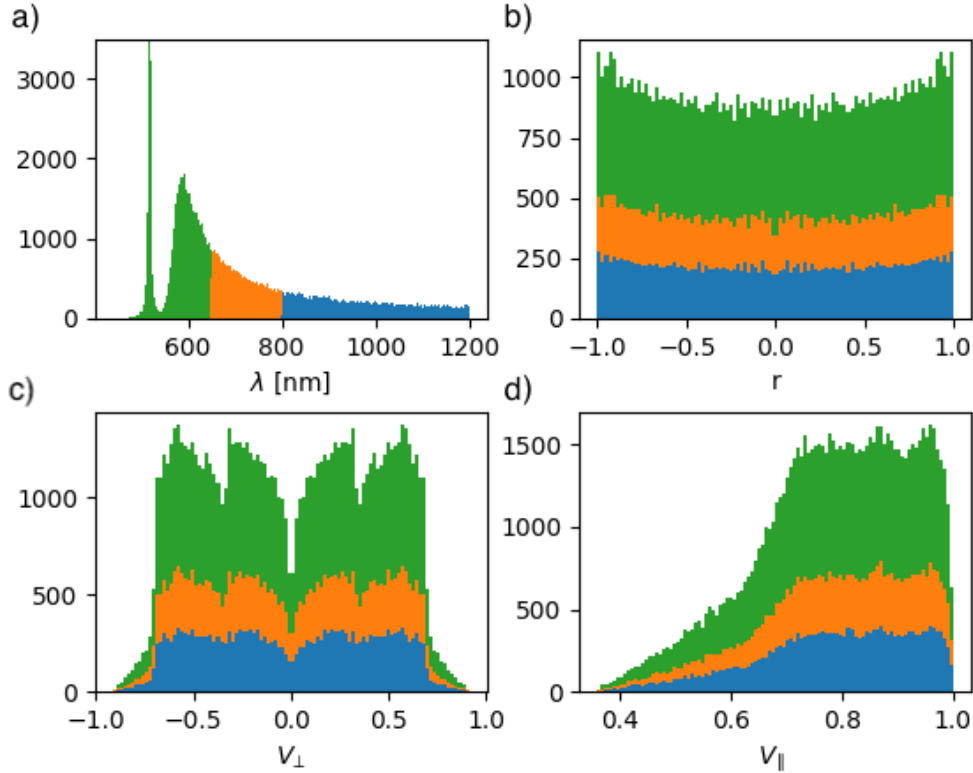


Figure D.3: Statistical analysis of simulated detected photons. a) Spectral analysis of the detected photons after transmission through the waveguide, colour coded into three groups: $\lambda \leq 650 \text{ nm}$, $650 \text{ nm} < \lambda \leq 800 \text{ nm}$ and $800 \text{ nm} < \lambda$. b) Spatially resolved cross-section of the measured photons. c) Angular distributions in terms of normalised momentum vector with respect to the c) perpendicular and d) parallel components.

reflected between the waveguide core-cladding interface and the outermost QDs from the centre of the waveguide.

In fig.D.3c there is a tendency for rays to transmit through the interface with a nonzero perpendicular component. We explain this bias by considering rays with purely zero perpendicular component, since fig.D.3 show only the subset of rays that have been emitted by a QD, rays that have been emitted with zero perpendicular component (and hence travel parallel to the length of the waveguide), will likely interact with the next neighbouring QD in the cubic mesh. Therefore, this decreases the likelihood that the detector senses a ray with a zero perpendicular component. Furthermore, we observe a disinclination of rays with a normalised perpendicular component of ~ 0.35 . We attribute this to the scattering of rays in the QD mesh. Lastly, rays with unity perpendicular components will not propagate to the interface, and hence we observe zero counts of such rays.

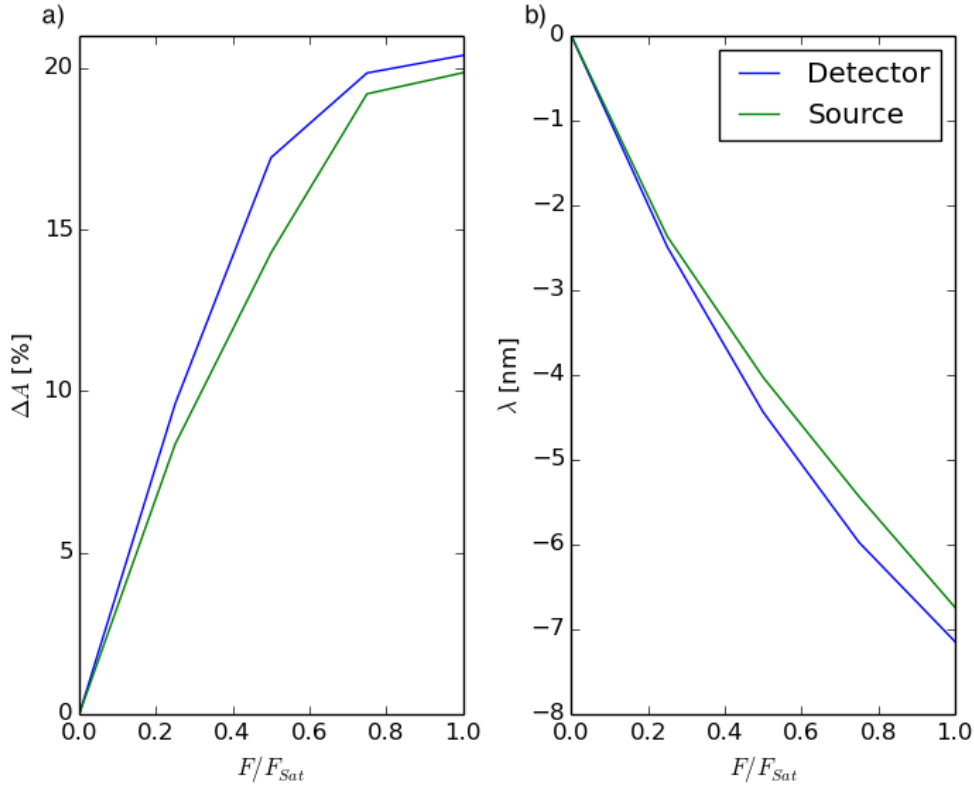


Figure D.4: **Simulated trend of the intensity and wavelength.** a) Theoretical amplitude of the photonic distribution measured at the detector as a function of the applied force, where the latter is applied near the detector (source) and labelled in blue (green). The applied forces (F) are normalised by the saturation limit (F_{sat}). b) Wavelength shift of the maxima of the distribution's peak, as a function of waveguide compression.

In fig.D.3d a propensity of rays with $0.7 - 1$ normalised parallel components are observed. This can be explained through the geometry of the simulated waveguide; rays that transmits through the waveguide-detector interface likely has a large parallel component, such that no obstructing QDs are in the path of propagation. Furthermore, no counts of rays with a parallel component $< \sim 0.35$ was detected. This is due to the critical angle of the interface; the angle of incidence of such rays are less than θ_c between the PMMA waveguide core and vacuum.

We present the skewed Gaussian-fitted trend of the simulated piezoelectric driven emission as a function of compressive force applied onto the middle waveguide segment (green) and last waveguide segment (blue) in fig. D.4a, and the wavelength shift trend in fig.D.4b. The percentage increase (ΔA) of the amplitude is evaluated with respect to the ambient conditions. The range of forces considered are normalised to a saturation force F_{sat} , where the amplitude increase of the signal saturates. This increase in amplitude and

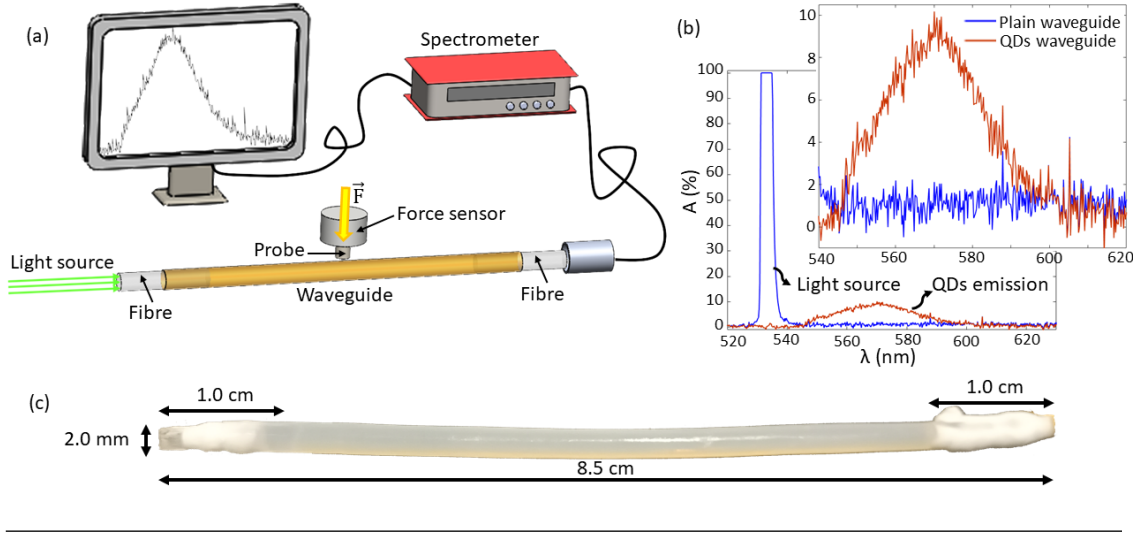


Figure D.5: **QDs piezoelectric effect in composite polymer waveguides.** a) Schema of the experimental setup. b) Output spectrum of a plain polymer waveguide (without QDs) and a QDs-doped waveguide. c) Waveguide prototype: compact, flexible and compressible.

subsequent saturation is due to the growth and assimilation of the two features shown in fig. D.1b.

Intensity and wavelength trends are more pronounced for the 'Detector' simulations. We explain this due to the likelihood of a QD emitted ray to become scattered out of the waveguide (WG loss), or be absorbed (QD loss) and re-emitted by a subsequent QD; the closer to the detector this compressive force is applied, the less likely that the signal information is overwritten by these effects from a subsequent QD.

d.3.3 Experimental results

The experimental setup is shown in fig.D.5a. A collimated laser diode ($\lambda_{em} \sim 532$ nm, 4.5 mW, Thorlabs) injects light into a cylindrical polymer waveguide of 8.5 cm length and diameter of 2.5 mm. A long-pass filter ($\lambda_{cut-on} \sim 550$ nm, Thorlabs) was placed at the output of the waveguide to filter out the light coming from the laser and isolate the signal emitted by the QDs. The output signal is collected by a lens telescope and sent to the spectrometer (Thorlabs, CCS200/M). A 6-axes force/torque sensor (ATI Nano-17, resolution 0.003 N) was mounted on a manual translation stage (Thorlabs, resolution 10 μ m) which was moved downwards to progressively compress the waveguide. A circular probe of 8 mm diameter mounted on the calibration force sensor was used as compression probe (fig.D.5a).

Fig.D.5b shows a comparison between two spectra, the first one acquired from a plain

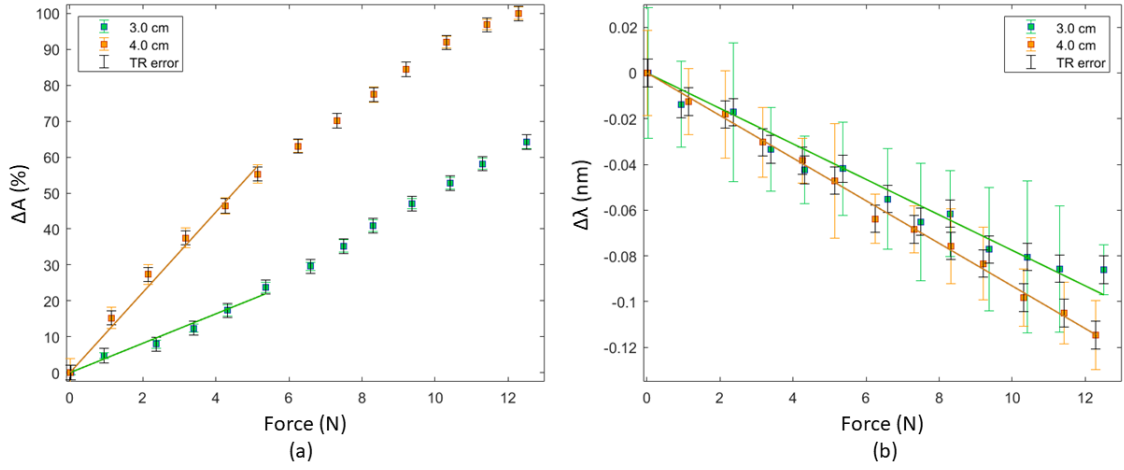


Figure D.6: **Amplitude modulation and wavelength shift calibration.** The waveguide was compressed on two different locations: 3 cm and 4 cm from its input surface. For each force value, amplitude modulation a) and wavelength shift b) were measured.

waveguide (not containing QDs) and the other one from a waveguide containing QDs. For both the acquisitions, the same integration time of 5 s was set on the spectrometer to get a good QDs signal-to-noise ratio. In the case of the plain waveguide some laser light (peak around 532 nm) can still reach the spectrometer despite the presence of the long-pass filter, since scattering and absorption effects related to QDs do not occur in this waveguide. Also, the long integration time, required to detect the QDs signal, brings the laser peak to saturation, while the rest of the spectral profile on the range [540-620]nm is flat (blue spectrum in fig. D.5b).

In the doped waveguide instead, QDs absorb part of the laser light and eventually re-emit it at longer wavelength. The result is a spectral distribution stretching on the range [550-600] nm (red spectrum in fig. D.5b). This emission is identifiable as the piezoelectric dipole emission, showing its characteristic properties as predicted by the single QD model: width of ~ 50 nm and skewed blue with a trailing edge towards red.

A calibration experiment was carried out to determine the characteristic trend of intensity and wavelength modulation as a function of the force applied on two different locations of the waveguide: 3 cm and 4 cm from the input surface of the waveguide. The force applied covers the range [0-12] N, with a step of 1 N. The maximum value of 12 N is the mechanical limit imposed by the experimental setup in use and the amplitude corresponding to this force value was used as normalisation factor. The integration time of the spectrometer was set to 5 s. For each force value, 10 repeated spectra were acquired. A Gaussian fit was applied on each one of the 10 spectra, then the mean of the coefficients

was calculated to get the final Gaussian fit for each force value. The amplitude coefficient of the final averaged Gaussian trend was considered to get the modulation of the peak amplitude of the signal (fig.D.6a), and the wavelength shift as a function of force (fig.D.6b). The error bars were calculated as standard deviation on the 10 repeated measurements for each force value. Results in fig.D.6a show a linear trend between $[0-5] \text{ N}$ with $R^2 \sim 0.98$; the rest of the trend still presents a linear behaviour with a different slope. Also in fig.D.6b a linear trend is observed: although the standard deviation error bars are quite large with a maximum value of $\pm 0.03 \text{ nm}$, the mean values follow the fit line pretty well with $R^2 > 0.97$. Both intensity modulation and wavelength shift corresponding to the pressing location at 4 cm are more pronounced and this is in accordance with the simulation results. This result is related to the likelihood for a QD emitted ray to be scattered out of the waveguide or absorbed (but not re-emitted) or absorbed and re-emitted by a subsequent QD. For QDs further from the waveguide output, these effects are more likely, causing light loss and then a lower light intensity detected at the output, as well as a less pronounced blue-shift. The different slopes obtained for both amplitude and wavelength suggest the possibility to distinguish between the two pressing positions along the waveguide combining the measurement of the two parameters. The black error bars take into account the signal drift occurring during the acquisition time for each force value.

Although it was not possible to determine how the force applied on the waveguide translates to the force sensed by each single QD in the waveguide, the overall phenomenon described by the simulation analysis is confirmed by the experimental results, leading to the same modulation effect of the analysed light properties.

Both in the experimental and simulation results, the trends are more pronounced when the force is applied closer to the detector. This can be explained by the fact that the closer to the detector this compressive force is applied, the less likely for a QD emitted ray to be scattered out of the waveguide, or absorbed and not re-emitted (these two events would reduce the amplitude variation), or to be absorbed and re-emitted by a subsequent QD (this event would reduce the wavelength variation). This observation suggests that not only the pressure can be detected, but also the location of the applied force can be obtained, as both light amplitude and wavelength are affected differently through the scattering process.

D.4 Methods

d.4.1 Light propagation in a waveguide

Waveguides are made by an inner core and an outer covering layer called cladding. The behaviour of the light at the interface between two media, such as core and cladding, respectively with index of refraction n_1 and n_2 , is well described by Snell's law [279]. From Snell's law, the equation of the critical angle can be deduced as follows:

$$\theta_c = \arcsin\left(\frac{n_2}{n_1}\right)$$

Assuming that the core refractive index n_1 is higher than the cladding refractive index n_2 , all the rays having angle of incidence on the interface $\theta > \theta_c$ are totally reflected into the core. This phenomenon is called total internal reflection (TIR). All the rays satisfying the above angular condition are transmitted through the core.

d.4.2 Waveguide fabrication

A PTFE sleeve (clear Polytetrafluoroethylene, 1.9 mm bore diameter, 0.3 mm wall thickness) was employed as cladding. The main material being used to create the core was PMMA powder (Polymethyl methacrylate, average Mw 120,000 by GPC, Sigma-Aldrich). The typical refractive index value is around 1.50 at 500 nm for PMMA and 1.38 at 500 nm for PTFE. The PMMA powder was diluted in the organic solvent DMF (N,N-Dimethylformamide, anhydrous, 99.8%, Sigma-Aldrich) at 22wt%. The solution was mixed with a stirrer at 1100 rpm for about 5 hours. The core-shell CdSe/ZnS QDs with emission wavelength of 560 nm (powder form, PlasmaChem GmbH) was diluted in toluene (Anhydrous, 99.8%, Sigma-Aldrich) with a mass concentration of 5mg ml⁻¹. QDs were added to the polymer solution in the concentration of 0.06wt% and mixed for 30min using the stirrer. The final solution was placed in the ultrasonic bath for 15 minutes to degas. Then the polymeric composite material was injected into a PTFE tube using a syringe. The filled tube was left to dry for 24 hours at room temperature and then for 72 hours at 60°C in the oven. After the curing process, the polymeric composite material containing QDs has a gel-form and this allows the waveguide to be flexible. Due to the low concentration of QDs embedded into the waveguide core, it can be assumed that the nanoparticle integration does not affect macroscopically the refractive index of the core,

therefore the requirements for the light transmission through the waveguide are satisfied. An optical fibre of 1 cm length was inserted at the input and output of the PTFE tube. The fibre was selected so that core diameter and refractive index were similar to the waveguide core (diameter ~ 1.9 mm, $n \sim 1.5$) to minimise the light losses due to the refractive index change at the interface between the optical fiber and the waveguide core. The optical fibres were firmly fixed inside the PTFE tube using some thread sealing tape and further anchored to the experimental desk using some metal plates (see fig.D.5c). When a force is applied on the waveguide, the two optical fibres assume the role of stoppers and keep the soft material of the waveguide under compression.

The fabrication process of the plain optical fibre (not containing QDs) follows the same procedure as described above, except the phase of QDs integration.

Appendix E

Image Processing Algorithm For ROI Identification

```
1  close  all
2  clear  all
3
4  %% IMPORT IMAGE:
5
6  I0_1 = imread( '.\Position\2\3.png' );
7  figure , imshow(I0_1);
8
9  %% INITIAL CROP
10 % to keep the portion of the image occupied by the fibers
    (4 in this case):
11
12 xmin_0 = 600;
13 ymin_0 = 80;
14 width_0 = 1050;
15 height_0 = 920;
16 I0_1 = imcrop(I0_1,[xmin_0 ymin_0 width_0 height_0]);
17 figure , imshow(I0_1);
18
19 %% CROP SQUARES OCCUPIED BY THE FIBERS
20 % to identify the area of the image occupied by each fiber
21 % and crop the image in as many squares as the number of
    fibers:
22
23 xmin_1 = 20;
24 ymin_1 = 370;
25 width_1 = 430;
26 height_1 = 430;
```

```
27 I1singleFiber = imcrop(I0_1,[xmin_1 ymin_1 width_1 height_1
    ]);
28 figure , imshow(I1singleFiber); % Square including fiber 1
29
30 xmin_2 = 150;
31 ymin_2 = 10;
32 width_2 = 450;
33 height_2 = 430;
34 I2singleFiber = imcrop(I0_1,[xmin_2 ymin_2 width_2 height_2
    ]);
35 figure , imshow(I2singleFiber); % Square including fiber 2
36
37 xmin_3 = 600;
38 ymin_3 = 120;
39 width_3 = 450;
40 height_3 = 450;
41 I3singleFiber = imcrop(I0_1,[xmin_3 ymin_3 width_3 height_3
    ]);
42 figure , imshow(I3singleFiber); % Square including fiber 3
43
44 xmin_4 = 400;
45 ymin_4 = 470;
46 width_4 = 450;
47 height_4 = 450;
48 I4singleFiber = imcrop(I0_1,[xmin_4 ymin_4 width_4 height_4
    ]);
49 figure , imshow(I4singleFiber); % Square including fiber 4
50
51 %%%%%%%%%%%%%%%%%%%%%%%%%%%%%%%%%%%%%%%%%%%%%%%%%%%%%%%%%%%%%%%%%%%%%%%%%%
52 %% Identification of the ROI for Fiber 1 %%
53 %%%%%%%%%%%%%%%%%%%%%%%%%%%%%%%%%%%%%%%%%%%%%%%%%%%%%%%%%%%%%%%%%%%%%%%%%%
54
55 ImageDim1 = size(I0_1);
```

```
56 I1map = zeros(ImageDim1);
57 figure , imshow(I0_1);
58 I1map(ymin_1:(ymin_1+height_1),xmin_1:(xmin_1+width_1),:) =
    1;
59 figure , imshow(I1map);
60
61 I1 = im2double(I0_1).*I1map;
62 figure , imshow(I1);
63
64 %% FIND INTENSITY THRESHOLD OF THE SQUARE including the
    first fiber
65 % use the histogram of the pixel intensity values to find
    the threshold
66 % and include in the ROI just the pixel with intensity
    higher than the threshold:
67
68 I1=imcrop(I1,[xmin_1 ymin_1 width_1 height_1]);
69 figure , imshow(I1);
70 [counts , grayLevels]=imhist(I1);
71 figure('DefaultAxesFontSize',18),bar(grayLevels ,counts ,'
    FaceColor',[0.93 0.70 0.19],'EdgeColor',[0.94 0.39 0], '
    BarWidth',1);
72 xlim([-0.0035 0.5]);
73 ylim([0 0.35*10^5]);
74 xlabel('Intensity')
75 ylabel('Counts (#)')
76
77 indI1 = find(I1>0.28);
78 szI1 = size(I1);
79 I1 = zeros(szI1);
80 I1(indI1) = 1;
81 figure , imshow(I1);
82
```

```
83 BW1 = im2bw(I1 , graythresh(I1));%Read grayscale image into
    the workspace
84 figure , imshow(BW1);
85
86 %% REMOVE SMALL CONNECTED REGIONS FROM ROI
87 % Removal of all connected regions with fewer than 50
    pixels:
88
89 BW1 = bwareaopen(BW1, 50);
90 figure , imshow(BW1);
91
92 %% FILL THE HOLES:
93
94 BW1 = imfill(BW1, 'holes');
95 %figure , imshow(BW1);
96
97 %% IDENTIFY THE CONNECTED REGIONS in the ROI:
98
99 [labelsI1 ,n1] = bwlabel(BW1, 8);
100 vRegion1 = [length(find(labelsI1==1)), length(find(labelsI1
    ==2)), length(find(labelsI1==3))];
101
102 %% SELECT THE LARGEST CONNECTED REGION
103 % Only the largest connected region is included in the ROI,
104 % all the other regions are excluded:
105
106 [max1, ind1] = max(vRegion1);
107 mainRegion1 = find(labelsI1==ind1);
108 labelsI1 = zeros(size(labelsI1));
109 labelsI1(mainRegion1) = 1;
110 figure , imshow(labelsI1 , []);
111
112 %% DILATE THE IMAGE TO IMPROVE THE ROI CONTOUR:
```

```
113 % to get a smoother ROI contour:
114
115 labelsI1 = imdilate(labelsI1 , strel('disk',1));
116 figure , imshow(labelsI1 , []);
117
118 %% FILL THE HOLES:
119
120 labelsI1 = imfill(labelsI1 , 'holes');
121 figure , imshow(labelsI1 , []);
```

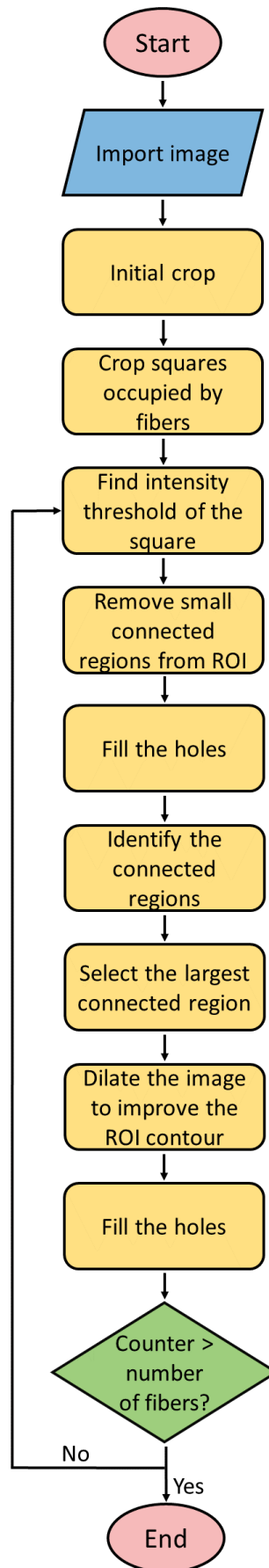


Figure E.1: **ROI detection algorithm.** Flow chart for the algorithm of identification of the ROI for each fiber contained in the starting image.

BIBLIOGRAPHY

- [1] Allison Okamura et al. “Haptics for Robot-Assisted Minimally Invasive Surgery.” In: Jan. 2007, pp. 361–372.
- [2] Wael Othman et al. “Tactile Sensing for Minimally Invasive Surgery: Conventional Methods and Potential Emerging Tactile Technologies”. In: *Frontiers in Robotics and AI* 8 (Jan. 2022). DOI: [10.3389/frobt.2021.705662](https://doi.org/10.3389/frobt.2021.705662).
- [3] Camran Nezhat et al. “Robotic-Assisted Laparoscopy vs Conventional Laparoscopy for the Treatment of Advanced Stage Endometriosis”. In: *Journal of minimally invasive gynecology* 22 (June 2014). DOI: [10.1016/j.jmig.2014.06.002](https://doi.org/10.1016/j.jmig.2014.06.002).
- [4] Sergio Portoles et al. “Evaluation of Haptic Feedback on Bimanually Teleoperated Laparoscopy for Endometriosis Surgery”. In: *IEEE Transactions on Biomedical Engineering* PP (Sept. 2018), pp. 1–1. DOI: [10.1109/TBME.2018.2870542](https://doi.org/10.1109/TBME.2018.2870542).
- [5] Gregory Tholey, Jaydev Desai, and Andres Castellanos. “Force Feedback Plays a Significant Role in Minimally Invasive Surgery: Results and Analysis”. In: *Annals of surgery* 241 (Feb. 2005), pp. 102–9. DOI: [10.1097/01.sla.0000149301.60553.1e](https://doi.org/10.1097/01.sla.0000149301.60553.1e).
- [6] Farshid Amirabdollahian et al. “Prevalence of haptic feedback in robot-mediated surgery: a systematic review of literature”. In: *Journal of Robotic Surgery* 12 (Mar. 2018). DOI: [10.1007/s11701-017-0763-4](https://doi.org/10.1007/s11701-017-0763-4).
- [7] Caroline Cao et al. “Can Surgeons Think and Operate with Haptics at the Same Time?” In: *Journal of gastrointestinal surgery : official journal of the Society for Surgery of the Alimentary Tract* 11 (Dec. 2007), pp. 1564–9. DOI: [10.1007/s11605-007-0279-8](https://doi.org/10.1007/s11605-007-0279-8).
- [8] James Gwilliam et al. “Human vs. robotic tactile sensing: Detecting lumps in soft tissue”. In: Apr. 2010, pp. 21–28. DOI: [10.1109/HAPTIC.2010.5444685](https://doi.org/10.1109/HAPTIC.2010.5444685).
- [9] “Safe and Effective Abdominal Pressure During Colonoscopy: Forearm Versus Open Hand Technique”. In: *Gastroenterology Nursing* 32 (Jan. 2009), pp. 31–32. DOI: [10.1097/SGA.0b013e31819c0e84](https://doi.org/10.1097/SGA.0b013e31819c0e84).

- [10] Julius Bernth et al. “Endoscope Force Generation and Intrinsic Sensing with Environmental Scaffolding”. In: May 2019, pp. 1940–1946. DOI: [10.1109/ICRA.2019.8793726](https://doi.org/10.1109/ICRA.2019.8793726).
- [11] Fabrizio Stracci, Manuel Zorzi, and Grazia Grazzini. “Colorectal Cancer Screening: Tests, Strategies, and Perspectives”. In: *Frontiers in Public Health* 210 (Oct. 2014). DOI: [10.3389/fpubh.2014.00210](https://doi.org/10.3389/fpubh.2014.00210).
- [12] Claudia D’Ettorre et al. “Accelerating Surgical Robotics Research: A Review of 10 Years With the da Vinci Research Kit”. In: *IEEE Robotics Automation Magazine* PP (Sept. 2021), pp. 2–24. DOI: [10.1109/MRA.2021.3101646](https://doi.org/10.1109/MRA.2021.3101646).
- [13] Soham Roy et al. “Medrobotics Flex System for Laryngeal Surgery: A Feasible Study in Two Cadavers”. In: *International Journal of Head and Neck Surgery* 7 (2016), pp. 204–206.
- [14] Andrew Brodie and Nikhil Vasdev. “The future of robotic surgery”. In: *The Annals of The Royal College of Surgeons of England* 100.Supplement 7 (2018). PMID: 30179048, pp. 4–13. DOI: [10.1308/rcsann.sup2.4](https://doi.org/10.1308/rcsann.sup2.4). eprint: <https://doi.org/10.1308/rcsann.sup2.4>. URL: <https://doi.org/10.1308/rcsann.sup2.4>.
- [15] Luigi Manfredi. “Endorobots for Colonoscopy: Design Challenges and Available Technologies”. In: *Frontiers in Robotics and AI* 8 (July 2021). DOI: [10.3389/frobt.2021.705454](https://doi.org/10.3389/frobt.2021.705454).
- [16] *AMBOSS Large intestine*. https://www.amboss.com/us/knowledge/Large_intestine. Accessed: 2023-03-27.
- [17] Jeffrey D. Hawel. “Force Application During Colonoscopy as a Marker of Competence: Development of a Novel Training Device”. MA thesis. The University of Western Ontario, 2020.
- [18] P. Frühmorgen and Ludwig Demling. “Complications of diagnostic and therapeutic colonoscopy in the Federal Republic of Germany. Results of an inquiry.” In: *Endoscopy* 11 2 (1979), pp. 146–50.
- [19] Mohammad Sarhan, Alexius Ramcharan, and Sarma Ponnappalli. “Splenic Injury after Elective Colonoscopy”. In: *JSLS : Journal of the Society of Laparoendoscopic Surgeons / Society of Laparoendoscopic Surgeons* 13 (Nov. 2008), pp. 616–9.

- [20] Lawrence J. Damore et al. "Colonoscopic perforations". In: *Diseases of the Colon & Rectum* 39 (1996), pp. 1308–1314.
- [21] Earl V. Thompson and Jonathan R. Snyder. "Recognition and Management of Colonic Perforation following Endoscopy". In: *Clinics in Colon and Rectal Surgery* 32 (2019), pp. 183–189.
- [22] Shi-Lun Cai et al. "Management of iatrogenic colorectal perforation: From surgery to endoscopy". In: *World journal of gastrointestinal endoscopy* 7 (July 2015), pp. 819–23. DOI: [10.4253/wjge.v7.i8.819](https://doi.org/10.4253/wjge.v7.i8.819).
- [23] Corey W. Iqbal et al. "Surgical management and outcomes of 165 colonoscopic perforations from a single institution." In: *Archives of surgery* 143 7 (2008), 701–6, discussion 706–7.
- [24] Vinay Kumar Rai and Nitin Mishra. "Colonoscopic Perforations". In: *Clinics in Colon and Rectal Surgery* 31 (2018), pp. 41–46.
- [25] Lucas Chartier, Erin Arthurs, and Maida Sewitch. "Patient Satisfaction with Colonoscopy: A Literature Review and Pilot Study". In: *Canadian journal of gastroenterology = Journal canadien de gastroenterologie* 23 (Apr. 2009), pp. 203–9. DOI: [10.1155/2009/903545](https://doi.org/10.1155/2009/903545).
- [26] Gianpiero Manes. "H. Messmann, Atlas of Colonoscopy. Techniques – Diagnosis – Interventional Procedures, Thieme Verlag, Stuttgart, Germany (2006) ISBN 3131405716 236 pp., Price €129.95". In: *Digestive and Liver Disease - DIG LIVER DIS* 38 (Oct. 2006), pp. 787–787. DOI: [10.1016/j.dld.2006.07.003](https://doi.org/10.1016/j.dld.2006.07.003).
- [27] Syed Shah et al. "Magnetic imaging of colonoscopy: An audit of looping, accuracy and ancillary maneuvers". In: *Gastrointestinal endoscopy* 52 (Aug. 2000), pp. 1–8. DOI: [10.1067/mge.2000.107296](https://doi.org/10.1067/mge.2000.107296).
- [28] Anders Mark-Christensen, Søren Brandsborg, and Lene Iversen. "Magnetic endoscopic imaging as an adjuvant to colonoscopy: A systematic review and analysis of randomized controlled trials". In: *Endoscopy* 47 (Dec. 2014). DOI: [10.1055/s-0034-1390767](https://doi.org/10.1055/s-0034-1390767).
- [29] Blake Hannaford et al. "Performance Evaluation of a Six-Axis Generalized Force-Reflecting Teleoperator". In: *Systems, Man and Cybernetics, IEEE Transactions on* 21 (June 1991), pp. 620–633. DOI: [10.1109/21.97455](https://doi.org/10.1109/21.97455).

- [30] Michael J. Massimino and Thomas B. Sheridan. “Teleoperator Performance with Varying Force and Visual Feedback”. In: *Human Factors: The Journal of Human Factors and Ergonomics Society* 36 (1994), pp. 145–157.
- [31] Christopher Wagner, Nicholas Stylopoulos, and Robert Howe. “The Role of Force Feedback in Surgery: Analysis of Blunt Dissection.” In: Jan. 2002, pp. 73–79. DOI: [10.1109/HAPTIC.2002.998943](https://doi.org/10.1109/HAPTIC.2002.998943).
- [32] Claudio Pacchierotti et al. “Two Finger Grasping Simulation with Cutaneous and Kinesthetic Force Feedback”. In: vol. 7282. June 2012, pp. 373–382. ISBN: 978-3-642-31400-1. DOI: [10.1007/978-3-642-31401-8_34](https://doi.org/10.1007/978-3-642-31401-8_34).
- [33] Leonardo Meli, Claudio Pacchierotti, and Domenico Prattichizzo. “Sensory Subtraction in Robot-Assisted Surgery: Fingertip Skin Deformation Feedback to Ensure Safety and Improve Transparency in Bimanual Haptic Interaction”. In: *Biomedical Engineering, IEEE Transactions on* 61 (Apr. 2014), pp. 1318–1327. DOI: [10.1109/TBME.2014.2303052](https://doi.org/10.1109/TBME.2014.2303052).
- [34] Nicola Diolaiti et al. “Stability of Haptic Rendering: Discretization, Quantization, Time Delay, and Coulomb Effects”. In: *Robotics, IEEE Transactions on* 22 (May 2006), pp. 256–268. DOI: [10.1109/TR0.2005.862487](https://doi.org/10.1109/TR0.2005.862487).
- [35] Domenico Prattichizzo, Claudio Pacchierotti, and Giulio Rosati. “Cutaneous Force Feedback as a Sensory Subtraction Technique in Haptics”. In: *IEEE Trans Haptics November* 5 (Aug. 2011). DOI: [10.1109/TOH.2012.15](https://doi.org/10.1109/TOH.2012.15).
- [36] Ryan Schoonmaker and Caroline Cao. “Vibrotactile force feedback system for minimally invasive surgical procedures”. In: Nov. 2006, pp. 2464–2469. ISBN: 1-4244-0100-3. DOI: [10.1109/ICSMC.2006.385233](https://doi.org/10.1109/ICSMC.2006.385233).
- [37] Weston Griffin, William Provancher, and Mark Cutkosky. “Feedback Strategies for Telemanipulation with Shared Control of Object Handling Forces”. In: *Presence* 14 (Dec. 2005), pp. 720–731. DOI: [10.1162/105474605775196634](https://doi.org/10.1162/105474605775196634).
- [38] Masaya Kitagawa et al. “Effect of sensory substitution on suture manipulation forces for surgical teleoperation”. In: *Studies in health technology and informatics* 98 (Feb. 2004), pp. 157–63. DOI: [10.3233/978-1-60750-942-4-157](https://doi.org/10.3233/978-1-60750-942-4-157).
- [39] Xiandi Wang et al. “Recent Progress in Electronic Skin”. In: *Advanced Science* 2 (July 2015). DOI: [10.1002/advs.201500169](https://doi.org/10.1002/advs.201500169).

- [40] Uzabakirho Pierre Claver and Gang Zhao. “Recent Progress in Flexible Pressure Sensors Based Electronic Skin”. In: *Advanced Engineering Materials* 23 (Feb. 2021), p. 2001187. DOI: [10.1002/adem.202001187](https://doi.org/10.1002/adem.202001187).
- [41] A.S. Fiorillo, Davide C. Critello, and Salvatore Pullano. “Theory, Technology and Applications of Piezoresistive Sensors: a Review”. In: *Sensors and Actuators A: Physical* 281 (July 2018). DOI: [10.1016/j.sna.2018.07.006](https://doi.org/10.1016/j.sna.2018.07.006).
- [42] Kang Lee et al. “Fabrication of Polymer-based Flexible Tactile Sensing Module with Metal Strain Gauges and Interconnector”. In: (Oct. 2006), pp. 742–745. DOI: [10.1109/ICSENS.2007.355575](https://doi.org/10.1109/ICSENS.2007.355575).
- [43] Fenlan Xu et al. “Recent Developments for Flexible Pressure Sensors: A Review”. In: *Micromachines* 9 (Nov. 2018), p. 580. DOI: [10.3390/mi9110580](https://doi.org/10.3390/mi9110580).
- [44] Z. H. Zhu. “Piezoresistive Strain Sensors Based on Carbon Nanotube Networks”. In: *IEEE Nanotechnology Magazine* (Apr. 2015), pp. 11–23. DOI: [10.1109/MNANO.2015.2409412](https://doi.org/10.1109/MNANO.2015.2409412).
- [45] Ning Hu et al. “Ultrasensitive strain sensors made from metal-coated carbon naofiller/epoxy composites”. In: *Carbon* 51 (Jan. 2013), pp. 202–212. DOI: [10.1016/j.carbon.2012.08.029](https://doi.org/10.1016/j.carbon.2012.08.029).
- [46] Shu Gong et al. “A wearable and highly sensitive pressure sensor with ultrathin gold nanowires”. In: *Nature communications* 5 (Feb. 2014), p. 3132. DOI: [10.1038/ncomms4132](https://doi.org/10.1038/ncomms4132).
- [47] R.s Timsit. “Electrical Contact Resistance: Properties of Stationary Interfaces”. In: *Components and Packaging Technologies, IEEE Transactions on* 22 (Apr. 1999), pp. 85–98. DOI: [10.1109/6144.759357](https://doi.org/10.1109/6144.759357).
- [48] Takao Someya et al. “A Large-Area, Flexible Pressure Sensor Matrix with Organic Field-Effect Transistors for Artificial Skin Applications”. In: *Proceedings of the National Academy of Sciences of the United States of America* 101 (Aug. 2004), pp. 9966–70. DOI: [10.1073/pnas.0401918101](https://doi.org/10.1073/pnas.0401918101).
- [49] MI Tiwana and Nigel Lovell. “A Review of Tactile Sensing Technologies with Applications in Biomedical Engineering”. In: *Sensors and Actuators A: Physical* 179 (June 2012), pp. 17–31. DOI: [10.1016/j.sna.2012.02.051](https://doi.org/10.1016/j.sna.2012.02.051).

- [50] Wufan Chen and Xin Yan. “Progress in achieving high-performance piezoresistive and capacitive flexible pressure sensors: A review”. In: *Journal of Materials Science Technology* 43 (Apr. 2020). DOI: [10.1016/j.jmst.2019.11.010](https://doi.org/10.1016/j.jmst.2019.11.010).
- [51] Rajesh Surapaneni et al. “A three-axis high-resolution capacitive tactile imager system based on floating comb electrodes”. In: *Journal of Micromechanics and Microengineering* 23 (May 2013), p. 075004. DOI: [10.1088/0960-1317/23/7/075004](https://doi.org/10.1088/0960-1317/23/7/075004).
- [52] Stefan Mannsfeld et al. “Highly sensitive flexible pressure sensors with microstructured rubber dielectric layers”. In: *Nature materials* 9 (Oct. 2010), pp. 859–64. DOI: [10.1038/nmat2834](https://doi.org/10.1038/nmat2834).
- [53] Yongsong Luo et al. “Flexible Capacitive Pressure Sensor Enhanced by Tilted Micropillar Arrays”. In: *ACS Applied Materials Interfaces* 11 (Apr. 2019). DOI: [10.1021/acsami.9b03718](https://doi.org/10.1021/acsami.9b03718).
- [54] Gregor Schwartz et al. “Flexible polymer transistors with high pressure sensitivity for application in electronic skin and health monitoring”. In: *Nature communications* 4 (May 2013), p. 1859. DOI: [10.1038/ncomms2832](https://doi.org/10.1038/ncomms2832).
- [55] Tie Li et al. “Flexible Capacitive Tactile Sensor Based on Micropatterned Dielectric Layer”. In: *Small* 12 (June 2016). DOI: [10.1002/smll.201600760](https://doi.org/10.1002/smll.201600760).
- [56] Cheng Chi et al. “Recent Progress in Technologies for Tactile Sensors”. In: *Sensors* 18 (Mar. 2018), p. 948. DOI: [10.3390/s18040948](https://doi.org/10.3390/s18040948).
- [57] Guoquan Suo et al. “Piezoelectric and Triboelectric Dual Effects in Mechanical Energy Harvesting Using BaTiO₃/Polydimethylsiloxane Composite Film”. In: *ACS Applied Materials Interfaces* 8 (Dec. 2016). DOI: [10.1021/acsami.6b11108](https://doi.org/10.1021/acsami.6b11108).
- [58] Xiaojuan Hou et al. “Flexible Piezoelectric Nanofibers/PDMS-based Pressure Sensor for Self-powered Human Motion Monitoring”. In: *Energy Technology* 8 (Mar. 2020). DOI: [10.1002/ente.201901242](https://doi.org/10.1002/ente.201901242).
- [59] Majid Al-Ruqeishi and Tariq Mohiuddin. “Piezoelectric Nanogenerator Based on ZnO Nanorods”. In: *Arabian Journal of Chemistry* 12 (Dec. 2016). DOI: [10.1016/j.arabjc.2016.12.010](https://doi.org/10.1016/j.arabjc.2016.12.010).

- [60] Mingyuan Ma et al. “Self-powered flexible antibacterial tactile sensor based on triboelectric-piezoelectric-pyroelectric multi-effect coupling mechanism”. In: *Nano Energy* 66 (Sept. 2019), p. 104105. DOI: [10.1016/j.nanoen.2019.104105](https://doi.org/10.1016/j.nanoen.2019.104105).
- [61] Kyungrim Kim et al. “Static Force Measurement Using Piezoelectric Sensors”. In: *Journal of Sensors* 2021 (Mar. 2021), pp. 1–8. DOI: [10.1155/2021/6664200](https://doi.org/10.1155/2021/6664200).
- [62] G.M. Krishna and K. Rajanna. “Tactile sensor based on piezoelectric resonance”. In: *IEEE Sensors Journal* 4.5 (2004), pp. 691–697. DOI: [10.1109/JSEN.2004.833505](https://doi.org/10.1109/JSEN.2004.833505).
- [63] Frank Shellock, Terry Woods, and John Crues. “MR Labeling Information for Implants and Devices: Explanation of Terminology”. In: *Radiology* 253 (Oct. 2009), pp. 26–30. DOI: [10.1148/radiol.2531091030](https://doi.org/10.1148/radiol.2531091030).
- [64] Hao Su et al. “Fiber Optic Force Sensors for MRI-Guided Interventions and Rehabilitation: A Review”. In: *IEEE Sensors Journal* PP (Jan. 2017), pp. 1–1. DOI: [10.1109/JSEN.2017.2654489](https://doi.org/10.1109/JSEN.2017.2654489).
- [65] Roger Gassert et al. “Sensors for Applications in Magnetic Resonance Environments”. In: *Mechatronics, IEEE/ASME Transactions on* 13 (July 2008), pp. 335–344. DOI: [10.1109/TMECH.2008.924113](https://doi.org/10.1109/TMECH.2008.924113).
- [66] Samuel Kesner and Robert Howe. “Design Principles for Rapid Prototyping Forces Sensors Using 3-D Printing”. In: *IEEE/ASME transactions on mechatronics : a joint publication of the IEEE Industrial Electronics Society and the ASME Dynamic Systems and Control Division* PP (July 2011), pp. 1–5. DOI: [10.1109/TMECH.2011.2160353](https://doi.org/10.1109/TMECH.2011.2160353).
- [67] Hao Su and Gregory Fischer. “A 3-Axis Optical Force/Torque Sensor for Prostate Needle Placement in Magnetic Resonance Imaging Environments”. In: Dec. 2009, pp. 5–9. DOI: [10.1109/TEPRA.2009.5339654](https://doi.org/10.1109/TEPRA.2009.5339654).
- [68] Pinyo Puangmali et al. “Miniature 3Axis Distal Force Sensor for Minimally Invasive Surgical Palpation”. In: *IEEE-ASME Transactions on Mechatronics - IEEE-ASME TRANS MECHATRON* 17 (Aug. 2012), pp. 646–656. DOI: [10.1109/TMECH.2011.2116033](https://doi.org/10.1109/TMECH.2011.2116033).

- [69] Panagiotis Polygerinos et al. “MRI-Compatible Intensity-Modulated Force Sensor for Cardiac Catheterization Procedures”. In: *IEEE transactions on bio-medical engineering* 58 (Nov. 2010), pp. 721–6. DOI: [10.1109/TBME.2010.2095853](https://doi.org/10.1109/TBME.2010.2095853).
- [70] Alfredo Lamberti et al. “Detection, Localization and Quantification of Impact Events on a Stiffened Composite Panel with Embedded Fiber Bragg Grating Sensor Networks”. In: *Sensors* 17 (Apr. 2017), p. 743. DOI: [10.3390/s17040743](https://doi.org/10.3390/s17040743).
- [71] Daniela Presti et al. “Fiber Bragg Gratings for Medical Applications and Future Challenges: A Review”. In: *IEEE Access* PP (Aug. 2020), pp. 1–1. DOI: [10.1109/ACCESS.2020.3019138](https://doi.org/10.1109/ACCESS.2020.3019138).
- [72] K.O. Hill and Gerald Meltz. “Fiber Bragg Grating Technology Fundamentals and Overview”. In: *Lightwave Technology, Journal of* 15 (Sept. 1997), pp. 1263–1276. DOI: [10.1109/50.618320](https://doi.org/10.1109/50.618320).
- [73] Berk Gonenc et al. “Design of 3-DOF Force Sensing Micro-Forceps for Robot Assisted Vitreoretinal Surgery”. In: *Conference proceedings : ... Annual International Conference of the IEEE Engineering in Medicine and Biology Society. IEEE Engineering in Medicine and Biology Society. Conference* 2013 (July 2013), pp. 5686–5689. DOI: [10.1109/EMBC.2013.6610841](https://doi.org/10.1109/EMBC.2013.6610841).
- [74] Santhi Analytis et al. “Detection of Membrane Puncture with Haptic Feedback using a Tip-Force Sensing Needle”. In: *IEEE International Conference on Intelligent Robots and Systems* 2014 (Oct. 2014), pp. 3975–3981. DOI: [10.1109/IROS.2014.6943121](https://doi.org/10.1109/IROS.2014.6943121).
- [75] Daniele Tosi. “Review and Analysis of Peak Tracking Techniques for Fiber Bragg Grating Sensors”. In: *Sensors* 17 (Oct. 2017), p. 2368. DOI: [10.3390/s17102368](https://doi.org/10.3390/s17102368).
- [76] Jas Singh, J. Potgieter, and Peter Xu. “Fibre optic force sensor for flexible bevel tip needles in minimally invasive surgeries”. In: *Int. J. of Biomechatronics and Biomedical Robotics* 2 (Jan. 2013), pp. 135–140. DOI: [10.1504/IJBBR.2013.058742](https://doi.org/10.1504/IJBBR.2013.058742).
- [77] Jinesh Mathew et al. “In-Fibre Fabry-Perot Cavity Sensor for High Temperature Applications”. In: *Journal of Lightwave Technology* 33 (June 2015), pp. 1–1. DOI: [10.1109/JLT.2015.2397936](https://doi.org/10.1109/JLT.2015.2397936).

- [78] Xuan Liu et al. “Miniature fiber-optic force sensor for vitreoretinal microsurgery based on low-coherence Fabry-Perot interferometry”. In: *Biomedical optics express* 3 (May 2012), pp. 1062–76. DOI: [10.1364/B0E.3.001062](https://doi.org/10.1364/B0E.3.001062).
- [79] Zonglai Mo et al. “A temperature-compensated optical fiber force sensor for minimally invasive surgeries”. In: Dec. 2015, p. 966850. DOI: [10.1117/12.2202539](https://doi.org/10.1117/12.2202539).
- [80] Arata et al. “Modular Optic Force Sensor for a Surgical Device Using a Fabry–Perot Interferometer”. In: *Applied Sciences* 9 (Aug. 2019), p. 3454. DOI: [10.3390/app9173454](https://doi.org/10.3390/app9173454).
- [81] Bing Yu, Anbo Wang, and Gary Pickrell. “Analysis of white-light fiber Fabry-Perot interferometric sensors”. In: *Proceedings of SPIE - The International Society for Optical Engineering* 5589 (Dec. 2004). DOI: [10.1117/12.570444](https://doi.org/10.1117/12.570444).
- [82] Stephen McKinley et al. “A single-use haptic palpation probe for locating subcutaneous blood vessels in robot-assisted minimally invasive surgery”. In: Aug. 2015, pp. 1151–1158. DOI: [10.1109/CoASE.2015.7294253](https://doi.org/10.1109/CoASE.2015.7294253).
- [83] Veaceslav Arabagi et al. “Biocompatible Pressure Sensing Skins for Minimally Invasive Surgical Instruments”. In: *IEEE Sensors Journal* 16 (Jan. 2015), pp. 1–1. DOI: [10.1109/JSEN.2015.2498481](https://doi.org/10.1109/JSEN.2015.2498481).
- [84] Amit Srivastava et al. “Design of an ultra thin strain sensor using superelastic nitinol for applications in minimally invasive surgery”. In: July 2016, pp. 794–799. DOI: [10.1109/AIM.2016.7576865](https://doi.org/10.1109/AIM.2016.7576865).
- [85] Uikyum Kim et al. “A Surgical Palpation Probe With 6-Axis Force/Torque Sensing Capability for Minimally Invasive Surgery”. In: *IEEE Transactions on Industrial Electronics* PP (Aug. 2017), pp. 1–1. DOI: [10.1109/tie.2017.2739681](https://doi.org/10.1109/tie.2017.2739681).
- [86] Feng Ju et al. “A variable-impedance piezoelectric tactile sensor with tunable sensing performance for tissue hardness sensing in robotic tumor palpation”. In: *Smart Materials and Structures* 27 (Oct. 2018). DOI: [10.1088/1361-665X/aae54f](https://doi.org/10.1088/1361-665X/aae54f).
- [87] Claudio Pacchierotti, Domenico Prattichizzo, and Katherine J. Kuchenbecker. “Cutaneous Feedback of Fingertip Deformation and Vibration for Palpation in Robotic Surgery”. In: *IEEE Transactions on Biomedical Engineering* 63.2 (2016), pp. 278–287. DOI: [10.1109/TBME.2015.2455932](https://doi.org/10.1109/TBME.2015.2455932).

- [88] Tianliang Li and Chaoyang Shi. “A High-Sensitivity Tactile Sensor Array Based on Fiber Bragg Grating Sensing for Tissue Palpation in Minimally Invasive Surgery”. In: *IEEE/ASME Transactions on Mechatronics* PP (July 2018), pp. 1–1. DOI: [10.1109/TMECH.2018.2856897](https://doi.org/10.1109/TMECH.2018.2856897).
- [89] Hao Su et al. “An MRI-Guided Telesurgery System Using a Fabry-Perot Interferometry Force Sensor and a Pneumatic Haptic Device”. In: *Annals of Biomedical Engineering* 45 (Apr. 2017). DOI: [10.1007/s10439-017-1839-z](https://doi.org/10.1007/s10439-017-1839-z).
- [90] Wenjie Lai et al. “An Integrated Sensor-Model Approach for Haptic Feedback of Flexible Endoscopic Robots”. In: *Annals of Biomedical Engineering* (Sept. 2019). DOI: [10.1007/s10439-019-02352-8](https://doi.org/10.1007/s10439-019-02352-8).
- [91] Tetsuyou Watanabe et al. “Force Sensor Attachable to Thin Fiberscopes/Endoscopes Utilizing High Elasticity Fabric”. In: *Sensors (Basel, Switzerland)* 14 (Mar. 2014), pp. 5207–20. DOI: [10.3390/s140305207](https://doi.org/10.3390/s140305207).
- [92] Sanja Dogramadzi et al. “Recording forces exerted on the bowel wall during colonoscopy: In vitro evaluation”. In: *The international journal of medical robotics + computer assisted surgery : MRCAS* 1 (Dec. 2005), pp. 89–97. DOI: [10.1002/rcs.61](https://doi.org/10.1002/rcs.61).
- [93] Max McCandless et al. “A Soft Robotic Sleeve for Safer Colonoscopy Procedures”. In: *IEEE Robotics and Automation Letters* PP (Apr. 2021), pp. 1–1. DOI: [10.1109/LRA.2021.3073651](https://doi.org/10.1109/LRA.2021.3073651).
- [94] Arjo Loeve, Paul Fockens, and Paul Breedveld. “Mechanical Analysis of Insertion Problems and Pain During Colonoscopy: Why Highly Skill-Dependent Colonoscopy Routines are Necessary in the First Place... and How They May be Avoided”. In: *Canadian journal of gastroenterology = Journal canadien de gastroenterologie* 27 (May 2013), pp. 293–302. DOI: [10.1155/2013/353760](https://doi.org/10.1155/2013/353760).
- [95] R. Kozarek et al. “Air-pressure-induced colon injury during diagnostic colonoscopy.” In: *Gastroenterology* 78 (1980), pp. 7–14.
- [96] Amore V. Burt. “PNEUMATIC RUPTURE OF THE INTESTINAL CANAL: WITH EXPERIMENTAL DATA SHOWING THE MECHANISM OF PERFORATION AND THE PRESSURE REQUIRED”. In: *Archives of Surgery* 22.6 (June 1931), pp. 875–902. ISSN: 0272-5533. DOI: [10.1001/archsurg.1931.01160060003001](https://doi.org/10.1001/archsurg.1931.01160060003001). eprint: <https://jamanetwork.com/journals/>

- jamasurgery/articlepdf/540467/archsurg_22_6_001.pdf. URL: <https://doi.org/10.1001/archsurg.1931.01160060003001>.
- [97] N. M. Desouza et al. “Combined MRI and fibreoptic colonoscopy: technical considerations and clinical feasibility”. In: *Minimally Invasive Therapy & Allied Technologies* 9.1 (2000), pp. 25–30. DOI: [10.3109/13645700009063042](https://doi.org/10.3109/13645700009063042). eprint: <https://doi.org/10.3109/13645700009063042>. URL: <https://doi.org/10.3109/13645700009063042>.
- [98] OpenStax University Physics - All Volumes. Derived from University Physics by OpenStax University Physics. In: (). URL: <https://cnx.org/contents/pZH6GMP0@1.39:ndvbjZv5@2/Total-Internal-Reflection.%20Accessed%2001%20March%202020..>
- [99] Katsunari Okamoto. “Chapter 1 - Wave theory of optical waveguides”. In: *Fundamentals of Optical Waveguides (Second Edition)*. Ed. by Katsunari Okamoto. Second Edition. Burlington: Academic Press, 2006, pp. 1–12. ISBN: 978-0-12-525096-2. DOI: <https://doi.org/10.1016/B978-012525096-2/50002-7>. URL: <https://www.sciencedirect.com/science/article/pii/B9780125250962500027>.
- [100] Martin H. Weik. “Fresnel reflection loss”. In: *Computer Science and Communications Dictionary*. Boston, MA: Springer US, 2001, pp. 657–657. ISBN: 978-1-4020-0613-5. DOI: [10.1007/1-4020-0613-6_7725](https://doi.org/10.1007/1-4020-0613-6_7725). URL: https://doi.org/10.1007/1-4020-0613-6_7725.
- [101] Orazio Svelto. *Principles Of Lasers*. Springer, Boston, MA, 2010. ISBN: 978-1-4419-3289-1. DOI: [10.1007/978-1-4757-6266-2](https://doi.org/10.1007/978-1-4757-6266-2). URL: <https://doi.org/10.1007/978-1-4757-6266-2>.
- [102] Omary MA and Patterson HH. “Luminescence, Theory”. In: *Encyclopedia of Spectroscopy and Spectrometry*. Ed. by John L. Holmes John Lindon George E. Tranter. First Edition. Elsevier, 2000, pp. 1372–1391. ISBN: 0-12-226680-3. DOI: [10.1016/B978-0-12-374413-5.00193-7](https://doi.org/10.1016/B978-0-12-374413-5.00193-7). URL: <https://vdoc.pub/documents/encyclopedia-of-spectroscopy-and-spectrometry-6sn2qnvddv00>.
- [103] Philip Yip. “Nanometrology using Time-Resolved Fluorescence”. PhD thesis. Apr. 2016. DOI: [10.13140/RG.2.1.4045.2084](https://doi.org/10.13140/RG.2.1.4045.2084).

- [104] Joseph R. Lakowicz. “Introduction to Fluorescence”. In: *Lakowicz J.R. (eds) Principles of Fluorescence Spectroscopy. Springer, Boston, MA, 2006 (1999)*. DOI: https://doi.org/10.1007/978-1-4757-3061-6_1.
- [105] “Nanoscience vs Nanotechnology—Defining the Field”. In: *ACS Nano* 9.3 (2015). PMID: 25802086, pp. 2215–2217. DOI: [10.1021/acs.nano.5b01418](https://doi.org/10.1021/acs.nano.5b01418). eprint: <https://doi.org/10.1021/acs.nano.5b01418>. URL: <https://doi.org/10.1021/acs.nano.5b01418>.
- [106] Chuanhui Huang et al. “Effect of structure: A new insight into nanoparticle assemblies from inanimate to animate”. In: *Science Advances* 6 (May 2020), eaba1321. DOI: [10.1126/sciadv.aba1321](https://doi.org/10.1126/sciadv.aba1321).
- [107] V. Pokropivny and V. Skorokhod. “Classification of nanostructures by dimensionality and concept of surface forms engineering in nanomaterial science”. In: *Materials Science and Engineering: C* 27 (Sept. 2007), pp. 990–993. DOI: [10.1016/j.msec.2006.09.023](https://doi.org/10.1016/j.msec.2006.09.023).
- [108] Xiaobo Chen and Annabella Selloni. “Introduction: Titanium Dioxide (TiO₂) Nanomaterials”. In: *Chemical reviews* 114 (Oct. 2014), pp. 9281–2. DOI: [10.1021/cr500422r](https://doi.org/10.1021/cr500422r).
- [109] Shu Gong and Wenlong Cheng. “One-Dimensional Nanomaterials for Soft Electronics”. In: *Advanced Electronic Materials* 3 (Dec. 2016), p. 1600314. DOI: [10.1002/aelm.201600314](https://doi.org/10.1002/aelm.201600314).
- [110] Fatma Hadeif. “An Introduction to Nanomaterials”. In: May 2018, pp. 1–58. ISBN: 978-3-319-76089-6. DOI: [10.1007/978-3-319-76090-2_1](https://doi.org/10.1007/978-3-319-76090-2_1).
- [111] Bansi Dhar Malhotra and Md. Azahar Ali. “Chapter 1 - Nanomaterials in Biosensors: Fundamentals and Applications”. In: *Nanomaterials for Biosensors*. Ed. by Bansi Dhar Malhotra and Md. Azahar Ali. Micro and Nano Technologies. William Andrew Publishing, 2018, pp. 1–74. ISBN: 978-0-323-44923-6. DOI: <https://doi.org/10.1016/B978-0-323-44923-6.00001-7>. URL: <https://www.sciencedirect.com/science/article/pii/B9780323449236000017>.
- [112] Gregory Guisbiers, Sergio Mejía-Rosales, and Leonard Francis. “Nanomaterial Properties: Size and Shape Dependencies”. In: *Journal of Nanomaterials* 2012 (Dec. 2012). DOI: [10.1155/2012/180976](https://doi.org/10.1155/2012/180976).

- [113] Sneha Mohan Bhagyaraj and Oluwatobi Oluwafemi. “Nanotechnology: The Science of the Invisible”. In: Jan. 2018, pp. 1–18. ISBN: 9780081019757. DOI: [10.1016/B978-0-08-101975-7.00001-4](https://doi.org/10.1016/B978-0-08-101975-7.00001-4).
- [114] Oleg D. Neikov. “Chapter 4 - Nanopowders”. In: *Handbook of Non-Ferrous Metal Powders*. Ed. by Oleg D. Neikov et al. Oxford: Elsevier, 2009, pp. 80–101. ISBN: 978-1-85617-422-0. DOI: <https://doi.org/10.1016/B978-1-85617-422-0.00004-5>. URL: <https://www.sciencedirect.com/science/article/pii/B9781856174220000045>.
- [115] Karl F. Renk. “Quantum Wire and Quantum Dot Laser”. In: *Basics of Laser Physics: For Students of Science and Engineering*. Cham: Springer International Publishing, 2017, pp. 521–532. ISBN: 978-3-319-50651-7. DOI: [10.1007/978-3-319-50651-7_27](https://doi.org/10.1007/978-3-319-50651-7_27). URL: https://doi.org/10.1007/978-3-319-50651-7_27.
- [116] Anika Asha and Ravin Narain. “Nanomaterials properties”. In: Jan. 2020, pp. 343–359. ISBN: 9780128168066. DOI: [10.1016/B978-0-12-816806-6.00015-7](https://doi.org/10.1016/B978-0-12-816806-6.00015-7).
- [117] Emil Roduner. “Size matters: why nanomaterials are different”. In: *Chem. Soc. Rev.* 35 (7 2006), pp. 583–592. DOI: [10.1039/B502142C](https://doi.org/10.1039/B502142C). URL: <http://dx.doi.org/10.1039/B502142C>.
- [118] X. Tong and Z.M. Wang. *Core/Shell Quantum Dots: Synthesis, Properties and Devices*. Lecture Notes in Nanoscale Science and Technology. Springer International Publishing, 2020. ISBN: 9783030465964. URL: <https://books.google.fr/books?id=hOPuDwAAQBAJ>.
- [119] Peter Reiss, Myriam Protière, and Liang Li. “Core/Shell semiconductor nanocrystals.” In: *Small* 5 2 (2009), pp. 154–68.
- [120] Xiangkai Liu et al. “Optimum Quantum Yield of the Light Emission from 2 to 10 nm Hydrosilylated Silicon Quantum Dots”. In: *Particle Particle Systems Characterization* 33 (Dec. 2015), n/a–n/a. DOI: [10.1002/ppsc.201500148](https://doi.org/10.1002/ppsc.201500148).
- [121] Tae-Ho Kim et al. “Fully Stretchable Optoelectronic Sensors Based on Colloidal Quantum Dots for Sensing Photoplethysmographic Signals”. In: *ACS nano* 11.6 (June 2017), pp. 5992–6003. ISSN: 1936-0851. DOI: [10.1021/acsnano.7b01894](https://doi.org/10.1021/acsnano.7b01894).

- [122] Shikha Jindal et al. “Green synthesis of CuInS₂/ZnS core-shell quantum dots by facile solvothermal route with enhanced optical properties”. In: *Journal of Physics and Chemistry of Solids* 114 (Nov. 2017). DOI: [10.1016/j.jpcs.2017.11.026](https://doi.org/10.1016/j.jpcs.2017.11.026).
- [123] Peter Reiss, Myriam Protière, and Liang Li. “Core/Shell Semiconductor Nanocrystals”. In: *Small (Weinheim an der Bergstrasse, Germany)* 5 (Jan. 2009), pp. 154–68. DOI: [10.1002/smll.200800841](https://doi.org/10.1002/smll.200800841).
- [124] MA Hines and guyot-sionnest Philippe. “ChemInform Abstract: Synthesis and Characterization of Strongly Luminescing ZnS-Capped CdSe Nanocrystals”. In: *Cheminform* 27 (May 2010). DOI: [10.1002/chin.199619004](https://doi.org/10.1002/chin.199619004).
- [125] Jordi Aguilera Sigalat et al. “Highly fluorescent and photostable organic-and water-soluble CdSe/ZnS core-shell quantum dots capped with thiols”. In: *RSC Advances* 2 (Feb. 2012), p. 1632. DOI: [10.1039/c1ra01005k](https://doi.org/10.1039/c1ra01005k).
- [126] N. Fernández-Delgado et al. “Structural and chemical characterization of CdSe-ZnS core-shell quantum dots”. In: *Applied Surface Science* 457 (June 2018). DOI: [10.1016/j.apsusc.2018.06.149](https://doi.org/10.1016/j.apsusc.2018.06.149).
- [127] Eva Bladt et al. “Atomic Structure of Wurtzite CdSe (Core)/CdS (Giant Shell) Nanobullets Related to Epitaxy and Growth”. In: *Journal of the American Chemical Society* 138 (Oct. 2016). DOI: [10.1021/jacs.6b06443](https://doi.org/10.1021/jacs.6b06443).
- [128] Laurent Balet et al. “Inverted Core/Shell Nanocrystals Continuously Tunable between Type-I and Type-II Localization Regimes”. In: *Nano Letters - NANO LETT* 4 (July 2004). DOI: [10.1021/nl049146c](https://doi.org/10.1021/nl049146c).
- [129] Sungjee Kim et al. “Type-II quantum dots: CdTe/CdSe(core/shell) and CdSe/ZnTe(core/shell) heterostructures”. In: *Journal of the American Chemical Society* 125 (Oct. 2003), pp. 11466–7. DOI: [10.1021/ja0361749](https://doi.org/10.1021/ja0361749).
- [130] Patrick Winter et al. “Piezoelectric Effect at Nanoscale”. In: Jan. 2012, pp. 2085–2099. ISBN: 978-90-481-9750-7. DOI: [10.1007/978-90-481-9751-4_273](https://doi.org/10.1007/978-90-481-9751-4_273).
- [131] Walter Guyton Cady. “Piezoelectricity : an introduction to the theory and applications of electromechanical phenomena in crystals”. In: 1946.
- [132] Z. L. Wang. “Nanopiezotronics”. In: *Advanced Materials* (Mar. 2007). DOI: [10.1002/adma.200602918](https://doi.org/10.1002/adma.200602918).

- [133] Zhong Wang. “Nanogenerators, self-powered systems, blue energy, piezotronics and piezo-phototronics – A recall on the original thoughts for coining these fields”. In: *Nano Energy* 54 (Oct. 2018). DOI: [10.1016/j.nanoen.2018.09.068](https://doi.org/10.1016/j.nanoen.2018.09.068).
- [134] Kyle B. Ford et al. “Optical response to low applied pressure in a quantum dot nanocomposite”. In: *Materials Letters* 106 (2013), pp. 301–303.
- [135] Esteban Pedrueza et al. “The effect of quantum size confinement on the optical properties of PbSe nanocrystals under exposure to heat and hydrostatic pressure.” In: *Nanotechnology* 24 20 (2013), p. 205701.
- [136] Yan Cheng Lin et al. “Photoluminescence and time-resolved carrier dynamics in thiol-capped CdTe nanocrystals under high pressure.” In: *Nanoscale* 5 8 (2013), pp. 3400–5.
- [137] Bosang Kim et al. “Interdot interactions and band gap changes in CdSe nanocrystal arrays at elevated pressure”. In: *Journal of Applied Physics* 89 (June 2001), pp. 8127–8140. DOI: [10.1063/1.1369405](https://doi.org/10.1063/1.1369405).
- [138] Hai Ming Fan et al. “High pressure photoluminescence and Raman investigations of CdSe/ZnS core/shell quantum dots”. In: *Applied Physics Letters* 90 (Feb. 2007), pp. 021921–021921. DOI: [10.1063/1.2430772](https://doi.org/10.1063/1.2430772).
- [139] C Yuan et al. “Studies on the electronic and vibrational states of colloidal CdSe/ZnS quantum dots under high pressures”. In: *Nanotechnology* 18 (Apr. 2007), p. 185402. DOI: [10.1088/0957-4484/18/18/185402](https://doi.org/10.1088/0957-4484/18/18/185402).
- [140] Robert Meulenbergh and Geoffrey Strouse. “Pressure-induced electronic coupling in CdSe semiconductor quantum dots”. In: *Physical Review B* 66 (July 2002). DOI: [10.1103/PhysRevB.66.035317](https://doi.org/10.1103/PhysRevB.66.035317).
- [141] Paulo Antunes et al. “Mechanical Properties of Optical Fibers”. In: Feb. 2012. ISBN: 978-953-51-0091-1. DOI: [10.5772/26515](https://doi.org/10.5772/26515).
- [142] Yue Li et al. “Optical-Waveguide Based Tactile Sensing for Surgical Instruments of Minimally Invasive Surgery”. In: *Frontiers in Robotics and AI* 8 (2022). ISSN: 2296-9144. DOI: [10.3389/frobt.2021.773166](https://doi.org/10.3389/frobt.2021.773166). URL: <https://www.frontiersin.org/articles/10.3389/frobt.2021.773166>.
- [143] Federica De Chiara et al. “Design of optical waveguide channels for 3D distributed tactile sensing”. In: *2021 IEEE Sensors*. 2021, pp. 1–4. DOI: [10.1109/SENSORS47087.2021.9639611](https://doi.org/10.1109/SENSORS47087.2021.9639611).

- [144] Danqian Cao et al. “Polymer-Based Optical Waveguide Triaxial Tactile Sensing for 3-Dimensional Curved Shell”. In: *IEEE Robotics and Automation Letters* 7 (Apr. 2022), pp. 1–1. DOI: [10.1109/LRA.2022.3146596](https://doi.org/10.1109/LRA.2022.3146596).
- [145] M.K. Barnoski. “CHAPTER 3 - COUPLING COMPONENTS FOR OPTICAL FIBER WAVEGUIDES”. In: *Fundamentals of Optical Fiber Communications (Second Edition)*. Ed. by Michael K. Barnoski. Second Edition. Academic Press, 1981, pp. 147–186. ISBN: 978-0-12-079151-4. DOI: <https://doi.org/10.1016/B978-0-12-079151-4.50007-8>. URL: <https://www.sciencedirect.com/science/article/pii/B9780120791514500078>.
- [146] Dietrich Marcuse. “Microdeformation losses of single-mode fibers”. In: *Appl. Opt.* 23.7 (Apr. 1984), pp. 1082–1091. DOI: [10.1364/AO.23.001082](https://doi.org/10.1364/AO.23.001082). URL: <http://opg.optica.org/ao/abstract.cfm?URI=ao-23-7-1082>.
- [147] Crespi A. “Integrated optical circuits for biosensing and quantum information by femtosecond laser microfabrication”. PhD thesis. Politecnico di Milano, 2012.
- [148] Roger French et al. “Optical properties of materials for concentrator photovoltaic systems”. In: vol. 95. July 2009, pp. 000394–000399. DOI: [10.1109/PVSC.2009.5411657](https://doi.org/10.1109/PVSC.2009.5411657).
- [149] F. J. J. Clarke. “Problems of spectrofluorimetric standards for reflection and colorimetric use”. In: *NPL Report MOM 12, National Physical Laboratory Division of Mechanical and Optical Metrology* (Aug. 1975).
- [150] P. J. Clarke. “A national measurement good practice guide no. 97 - Regular Transmittance Measurements”. In: *NPL Report, National Physical Laboratory Division of Mechanical and Optical Metrology* (Mar. 2006).
- [151] Sukhwinder Bhullar, Ayşe Çelik Bedeloğlu, and Martin Jun. “Characterization and Auxetic effect of Polytetrafluoroethylene Tubular structure”. In: *International Journal of Advanced Science and Engineering* 1 (Jan. 2014), pp. 8–13.
- [152] Min K. Yang, Roger H. French, and Edward W. Tokarsky. “Optical properties of Teflon® AF amorphous fluoropolymers”. In: *Journal of Micro/Nanolithography, MEMS, and MOEMS* 7.3 (2008), pp. 1–9. DOI: [10.1117/1.2965541](https://doi.org/10.1117/1.2965541). URL: <https://doi.org/10.1117/1.2965541>.

- [153] Raja Izamshah et al. “Study of Surface Roughness on Milling Unfilled-polyetheretherketones Engineering Plastics”. In: *Procedia Engineering* 68 (Dec. 2013), pp. 654–660. DOI: [10.1016/j.proeng.2013.12.235](https://doi.org/10.1016/j.proeng.2013.12.235).
- [154] Fred Rost. “Fluorescence Microscopy, Applications.” In: *Encyclopedia of Spectroscopy and Spectrometry, Third Edition, Elsevier Ltd, Ashfield, New South Wales, Australia* (2017), pp. 565–570. DOI: https://doi.org/10.1007/978-1-4757-3061-6_1.
- [155] Federica De Chiara, Shuxin Wang, and Hongbin Liu. “Creating a Soft Tactile Skin Employing Fluorescence Based Optical Sensing”. In: *IEEE Robotics and Automation Letters* 5 (2020), pp. 3375–3381.
- [156] Asghar Ataollahi et al. “Tactile sensor array using prismatic-tip optical fibers for dexterous robotic hands”. In: *2010 IEEE/RSJ International Conference on Intelligent Robots and Systems*. 2010, pp. 910–915. DOI: [10.1109/IRROS.2010.5649109](https://doi.org/10.1109/IRROS.2010.5649109).
- [157] Asghar Ataollahi et al. “Novel Force Sensing Approach Employing Prismatic-Tip Optical Fiber Inside an Orthoplanar Spring Structure”. In: *Mechatronics, IEEE/ASME Transactions on* 19 (Feb. 2014), pp. 121–130. DOI: [10.1109/TMECH.2012.2222906](https://doi.org/10.1109/TMECH.2012.2222906).
- [158] Hui Xie et al. “An Optical Tactile Array Probe Head for Tissue Palpation During Minimally Invasive Surgery”. In: *IEEE Sensors Journal* 14 (June 2014), pp. 3283–3291. DOI: [10.1109/JSEN.2014.2328182](https://doi.org/10.1109/JSEN.2014.2328182).
- [159] *Refractive Index Database*. <https://refractiveindex.info/>. Accessed: 2021-08-21.
- [160] Marta Elena Día-García and Rosana Badía-Laiño. “Fluorescence - Instrumentation”. In: *Encyclopedia of Analytical Science (Third Edition)*. Ed. by Paul Worsfold et al. Third Edition. Oxford: Academic Press, 2019, pp. 292–300. ISBN: 978-0-08-101984-9. DOI: <https://doi.org/10.1016/B978-0-12-409547-2.14507-X>. URL: <https://www.sciencedirect.com/science/article/pii/B978012409547214507X>.
- [161] Thorsten Wohland, Sudipta Maiti, and Radek Macháň. *An Introduction to Fluorescence Correlation Spectroscopy*. 2053-2563. IOP Publishing, 2020. ISBN:

- 978-0-7503-2080-1. DOI: [10.1088/978-0-7503-2080-1](https://doi.org/10.1088/978-0-7503-2080-1). URL: <http://dx.doi.org/10.1088/978-0-7503-2080-1>.
- [162] Nathalie Vicente et al. “Photobleaching correction in fluorescence microscopy images”. In: *Journal of Physics: Conference Series* 90 (Dec. 2007), p. 012068. DOI: [10.1088/1742-6596/90/1/012068](https://doi.org/10.1088/1742-6596/90/1/012068).
- [163] Dennis Yang et al. “Evaluation of interventional endoscopy unit efficiency metrics at a tertiary academic medical center”. In: *Endoscopy International Open* 4 (Dec. 2015). DOI: [10.1055/s-0041-108082](https://doi.org/10.1055/s-0041-108082).
- [164] Yu. O. Barmenkov, A. N. Starodumov, and A. A. Lipovskii. “Temperature fiber sensor based on semiconductor nanocrystallite-doped phosphate glasses”. In: *Applied Physics Letters* 73.4 (1998), pp. 541–543. DOI: [10.1063/1.121926](https://doi.org/10.1063/1.121926). eprint: <https://doi.org/10.1063/1.121926>. URL: <https://doi.org/10.1063/1.121926>.
- [165] P. A. S. Jorge et al. “Luminescence-Based Optical Fiber Chemical Sensors”. In: *Fiber and Integrated Optics* 24.3-4 (2005), pp. 201–225. DOI: [10.1080/01468030590922731](https://doi.org/10.1080/01468030590922731). eprint: <https://doi.org/10.1080/01468030590922731>. URL: <https://doi.org/10.1080/01468030590922731>.
- [166] P A S Jorge et al. “Quantum dots as self-referenced optical fibre temperature probes for luminescent chemical sensors”. In: *Measurement Science and Technology* 17.5 (Apr. 2006), pp. 1032–1038. DOI: [10.1088/0957-0233/17/5/s16](https://doi.org/10.1088/0957-0233/17/5/s16). URL: <https://doi.org/10.1088/0957-0233/17/5/s16>.
- [167] Gonzaga de Bastida et al. “Quantum Dots-Based Optical Fiber Temperature Sensors Fabricated by Layer-by-Layer”. In: *IEEE Sensors Journal* 6.6 (2006), pp. 1378–1379. DOI: [10.1109/JSEN.2006.884436](https://doi.org/10.1109/JSEN.2006.884436).
- [168] Javier Bravo et al. “Fiber optic temperature sensor depositing quantum dots inside hollow core fibers using the layer by layer technique”. In: *Third European Workshop on Optical Fibre Sensors*. Ed. by Antonello Cutolo, Brian Culshaw, and José Miguel López-Higuera. Vol. 6619. International Society for Optics and Photonics. SPIE, 2007, pp. 235–238. URL: <https://doi.org/10.1117/12.738388>.
- [169] Antonio Bueno et al. “Temperature Sensor Based on Colloidal Quantum Dots–PMMA Nanocomposite Waveguides”. In: *IEEE Sensors Journal* 12 (Oct. 2012), pp. 3069–3074. DOI: [10.1109/JSEN.2012.2210037](https://doi.org/10.1109/JSEN.2012.2210037).

- [170] Guosheng Zhang et al. “A Low Loss Quantum-Dot-Doped Optical Fiber Temperature Sensor Based on Flexible Print Technology”. In: *IEEE Photonics Journal* 12.3 (2020), pp. 1–8. DOI: [10.1109/JPHOT.2020.2974905](https://doi.org/10.1109/JPHOT.2020.2974905).
- [171] Yi Cai et al. “Optical fiber sensors for metal ions detection based on novel fluorescent materials”. In: *Frontiers in Physics* 8, 552 (Nov. 2020), p. 552. DOI: [10.3389/fphy.2020.598209](https://doi.org/10.3389/fphy.2020.598209).
- [172] Jingjing Guo et al. “Quantum Dots-Doped Tapered Hydrogel Waveguide for Ratiometric Sensing of Metal Ions”. In: *Analytical Chemistry* 90 (Sept. 2018). DOI: [10.1021/acs.analchem.8b03787](https://doi.org/10.1021/acs.analchem.8b03787).
- [173] Federica De Chiara et al. *Sensing applied pressure by triggering electronic quantum many-body excitations in an optical waveguide*. 2021. DOI: [10.48550/ARXIV.2106.13004](https://doi.org/10.48550/ARXIV.2106.13004). URL: <https://arxiv.org/abs/2106.13004>.
- [174] J Mason et al. “Novel fluorescence-based approaches for the study of biogenic amine transporter localization, activity, and regulation”. In: *Journal of neuroscience methods* 143 (May 2005), pp. 3–25. DOI: [10.1016/j.jneumeth.2004.09.028](https://doi.org/10.1016/j.jneumeth.2004.09.028).
- [175] Nataliya Panchuk-Voloshina et al. “Alexa Dyes, a Series of New Fluorescent Dyes that Yield Exceptionally Bright, Photostable Conjugates”. In: *The journal of histochemistry and cytochemistry : official journal of the Histochemistry Society* 47 (Oct. 1999), pp. 1179–88. DOI: [10.1177/002215549904700910](https://doi.org/10.1177/002215549904700910).
- [176] Christian Eggeling, Andreas Volkmer, and Claus Seidel. “Molecular Photobleaching Kinetics of Rhodamine 6G by One- and Two-Photon Induced Confocal Fluorescence Microscopy”. In: *Chemphyschem : a European journal of chemical physics and physical chemistry* 6 (May 2005), pp. 791–804. DOI: [10.1002/cphc.200400509](https://doi.org/10.1002/cphc.200400509).
- [177] Yufeng Zhou et al. “Harnessing the properties of colloidal quantum dots in luminescent solar concentrators”. In: *Chemical Society Reviews* 47 (June 2018). DOI: [10.1039/C7CS00701A](https://doi.org/10.1039/C7CS00701A).
- [178] Sadra Sadeghi et al. “Ultra-Efficient and High-Quality White Light-Emitting Devices using Fluorescent Proteins in Aqueous Medium”. In: *Advanced Materials Technologies* 5 (May 2020). DOI: [10.1002/admt.202000061](https://doi.org/10.1002/admt.202000061).

- [179] Wilfried van Sark et al. “Photooxidation and Photobleaching of Single CdSe/ZnS Quantum Dots Probed by Room-Temperature Time-Resolved Spectroscopy”. In: *Phys. Chem. B* 105 (Aug. 2001). DOI: [10.1021/jp012018h](https://doi.org/10.1021/jp012018h).
- [180] Alicia De San Luis González. “Nanostructured polymeric aqueous dispersions containing quantum dots”. In: 2018.
- [181] Ute Resch-Genger et al. “Quantum Dots Versus Organic Dyes as Fluorescent Labels”. In: *Nature methods* 5 (Oct. 2008), pp. 763–75. DOI: [10.1038/nmeth.1248](https://doi.org/10.1038/nmeth.1248).
- [182] Bin Li et al. “Suppressing the Fluorescence Blinking of Single Quantum Dots Encased in N-type Semiconductor Nanoparticles”. In: *Scientific Reports* 6 (Sept. 2016), p. 32662. DOI: [10.1038/srep32662](https://doi.org/10.1038/srep32662).
- [183] Changgang Yang et al. “Suppressing the photobleaching and photoluminescence intermittency of single near-infrared CdSeTe/ZnS quantum dots with p-phenylenediamine”. In: *Optics Express* 26 (Apr. 2018), p. 11889. DOI: [10.1364/OE.26.011889](https://doi.org/10.1364/OE.26.011889).
- [184] Masaru Kuno et al. ““On”/“off” fluorescence intermittency of single semiconductor quantum dots”. In: *The Journal of Chemical Physics* 115 (July 2001), pp. 1028–1040. DOI: [10.1063/1.1377883](https://doi.org/10.1063/1.1377883).
- [185] Yonglei Sun et al. “Fast Lifetime Blinking in Compact CdSe/CdS Core/Shell Quantum Dots”. In: *The Journal of Physical Chemistry C* 125 (July 2021), pp. 15433–15440. DOI: [10.1021/acs.jpcc.1c03949](https://doi.org/10.1021/acs.jpcc.1c03949).
- [186] J Mason et al. “Novel fluorescence-based approaches for the study of biogenic amine transporter localization, activity, and regulation”. In: *Journal of neuroscience methods* 143 (May 2005), pp. 3–25. DOI: [10.1016/j.jneumeth.2004.09.028](https://doi.org/10.1016/j.jneumeth.2004.09.028).
- [187] Bong Hoon Kim et al. “Multilayer Transfer Printing for Pixelated, Multi-Color Quantum Dot Light-Emitting Diodes”. In: *ACS nano* 10 (Apr. 2016). DOI: [10.1021/acsnano.5b06387](https://doi.org/10.1021/acsnano.5b06387).
- [188] Michelle Regulacio and Ming-Yong Han. “Composition-Tunable Alloyed Semiconductor Nanocrystals”. In: *Accounts of chemical research* 43 (Mar. 2010), pp. 621–30. DOI: [10.1021/ar900242r](https://doi.org/10.1021/ar900242r).

- [189] Haiguang Zhao et al. “Size Dependence of Temperature-Related Optical Properties of PbS and PbS/CdS Core/Shell Quantum Dots”. In: *The Journal of Physical Chemistry C* 118 (Sept. 2014), pp. 20585–20593. DOI: [10.1021/jp503617h](https://doi.org/10.1021/jp503617h).
- [190] Xiaopeng Zheng et al. “Quantum Dots Supply Bulk- and Surface-Passivation Agents for Efficient and Stable Perovskite Solar Cells”. In: (May 2019). DOI: [10.1016/j.joule.2019.05.005](https://doi.org/10.1016/j.joule.2019.05.005).
- [191] Bashir O. Dabbousi et al. “(CdSe)ZnS Core-Shell Quantum Dots - Synthesis and Characterization of a Size Series of Highly Luminescent Nanocrystallites”. In: *Journal of Physical Chemistry B* 101 (1997), pp. 9463–9475.
- [192] Xiaoyong Wang et al. “Surface-Related Emission in Highly Luminescent CdSe Quantum Dots”. In: *Nano Letters - NANO LETT* 3 (July 2003). DOI: [10.1021/nl0342491](https://doi.org/10.1021/nl0342491).
- [193] Dmitri Talapin et al. “CdSe/CdS/ZnS and CdSe/ZnSe/ZnS core-shell-shell nanocrystals”. In: *Journal of Physical Chemistry B - J PHYS CHEM B* 108 (Nov. 2004). DOI: [10.1021/jp046481g](https://doi.org/10.1021/jp046481g).
- [194] Huiyun Liu. “Quantum dot optoelectronic devices: lasers, photodetectors and solar cells”. In: *Journal of Physics D Applied Physics* 48 (Aug. 2015), p. 363001. DOI: [10.1088/0022-3727/48/36/363001](https://doi.org/10.1088/0022-3727/48/36/363001).
- [195] Prem Prabhakaran et al. “Quantum dots (QDs) for photonic applications”. In: *Optical Materials Express* 2 (May 2012), pp. 578–593. DOI: [10.1364/OME.2.000578](https://doi.org/10.1364/OME.2.000578).
- [196] Christopher Murray, D. Norris, and M. Bawendi. “Murray, C.B., Norris, D.J. Bawendi, M.G. Synthesis and characterization of nearly monodisperse CdE (E = S, Se, Te) semiconductor nanocrystallites. J. Am. Chem. Soc. 115, 87068715”. In: *Journal of The American Chemical Society - J AM CHEM SOC* 115 (Nov. 1992). DOI: [10.1021/ja00072a025](https://doi.org/10.1021/ja00072a025).
- [197] Lianhua Qu, Z. Peng, and Xiaogang Peng. “Qu, L., Peng, Z.A. Peng, X. Alternative routes toward high quality CdSe nanocrystals. Nano Lett. 1, 333-337”. In: *Nano Letters - NANO LETT* 1 (June 2001). DOI: [10.1021/nl0155532](https://doi.org/10.1021/nl0155532).

- [198] Dmitri Talapin et al. “Highly Luminescent Monodisperse CdSe and CdSe/ZnS Nanocrystals Synthesized in a HexadecylamineTrioctylphosphine OxideTrioctylphosphine Mixture”. In: *Nano Letters - NANO LETT* 1 (Mar. 2001). DOI: [10.1021/nl0155126](https://doi.org/10.1021/nl0155126).
- [199] A. Gadalla, Mahmoud Sayed Abd El-sadek, and R. Hamood. “Characterization of CdSe core and CdSe/ZnS core/shell quantum dots synthesized using a modified method”. In: *Chalcogenide Letters* 14 (July 2017), pp. 239–249.
- [200] Pedro Jorge et al. “Optical Fiber Sensing Using Quantum Dots”. In: *Sensors* 7 (Dec. 2007). DOI: [10.3390/s7123489](https://doi.org/10.3390/s7123489).
- [201] Sunil Kumar, Rajesh Purohit, and M.M. Malik. “Properties and Applications of Polymer Matrix Nano Composite Materials”. In: *Materials Today: Proceedings* 2.4 (2015). 4th International Conference on Materials Processing and Characterization, pp. 3704–3711. ISSN: 2214-7853. DOI: <https://doi.org/10.1016/j.matpr.2015.07.148>. URL: <https://www.sciencedirect.com/science/article/pii/S2214785315003934>.
- [202] Jiahao Yu, Xiongbin Wang, and Rui Chen. “Optical waveguiding properties of colloidal quantum dots doped polymer microfibers”. In: *Opt. Express* 26.10 (May 2018), pp. 13408–13415. DOI: [10.1364/OE.26.013408](https://doi.org/10.1364/OE.26.013408). URL: <http://www.opticsexpress.org/abstract.cfm?URI=oe-26-10-13408>.
- [203] George Odian. *Principles of Polymerization, Fourth Edition*. John Wiley Sons, Inc., 2004. DOI: [10.1002/047147875X](https://doi.org/10.1002/047147875X).
- [204] Jordan M. Kaiser and Brian K. Long. “Recent developments in redox-active olefin polymerization catalysts”. In: *Coordination Chemistry Reviews* 372 (2018), pp. 141–152. ISSN: 0010-8545. DOI: <https://doi.org/10.1016/j.ccr.2018.06.007>. URL: <https://www.sciencedirect.com/science/article/pii/S0010854518300638>.
- [205] Rouaida M. Abozaid et al. “Optical properties and fluorescence of quantum dots CdSe/ZnS-PMMA composite films with interface modifications”. In: *Optical Materials* 92 (2019), pp. 405–410. ISSN: 0925-3467. DOI: <https://doi.org/10.1016/j.optmat.2019.05.012>. URL: <https://www.sciencedirect.com/science/article/pii/S0925346719303131>.

- [206] Joseba Zubia and Jon Arrue. “Plastic Optical Fibers: An Introduction to Their Technological Processes and Applications”. In: *Optical Fiber Technology* 2 (Apr. 2001), pp. 101–140. DOI: [10.1006/ofte.2000.0355](https://doi.org/10.1006/ofte.2000.0355).
- [207] Olaf Ziemann et al. *POF Polymer Optical Fibers for Data Communication*. Springer, Berlin, Heidelberg, 2002. DOI: <https://doi.org/10.1007/978-3-662-04861-0>.
- [208] Hongyi Zhang et al. “Photo-instability of CdSe/ZnS quantum dots in poly(methylmethacrylate) film”. In: *Journal of Applied Physics* 114.24 (Dec. 2013). ISSN: 0021-8979. DOI: [10.1063/1.4857055](https://doi.org/10.1063/1.4857055). URL: <https://www.osti.gov/biblio/22217728>.
- [209] Amjad Y. Nazzal et al. “Environmental Effects on Photoluminescence of Highly Luminescent CdSe and CdSe/ZnS Core/Shell Nanocrystals in Polymer Thin Films”. In: *The Journal of Physical Chemistry B* 108.18 (2004), pp. 5507–5515. DOI: [10.1021/jp035361q](https://doi.org/10.1021/jp035361q). eprint: <https://doi.org/10.1021/jp035361q>. URL: <https://doi.org/10.1021/jp035361q>.
- [210] Rouaida Mohamed Abozaid et al. “Polymer composite films and nanofibers doped with core-shell quantum dots”. In: *Journal of Optoelectronics and Advanced Materials* 22.1-2 (2020), pp. 67–74.
- [211] Wilfried van Sark et al. “Blueing, Bleaching, and Blinking of Single CdSe/ZnS Quantum Dots”. In: *ChemPhysChem* 3 (Oct. 2002), pp. 871–879. DOI: [10.1002/1439-7641\(20021018\)3:10<871::AID-CPHC871>3.0.CO;2-T](https://doi.org/10.1002/1439-7641(20021018)3:10<871::AID-CPHC871>3.0.CO;2-T).
- [212] Yan Zhang, Jiaheng Nie, and Lijie Li. “Piezotronic effect on the luminescence of quantum dots for micro/nano-newton force measurement”. In: *Nano Research* 11.4 (Mar. 2018), pp. 1977–1986. DOI: [10.1007/s12274-017-1814-x](https://doi.org/10.1007/s12274-017-1814-x). URL: <https://doi.org/10.1007/s12274-017-1814-x>.
- [213] B. O. Dabbousi et al. “(CdSe)ZnS Core-Shell Quantum Dots: Synthesis and Characterization of a Size Series of Highly Luminescent Nanocrystallites”. In: *The Journal of Physical Chemistry B* 101.46 (1997), pp. 9463–9475. DOI: [10.1021/jp971091y](https://doi.org/10.1021/jp971091y). eprint: <https://doi.org/10.1021/jp971091y>. URL: <https://doi.org/10.1021/jp971091y>.
- [214] *pvtrace*. URL: <https://pypi.org/project/pvtrace/> (visited on 04/16/2022).

- [215] Tung-Ting Ke et al. “CdSe Quantum Dots Embedded in Matrices: Characterization and Application for Low-Pressure and Temperature Sensors”. In: *IEEE Sensors Journal* 16 (Apr. 2016), pp. 1–1. DOI: [10.1109/JSEN.2016.2521865](https://doi.org/10.1109/JSEN.2016.2521865).
- [216] Bo Li et al. “Pressure-dependent photoluminescence of CdSe/ZnS quantum dots: Critical point of different pressure regimes”. In: *Physics Letters A* 383 (Feb. 2019). DOI: [10.1016/j.physleta.2019.01.059](https://doi.org/10.1016/j.physleta.2019.01.059).
- [217] Jianjun Tian and Betzaida Garcia. “Semiconductor quantum dot-sensitized solar cells”. In: *Nano reviews* 4 (Oct. 2013). DOI: [10.3402/nano.v4i0.22578](https://doi.org/10.3402/nano.v4i0.22578).
- [218] Nina Sultanova, S. Kasarova, and I. Nikolov. “Dispersion Properties of Optical Polymers”. In: *ACTA PHYSICA POLONICA A* 116 (Oct. 2009), pp. 585–587. DOI: [10.12693/APhysPolA.116.585](https://doi.org/10.12693/APhysPolA.116.585).
- [219] Nor Hamizi and Mohd Johan. “Optical Properties of CdSe Quantum Dots via Non-TOP based Route”. In: *International Journal of Electrochemical Science* 7 (Sept. 2012).
- [220] A. Schiavi and A. Prato. “Non-linear stress relaxation of polymers: experimental evidences and stretched exponential model”. In: (July 2016).
- [221] Norbert Reitingner et al. “Radiationless energy transfer in CdSe/ZnS quantum dot aggregates embedded in PMMA”. In: *physica status solidi (a)* 208 (Mar. 2011), pp. 710–714. DOI: [10.1002/pssa.201026590](https://doi.org/10.1002/pssa.201026590).
- [222] Wei Chen et al. “Tactile Sensors for Friction Estimation and Incipient Slip Detection – Towards Dexterous Robotic Manipulation: A Review”. In: *IEEE Sensors Journal* PP (Sept. 2018), pp. 1–1. DOI: [10.1109/JSEN.2018.2868340](https://doi.org/10.1109/JSEN.2018.2868340).
- [223] Shan Luo et al. “Robotic Tactile Perception of Object Properties: A Review”. In: *Mechatronics* 48 (Dec. 2017). DOI: [10.1016/j.mechatronics.2017.11.002](https://doi.org/10.1016/j.mechatronics.2017.11.002).
- [224] Hanna Yousef, Mehdi Boukallel, and Kaspar Althoefer. “Tactile sensing for dexterous in-hand manipulation in robotics—A review”. In: *Sensors and Actuators A: Physical* 167 (June 2011), pp. 171–187. DOI: [10.1016/j.sna.2011.02.038](https://doi.org/10.1016/j.sna.2011.02.038).
- [225] Johan Tegin and Jan Wikander. “Tactile sensing in intelligent robotic manipulation—A review”. In: *Industrial Robot: An International Journal* 32 (Feb. 2005). DOI: [10.1108/01439910510573318](https://doi.org/10.1108/01439910510573318).

- [226] Liang Zou et al. “Novel Tactile Sensor Technology and Smart Tactile Sensing Systems: A Review”. In: *Sensors* 17 (Nov. 2017), p. 2653. DOI: [10.3390/s17112653](https://doi.org/10.3390/s17112653).
- [227] Andreas Janshoff and Claudia Steinem. “Piezoelectric Sensors”. In: 2007. DOI: [10.1007/978-3-540-36568-6](https://doi.org/10.1007/978-3-540-36568-6).
- [228] MI Tiwana and Nigel Lovell. “A Review of Tactile Sensing Technologies with Applications in Biomedical Engineering”. In: *Sensors and Actuators A: Physical* 179 (June 2012), pp. 17–31. DOI: [10.1016/j.sna.2012.02.051](https://doi.org/10.1016/j.sna.2012.02.051).
- [229] Pinyo Puangmali et al. “State-of-the-Art in Force and Tactile Sensing for Minimally Invasive Surgery”. In: *IEEE Sensors Journal* 8.4 (2008), pp. 371–381. DOI: [10.1109/JSEN.2008.917481](https://doi.org/10.1109/JSEN.2008.917481).
- [230] Sijie Yang. “A review on actuation and sensing techniques for MEMS-based microgrippers”. In: *Journal of Micro-Bio Robotics* 13 (Oct. 2017), pp. 1–14. DOI: [10.1007/s12213-017-0098-2](https://doi.org/10.1007/s12213-017-0098-2).
- [231] S. Tadigadapa and Kiron Mateti. “Piezoelectric MEMS Sensors: State-of-the-Art and Perspectives”. In: *Measurement Science and Technology* 20 (July 2009), p. 092001. DOI: [10.1088/0957-0233/20/9/092001](https://doi.org/10.1088/0957-0233/20/9/092001).
- [232] Paul Regtien and Edwin Dertien. *Sensors for Mechatronics*. Jan. 2012. DOI: [10.1016/C2011-0-06204-X](https://doi.org/10.1016/C2011-0-06204-X).
- [233] Alan Morris and Reza Langari. *Measurement and Instrumentation*. Jan. 2012. DOI: [10.1016/C2009-0-63052-X](https://doi.org/10.1016/C2009-0-63052-X).
- [234] Hongbin Liu et al. “Rolling Indentation Probe for Tissue Abnormality Identification During Minimally Invasive Surgery”. In: *Robotics, IEEE Transactions on* 27 (July 2011), pp. 450–460. DOI: [10.1109/TR0.2011.2127210](https://doi.org/10.1109/TR0.2011.2127210).
- [235] Pencilla Lang. “Optical Tactile Sensors for Medical Palpation”. In: *Canada-Wide Science Fair* (Mar. 2004), pp. 1–7.
- [236] Nathan Lepora, Kirsty Aquilina, and Luke Cramphorn. “Exploratory Tactile Servoing With Active Touch”. In: *IEEE Robotics and Automation Letters* PP (Jan. 2017), pp. 1–1. DOI: [10.1109/LRA.2017.2662071](https://doi.org/10.1109/LRA.2017.2662071).
- [237] Wenzhen Yuan et al. “Shape-independent Hardness Estimation Using Deep Learning and a GelSight Tactile Sensor”. In: (Apr. 2017).

- [238] Yancheng Wang et al. “Flexible Tactile Sensor Array for Distributed Tactile Sensing and Slip Detection in Robotic Hand Grasping”. In: *Sensors and Actuators A: Physical* 297 (Aug. 2019). DOI: [10.1016/j.sna.2019.07.036](https://doi.org/10.1016/j.sna.2019.07.036).
- [239] Mohammad Saadatzi et al. “Modeling and Fabrication of Scalable Tactile Sensor Arrays for Flexible Robot Skins”. In: *IEEE Sensors Journal* PP (May 2019), pp. 1–1. DOI: [10.1109/JSEN.2019.2915362](https://doi.org/10.1109/JSEN.2019.2915362).
- [240] Lona Vyas et al. “Flexible robotics”. In: *BJU international* 107 (Jan. 2011), pp. 187–9. DOI: [10.1111/j.1464-410X.2010.09886.x](https://doi.org/10.1111/j.1464-410X.2010.09886.x).
- [241] Hui Xie et al. “A Fiber-Optics-Based Body Contact Sensor for a Flexible Manipulator”. In: *IEEE Sensors Journal* 15.6 (2015), pp. 3543–3550. DOI: [10.1109/JSEN.2015.2392384](https://doi.org/10.1109/JSEN.2015.2392384).
- [242] Junghwan Back et al. “Feasibility study- novel optical soft tactile array sensing for minimally invasive surgery”. In: *2015 IEEE/RSJ International Conference on Intelligent Robots and Systems (IROS)*. 2015, pp. 1528–1533. DOI: [10.1109/IROS.2015.7353570](https://doi.org/10.1109/IROS.2015.7353570).
- [243] Liu da, Dapeng Zhang, and Tianmiao Wang. “Overview of the vascular interventional robot”. In: *The international journal of medical robotics + computer assisted surgery : MRCAS* 4 (Dec. 2008), pp. 289–94. DOI: [10.1002/rcs.212](https://doi.org/10.1002/rcs.212).
- [244] Zhanat Kappasov, Juan Antonio Corrales Ramon, and Veronique Perdereau. “Tactile sensing in dexterous robot hands — Review”. In: *Robotics and Autonomous Systems* 74 (July 2015). DOI: [10.1016/j.robot.2015.07.015](https://doi.org/10.1016/j.robot.2015.07.015).
- [245] Hanna Yousef, Mehdi Boukallel, and Kaspar Althoefer. “Tactile sensing for dexterous in-hand manipulation in robotics—A review”. In: *Sensors and Actuators A: Physical* 167 (June 2011), pp. 171–187. DOI: [10.1016/j.sna.2011.02.038](https://doi.org/10.1016/j.sna.2011.02.038).
- [246] Ravinder S. Dahiya et al. “Tactile Sensing—From Humans to Humanoids”. In: *IEEE Transactions on Robotics* 26.1 (2010), pp. 1–20. DOI: [10.1109/TR0.2009.2033627](https://doi.org/10.1109/TR0.2009.2033627).
- [247] Hiroyuki Nakamoto et al. “Development of tactile sensor using magnetic elements”. In: *2011 IEEE Workshop on Robotic Intelligence In Informationally Structured Space*. 2011, pp. 37–42. DOI: [10.1109/RIISS.2011.5945783](https://doi.org/10.1109/RIISS.2011.5945783).

- [248] Sunjong Oh et al. "Remote tactile sensing system integrated with magnetic synapse". In: *Scientific Reports* 7 (Dec. 2017). DOI: [10.1038/s41598-017-17277-2](https://doi.org/10.1038/s41598-017-17277-2).
- [249] Takumi Kawasetsu et al. "Mexican-Hat-Like Response in a Flexible Tactile Sensor Using a Magnetorheological Elastomer". In: *Sensors* 18 (Feb. 2018), p. 587. DOI: [10.3390/s18020587](https://doi.org/10.3390/s18020587).
- [250] Hongbo Wang et al. "Design Methodology for Magnetic Field-Based Soft Tri-Axis Tactile Sensors". In: *Sensors* 16 (Aug. 2016). DOI: [10.3390/s16091356](https://doi.org/10.3390/s16091356).
- [251] Masahiro Ohka, H. Kobayashi, and Y. Mitsuya. "Sensing characteristics of an optical three-axis tactile sensor mounted on a multi-fingered robotic hand". In: Sept. 2005, pp. 493–498. DOI: [10.1109/IR0S.2005.1545264](https://doi.org/10.1109/IR0S.2005.1545264).
- [252] Hisham Hisham. "Optical Fiber Sensing Technology: Basics, Classifications and Applications". In: *American Journal of Remote Sensing* 6 (Feb. 2018). DOI: [10.11648/j.ajrs.20180601.11](https://doi.org/10.11648/j.ajrs.20180601.11).
- [253] Panagiotis Polygerinos et al. "MRI-Compatible Intensity-Modulated Force Sensor for Cardiac Catheterization Procedures". In: *IEEE Transactions on Biomedical Engineering* 58.3 (2011), pp. 721–726. DOI: [10.1109/TBME.2010.2095853](https://doi.org/10.1109/TBME.2010.2095853).
- [254] Riadh Kadhim. "STRAIN MEASUREMENT BY USING PHASE MODULATED FIBER OPTIC SENSORS TECHNOLOGY". In: *Diyala Journal of Engineering Sciences* 8 (Mar. 2015), pp. 27–41. DOI: [10.24237/djes.2015.08103](https://doi.org/10.24237/djes.2015.08103).
- [255] J.David Zook et al. "Fiber-optic vibration sensor based on frequency modulation of light-excited oscillators". In: *Sensors and Actuators A: Physical* 83 (Jan. 2004), pp. 270–276. DOI: [10.1016/S0924-4247\(99\)00379-9](https://doi.org/10.1016/S0924-4247(99)00379-9).
- [256] R.E. Saad et al. "Distributed-force recovery for a planar photoelastic tactile sensor". In: *IEEE Transactions on Instrumentation and Measurement* 45.2 (1996), pp. 541–546. DOI: [10.1109/19.492783](https://doi.org/10.1109/19.492783).
- [257] Amjad Y. Nazzal et al. "Photoactivated CdSe Nanocrystals as Nanosensors for Gases". In: *Nano Letters* 3.6 (2003), pp. 819–822. DOI: [10.1021/nl0340935](https://doi.org/10.1021/nl0340935). eprint: <https://doi.org/10.1021/nl0340935>. URL: <https://doi.org/10.1021/nl0340935>.

- [258] Radislav Potyrailo and Andrew Leach. “Selective gas nanosensors with multisize CdSe nanocrystal/polymer composite films and dynamic pattern recognition”. In: *Applied Physics Letters* 88 (Mar. 2006), pp. 134110–134110. DOI: [10.1063/1.2190272](https://doi.org/10.1063/1.2190272).
- [259] Manuela F. Frasco and Nikos Chaniotakis. “Semiconductor Quantum Dots in Chemical Sensors and Biosensors”. In: *Sensors* 9.9 (2009), pp. 7266–7286. ISSN: 1424-8220. DOI: [10.3390/s90907266](https://doi.org/10.3390/s90907266). URL: <https://www.mdpi.com/1424-8220/9/9/7266>.
- [260] Raúl J. Martín-Palma, Miguel Manso, and Vicente Torres-Costa. “Optical Biosensors Based on Semiconductor Nanostructures”. In: *Sensors* 9.7 (2009), pp. 5149–5172. ISSN: 1424-8220. DOI: [10.3390/s90705149](https://doi.org/10.3390/s90705149). URL: <https://www.mdpi.com/1424-8220/9/7/5149>.
- [261] Qiang Ma and Xingguang Su. “Recent advances and applications in QDs-based sensors”. In: *Analyst* 136 (23 2011), pp. 4883–4893. DOI: [10.1039/C1AN15741H](https://doi.org/10.1039/C1AN15741H). URL: <http://dx.doi.org/10.1039/C1AN15741H>.
- [262] Fei Ma, Chen-chen Li, and Chun-yang Zhang. “Development of quantum dot-based biosensors: principles and applications”. In: *Journal of Materials Chemistry B* 6 (Aug. 2018). DOI: [10.1039/C8TB01869C](https://doi.org/10.1039/C8TB01869C).
- [263] Ibrahim Khan, Khalid Saeed, and Idrees Khan. “Nanoparticles: Properties, applications and toxicities”. In: *Arabian Journal of Chemistry* 12.7 (2019), pp. 908–931. ISSN: 1878-5352. DOI: <https://doi.org/10.1016/j.arabjc.2017.05.011>. URL: <https://www.sciencedirect.com/science/article/pii/S1878535217300990>.
- [264] Dnyandeo Pawar and Sangeeta Kale. “A review on nanomaterial-modified optical fiber sensors for gases, vapors and ions”. In: *Microchimica Acta* 186 (Mar. 2019). DOI: [10.1007/s00604-019-3351-7](https://doi.org/10.1007/s00604-019-3351-7).
- [265] Byoungho Lee. “Lee, B.: Review of the Present Status of Optical Fiber Sensors. Optical Fiber Technology 9, 57-79”. In: *Optical Fiber Technology* 9 (Apr. 2003), pp. 57–79. DOI: [10.1016/S1068-5200\(02\)00527-8](https://doi.org/10.1016/S1068-5200(02)00527-8).
- [266] Aitor Urrutia, Javier Goicoechea, and Francisco Arregui. “Optical Fiber Sensors Based on Nanoparticle-Embedded Coatings”. In: *Journal of Sensors* 2015 (July 2015), pp. 1–18. DOI: [10.1155/2015/805053](https://doi.org/10.1155/2015/805053).

- [267] Elosua Cesar et al. “Micro and Nanostructured Materials for the Development of Optical Fibre Sensors”. In: *Sensors* 17 (Oct. 2017), p. 2312. DOI: [10.3390/s17102312](https://doi.org/10.3390/s17102312).
- [268] Bing Yin et al. “Piezo-phototronic effect enhanced pressure sensor based on ZnO/NiO core/shell nanorods array”. In: *Nano Energy* 21 (2016), pp. 106–114. ISSN: 2211-2855. DOI: <https://doi.org/10.1016/j.nanoen.2016.01.007>. URL: <https://www.sciencedirect.com/science/article/pii/S2211285516000185>.
- [269] Mingzeng Peng et al. “High-Resolution Dynamic Pressure Sensor Array Based on Piezo-phototronic Effect Tuned Photoluminescence Imaging”. In: *ACS nano* 9 (Feb. 2015). DOI: [10.1021/acs.nano.5b00072](https://doi.org/10.1021/acs.nano.5b00072).
- [270] Bing Yin et al. “Piezo-phototronic effect enhanced pressure sensor based on ZnO/NiO core/shell nanorods array”. In: *Nano Energy* 21 (2016), pp. 106–114. ISSN: 2211-2855. DOI: <https://doi.org/10.1016/j.nanoen.2016.01.007>. URL: <https://www.sciencedirect.com/science/article/pii/S2211285516000185>.
- [271] “The enhanced performance of piezoelectric nanogenerator via suppressing screening effect with Au particles/ZnO nanoarrays Schottky junction”. In: *Nano Research* 9 (2016), pp. 372–379. DOI: <https://doi.org/10.1007/s12274-015-0916-6>.
- [272] Sebastian Reparaz et al. “Size-dependent strain effects in self-assembled CdSe quantum dots with Zn_{0.38}Cd_{0.23}Mg_{0.39}Se barriers”. In: *Applied Physics Letters* 89 (Jan. 2007), pp. 231109–231109. DOI: [10.1063/1.2402881](https://doi.org/10.1063/1.2402881).
- [273] Charina Choi et al. “Strain-Dependent Photoluminescence Behavior of CdSe/CdS Nanocrystals with Spherical, Linear, and Branched Topologies”. In: *Nano letters* 9 (Sept. 2009), pp. 3544–9. DOI: [10.1021/nl9017572](https://doi.org/10.1021/nl9017572).
- [274] C. Choi et al. “Luminescent nanocrystal stress gauge”. In: *Proceedings of the National Academy of Sciences* 107 (2010), pp. 21306–21310.
- [275] O. Madelung, U. Rössler, and M. Schulz, eds. *Landolt-Börnstein - Group III Condensed Matter · Volume 41B: “II-VI and I-VII Compounds; Semimagnetic Compounds” in SpringerMaterials* (https://doi.org/10.1007/10681719_602). ac-

- cessed 2021-06-07. DOI: [10.1007/10681719_602](https://doi.org/10.1007/10681719_602). URL: https://materials.springer.com/lb/docs/sm_lbs_978-3-540-31359-5_602.
- [276] Sayed M. B. Albahrani et al. “Quantum dots to probe temperature and pressure in highly confined liquids”. In: *RSC Adv.* 8 (41 2018), pp. 22897–22908. DOI: [10.1039/C8RA03652G](https://doi.org/10.1039/C8RA03652G). URL: <http://dx.doi.org/10.1039/C8RA03652G>.
- [277] Sayed M. B. Albahrani et al. “Quantum dots to probe temperature and pressure in highly confined liquids”. In: *RSC Adv.* 8 (41 2018), pp. 22897–22908. DOI: [10.1039/C8RA03652G](https://doi.org/10.1039/C8RA03652G). URL: <http://dx.doi.org/10.1039/C8RA03652G>.
- [278] Bo Li et al. “Pressure-dependent photoluminescence of CdSe/ZnS quantum dots: Critical point of different pressure regimes”. In: *Physics Letters A* 383 (Feb. 2019). DOI: [10.1016/j.physleta.2019.01.059](https://doi.org/10.1016/j.physleta.2019.01.059).
- [279] Francis Arthur Jenkins and Harvey Elliott White. *Fundamentals of Optics - 4th Edition*. Houston, TX, U.S.A.: Mcgraw-Hill College, 1976.